Rotor Eddy Current Loss Prediction and Demagnetization Assessment in Permanent Magnet Machines

by

Sreeju S Nair

A thesis submitted in fulfilment of the requirements for the degree of Doctor of Philosophy

Department of Electronic and Electrical Engineering
Faulty of Engineering
The University of Sheffield

January 2017

ABSTRACT

Electrical machines with rare-earth permanent magnets (PMs) exhibit high torque density and good efficiency over a wide operation range. However, the increased rotor eddy current loss under worst operating conditions can reduce the machine efficiency and also increases the magnet operating temperature which in turn may result in its partial demagnetization especially under the event of faults.

The research underpinned in this thesis describes the methods to tackle the issues concerning the machine complexities and also the computational burden while predicting 3-dimensional (3D) rotor eddy current loss in PM machines. Magnet loss variation with change in field weakening angle is studied comprehensively based on the interaction between armature and the slotting harmonics and also with change in the magnet pole arc angle. The novel 3D Fourier method proposed in this thesis accounts for the natural eddy current boundaries within the magnet, derives the pattern of eddy current loss variations associated with different magnetic field harmonic components with increase in axial and circumferential number of segmentations of PMs in surface mounted PM (SPM) machines. The significance of the eddy current source (flux density variations) components and the eddy current density components towards the contribution of the magnet loss is examined. The diffusion of the magnetic field along the axial and circumferential direction is included in the proposed method to accurately predict the rotor eddy current loss at high frequency operating conditions. The total 3D magnet loss accounting all the armature harmonic frequencies is predicted for SPM and interior permanent magnet (IPM) machines with increase in axial and circumferential number of segmentations. The after effects of the increased rotor eddy current loss is investigated in detail towards the last part of the thesis. The continuous demagnetization assessment method is proposed to assess the partial demagnetization in PMs when the machine is operating under different fault conditions at increased magnet temperatures and also predicts the post fault performance.

ഓം ഹരി ശ്രീ ഗണപതയേ നമഃ

ഗുരുനാഥാൻ തുണചെയ്ക സന്തതം

തിരുനാമങ്ങൾ നാവിന്മേലെപ്പോഴും

പിരിയാതെയിരിക്കണം നമ്മുടെ

നരജന്മം സഫലമാക്കീടുവാൻ !

My (guru) teacher please help me always to keep the sacred knowledge always in my tongue, and thereby making my life fruitful.

(Njanappana of Poonthanam,Verse 1)

This Thesis is Dedicated

To My Parents,

K.M Sreedharan Nair

C.K Saraswathi Amma

And

My Family

ACKNOWLEDGEMENTS

Let me express my sincere gratitude to Prof. Jiabin Wang for guiding and sailing me through this enduring Journey, called PhD. He has offered me loads of favours and encouragements when I got confused and lost in my research work. He had spent plenty of time on our 3 years' weekly meetings and also for correcting my project reports and publications. I feel extremely fortunate to have him as my supervisor who helped me to gain the technical expertise and the interpersonal skills during the course of my research degree. I would also like to express my indebtedness to ABB Corporate Research-Sweden for funding the research work and guiding me throughout the course of my research program. I wish to thank Dr. Robert Chin, Dr. Iakovos Manolas, Dr. Dmitry Svechkarenko and Dr. Minos Beniakar of ABB Corporate Research-Sweden for their valuable inputs during our project review meetings. I also wish to thank my second supervisor, Prof. Kais Atallah and also the head of electrical machines and drives group Prof. Zi-Qiang Zhu for their continuous motivation.

I also would like to express my great thanks to my colleagues (also friends) who contributed to this thesis, including Dr. Vipulkumar I. Patel for his help on demagnetization studies, Liang Chen for helping me to develop a computationally efficient MATLAB scrip for 3D magnet loss predictions and also for the brainstorming sessions we had together, Dr. Tianfu Sun for his help while performing experimental testing, Dr. Bhaskar Sen for the technical expertise on analytical computations, Dr. Xiao Chen and Bo Wang for their help on frozen permeability computations.

My acknowledgements are also given to the dedicated technicians in EMD group, particularly John A. Wilkinson for his help on the development of my rotor prototypes and the experimental setup. Also thanks to my friends and previous colleagues S. Janardana and Arpee Raju for their timely help in drafting the machine drawings before prototyping.

My friends, particularly from the department Chaohui Liu, Mikail Koc, Dr. Premlal Balakrishnapillai, Dhilli Babu, also deserve my big thanks. They award me a joyful and wonderful PhD life which will never be forgotten.

I am also grateful to my former supervisors Prof. Krishna Vasudevan (in my engineering studies at IIT Madras, India), Dr. Jabez Dhinagar (my HOD at TVS motor company Ltd. India) for their recommendations to my PhD application at the very beginning.

Last but not the least, I would like to thank my parents, my in-laws, my beloved wife Remya and my little princes Sreeya who are always concerned about me, encouraged me and feel pride of me. I love you all.

TABLE OF CONTENTS

CHAPTER 1
Introduction to Rotor Eddy Current Loss Prediction in Permanent Magnet Machines

1.1 Introduction

Permanent magnet (PM) machines especially employing rare earth magnets are used in a variety of low, medium and high speed applications such as machine tools [1-3], compressors [4, 5], automotive- electric and hybrid [6-11] , aerospace[12, 13], wind power generations [14, 15] etc. These machines are distinct from their magnet less counter parts due to their higher efficiency, higher power and torque density, lighter weight, reduced torque ripple and better power factor [16, 17]. These attributes are particularly attractive for PM machines despite of its relatively high cost due to PMs.

However, the remanent induction associated with majority of ferrite and rare earth magnets, such as NdFeB, used in PM machines are quite sensitive to their temperature rise during operation, any reduction of which can degrade the machine performance under operation. The magnet temperature rise is predominantly associated with the rotor losses, which is worsened by the poor heat transfer from the rotor by convection through the machine air gap and also the limited heat dissipation via shaft.

The rotor loss in PM machines is mainly associated with the eddy currents in the magnets and in the rotor retaining sleeve (mostly for surface mounted PM machines designed for high speed applications) which results from the change in the rotor magnetic field with respect to time. The presence of hysteresis loss in magnets are generally very low in comparison with the eddy current loss. This is because a well-designed electrical machine exhibits negligible hysteresis loss in their magnets as they are operating only in the second quadrant of the B-H curve and the minor loops formed from the flux density variations are insignificant [18-20].

This chapter discusses causes of rotor eddy current loss and the necessity of rotor eddy current loss prediction, outlines the current state of art, and identifies the remaining problems which are needed to be addressed in the computationally effective rotor eddy current loss prediction in PM machines. Subsequently, the overview of this thesis and the list of publications are presented.

1.2 Cause of Rotor Eddy Current Loss

The eddy current loss associated with the magnets and the retaining sleeve are affected by the machine configuration such as stator structure (slot-less or slotted), winding configuration (integral slot distributed winding or fractional slot-concentrated winding), PM topology (surface mounted or interior) and also magnet segmentation (circumferential, axial). In addition to machine configuration its operating conditions (normal or field weakening), inverter drive mode, viz., brushless DC (BLDC) or brushless AC (BLAC) and the carrier frequency of the inverter switching also affects the rotor eddy current loss.

Surface mounted permanent magnet (SPM) machines with slot-less winding is expected to have higher magnet losses due to direct exposure of the magnets towards the temporal and spatial armature harmonics. The variation of the magnetic field in the magnets due to the presence of stator slot openings causes no-load eddy current loss component in them, the quantity of which is being dependent on the width of the slot openings and also the pole/slot number combination. The concentrated winding configuration, also known as modular [8, 21-25], is expected to deliver high efficiency and high torque density. However, in modular PM machines, the stator magneto motive force (MMF) distribution has a larger amount of space harmonics, and also the fundamental stator MMF has fewer poles than the PM rotor. The torque being developed by the interaction of a higher order stator space harmonic MMF with the field of the permanent magnets. Consequently, both the lower and higher order space harmonic MMFs rotating at different speeds to that of the rotor magnets can induce significant eddy currents in the magnets and incur

loss. In BLDC mode of operation, the armature current will have rich temporal harmonics and hence expected to produce more magnet losses in comparison to sinusoidal operation. The slotting effect does not change the contents of the armature reaction field but affects the magnitudes of harmonics at different operating conditions. The carrier harmonics produced by the PWM inverter may also cause relatively large harmonic eddy-current losses while using magnets with larger conductivity, and when the frequency of the carrier is over a few kHz. The method of axial and circumferential segmentations [26, 27] is devised for directly reducing the magnet eddy current loss without altering the PM machine topology. This method of magnet segmentation is illustrated in Fig. 1-1.

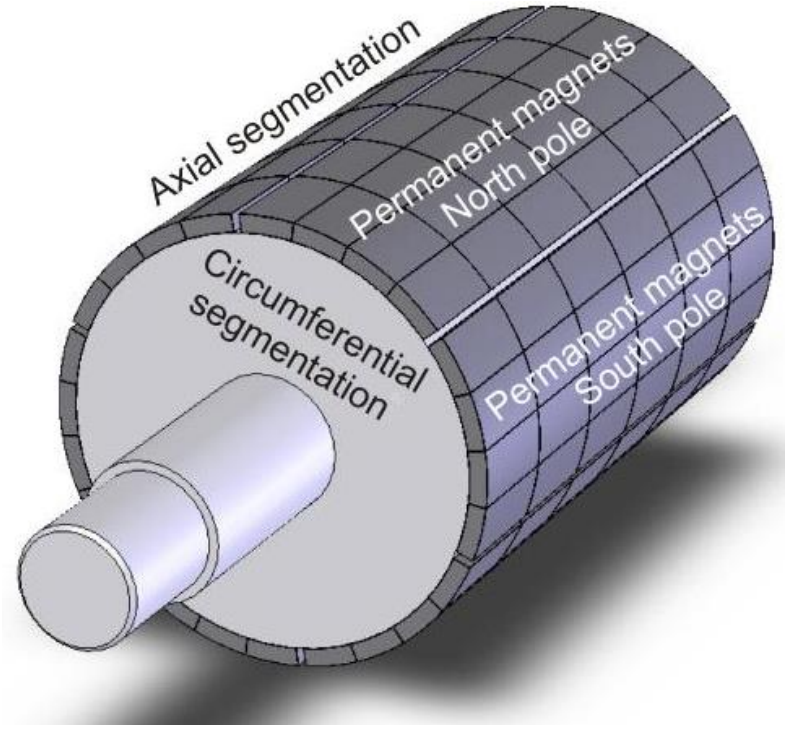

Fig. 1-1. Axial and circumferential segmentation for the permanent magnets (Ref. www.emeraldinsight.com).

For an interior permanent magnet (IPM) machine the rotor eddy current loss can also become significant while operating at high speeds and at high current conditions. This is because the flux barrier becomes saturated under these conditions. Hence for IPM machines the eddy currents in magnets due to space and time harmonics and sub harmonics, caused by modular winding,

slotting effect, inverter drives can become large at the worst operating conditions of the machine.

Hence eddy current loss in the rotor are more significant in PM machines with,

(1) Large slot openings
(2) Concentrated windings
(3) Fed with non-sinusoidal currents
(4) No magnet segmentations
(5) High fundamental frequency –high speed or high pole numbers
(6) High power density

1.3 Necessity of Rotor Loss Prediction

The rotor loss can result in reduction in the machine efficiency and also the overheating of permanent magnets especially at high speeds and at high current conditions which may in the worst case can lead to its partial irreversible demagnetization [28, 29]. The risk of irreversible partial demagnetization in PM machines at increased magnet temperatures can be intensified further in the event of a transient short circuit under worst operating conditions [30]. Therefore, it is important from a designer point of view to accurately determine these losses at worst ever operating conditions of the machine to avoid any abysmal performance throughout the life cycle of the machine. The loss calculation also helps in predicting the magnet temperature and hence to determine their demagnetization pattern while operating at different load conditions of the PM machine. Also an accurate loss estimation helps the designer to predict the machine efficiency more precisely and thereby devising the necessary changes in the machine topology and the number of axial and circumferential segments in the magnets for minimizing it.

1.4 Current State-of-the-art of Rotor Loss Prediction in PM Machines

Techniques adopted for estimating the rotor eddy current loss can broadly be classified in to numerical, analytical, quasi numerical and reduced step numerical methods.

1.4.1 Numerical Methods

The present day finite element based commercial tools for 2D and 3D analysis of electromagnetic fields have reached a high level of maturity and the accuracy of analysis is guaranteed as long as the model is correctly formulated. Also the advent of faster computational resources has made the numerical calculations viable, but still time consuming for rotor eddy current computations, particularly when 3D analysis becomes necessary. 2D time stepped finite element analysis (FEA) can be used to quickly estimate the magnet eddy current loss as explained in [7, 31-36]. Such an analysis also allows to study the effect of circumferential segmentation in reducing the losses. The need to account for end effects in magnet loss calculation is apparent with the introduction of axial segmentation which makes the 3D-analysis [26, 27, 37-41] indispensable. The method of implementation of FEA for IPM machines and axial flux PM machines in evaluating magnet loss is explained in [38, 42-45]. 3D time stepped finite element methods are feasible in evaluating the eddy current losses in machines having axial and circumferential magnet segments with very good accuracy.

However, the 3D numerical methods are very time consuming and also requires very large memory for the solution especially when the eddy current reaction has also been taken in to account. The increase in number of time steps when the loss associated with higher order switching harmonic components are to be evaluated worsens the scenario. Numerical methods also lack the physical insight of the mechanism of magnet eddy current loss

production and hence cannot easily contribute to further electromagnetic design changes in reducing them.

1.4.2 Analytical Methods

The analytical methods in magnet eddy current loss estimation are evolved in association with the refinements in analytical PM machine models to accommodate various machine complexities and hence to represent a realistic machine. These PM machine models are used to determine the magnetic field distribution in the magnet.

The major machine complexities which are needed to be addressed in analytical magnet loss estimation are,

(1) The effect of curvature and circumferential segmentation of the magnets
(2) The reaction effect of the eddy currents in magnets
(3) The slotting effect in the distribution of flux density in the air gap
(4) The 3D/ end effects of the eddy currents and axial segmentations
(5) Non-linear characteristics of stator/rotor cores

The eddy current loss production and flux penetration in ferromagnetic plates due to the traveling field reported by N. Kesavamuthy *et al.* [46] and also the text book by R. L. Stroll [47] gives the basic understanding of the field distribution and loss evaluation in the materials of finite thickness. A brief summary of the development process of eddy current loss evaluation in rotating electrical machines is given by A. Jasscal *et al.* in [48].

The method of analytical loss estimation can be classified based on the machine complexity addressed as (1) resistance limited methods, (2) methods accounting eddy current reaction, (3) methods accounting slotting (employing relative permeance or subdomain models) and (4) 3D analytical methods accounting end effects.

1.4.2.1 Resistance limited methods

In an earlier attempt H. Polinder *et al.* in [49] evaluated eddy current loss in segmented magnets employing magnet loss resistances in equivalent circuits. There after most of the 2D analytical slot less machine models assumes infinitely permeable iron materials, the flux density associated with the air gap is predicted by solving the Laplace equation, while it is predicted within the magnets by the solution to the Poisson equation. The effect of eddy currents on the main field is neglected and hence the eddy current flow is termed as resistance limited. Initial magnet eddy current loss models using homogenous, isotropic core materials approximates the stator excitation as a current sheet of infinitesimal thickness in the air gap as shown in Fig. 1-2.

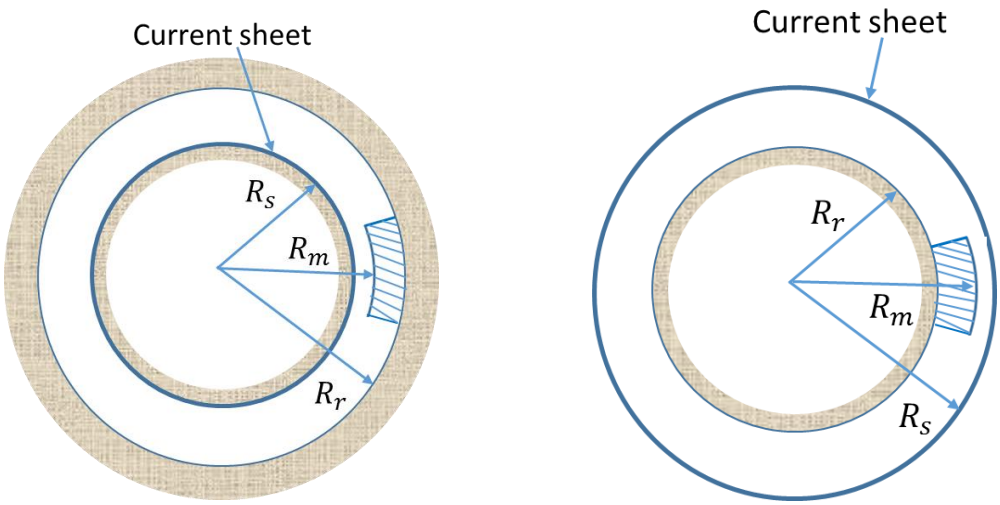

Fig. 1-2. Simplified analytical model. (a) External rotor motor, (b) Internal rotor motor.

where R_s, R_r, R_m are the stator bore, rotor and magnet radius respectively.

Z. Q. Zhu *et al.* [50, 51] developed an analytical model for predicting magnetic field for interior and exterior rotor SPM machines accounting for the magnet relative permeability, which is expanded later in [52] to include the parallel magnetization and also the overlapping, non-overlapping winding configurations. Resistance limited method considering magnets with higher resistivity is reported in [22, 53-58] for predicting magnet losses in PM machines with modular and other winding configurations. The modelling and

analysis of eddy current loss in the magnets of machines operated by PWM inverters for electric vehicle applications is developed by X. Ding *et al.* in [59] without accounting eddy current reaction effect.

In these methods the skin depth, at the inducing frequencies of interest, is assumed to be greater than both the pole arc and the radial thickness of the magnets. Hence the reaction effect of eddy currents is neglected in loss evaluation. The magnetic vector potential in the magnet is computed using the Laplace equation, and the induced eddy current density is obtained by temporal derivation of the potential. The effect of circumferential segmentation in reducing the magnet losses is studied by adding an equivalent current density with the temporal derivation of the magnetic vector potential to ensure the net current in each magnet block is zero.

J.Wang *et al.* in [60] explained that the eddy current loss associated with each of the circumferential segments in a SPM machine with modular winding configuration may also differ by a large margin. This is due to the fact that some of the forward and backward rotating space harmonics of different order may yield same frequency harmonic in the rotor. In [61] A. Rahideh *et al.* divides the SPM machine in to eight annular regions: shaft, rotor back-iron, magnets, retaining sleeve, airspace, winding, stator back-iron and exterior, calculates the eddy current loss in the magnets while considering finite permeability and linear magnetization characteristic for core materials.

1.4.2.2 Methods accounting eddy current reaction

The eddy current loss evaluation method including the eddy current reaction effect at high frequencies is first reported by F. Deng *et al.* in [62, 63]. Z.Q. Zhu *et al.* [64] presented an improved analytical model to incorporate the eddy current reaction effect which caters either overlapping and non-overlapping stator windings. This model evaluates the losses associated with the magnets and the retaining sleeve if fitted to the rotors of SPM machines. This model computes the eddy current loss based on Poynting's theorem to

avoid the integration of Bessel functions with the complex arguments. A similar approach is presented by M. Markovic *et al.* [65] for evaluating losses in ring type magnets, where the machine is divided in to three layers viz. shaft, magnet and the air gap. The shaft and the magnet are conducting, therefore, the diffusion equation is applied in these regions while the Laplace equation is applied to the machine air gap. The relation between the rotor loss and the combination of the slot and pole numbers for a fractional–slot PM machines is investigated by N. Bianchi *et al.* in [66-68].

1.4.2.3 Methods accounting slotting effect

The method of loss estimation accounting the effect of slotting can be based on the machine models employing relative permeance or subdomain models.

1.4.2.3.1 Methods employing relative permeance models

The attempt to include the stotting effect in rotor loss calculation can be traced back to the model proposed by Z.Q .Zhu *et al.* in [69]. The modifying effect on the magnetic field by slotting is included by introducing a 2D permeance function calculated using the conformal transformation [70] method. This model is used for estimating eddy current loss in the magnets and the retaining sleeve. A similar approach is used by D. A. Wills *et al.* [71] to evaluate the magnet eddy current loss under no load conditions due to the effect of slotting. These methods give erroneous results in the loss evaluation as the predicted flux density due to slotting is far deviating from the actual values.

An improved relative permeance model is subsequently proposed by Z. X. Fang *et al.* in [72] for predicting the open-circuit (no-load) magnet loss based on the 2D magnetic field model, relative air gap permeance and Carter coefficient, while the conventional one uses only a 1-D field model and neglects the Carter coefficient. This method gives a better estimation of no-load magnet losses, but the results deviate from the actual values when the loss due to

armature reaction is considered. The method proposed by C. Bode *et al.* [73] considers the effect of stator slotting by using a relative magnetic conductance function while the end effects are accounted by using a correction factor.

While the improved flux density assessment models are proposed in [74-76] by employing complex relative permeability to predict magnet loss in [77] by A.A. Qazalbash *et al.*, a better accurate subdomain models are preferred for loss estimation in permanent magnets. The methods [72, 73, 77] referred in this section also accounts for the eddy current reaction effect while incorporating the slotting effect in the 2D magnet loss evaluation.

1.4.2.3.2 Methods employing subdomain models

A more accurate method for the estimation of the flux density distribution at different regions of the SPM machine with infinitely permeable core materials and isotopic magnetic materials is developed by F. Dubas *et al.* [78] by dividing the PM machine in to three different subdomains viz. magnet, air gap and slot. The method proposes the solution of Laplace's equation in the air-gap (i.e., concentric region) and the slots on the stator (i.e., nonconcentric regions), and of Poisson's equation in the PMs (i.e., concentric region) with constant magnetic permeability by using the Fourier's series and the method of separating variables. This model is refined to exact subdomain model considering the interaction between the slots by T. Lubin *et al.* [79] and extended for any pole and slot combinations by Z.Q Zhu *et al.* in [80].

Bellara *et al.* in [81] has reported analytical prediction of open-circuit eddy-current loss in armature winding and permanent magnets for series double excitation synchronous machines. The method uses the solution of Maxwell equations in subdomain regions viz. stator slots, air gap, PM region and rotor slots with proper boundary conditions and Gaussian elimination method. In [82] another model for predicting open circuit eddy current loss in permanent magnets of surface mounted PM machines using the aforementioned exact subdomain model [80] is developed by the same authors. Here the interaction

between the harmonics of the same frequency in the rotor reference produced due to the special harmonics of different order is revealed. The influence of the slot and pole number combination, slot-opening to slot-pitch ratio, pole-arc to pole-pitch ratio, circumferential segmentation, and rotational symmetry order on the open-circuit magnetic field distribution is also investigated in the developed model.

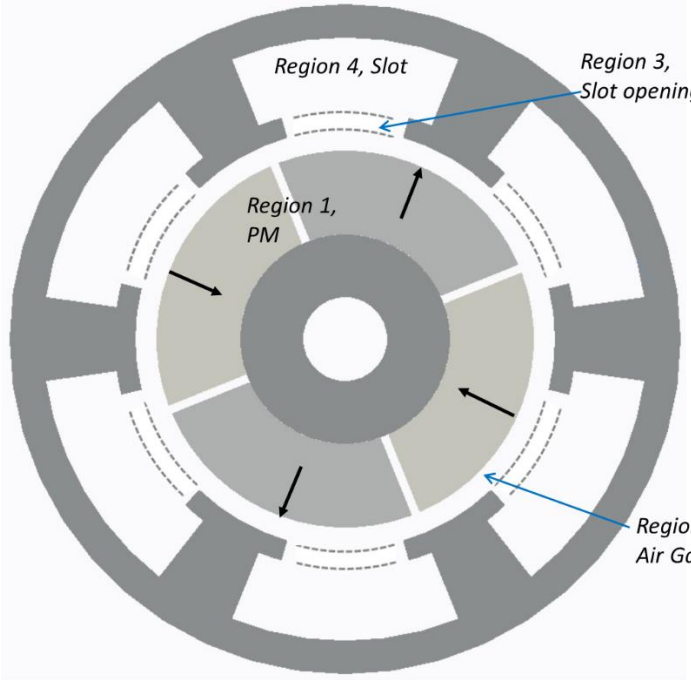

Fig. 1-3. More accurate subdomain model illustrating four regions.

The sub domain model is further improved by including stator tooth tips to address the semi-closed slots by T. Lubin *et al.* in [83] , and L. J. Wu *et al.* in [84, 85]. These models suitable for any pole-slot combination have included a slot opening subdomain, in addition to the other three subdomains as shown in Fig. 1-3.

An analytical model for evaluating no-load eddy current loss in magnet due to slotting is reported by Barriere *et al.* [86] . It uses the subdomain model and considers the eddy current reaction effect. This method agrees with the fact that if the diffusion phenomenon is neglected, magnet's segmentation for loss reduction can be studied analytically as proposed in [60]. This is because, after integration of the current density together with a constant current source, the

total current over each insulated magnet block can be made zero. If the eddy current reaction effect is considered, this fictitious current which is added to make the net current zero also undergoes diffusion and hence the zero mean current over the magnet block cannot be satisfied. Therefore, the method proposed by O. Barriere *et al.* in [86] considers the diffusion equation inclusive of the fictitious current source and solves it using Fredholm theory of integral equations

1.4.2.4 3D Analytical methods

To account for the end effects and to study the effect of axial segmentation in reducing magnet losses several approximate methods are developed in [87-90] based on the physics of eddy current flow on the axial plane of the magnet. The model proposed by W. Y. Huang *et al.* [87] considers the skin effect due to the eddy current diffusion and explains the anomaly of segmentation, i.e. the increase rather than decrease in magnet loss due to excessive segmentation at high frequency.

The concept of current vector potential is introduced to solve a differential equation involving Faradays law by M. Mirzaei *et al.* [91] for finding the axial and tangential component of the eddy current density in the magnets. The method evaluates the reduction in eddy current loss in the magnet due to axial and circumferential segmentation, neglecting the effect of the tangential component of the flux density in the magnet. Another 3D analytical model considering the reaction effect of eddy current is developed by the same authors above in [92] , also only considers the radial component of the magnet flux density. This loss model is developed by the solution of three linear equations based on Ohms law, Ampere's law and the fact that the divergence of eddy current density along the axial plane of the magnet perpendicular to the radial magnetic field is zero.

An analytical model of eddy current losses in magnet volume is developed by B. Aslan *et al.* in [93] by studying the interaction between the MMF

harmonic wavelengths and the magnet pole dimensions. The results due to the interaction is generalized using various sub models in order to cover all possible forms of induced 3D eddy-current paths. A 3D eddy current loss model for magnets published by J. Pyrhonen *et al.* [94] considers only machines with narrow slot openings using Carter's coefficient and discards the variation of the field produced by the permanent magnets and slotting. This model fails to replicate the flux density undulations accurately. The model presented by F. Martin *et al.* [95] calculates the current density induced in the magnet by solving a 2D magneto-dynamic problem which is as comparable to the one in a conductive ring. The effect of circumferential segmentation is addressed after decomposing the armature magneto motive force (MMF) which produces the eddy currents in the magnets in to Fourier series whose period is equal to the width of the magnet. The axial length is accommodated in the loss calculation by introducing a suitable correction factor.

Analytical evaluation of magnetic flux density in the magnet associated with an interior permanent magnet machine is more difficult due to high saturation level and its complex geometry of the rotor. However, there are a few 3D analytical [96, 97] and theoretical methods [27, 90] to evaluate the magnets loss employing simplifying assumptions. Among the 3D analytical methods the methods described in [88, 91, 93] are mainly resistance limited assuming the skin depth for the eddy currents is sufficiently larges than the wavelength of the alternating field under the normal operating conditions of the machine.

1.4.3 Computationally efficient methods: quasi numerical and reduced step numerical methods

The difficulty in accommodating different machine complexities at the same time in formulating the eddy current loss and also to minimize the loss evaluation time has forced the designers to arrive at several computationally efficient methods for evaluating it. These methods are either partially

analytical and partially numerical employing the results from 2D analytical methods in 3D FEA or it can be reduced step 3D FEA or combined 2D and 3D FEA's.

In [98] J.D. Ede *et al.* employs the rate of flux density variation derived analytically or from magneto static finite element analysis as the excitation input in 3D magneto- static eddy current loss computation. While in [99] J. Wang *et al.* explains a more computationally efficient method as it calculates 3D eddy current loss via magneto static field analogy by which only the magneto static field in a few magnet blocks need to be computed. Both the methods intended to study the impact of axial segmentation in magnet loss use resistance limited approximation in evaluating it.

Another resistance limited method reported in [39] does the 3D frequency domain FEA at each remarkable harmonic field using the results of the harmonic gap flux densities obtained by the 2D time stepped analysis. In [100] X. Wu *et al.* adopted a loss mapping procedure as an alternative for direct 3D finite element prediction of magnet loss in SPM machines.

There are also a few computationally efficient numerical methods developed for 3D magnet loss prediction in IPM machines[43, 101-105]. In [104] K. Yamazaki *et al.* does the 3D frequency domain analyses at each remarkable harmonic field using a differential permeability to accommodate the saturation effect, while the differential permeability is determined by the flux density distribution calculated numerically by the 2D time-domain analysis. This model is modified by T. Okitsu *et al.* in [103] to compensate the field due to eddy current reaction when performing the 3D analysis, using an equivalent air gap calculated based on the equivalent magnetic circuit. This idea of equivalent air gap is extended to surface mounted PM machines by the same authors in [106]. This method saves the computation time for loss evaluation as it models only the magnet with an equivalent air gap while performing the 3D finite element analysis.

1.5 Summary of the Developments in Evaluating PM Eddy Current Loss and the Remaining Problems to be Addressed

Table 1-1 summarise the current state of the art in analytical modelling and computation of 2D and 3D eddy currents and their reduction with axial and circumferential segmentation for SPM machines.

It is observed that when slotting effect is neglected, the analytical methods for predicting 2D eddy current loss in magnets and retaining sleeve of SPM machines have been well established. When the slotting effect is considered, the analytical prediction has reached only up to the level of predicting the no load losses accounting eddy current reaction effect. However, any of the 2D analytical models proves ineffective to consider 3D end effects and the loss minimization by axial segmentation. The 3D analytical methods developed so far are mainly for slot-less machines and also ignores the field produced by the PM itself. Also most of the reduced order numerical and quasi numerical methods are quite complicated to implement.

Since 3D time-step FE analysis of eddy current loss in rotor magnets are still very time consuming with today's state of art computing facilities, it is imperative to develop computationally efficient techniques for the prediction of 3D eddy current loss in magnets and retaining sleeve which account for the effect of slotting with magnet field in SPM machines. Further, the magnet loss evaluation methods developed so far for IPM machines are mainly numerical and is time consuming even if reduced step 3D analysis has to be employed. Also the analytical loss evaluation methods discussed in literature for the retaining sleeve is mainly limited to 2D and hence cannot be used to predict the loss with increase in axial segmentations.

Hence it has a great scope of improvement with more computationally efficient methods. These computationally efficient methods can either be

totally analytical from field calculations to the 3D eddy current formulation or it can be partly analytical using the field information's from the 2D time-stepped finite element analysis which can also include the material non linearity and complex geometry in to account.

Table 1-1. Summary of the Complexities Addressed so Far in Different Methods of Eddy Current Loss Modelling for SPM Machines.

Method	Winding (Distributed/ Concentrated) Magnetization (Parallel and Radial)	Segmentation without reaction effect	Eddy current reaction effect	End effect
Analytical 2D	Addressed	Addressed	Addressed	By correction factor
Analytical 2D + Slotting	Addressed	Addressed	Only no-load without segmentation	By correction factor
Analytical 3D	Not addressed (ignores PM field)	Addressed	Addressed	Addressed
Analytical 3D + Slotting	Not addressed	Not addressed	Not addressed	Not addressed

1.6 Outline of Thesis

The thesis will be mainly focused on developing computationally efficient techniques for prediction of rotor eddy current loss in PM machines. Also the partial demagnetization of magnets under different fault conditions is investigated for an IPM machine when the magnets undergo increased temperature rise because of eddy current loss. This thesis is structured as follows:

Chapter 1 establishes the importance of the rotor eddy current loss evaluation in PM machines and investigates on the current state of art. The chapter summarizes the remaining machine complexities which are needed to be addressed in predicting magnet/sleeve loss with improved computational efficiency. The outline and major contribution of the thesis as well as a list of publications as a result of the studies are presented.

Chapter 2 proposes a novel analytical technique for predicting 3D magnet eddy current losses accounting the slotting effect of any pole–slot combinations for a surface mounted permanent magnet machine under any conditions of load. The slotting effect is incorporated from a subdomain model and the 3D boundary conditions are imposed with the current vector potential to represent the 3D eddy currents circulating in the magnets. The proposed model in polar coordinate system is demonstrated on a fractional slot PM magnet machine by analysing its magnet losses as functions of axial and circumferential segmentations. The interaction of the armature reaction field with the slotting harmonics is analysed and their effect on eddy current loss in rotor magnets is established.

Chapter 3 develops a more computationally efficient analytical method, for accurate 3D eddy current loss prediction in the rotor PMs of SPM machines considering slotting effect. Sub-domain model incorporating stator tooth tips is employed to generate the information on radial and tangential time-derivatives of 2D magnetic field (eddy current sources) within the magnet. The

distribution of the eddy current sources in 3D is established for the magnets by applying the eddy current boundary conditions and the Coulomb gauge imposed on the current vector potential. The method of variable separation is employed to derive analytically the 3D magnet eddy current distributions and the total magnet eddy current loss is subsequently established. 3D time-stepped FEA is employed to validate the proposed method for an 18-slot 8-pole PM machine. The eddy current loss variations in the rotor magnets with axial and circumferential numbers of segmentations are studied employing the proposed 3D Fourier method. The reduction of magnet eddy current loss is investigated with respect to harmonic wavelength of the source components to suggest a suitable segmentation for the rotor magnets in SPM machines.

Chapter 4 extends the computationally efficient method developed in Chapter 3, for the prediction of high frequency 3D eddy current loss accurately in the rotor PMs of SPM machines employing the 3D Fourier method. 2D FEA is used to generate the information on radial and tangential 2D eddy current sources within the magnet. The diffusion of eddy current sources along the axial plane of the magnet computed analytically is incorporated in the 3D Fourier method to establish the 3D eddy current source variations within the magnet. The modified method is validated with results from 3D time-stepped FEA for an 8-pole, 18-slot permanent magnet machine, evaluating its magnet loss considering axial and circumferential segmentation

Chapter 5 validates the 3D Fourier method on a 14-pole, 12-sot, SPM machine from experiments. Two SPM rotors are constructed one with magnets and the other one without magnets. The experimental validation is devised by the difference in power input measurements with the two rotors under locked rotor conditions. The phase current applied to the windings in the experiment are employed in the 2D FE model to generate the flux density information within the magnet. 3D magnet loss is evaluated at the stand still conditions of the rotor using the eddy current source values in the 3D Fourier method and are compared with the experimental results. Also the phase currents

measured from the experiments while the machine is delivering its peak power is employed in the proposed method to evaluate the magnet loss under the maximum speed operating conditions of the machine.

Chapter 6 proposes the 3D Fourier method for the prediction of 3D magnet eddy current loss in the rotors of IPM machines more accurately. 2D time-stepped FEA is employed to generate the radial and the tangential 2D magnetic field information within the magnet for application of the 3D Fourier technique. The method is validated with 3D time-stepped FEA for an 8 pole-18 slot IPM machine evaluating its resistance limited magnet loss with increase in axial and tangential segmentation. Magnet loss considering eddy current reaction at high frequencies is evaluated from the proposed method by employing the diffusion of the 2D magnetic field variation along the axial plane. The loss associated with all the frequencies together in the armature currents is evaluated by considering each of the harmonics separately in the proposed method by employing the frozen permeability to account for magnetic saturation. The results obtained are verified with 3D FEA evaluating the magnet loss at fundamental, 10 and 20 kHz time harmonics in armature currents.

Chapter 7 unrolls the retaining sleeve as a thin rectangular sheet of very small thickness. The developed 3D Fourier method in Chapter 3 is modified such that it can account for the boundary conditions that governs the eddy current flow in the retaining sleeve. The current vector potential is introduced, and the 3D sleeve eddy current distributions is analytically derived using the variable separation method. The total sleeve eddy current loss is subsequently established. For resistance limited loss evaluation, 2D Sub-domain model considering stator tooth tips is employed to generate radial and tangential field information within the sleeve. The diffusion of the field variation along the axial direction is included to consider the eddy current reaction while evaluating the loss associated with high frequency armature reaction harmonics. The results from the proposed method are validated from 3D time-

stepped FEA of the sleeve eddy current loss for an 8-pole, 18-slot permanent magnet machine at no load, and on load with fundamental, 10 and 20 kHz time harmonics in the armature currents.

Chapter 8 employs the more accurate recoil line approach based on 2-D transient FEA to assesses post demagnetization performance of a PM machine. An IPM machine behaviour after an event of short-circuit faults across its terminals is evaluated accurately as the method predicts continuous demagnetization of each magnet element undergoing partial irreversible demagnetization. Along with the short-circuit faults, a failure in position sensor or drive controller which may lead to large reverse voltage across the machine terminals that can eventually be more fatal and can cause reduction in its performance significantly due to high levels of demagnetization is also analysed as the worst case scenario. The experimental measurements are employed to validate the FE predicted post demagnetization performance in which a 6- phase IPM machine designed for EV traction is allowed to lose its phase synchronization with the inverter when it is forced to operate on a torque–speed envelope which is way beyond the voltage setting of the drive.

Chapter 9 summarises the finding of the studies described in the thesis and points out the scopes of the further research

1.7 Major Contributions of Thesis

The major contributions of this thesis include two aspects. First is the development of computationally efficient techniques for the accurate 3D magnet eddy current loss prediction in SPM, IPM machines and also in the retaining sleeve of SPM machines. The proposed 3D analytical method considering only the radial field component accounts for the slotting effect and also the field produced by the permanent magnet while evaluating the magnet eddy loss. The proposed technique is employed to evaluate the effect of slotting on magnet loss with increase in field weakening angle. A more accurate and computationally efficient 3D Fourier method is proposed

considering both the radial and circumferential field components in the loss evaluation. This method considers the harmonic interactions and also evaluates all the three components of the magnet eddy current loss. The relation between the variation of loss associated with different harmonic components in the magnetic field with increase in axial and circumferential segments is studied. The diffusion of the eddy current source components is included in the proposed 3D Fourier method to predict the magnet loss at high frequencies accounting eddy current reaction effect. The cause for the initial increase in magnet loss rather than reduction at lower number of segments at high frequency conditions is studied from the results obtained. The proposed method is experimentally validated on an SPM machine by evaluating its magnet loss under locked rotor conditions. The application of the 3D Fourier method to IPM machines and the loss evaluation accounting diffusion is proposed. Also the method of total magnet loss evaluation for all the harmonic components in the supply current for the IPM machines is established employing frozen permeability. Finally, the proposed 3D Fourier method is alerted to account for the boundary conditions of the retaining sleeve and hence to evaluate its eddy current loss with increase in axial segmentations both at low and high frequencies.

The second major contribution is to study the after effect of magnet eddy current loss which can result in increased magnet temperatures in an IPM machine. The continuous demagnetization method is proposed to conduct the partial demagnetization assessment at different faults and operating conditions of the machine. The continuous demagnetization method is validated by experiment in which the machine has lost its synchronization while operating at reduced dc link voltage and at deep field weakening. The magnet temperature is estimated from the 3D loss evaluated using the 3D Fourier method at the experimental conditions before implementing in the proposed method.

1.8 List of Publications

Several parts of the research work reported in this thesis have been presented by the author in international Journals and conferences during the course of his doctoral research. The various publications are listed as below. The journal and conference papers are preceded by J and C respectively.

Journal papers:

[J1] **S. S. Nair**, J. Wang, R. Chin, L. Chen, and T. Sun, "Analytical Prediction of 3D Magnet Eddy Current Losses in Surface Mounted PM Machines Accounting Slotting Effect " *Energy Conversion, IEEE Transactions on*, vol. pp, pp. 1-9, 2016, in press.

[J2] **S. S. Nair**, L. Chen, J. Wang, R. Chin, I.Manolas, and D.Svechkarenko, "Computationally efficient 3D analytical magnet loss prediction in SPM machines," *Electric Power Applications, IET,* vol. pp, pp. 1-10, 2016 , in press.

[J3] **S. S. Nair**, J. Wang, L. Chen, R. Chin, I. Manolas, and D. Svechkarenko, "Prediction of 3D High Frequency Eddy Current Loss in Rotor Magnets of SPM Machines," *Magnetics, IEEE Transactions on* vol. 52, pp. 1-10, 2016.

[J4] **S. S. Nair**, J. Wang, L. Chen, R. Chin, I. Manolas, and D. Svechkarenko, "Computationally Efficient 3D Eddy Current Loss Prediction in Magnets of Interior Permanent Magnet Machines," *Magnetics, IEEE Transactions on,* vol. 52, pp. 1-10, 2016.

[J5] **S. S. Nair**, V. I. Patel, and J. Wang, "Post-Demagnetization Performance Assessment for Interior Permanent Magnet AC Machines," *Magnetics, IEEE Transactions on,* vol. 52, pp. 1-10, 2016.

[J6] L. Chen, J. Wang, and **S. S. Nair**, "An analytical method for predicting 3D eddy current loss in permanent magnet machines based on generalized image theory," *Magnetics, IEEE Transactions on,* vol. 52, pp. 1-11, 2016.

[J7] V. I. Patel, J. Wang, and **S. S. Nair**, "Demagnetization Assessment of Fractional-Slot and Distributed Wound 6-Phase Permanent Magnet Machines," *Magnetics, IEEE Transactions on,* vol. 51, pp. 1-11, 2015.

[J8] **S. S. Nair**, J.Wang, T. Sun, and L.Chen, "Total magnet Loss Prediction in Surface Mounted Permananet Magnet Machines Accounting High Frequency Switching Harmonics," *Industry Applications, IEEE Transactions on.* (submitted for review).

Conference papers:

[C1] **S. S. Nair**, J. Wang, R. Chin, and L. Chen, "3D analytical slotting-effect model for predicting magnet eddy current loss in surface mounted PM machines," in *IEEE Magnetics Conference (INTERMAG)*, 2015, pp. 1-1P.

[C2] **S. S. Nair**, L.Chen, J.Wang, R.Chin, I.Manolas, and D.Svechkarenko, "3D analytical slotting-effect model for magnet loss prediction in SPM machines," in *Power Electronics, Machines and Drives (PEMD), 2016, 8th IET International Conference on.*, 2016,pp.1-6.

[C3] **S. S. Nair**, J. Wang, L. Chen, R. Chin, I. Manolas, and D. Svechkarenko, "Computationally efficent 3D rotor eddy current loss prediction in permanent magnet machines," in *Electrical Machines (ICEM), 2016 XXII International Conference on*, 2016, pp. 1-7.

[C4] **S. S. Nair**, J. Wang, L. Chen, R.Chin, I.Manolas, and D.Svechkarenko, "Prediction of 3D Eddy Current Loss in Reataining Sleeve of Surface Mounted Permanent Magnet Machines," *Electric Machines & Drives Conference (IEMDC), 2017 IEEE International.* (submitted for review).

CHAPTER 2
3D Analytical Magnet Eddy Current Loss Prediction in SPM Machines Accounting Slotting Effect

2.1 Introduction

As discussed in Chapter 1, an accurate prediction of magnet eddy current loss in high power density SPM machines not only enables the designer a better efficiency evaluation but also helps in preventing the excessive temperature rise in the magnets and hence reduce the risk of partial irreversible demagnetization.

In general, prediction of rotor eddy current loss necessitates simultaneous solutions for the governing Laplace and Poisson's equations of the magnetic and the electric current fields [21-23, 47, 54, 64]. Magnet loss evaluation considering slotting [69, 72, 77, 82, 107] in surface mounted PM machines are mostly limited to 2D in literature so far, employing either the relative permeance [52, 70, 74, 75] or the sub-domain models [80, 83-85]. Unless the slotting harmonics are considered in the loss evaluation, the no load magnet loss and its interaction with armature field harmonics at the diverse load conditions cannot be accurately quantified. All the above methods except [64, 72, 77] is resistance limited assuming the skin depth for the eddy currents is sufficiently larger than the wavelength of the alternating field under the normal operating conditions of the machine.

Also as discussed previously the accuracy of magnet loss evaluation is compromised in 2D loss evaluation methods if the axial length of PMs is comparable to its other machine dimensions since the flow of eddy currents in the magnets may become predominantly 3D. This is further compounded by the introduction of axial segmentation [26, 98] which makes the 3D analysis indispensable. In order to overcome the enormous computation time, larger memory for storage requirements in magnet loss evaluation encountered in

3D FEA [27] , 3D analytical methods [90-92] and computationally efficient reduced order numerical methods [99, 101, 106] have received significant interest in research communities. They are discussed in detail in Chapter 1. These 3D analytical models are mostly established on simplifying assumptions which inevitably compromise their accuracy, while most of the reduced order computationally efficient methods discussed in the literature are bit complicated to implement. The 3D analytical methods mentioned above ignore slotting effect and fails to consider the field produced by the permanent magnet in loss evaluation. Moreover, they also ignore instantaneous magnet loss variations while predicting the total magnet loss.

However, in [108] A. Masmoudi *et al.* combines relative permeance model and lumped resistance method in estimating 3D magnet loss associated with each harmonic flux density within the magnet. Likewise, in the other previously discussed 3D analytical methods, this method also ignores the flux density variations along the radial directions inside the magnet and hence incapable of predicting the eddy current density distribution quite accurately along the magnet. The 3D eddy current loss method for rotor surface magnets published in [94] by J. Pyrhonen *et al.* considers only machines with narrow slot openings using Carter's theory and hence fails to replicate the flux density undulations accurately with increase in slot openings. Underestimation of rotor temperatures can be resulted from the inaccuracy of the eddy current loss calculations. This can increase the risk of PM demagnetization. Therefore, computationally-efficient and accurate solution is essential for quantifying the eddy current losses.

This chapter presents a novel analytical method in polar coordinates for calculating the 3D magnet eddy current losses considering the slotting effect of any pole–slot combinations for a surface mounted permanent magnet machine under any conditions of load. The slotting effect with tooth tip is incorporated from the subdomain model and the 3D boundary conditions are imposed using the current vector potential, to represent the eddy currents

circulating in the magnets. Since the eddy current reaction effect becomes significant only at high operating frequencies [91, 101] the proposed method assumes resistance-limited eddy current in magnets and is sufficiently accurate for operating frequency up to a few kHz. The analytical method is demonstrated by calculating joule losses in the magnets for an 8- pole 18-slot SPM motor, with due account of the effect of axial and circumferential segmentations at peak load operating conditions of the machine. The effect of slotting in reducing the magnet loss with increase in field weakening angle is comprehensively assessed using the proposed method. Also the effect of change in magnet pole arc angle in varying magnet loss with change field weakening angle is studied towards the end of this chapter.

The main contents of this chapter is published by the author in [C1] and [J1], as detailed in Section 1.8.

2.2 Subdomain Model and Calculation of Flux Density Variation

2.2.1 Subdomain Model

The subdomain model developed by L. J. Wu *et al.* [84, 85] is employed in this chapter to develop the 3D eddy current loss prediction method for permanent magnets considering the effect of slotting in SPM machines. This model is suitable for any pole-slot combination of SPM machines under different conditions of load. A representative model illustrating the geometry under consideration in subdomain model is shown in Fig. 2-1.

The model assumes (i) infinitely permeable materials for iron core, (ii) negligible end effect, (iii) linear properties for the magnet, (iv) simplified slot but with tooth tips, (v) non-conductive stator/rotor laminations and (vi) winding areas with uniform distribution of current. The coils may be accommodated in the slots considering either overlapping or non over lapping double layer winding [84].

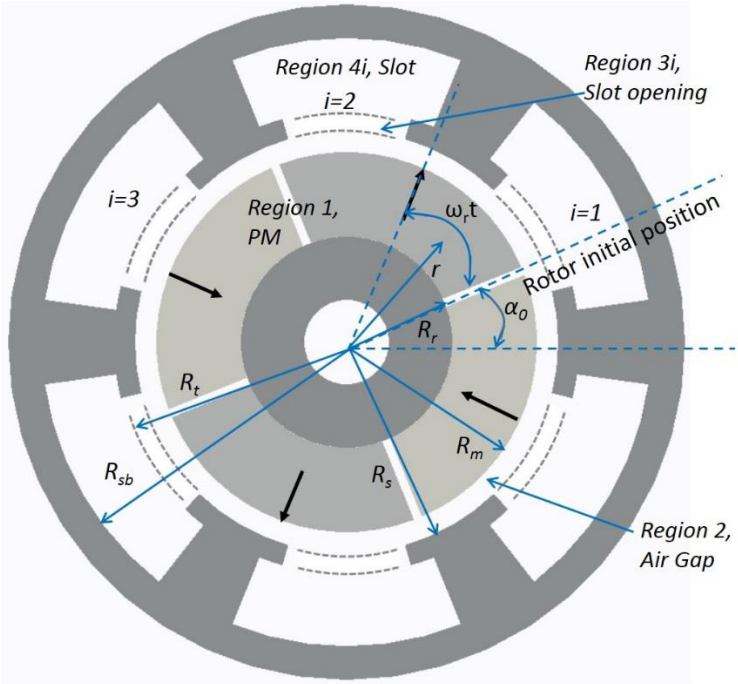

Fig. 2-1. Machine geometry for subdomain model illustrating regions and symbols.

2.2.2 Solution to 3D Magnetic Flux Density Variation

The subdomain model assumes 2D magnetic field and hence the magnetic vector potential (A) has only the z-component. If the eddy current reaction effect is neglected, the vector potential equation governing different regions can be defined in polar coordinate system as,

$$\frac{\partial^2 A_{z1}}{\partial r^2}+\frac{1}{r}\frac{\partial A_{z1}}{\partial r}+\frac{1}{r^2}\frac{\partial^2 A_{z1}}{\partial \alpha^2}=-\frac{\mu_0}{r}\left(M_\alpha-\frac{\partial M_r}{\partial \alpha}\right) \tag{2-1}$$

in the magnets,

$$\frac{\partial^2 A_{z3}}{\partial r^2}+\frac{1}{r}\frac{\partial A_{z3}}{\partial r}+\frac{1}{r^2}\frac{\partial^2 A_{z3}}{\partial \alpha^2}=-\mu_0 J \tag{2-2}$$

in the slots,

$$\frac{\partial^2 A_z}{\partial r^2}+\frac{1}{r}\frac{\partial A_z}{\partial r}+\frac{1}{r^2}\frac{\partial^2 A_z}{\partial \alpha^2}=0 \tag{2-3}$$

in the air gap (A_{z2}) and the slot opening (A_{z4}) regions. Where α and r are the circumferential and the radial positions, and M_r and M_α are the radial and the circumferential components of the magnet magnetization [80].

The subdomain model finds the solution to the Laplace's equation (2-3) in the air-gap and the slots opening regions while the solution to the Poisson's equation (2-1) & (2-2) is derived in the permanent magnet and the slot regions with current density. The continuity of normal flux density and tangential field intensity is used as the interface or boundary conditions, while the unknown coefficients are formulated using the Fourier series expansion. The coefficients are then calculated numerically [85], therefore the radial and tangential component of the magnetic flux density within the magnet, where the effect of eddy current reaction is neglected, is now known. The model is then verified for the different pole slot combinations using 2D time stepped finite element analysis.

The radial component of the flux density along the magnet [85] , which contributes to the magnet loss can be represented in the stator reference as,

$$B_r = \begin{Bmatrix} -\frac{1}{r}\sum_k k(C_{1k}A_1 + C_{2k}M_{\alpha ck} - C_{3k}M_{rsk})\, sin(k\alpha) \\ +\frac{1}{r}\sum_k k(C_{1k}C_1 + C_{2k}M_{\alpha sk} + C_{3k}M_{rck})\, cos(k\alpha) \end{Bmatrix} \tag{2-4}$$

where,

$$C_{1k} = [(r/R_m)^k + G_1(r/R_r)^{-k}] \tag{2-5}$$

$$C_{2k} = \frac{\mu_0}{(k^2-1)}[\, R_r k(r/R_r)^{-k} + r] \tag{2-6}$$

$$C_{3k} = \frac{\mu_0}{(k^2-1)}[\, R_r(r/R_r)^{-k} + kr] \tag{2-7}$$

$$G_1 = (R_r/R_m)^k \tag{2-8}$$

and $k/p = 1,3,5 \ldots$, where p is the number of rotor pole pairs. The geometric parameters for the stator and rotor are illustrated in Fig. 2-1.

The coefficients A_1 and C_1 are evaluated numerically employing the matrix inversion technique of the corresponding simultaneous equations in MABLAB [85] , the components directly related with magnetization viz. $M_{\alpha ck}, M_{rsk}, M_{\alpha sk}, M_{rck}$ can be expressed as,

$$M_{\alpha ck} = -M_{\alpha k}\, sin(k\alpha_0 + k\omega_r t) \tag{2-9}$$

$$M_{rsk} = \; M_{rk}\, sin(k\alpha_0 + k\omega_r t) \tag{2-10}$$

$$M_{\alpha sk} = \; M_{\alpha k}\, cos(k\alpha_0 + k\omega_r t) \tag{2-11}$$

$$M_{rck} = \; M_{rk}\, cos(k\alpha_0 + k\omega_r t) \tag{2-12}$$

The definition of $M_{\alpha k}$ and M_{rk} decides the radial or parallel magnetization for the magnets [84].

In the rotor reference, $\alpha = \theta_r + \omega_r t$, where θ_r and ω_r are rotor position and angular speed respectively. The radial component of flux density in (2-4) after substituting in the rotor reference frame becomes,

$$B_r = \left\{ \begin{matrix} -\frac{1}{r}\sum_k k(C_{1k}A_1 + \; C_{2k}M_{\alpha ck} - C_{3k}M_{rsk})\, sin\big(k(\theta_r + \omega_r t)\big) \\ +\frac{1}{r}\sum_k k(C_{1k}C_1 + \; C_{2k}M_{\alpha sk} + C_{3k}M_{rck})\, cos\big(k(\theta_r + \omega_r t)\big) \end{matrix} \right\} \tag{2-13}$$

The components directly related with magnetization $M_{\alpha ck}$ and $M_{\alpha sk}$ can be segregated after the expansion as,

$$\begin{aligned} &\frac{1}{r}C_{2k}k\big(-M_{\alpha ck}sin(k\theta_r + k\omega_r t) + M_{\alpha sk}cos(k\theta_r + k\omega_r t)\big) \\ &\qquad = \frac{1}{r}C_{2k}k\big(M_{\alpha k}cos(k\alpha_0 - k\theta_r)\big) \end{aligned} \tag{2-14}$$

and,

$$\begin{aligned} &\frac{1}{r}C_{3k}k\big(M_{rsk}sin(k\theta_r + k\omega_r t) + M_{rck}cos(k\theta_r + k\omega_r t)\big) \\ &\qquad = \frac{1}{r}C_{3k}k\big(M_{rk}cos(k\alpha_0 - k\theta_r)\big) \end{aligned} \tag{2-15}$$

(2-14) and (2-15) shows they are time-invariant and hence cannot contribute to the eddy currents and hence the magnet loss.

Thus the component of radial flux density in magnets resulting in eddy current becomes,

$$B_r = \sum_k [-C_k A_1 \sin(k\theta_r + k\omega_r t) + C_k C_1 \cos(k\theta_r + k\omega_r t)] \tag{2-16}$$

where $C_k = k/r\ C_{1k}$.

Now, the circumferential component of the flux density along the magnet [85] which can contribute to the magnet loss can be represented in the stator reference as,

$$B_t = \begin{Bmatrix} -\frac{1}{r}\sum_k (C_{4k}A_1 + C_{5k}M_{ack} - C_{6k}M_{rsk})\, cos(k\alpha) \\ -\frac{1}{r}\sum_k (C_{4k}C_1 + C_{5k}M_{ask} + C_{6k}M_{rck})\, sin(k\alpha) \end{Bmatrix} \tag{2-17}$$

where,

$$C_{4k} = k[(r/R_m)^k - G_1(r/R_r)^{-k}] \tag{2-18}$$

$$C_{5k} = \frac{\mu_0}{(k^2-1)}[-k^2 R_r(r/R_r)^{-k} + r] \tag{2-19}$$

$$C_{6k} = \frac{\mu_0 k}{(k^2-1)}[\ -R_r(r/R_r)^{-k} + r] \tag{2-20}$$

Likewise it is derived for the radial component of flux density, the circumferential component of the flux density at any radius '*r*' along the magnet [85] which contributes to the rotor loss can be represented in the rotor reference can be represented as,

$$B_t = \sum_k [-D_k A_1 \cos(k\theta_r + k\omega_r t) - D_k C_1 \sin(k\theta_r + k\omega_r t)] \tag{2-21}$$

where $D_k = -1/r\ C_{4k}$.

Now, the coefficients which accounts for the slotting effect viz. A_1 and C_1 varies with rotor position and can be expressed as Fourier series [107] ,

$$A_1 = \sum_l a_{1l} \cos(lp\omega_r t + \psi_{al}) \tag{2-22}$$

$$C_1 = \sum_l c_{1l} \cos(lp\omega_r t + \psi_{cl}) \tag{2-23}$$

where l=1, 2, 3...

Hence the radial and circumferential component of flux density B_r and B_t can be rewritten as a combination of space and time harmonics as :

$$B_r(r,\theta,t) = \sum_k \sum_l C_k \begin{bmatrix} a_{br}\, sin(k\theta_r + (k+lp)\omega_r t + \psi_{br}) \\ +a_{fr} sin\left(k\theta_r + (k-lp)\omega_r t + \psi_{fr}\right) \end{bmatrix} \tag{2-24}$$

$$B_t(r,\theta,t) = \sum_k \sum_l D_k \begin{bmatrix} a_{b\alpha}\, sin(k\theta_r + (k+lp)\omega_r t + \psi_{b\alpha}) \\ +a_{f\alpha} sin\left(k\theta_r + (k-lp)\omega_r t + \psi_{f\alpha}\right) \end{bmatrix} \tag{2-25}$$

where the magnitude components $a_{br}, a_{fr}, a_{b\alpha}, a_{f\alpha}$ can be are evaluated as,

$$a_{br} = \left| -a_{1l} e^{j\psi_{al}} - c_{1l} e^{j\left(\psi_{cl} - \frac{\pi}{2}\right)} \right| / 2 \tag{2-26}$$

$$a_{fr} = \left| -a_{1l} e^{-j\psi_{al}} + c_{1l} e^{-j\left(\psi_{cl} - \frac{\pi}{2}\right)} \right| / 2 \tag{2-27}$$

$$a_{b\alpha} = \left| -a_{1l} e^{j\left(\psi_{al} - \frac{\pi}{2}\right)} + c_{1l} e^{j\psi_{cl}} \right| / 2 \tag{2-28}$$

$$a_{f\alpha} = \left| a_{1l} e^{-j\left(\psi_{al} - \frac{\pi}{2}\right)} + c_{1l} e^{-j\psi_{cl}} \right| / 2 \tag{2-29}$$

also the phase components $\Psi_{br}, \Psi_{fr}, \Psi_{b\alpha}, \Psi_{f\alpha}$ as,

$$\psi_{br} = angle\left(-a_{1l} e^{j\psi_{al}} - c_{1l} e^{j\left(\psi_{cl} - \frac{\pi}{2}\right)} \right) \tag{2-30}$$

$$\psi_{fr} = angle\left(-a_{1l} e^{-j\psi_{al}} + c_{1l} e^{-j\left(\psi_{cl} - \frac{\pi}{2}\right)} \right) \tag{2-31}$$

$$\psi_{b\alpha} = angle\left(-a_{1l}e^{j\left(\psi_{al}-\frac{\pi}{2}\right)} + c_{1l}e^{j\psi_{cl}}\right) \tag{2-32}$$

$$\psi_{f\alpha} = angle\left(a_{1l}e^{-j\left(\psi_{al}-\frac{\pi}{2}\right)} + c_{1l}e^{-j\psi_{cl}}\right) \tag{2-33}$$

The definitions for other coefficients in (2.4)-(2.33) can be found in [84].

Since circumferential component of flux density is relatively small in SPM machines with radial magnetization, and its effect on eddy current loss is neglected [91]. Hence the eddy current loss due to radial component only is considered in the 3D magnet loss prediction in this chapter. The contribution of circumferential component towards the magnet loss is evaluated and is discussed in detail in Chapter 3.

The equation for B_r can be expressed as odd Fourier series, as shown in Fig. 2-2 along z direction satisfying the boundaries $-L_z/2 \le z \le L_z/2$ to create an alternating field along the magnets adjacent in axial direction. The part of the waveform in the range $-L_z/2 \le z \le L_z/2$ represents the flux density variation along the magnet in its axial direction which is assumed constant.

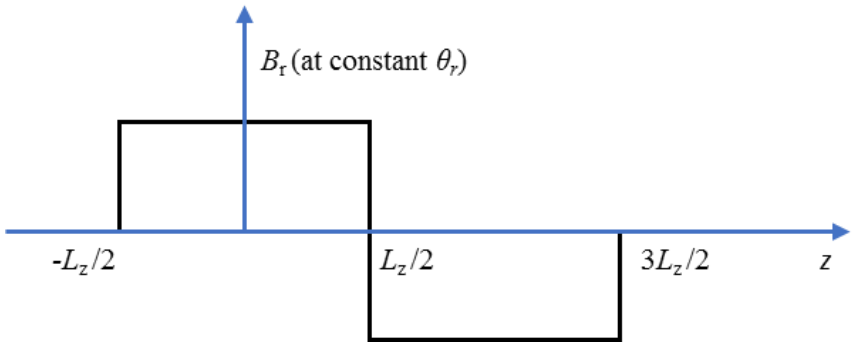

Fig. 2-2. Periodic expansion of magnet flux density in axial (*z*) direction.

Thus $B_r(r,\theta,t)$ in (2-21) can be expressed as Fourier series along z–direction as,

$$B_r(r,\theta,z,t) = \sum_{\lambda} B_r(r,\theta,t)\, 4/(\pi\lambda)\sin(0.5\pi\lambda)\cos(\lambda\pi z/L_z) \tag{2-34}$$

where λ=1, 2, 3... and L_z is the axial length of the magnet.

This expression ensures the z-component of the eddy current density zero at both axial ends of the magnet.

$\partial B_r/\partial t$ calculated from (2-34) forms the source for eddy current generation and can be derived as,

$$\frac{\partial B_r}{\partial t} = \sum_{\lambda}\sum_{k}\sum_{l}\begin{bmatrix} B_{rb}\cos(\lambda\pi z/L_z)\cos(k\theta_r + (k+lp)\omega_r t + \psi_{br}) \\ + B_{rf}\cos(\lambda\pi z/L_z)\cos\left(k\theta_r + (k-lp)\omega_r t + \psi_{fr}\right) \end{bmatrix} \quad (2\text{-}35)$$

where,

$$B_{rb} = a_{br}\,(k+lp)\omega_r\, C_{2k}\, 4/(\pi\lambda)\sin(0.5\pi\lambda) \quad (2\text{-}36)$$

and,

$$B_{rf} = a_{fr}\,(k-lp)\omega_r\, C_{2k}\, 4/(\pi\lambda)\sin(0.5\pi\lambda) \quad (2\text{-}37)$$

2.3 Current Vector Potential and Formulation of Eddy Current Prediction

The concept of the current vector potential is based on the fact that the divergence of the current density, $\vec{J}$ must equal to zero [91], i.e. $\nabla.\vec{J} = 0$.

This allows us to define a current vector potential $\vec{I}$ satisfying $\vec{J} = \nabla \times \vec{I}$. The current vector potential with only radial component but varies with $\theta - z$ can be described in cylindrical coordinates at a given time instant t as,

$$\vec{I}(\theta_r, z, t) = I_r\,\vec{r} + 0\overrightarrow{\theta_r} + \overrightarrow{0z} \quad (2\text{-}38)$$

The current vector potential also must be satisfying $\nabla.\vec{I} = 0$ to ensure the net current in a magnet is zero.

Now from the Faradays law,

$$\nabla \times \vec{J}/\sigma = -\partial B_r/\partial t \tag{2-39}$$

where σ is the conductivity of the magnetic material.

Substituting $\vec{I}$ for $\vec{J}$ in (2-36),

$$\nabla \times \left(\nabla \times \vec{I}\right)/\sigma = -\nabla^2 \vec{I}/\sigma = -\partial B_r/\partial t \tag{2-40}$$

The expansion of (2-40) as differential equation implies that $\vec{I}$ only has a radial component which satisfies,

$$1/\mathrm{r}^2\, \partial^2 I_r/\partial \theta_r{}^2 + \partial^2 I_r/\partial z^2 = -\partial B_r/\partial t \tag{2-41}$$

It is evident that the accuracy predicting $\vec{I}$ from the solution of (2-41) and hence the eddy current loss calculation is decided by the accuracy of the $\partial B_r/\partial t$ calculations.

Since the eddy current flows in the tangential direction on all surfaces in a magnet, the current vector potential $\vec{I}(\theta_r, z, t)$ must be zero on all magnet surfaces.

Hence the boundary conditions of (2-41) are given as:

$$\vec{I}(\theta_r = \theta_0) = \vec{I}(\theta_r = \beta_M + \theta_0) = 0 \tag{2-42}$$

$$\vec{I}(z = -L_z/2) = \vec{I}(z = +L_z/2) = 0 \tag{2-43}$$

where θ_0 is the starting edge of the magnet under consideration and β_M is the magnet pole arc angle in mechanical degrees.

It is worth noting that the boundary condition of the eddy current density at the two cylindrical surfaces is automatically satisfied by the current vector potential formulation of (2-41). The geometric parameters of the magnet with n_c circumferential segments and n_a axial segments are illustrated in Fig. 2-3.

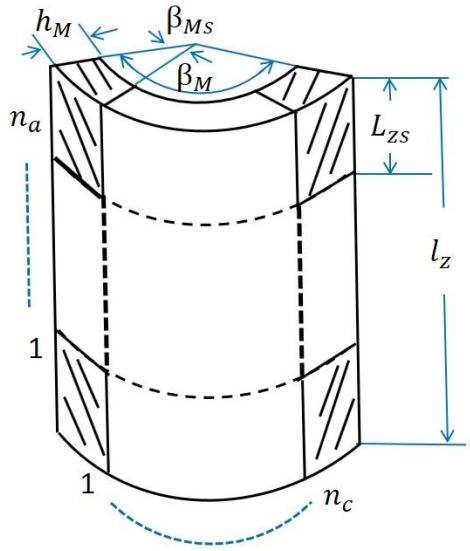

Fig. 2-3. Geometry of the magnet in cylindrical system illustrating segmentation.

The solution for the current vector potential satisfying the boundary conditions (2-42) and (2-43) can be derived as[109, 110],

$$I_r(\theta, z, t) =$$

$$-\sum_{\lambda}\sum_{k}\sum_{l}\left\{\begin{array}{c} B_{rb}\dfrac{cos(mz)}{(n^2+m^2)\sinh(mr\beta_M)}\cdot \\ \left[\begin{array}{c} sinh\left(mr\left(\theta_r-(\beta_M+\theta_0)\right)\right)cos(k\theta_0+(k+lp)\omega_r t+\psi_{br}) \\ -sinh\left(mr(\theta_r-\theta_0)\right)cos(k(\beta_M+\theta_0)+(k+lp)\omega_r t+\psi_{br}) \\ +sinh(mr\beta_M)cos(k\theta_r+(k+lp)\omega_r t+\psi_{br}) \end{array}\right] \end{array}\right\}$$

$$-\sum_{\lambda}\sum_{k}\sum_{l}\left\{\begin{array}{c} B_{rf}\dfrac{cos(mz)}{(n^2+m^2)\sinh(mr\beta_M)}\cdot \\ \left[\begin{array}{c} sinh\left(mr\left(\theta_r-(\beta_M+\theta_0)\right)\right)cos(k\theta_0+(k-lp)\omega_r t+\psi_{fr}) \\ -sinh\left(mr(\theta_r-\theta_0)\right)cos(k(\beta_M+\theta_0)+(k-lp)\omega_r t+\psi_{fr}) \\ +sinh(mr\beta_M)cos(k\theta_r+(k-lp)\omega_r t+\psi_{fr}) \end{array}\right] \end{array}\right\} \quad (2\text{-}44)$$

where $m = \lambda\pi/L_z$ and $n = k/r$.

The axial component J_z and the circumferential component J_θ of the eddy current at a radius 'r' can be derived from $\vec{J} = \nabla \times \vec{I}$ as $J_z(t) = -1/r \ .\partial I_r/\partial\theta_r$ and $J_\theta(t) = \partial I_r/\partial z$ respectively. They are given in (2-45) and (2-46) respectively.

$$J_z(\mathrm{t}) =$$

$$\sum_{\lambda}\sum_{k}\sum_{l}\left\{\begin{bmatrix} B_{rb}\dfrac{cos(mz)}{(n^2+m^2)\sinh(mr\beta_M)}\cdot \\ m.cosh\left(mr\left(\theta_r-(\beta_M+\theta_0)\right)\right)cos(k\theta_0+(k+lp)\omega_r t+\psi_{br}) \\ -m\,cosh\left(mr(\theta_r-\theta_0)\right)cos(k(\beta_M+\theta_0)+(k+lp)\omega_r t+\psi_{br}) \\ -k/r\ sinh(mr\beta_M)\,sin(k\theta_r+(k+lp)\omega_r t+\psi_{br}) \end{bmatrix}\right\}$$

$$+\sum_{\lambda}\sum_{k}\sum_{l}\left\{\begin{bmatrix} B_{rf}\dfrac{cos(mz)}{(n^2+m^2)\sinh(mr\beta_M)}\cdot \\ m.cosh\left(mr\left(\theta_r-(\beta_M+\theta_0)\right)\right)cos\left(k\theta_0+(k-lp)\omega_r t+\psi_{fr}\right) \\ -m\,cosh\left(mr(\theta_r-\theta_0)\right)cos\left(k(\beta_M+\theta_0)+(k-lp)\omega_r t+\psi_{fr}\right) \\ -k/r\ sinh(mr\beta_M)\,sin\left(k\theta_r+(k-lp)\omega_r t+\psi_{fr}\right) \end{bmatrix}\right\} \quad (2\text{-}45)$$

$$J_\theta(\mathrm{t}) =$$

$$\sum_{\lambda}\sum_{k}\sum_{l}\left\{\begin{bmatrix} B_{rb}\dfrac{m\,sin(mz)}{(n^2+m^2)\sinh(mr\beta_M)}\cdot \\ sinh\left(mr\left(\theta_r-(\beta_M+\theta_0)\right)\right)cos(k\theta_0+(k+lp)\omega_r t+\psi_{br}) \\ -sinh\left(mr(\theta_r-\theta_0)\right)cos(k(\beta_M+\theta_0)+(k+lp)\omega_r t+\psi_{br}) \\ +sinh(mr\beta_M)\,cos(k\theta_r+(k+lp)\omega_r t+\psi_{br}) \end{bmatrix}\right\}$$

$$+\sum_{\lambda}\sum_{k}\sum_{l}\left\{\begin{bmatrix} B_{rf}\dfrac{msin(mz)}{(n^2+m^2)\sinh(mr\beta_M)}\cdot \\ sinh\left(mr\left(\theta_r-(\beta_M+\theta_0)\right)\right)cos\left(k\theta_0+(k-lp)\omega_r t+\psi_{fr}\right) \\ -sinh\left(mr(\theta_r-\theta_0)\right)cos\left(k(\beta_M+\theta_0)+(k-lp)\omega_r t+\psi_{fr}\right) \\ +sinh(mr\beta_M)\,cos\left(k\theta_r+(k-lp)\omega_r t+\psi_{fr}\right) \end{bmatrix}\right\} \quad (2\text{-}46)$$

It is evident from Fig. 2-3 that the magnet segment of axial length of L_{zs} and the corresponding segment arc angle β_{Ms} needed to be substituted for L_z and β_M respectively when evaluating the solution to the current vector potential and hence the current densities while considering magnets with segmentations.

The eddy current loss in a magnet can be derived as the sum of each harmonic loss considering the flux density variations at different radial

distances throughout the entire radial thickness (h_M) of the magnet. The total magnet loss considering segmentation in the machine at any time instant can be approximated by averaging a magnet segment loss evaluated at these radial distances and multiplying with the total number of magnet segments as,

$$P_e(t) = \frac{1}{N_r}\sum_{R_r}^{R_m}\sum_{\lambda}\sum_{k}\sum_{l}\frac{h_M n_c n_a}{\sigma}\int_{\theta_0}^{\beta_{Ms}+\theta_0}\int_{-l_{Ms}/2}^{l_{Ms}/2}\left(J_{s\theta}^2 + J_{sz}^2\right).r d\theta_r.dz \tag{2-47}$$

where N_r is the number of radial position considered in the computation and J_{s_z} and J_{s_θ} are the axial and circumferential component of current density evaluated for the magnet segment.

2.4 Method of Implementation

2.4.1 Computation Process

The subdomain model is implemented in MATLAB and is run for an electrical cycle to evaluate harmonics components of the coefficients accounting slotting effect (A_1 and C_1) described in Section 2.2. As the accuracy of computation of these components depends on the number of samples collected in an electrical cycle, the model is run for 720 steps in an electrical cycle. The time step chosen corresponds to 0.5 electrical degree (0.125 mechanical degree) which is sufficient to include the variations of the highest order harmonics in the flux density within the magnet for an 8-pole, 18-slot SPM machine considered in this chapter. It is observed that the harmonics of the order above 54 can result only a negligible amount of eddy current loss for the above SPM machine as detailed in Chapter 3. The 3D source distribution over any radial distance is evaluated from (2-35). The axial and circumferential components of eddy current distribution at a time instant at different radial distances in a magnet is evaluated from (2-45) and (2-46) and the eddy current loss from (2-47), applying its physical boundary limits to the integration.

However, a better approximation can be obtained by computing the sum of loss in each circumferential magnet segment separately and adding them together to find the total magnet loss at different time instants. Loss variation among the different axial segments is neglected in such calculations. Because time varying eddy current densities repeats 6 times in a fundamental electric period for a three phase machine, it is necessary to calculate the eddy current loss at least for 1/6th of the electrical period while obtaining the average value. The loss repetition is decided by the lowest order space harmonics within the magnet. It can be observed from (2.35) and (2.47) that the magnet loss varies proportional to the square of the eddy current sources and hence it varies at twice the source frequency. The instantaneous loss variation for different harmonics, the instantaneous variation of loss among different magnet segments and their total is explained in detail in the next chapter (Section 3.6.3 and Section 3.8.3).

For the 18-slot, 8-pole machine under consideration the radial positions N_r is chosen as 50 while evaluating the 3D magnet loss from (22). The percentage difference when the number of radial position is increased to 60 is only 0.247% with respect to the results obtained when N_r=50. However the computation time for the magnet loss prediction per case is increased by 7 minutes when N_r is increased from 50 to 60. This shows the usage of more radial samples may results only in marginal improvement of accuracy at the expense of more time consumed.

2.4.2 Magnetic 3D End Effect

The influence of the end windings and the fringe effect, can cause the flux density due to the armature windings and the magnet decreases in the regions close to the axial ends of the machine. It is shown in a few studies analytically [111, 112] and by 3D FE [113, 114] that the affected length of the machine air gap in the axial direction is approximately equal to length equivalent to the sum of the magnet thickness and the air gap which is termed as equivalent air gap.

The region is said to be affected if the flux density in the region drops below 99% of the values that exists in the middle of the axial length. However, in most radial field machines this effect is negligible as the axial length is sufficiently larger than the equivalent air gap. For the machines with larger number of axially segmented magnets, the magnets segments which are at the axial ends on either sides may get affected causing a reduction in their flux density values. This can result in loss difference among the axially segmented magnets. In such cases 3D magneto-static field solutions may be obtained to adjust the flux density values before implementing in the proposed method for better accuracy, albeit the computation time will become much longer. However, for the machine under consideration, it is observed that the flux density variations w.r.t end effect is negligible from the magneto-static computations up to 12 axial segments, hence not included in the computation.

2.5 Finite Element Validation

The developed 3D eddy current loss prediction technique is applied to an 8-pole, 18-slot SPM machine with double layer overlapping winding configuration as shown in Fig. 2-4. The machine employs winding design features [115] to reduce space harmonics and hence reduced rotor eddy current loss, while retaining the merits of fractional slot per pole machine topology.

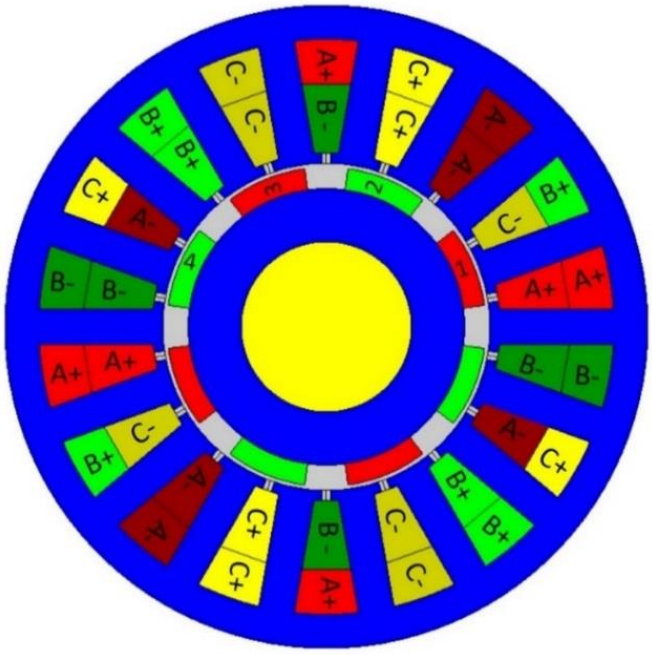

Fig. 2-4. 18-slot 8-pole machine with fractional-slot per pole winding configuration.

The key geometrical, physical parameters and specifications are listed in Table 2-1.

Table 2-1. Specifications and Key Dimensions of 18-slot, 8-pole SPM Machine

Parameter	Unit	Value
Continuous power	kW	5
Peak power	kW	10
Base speed	rpm	1350
Maximum speed	rpm	4500
No of turns per coil	-	6
Stator outer radius	mm	75.59
Motor stack length	mm	118
Air gap length	mm	0.955
Rotor radius	mm	37.5
Magnet thickness	mm	5.0
Magnet resistivity	Ω.m	$1.8x10^{-6}$
Magnet pole arc angle	°elec.	117.6
Magnet remanent flux density	T	1.1
Slot opening	mm	2.03
Slot opening depth	mm	2.375
Slot depth	mm	26.79
Shaft radius	mm	20.0

The eddy current and the associated loss are evaluated when the machine is operated at no load and also at peak load conditions with a peak phase current of 80A at 4500rpm.

2.5.1 2D FE Validation of the Eddy Current Sources

Before the eddy current loss in the magnets is evaluated by the developed analytical technique, it is insightful to have confidence on the analytically predicted source of eddy current generation $\partial B_r/\partial t$. The analytically and 2D- FE predicted $\partial B_r/\partial t$ variations with θ_r at r = 37.5mm, 35.0mm and 32.5 mm at $\omega_r t = 1.25^0$ of magnet–1 is compared in Fig. 2-5, Fig. 2-6 and Fig. 2-7 respectively for the peak load conditions mentioned above.

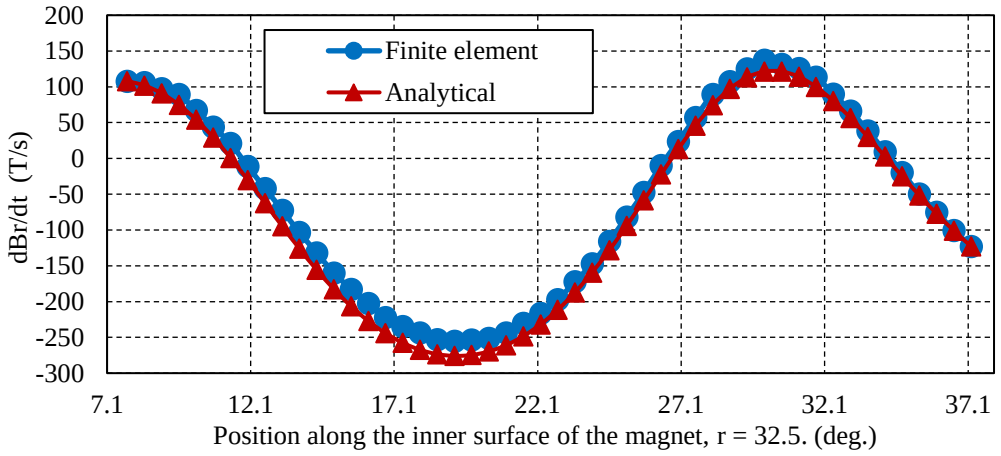

Fig. 2-5. $\partial B_r/\partial t$ comparison of 2D FE and slotting effect model at inner surface at $\omega_r t = 1.25^0$ of magnet–1.

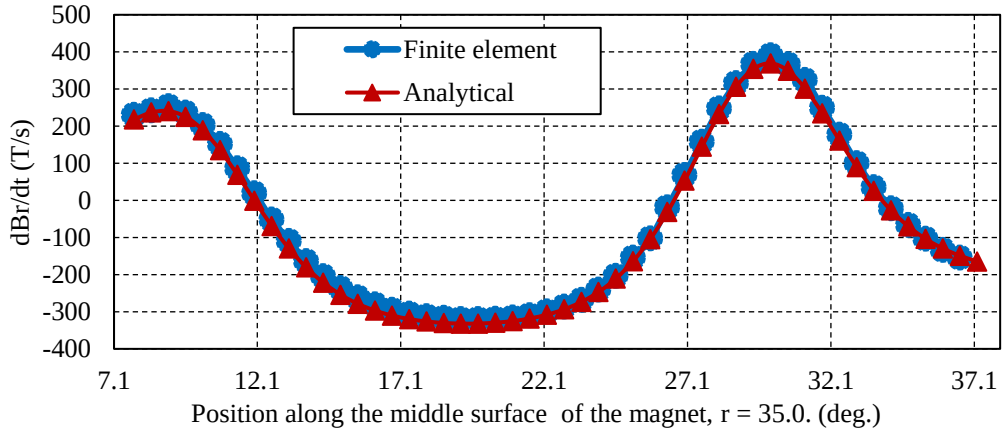

Fig. 2-6. $\partial B_r/\partial t$ comparison of 2D FE and slotting effect model at middle surface at $\omega_r t = 1.25^0$ of magnet–1.

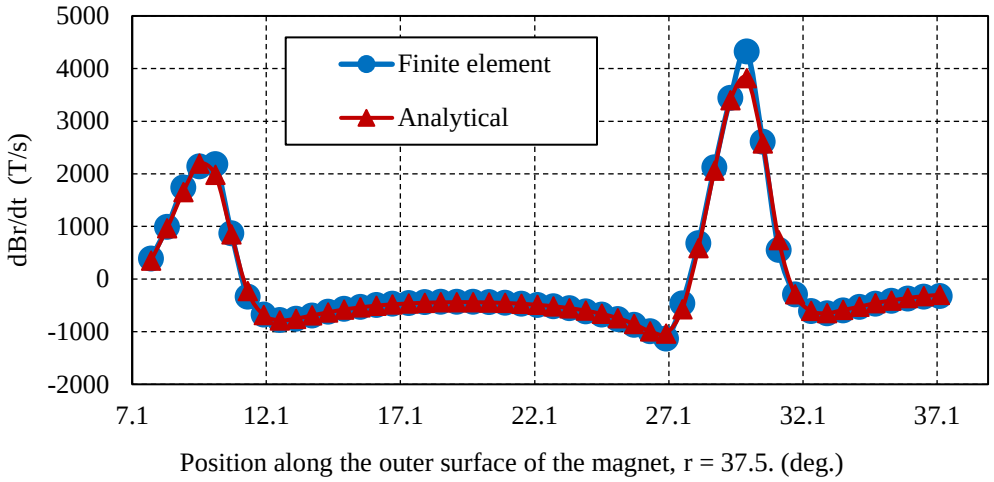

Fig. 2-7. $\partial B_r/\partial t$ comparison of 2D FE and slotting effect model at outer surface at $\omega_r t = 1.25^0$ of magnet–1.

As can be seen, $\partial B_r/\partial t$ predicted by the subdomain model considering slotting effect has shown good accuracy with the 2D transient FE analysis at the peak load. The slight difference is visible at the magnet inner surface due to core saturation which is neglected in the analytical model and also due to the simplified slot shaping [85] used in the subdomain model. The slot in the subdomain model accounting for tooth-tips has equal width angle. However in 2D FE model , the width angle increases when the position moves into the slot since the tooth body has the uniform width, as shown in the Fig. 2-8.

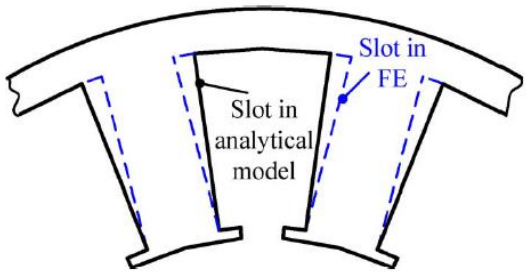

Fig. 2-8. Slot Shape in FE and subdomain model accounting for tooth tips [85].

2.5.2 3D FE Validation of the Proposed Method

To validate the developed method of predicting the 3D eddy current loss, the eddy current distribution and eddy current loss are also predicted by 3D time- stepped FE analysis using the model shown in Fig. 2-9.

Since the machine employs fractional slot per pole topology, circumferential symmetry exits only over 180 mechanical degrees. Thus, only a quarter of the machine need to be modelled in 3D FEAs (half the machine in circumferential direction and the half in axial direction). Tangential field boundary conditions are imposed on the top and the circumferential surface. In addition, perfect insulation boundaries are applied to the end surfaces of the magnets. However, the effect of end winding on flux density variations is neglected in the 3D FE analysis. To ensure the better calculation accuracy, the mesh density along the magnets needs to be reasonably high.

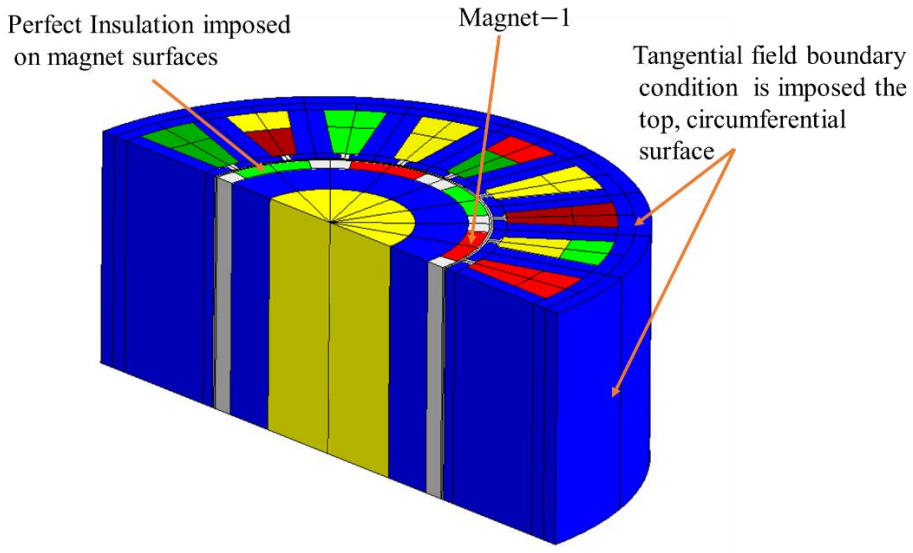

Fig. 2-9. Quarter model of the machine in Flux 2D and 3D based on symmetry.

3-phase sinusoidal currents of 80A peak is injected in the machine phases via the electrical circuit as shown in Fig. 2-10. The machine is considered to be operating with only *q*-axis current assuming no field weakening as simulated in the subdomain model. Magnets are defined as solid conductor regions short

circuited with resistances of higher value to ensure eddy currents circulating within it as shown in the figure below.

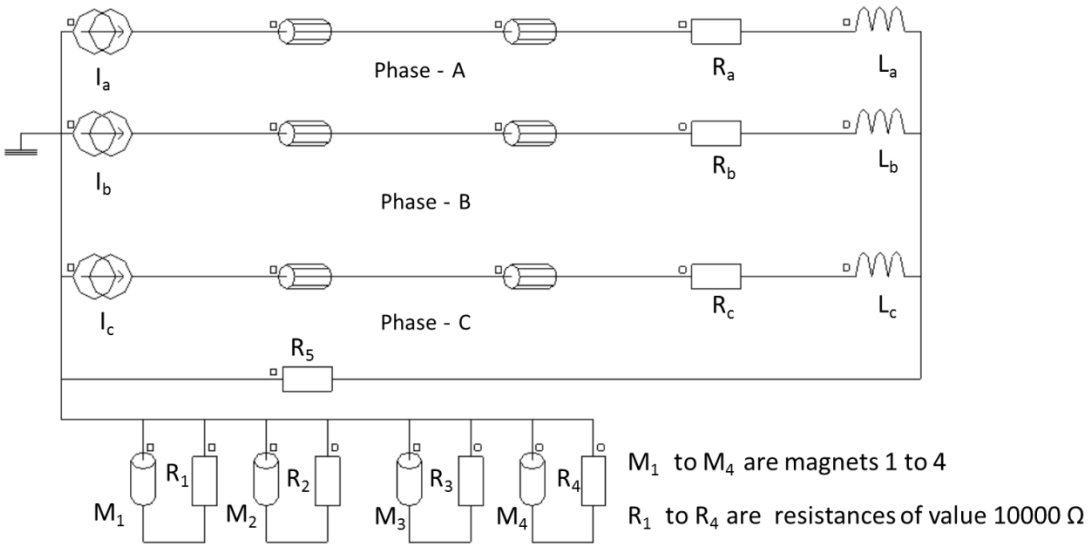

Fig. 2-10. Electrical circuit implemented in 3D-FEA for magnet loss evaluation.

3D FE analysis is carried out at peak load conditions at 4500 rpm. Fig. 2-11 compares analytically and 3D FE predicted z–component of the eddy current density distribution at the outer cylindrical surface of Magnet–1 indicated in Fig. 2-9 which is located at an angle of 24^0 at time =55.5μs when the machine is operating with two axial magnet segmentation and rotating at the speed of 4500 rpm.

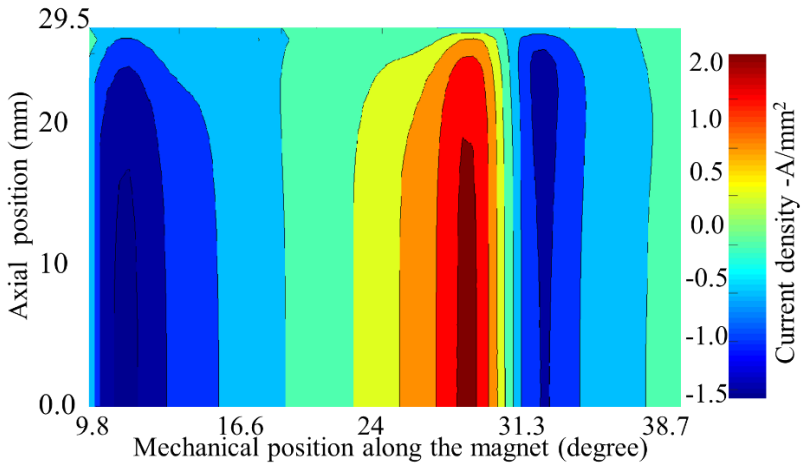

(a) Current density (J_{s_z}) from 3D analytical method, on the magnet outer surface.

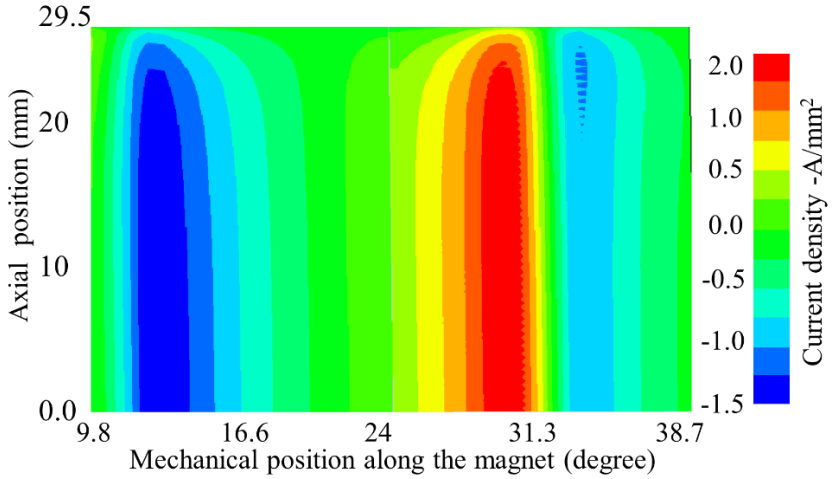

(b) Current density (J_{s_z}) from 3D FE on the magnet outer surface.

Fig. 2-11. Comparison of the z-component of eddy current density distribution for the upper half of Magnet -1 at its outside surface from analytical and 3D FE.

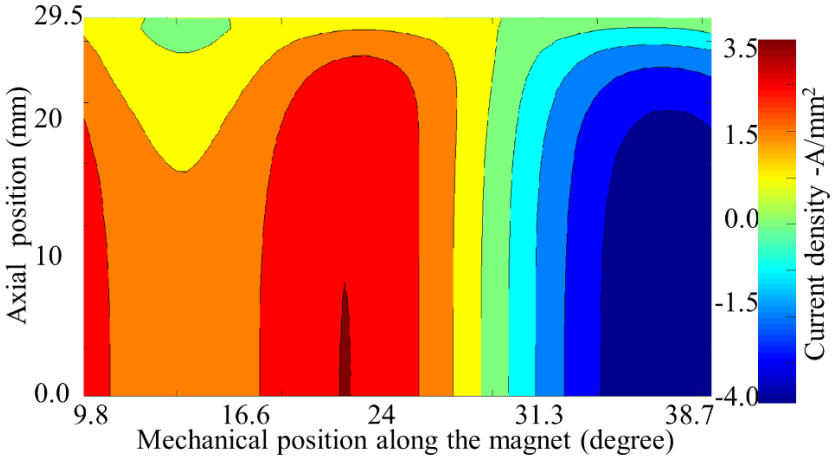

(a) Current density (J_{s_z}) from 3D analytical on the magnet inner surface.

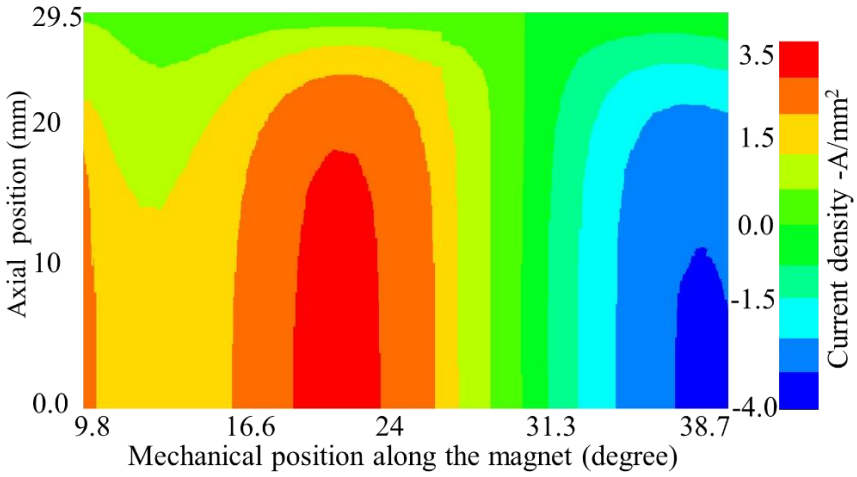

(b) Current density (J_{s_z}) from 3D FE on the magnet inner surface

Fig. 2-12. Comparison of the z-component of eddy current density distribution for the upper half of the magnet-1 at its outside surface from 3D analytical and 3D FE.

Fig. 2-12 gives the comparison of analytically and 3D FE predicted z-component of eddy current density distributions at the inner surface of Magnet -1.

A similar comparison for analytically and 3D FE predicted θ-component of the eddy current density distribution at the same operating conditions mentioned above for the outer and inner cylindrical surfaces of Magnet -1 is given in Fig. 2-13 and Fig. 2-14 respectively.

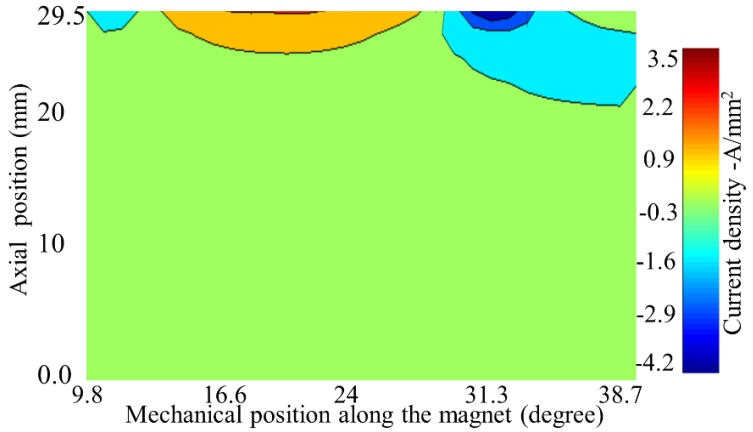

(a) Current density (J_{s_θ}) from 3D analytical method, on the magnet outer surface.

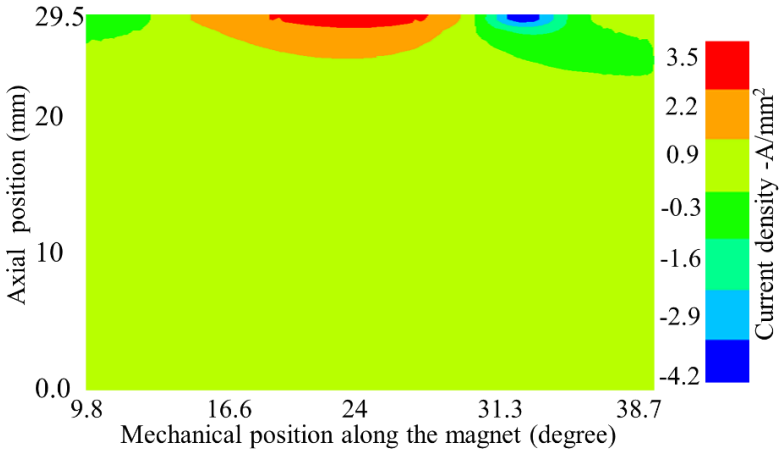

(b) Current density (J_{s_θ}) from 3D FE, on the magnet outer surface.

Fig. 2-13. Comparison of the θ-component of eddy current density distribution for the upper half of Magnet-1 at its outside surface from 3D analytical and 3D FE.

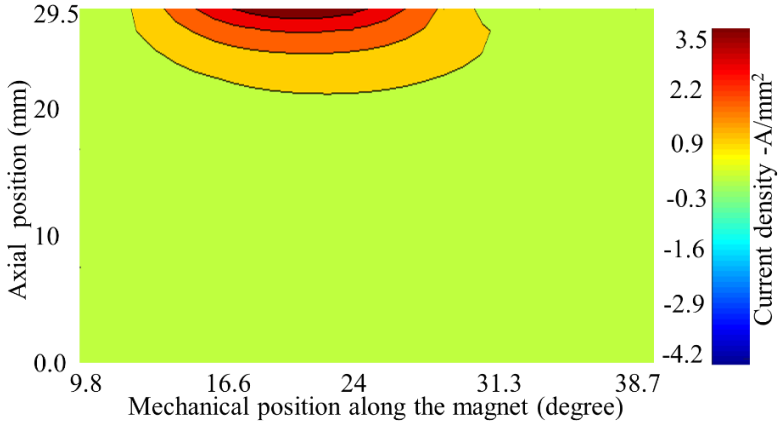

(a) Current density (J_{s_θ}) from 3D analytical method, on the magnet inner surface.

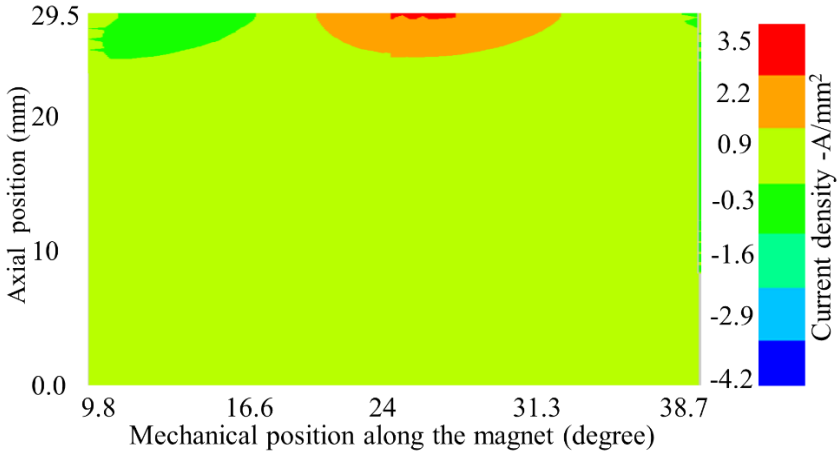

(b) Current density (J_{s_θ}) from 3D FE, on the magnet inner surface.

Fig. 2-14. Comparison of the θ-component of eddy current density distribution for the upper half of Magnet-1 at its inner surface from 3D analytical and 3D FE.

It can be observed that the z–and θ–component of eddy current density distribution from the analytical computation is matching with 3D FE with a good accuracy, except for a few meagre mismatches especially along the inner surface of the magnet, as a result of the $\partial B_r/\partial t$ discrepancy shown in Fig. 2-5. The differences observed in the analytically predicted θ–component of eddy current density distribution may not affect the magnet loss calculation to a larger extent as its values are lower when compared with the z–component values.

The analysis is repeated with different number of circumferential and axial segments at the peak load conditions of the machine and total magnet loss is evaluated. The results from 2D FE, 3D FE and 3D analytical for different axial segmentations with one and two circumferential segments at peak load conditions are shown in Fig. 2-15 and Fig. 2-16 respectively.

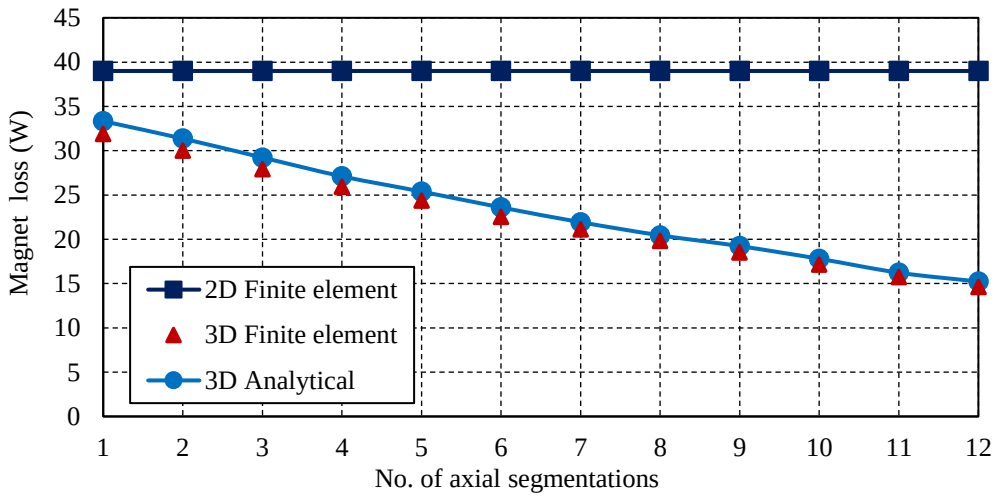

Fig. 2-15. Magnet losses comparison- peak load (Circumferential segments: 1).

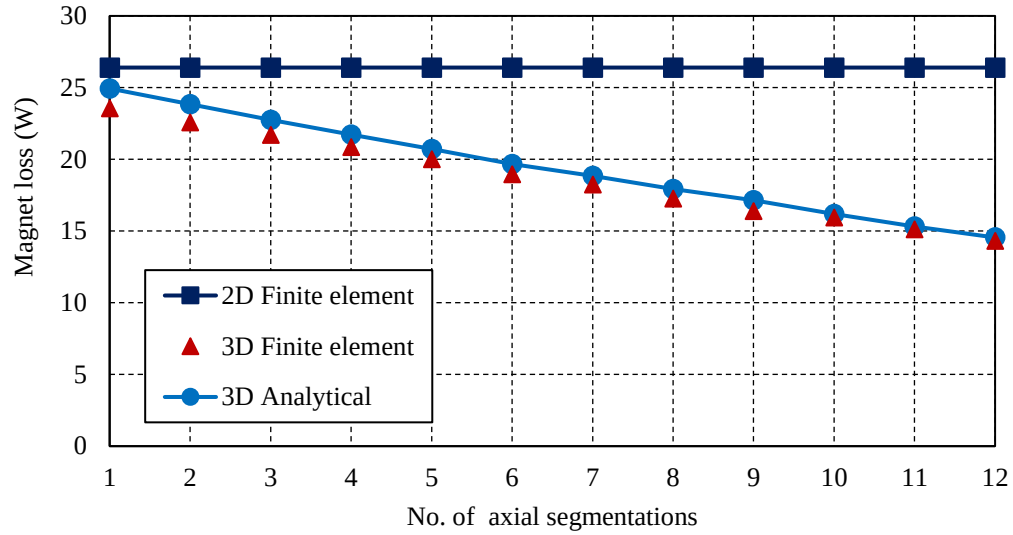

Fig. 2-16. Magnet losses comparison- peak load (Circumferential segments: 2).

The variation of magnet loss from 2D FE, 3D FE and 3D analytical for different circumferential segmentations with one axial segment at the peak load conditions are compared in Fig. 2-17.

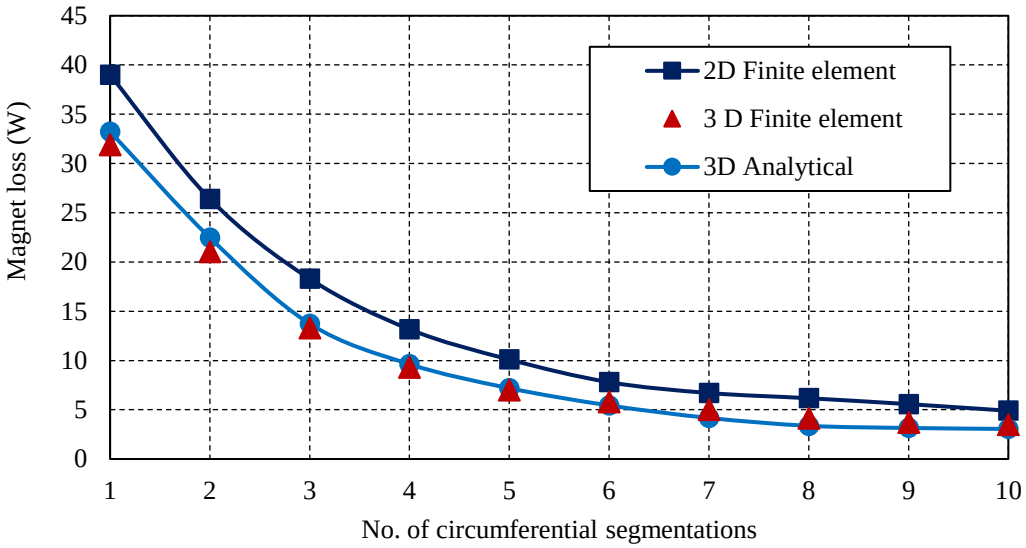

Fig. 2-17. Magnet losses comparison- peak load (Axial segments: 1).

It is evident from the results the analytical predictions agree very well with the 3D FE results. The minor deviation of the analytical predictions from the 3D FE results can be attributed to neglecting the tangential component of flux density in the loss prediction and also due to the error in the $\partial B_r/\partial t$

evaluation. Also the minor variation in the results predicted with that form 3D FE may also be attributed to the interaction of the harmonics of the same frequency in magnets [107] which is neglected in the proposed method. In contrast, significant errors occur in 2D FE eddy current loss predictions. This is because as discussed previously the 2D FE doesn't consider the end effects of the eddy current flow and hence cannot be used to predict the 3D eddy current loss.

As the proposed method is validated from 3D FE results, it can be used to predict the magnet loss at any load conditions. Fig. 2-18 shows the variation of 3D magnet loss at no load with increase in axial and circumferential segmentation predicted from the proposed method when the machine is running at a speed of 4500 rpm.

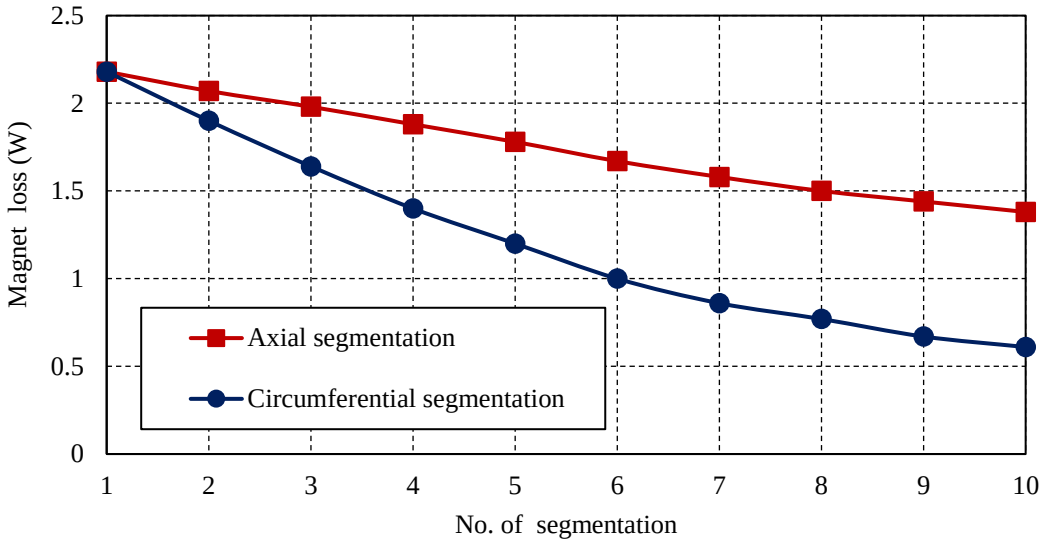

Fig. 2-18. No Load magnet variation with axial and circumferential segmentation predicted from the proposed method.

2.6 Computational Efficiency of the Proposed 3D Analytical Method

The computation time for the subdomain model to extract the flux density information at each operating condition is close to 22.45 minutes. While the computation time for the analytical model to predict the magnet loss at each

operating condition per case is about 20.5 minutes ($N_r = 50$) on a 64 GB RAM desktop computer (Intel(R) Core (TM) I7-5820K CPU, 3.3 GHz processor with 6 cores) in Matlab environment. However, it takes more than 60 hours for 3D FE with no axial segmentations ($n_a = 1$) for 8-pole, 18-slot SPM with the given dimensions. Also it takes almost 10 hours for 3D FE with 12 axial segmentations ($n_a = 12$).

2.7 Effect of Slotting in Varying Magnet Loss with Change in Field Weakening Angle

It is well known that the eddy current loss in the rotor magnets are contributed by both armature reaction field and slotting effect. Under some load conditions such as field weakening, it is observed that the slotting effect reduces the total eddy current loss [107, 116, 117] . In order to study the effect of slotting on reduction of magnet loss under field weakening, loss computations are performed by employing the proposed analytical technique with different values of the phase advance or field weakening angle 'γ' from 0^0 to 90^0 in steps of 30^0. $\gamma = 0^0$ corresponds to the phase current being in phase with the back EMF of the machine. Fig. 2-19 shows the comparison of magnet loss with increase in field weakening angle for the 18-slot 8-pole SPM machine, with magnet pole arc angle 'β_M' of 175^0 expressed in electrical degrees.

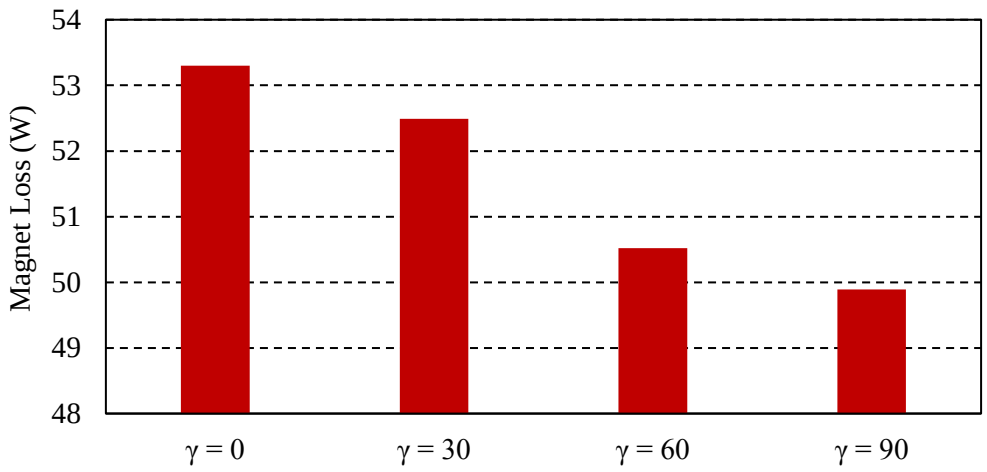

Fig. 2-19. Magnet losses comparison with increase in γ when supplied with 80A (peak) at 4500 rpm.

From the loss evaluation employing the proposed method, It is observed that the difference in loss from $\gamma = 0^0$ to $\gamma = 90^0$ is 3.41W, which is close to the no load magnet loss of 3.2W.

To apprehend the above observation, the magnet loss associated with the harmonics of the order which are integer multiples of the slot number 'N_s' is separated from the total loss. Fig. 2-20 compares the difference in magnet loss due to the harmonics whose order are integer multiples of N_s and the losses originated from all other harmonics with field weakening angle.

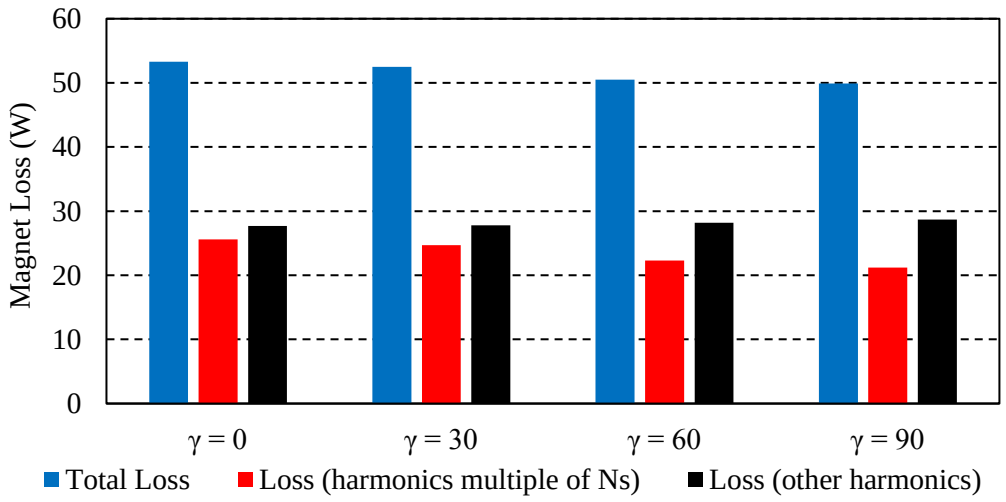

Fig. 2-20. Separation of losses due to harmonics which are multiple of N_s.

It is clear from Fig. 2-20 that the loss associated with harmonics which are integer multiples of N_s is reducing with increase in field weakening angle, while the loss associated with other harmonics is more or less the same.

It can be shown that the harmonic contents of the source of the eddy current generation $\partial B_r/\partial t$ associated with the slotting effect [82] in the rotor reference are of the order

$(\mu p \pm \upsilon N_s)\theta_r \pm \upsilon N_s \omega_r t$, where μ= 1, 3, 5… and υ= 1, 2, 3…

Similarly from [60], the harmonic orders of $\partial B_r/\partial t$ due to armature reaction in the rotor reference are identified as:

$np_s\theta_r + (np_s - p)\omega_r t$, n = 2, 5, 8… for the forward rotating harmonics and

$np_s\theta_r + (np_s + p)\omega_r t$, n = 1, 4, 7... for the backward rotating harmonics.

where p_s is the number of pole pairs associated with the stator winding.

For a given pole and slot number combination, and winding configuration, it can be shown that the slotting harmonics and a subset of the harmonics due to armature reaction have the same orders.

For the 18-slot 8-pole surface mounted PM machine considered in this study, $p_s$is equal to two, N_s= 18 and p = 4. Thus, the slotting harmonics are of the orders of 18, 36, 54…, and the armature reaction field seen by the rotor magnets also contains 18th, 36th, 54th..., harmonics.

Fig. 2-21 compares the magnitude of the major harmonic contents in $\partial B_r/\partial t$ which are evaluated from (2-32) at a point in the middle of Magnet– 1 at the peak load conditions, which results from the slotting harmonics and the harmonics due to armature reaction when γ = 0^0 , +90^0 and -90^0 . The slotting harmonics are evaluated from (2-32) at no load conditions at 4500 rpm, while the armature reaction harmonics at the same order are evaluated from the non –slotting model [60].

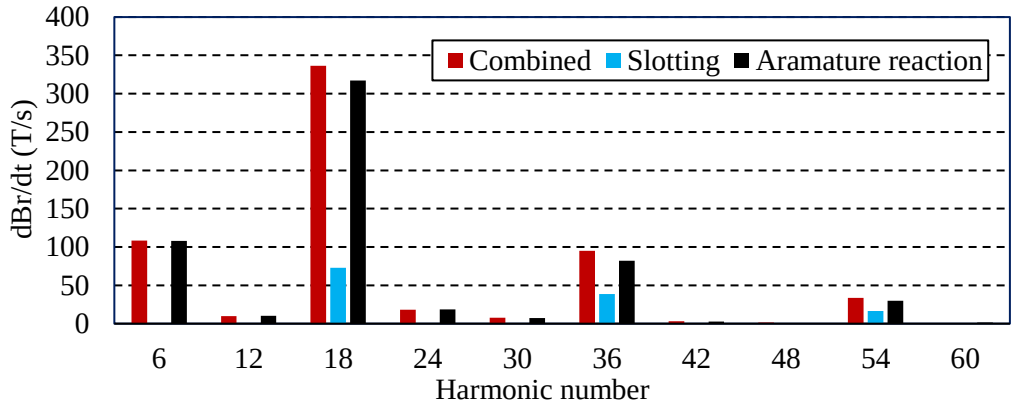

(a) Comparison of harmonic distribution at γ = 0^0

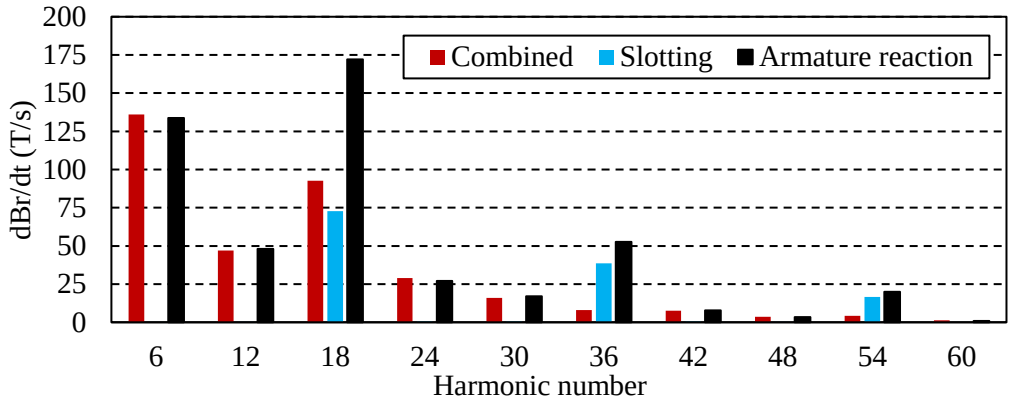

(b) Comparison of harmonic distribution at $\gamma = +90^0$

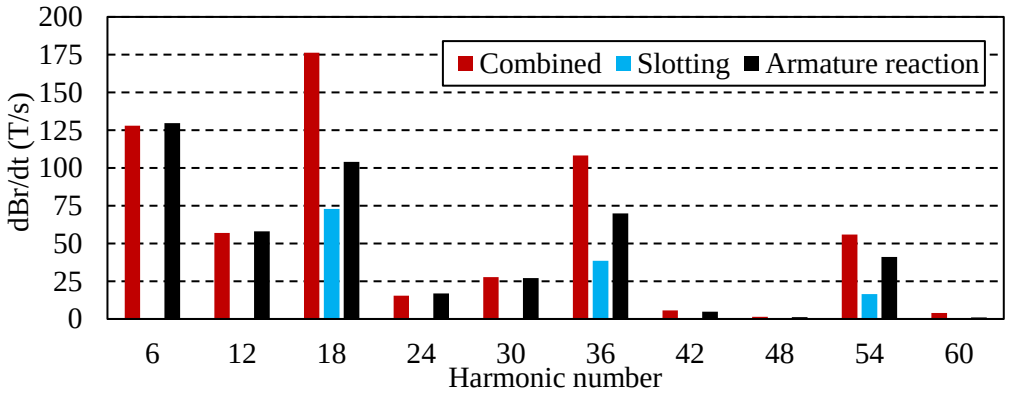

(c) Comparison of harmonic distribution at $\gamma = -90^0$

Fig. 2-21.Comparison of harmonic distribution due to armature reaction, slotting and their combination with γ .

It is observed that the phase angle between the slotting harmonics and the armature reaction harmonics is close to 0^0 when γ = -90^0, which represents phase retarding. This angle reaches close to $+90^0$ when $\gamma = 0^0$, and becomes close to 180^0 when $\gamma = +90^0$. Since the magnitude of $\partial B_r/\partial t$ harmonics of the same order is a vector sum of the slotting component and the armature reaction component, the influence of slotting harmonics on the eddy current loss will depend on operation condition.

In the field weakening operation when $\gamma > \sim 20^0$, the presence of the slotting harmonics tends to reduce the armature reaction harmonics of the same orders, and hence lead to the reduction of the eddy current loss in the rotor magnets [110]. It is worth noting that the phase advance angle close to -90^0 is not a practical scenario for the actual operating conditions of the machine, however is included in the analysis for the comparison purpose.

2.8 Effect of Magnet Pole Arc Angle in Varying Magnet Loss with Change in Field Weakening Angle

In order to understand the variation of the magnet loss with change in field weakening angle at a particular magnet pole arc angle, it is insightful to examine how the $\partial B_r/\partial t$ changes along the different points within the magnet for different values of γ. Hence $\partial B_r/\partial t$ is plotted as shown in Fig. 2-22 at six regular intervals along a line in the middle surface of Magnet –1 with β_M =175^0 when γ = 0^0 , +90^0 and -90^0 as the motor rotates from $\omega_r t$ = 0^0 to 50^0 at 4500 rpm. The maximum rotation of $\omega_r t$ = 50^0 is chosen as the eddy current loss within the magnet repeats every 60^0. This is because the lowest harmonics in the machine has the order of 6.

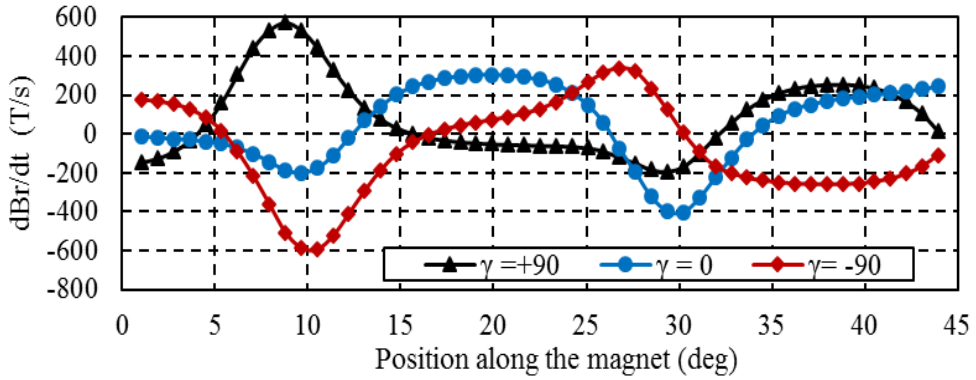

(a) $\partial B_r/\partial t$ variation at $\omega_r t$ = 0^0

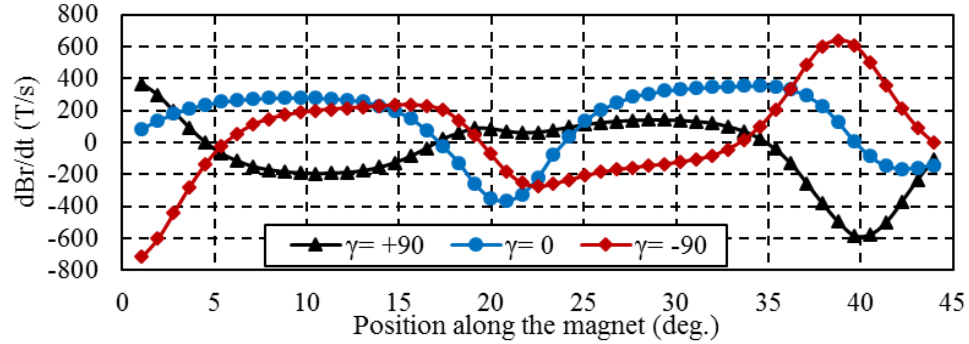

(b) $\partial B_r/\partial t$ variation at $\omega_r t$ = 10^0

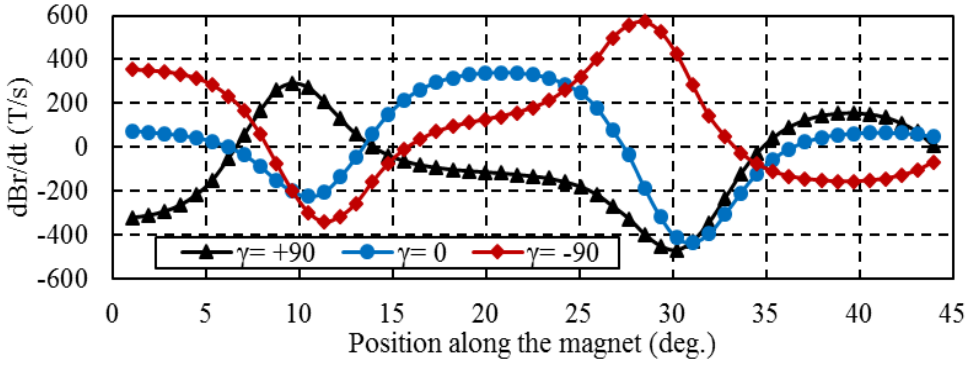

(c) $\partial B_r/\partial t$ variation at $\omega_r t = 20^0$

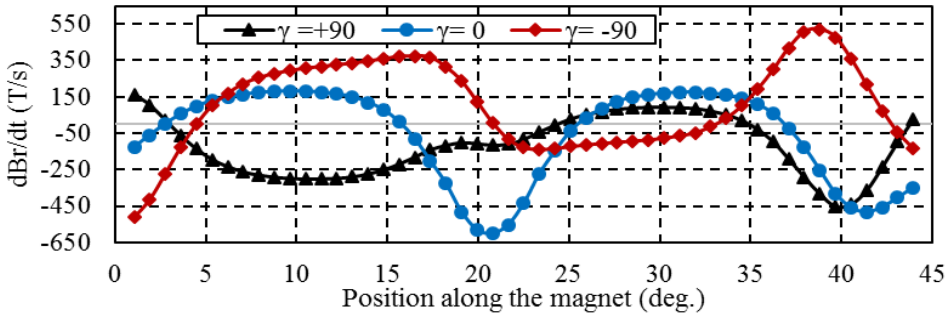

(d) $\partial B_r/\partial t$ variation at $\omega_r t = 30^0$

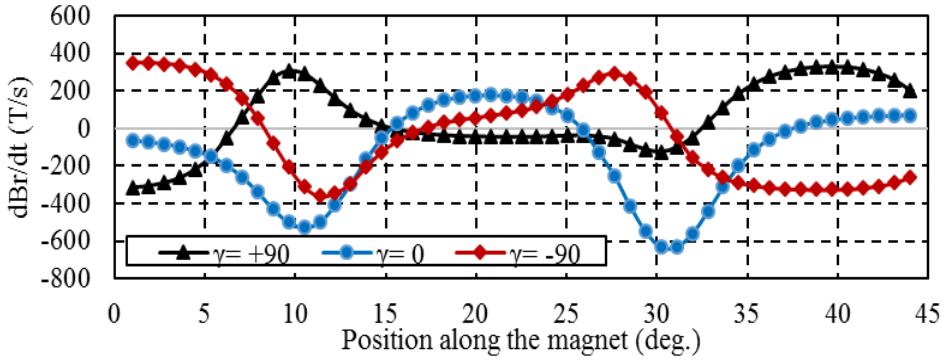

(e) $\partial B_r/\partial t$ variation at $\omega_r t = 40^0$

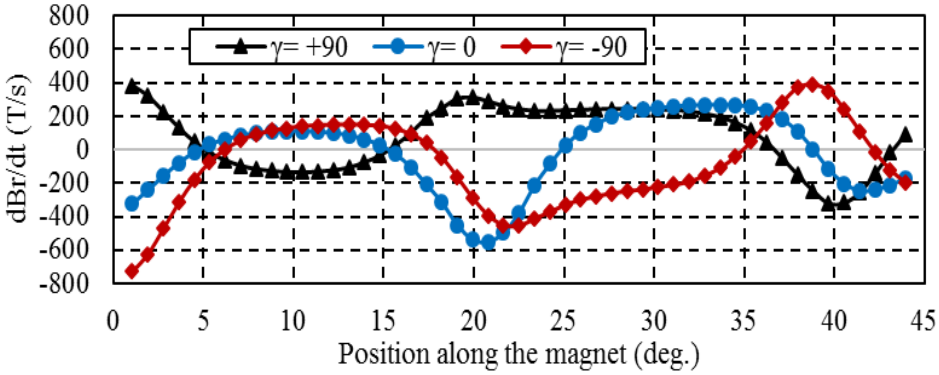

(f) $\partial B_r/\partial t$ variation at $\omega_r t = 40^0$

Fig. 2-22. $\partial B_r/\partial t$ variations on the middle surface of the magnet for $\gamma = 0^0$, $+90^0$ and -90^0 at intervals of 10^0 from $\omega_r t = 0^0$ to 50^0 .

It is observed from the figures that the magnitude of the $\partial B_r/\partial t$ values at the position between 15^0 to 30^0 inside the magnet pole is reduced for γ = $+90^0$ and -90^0 compared to the machine operation at γ = 0^0 in most of the cases considered. Also it is observed that the magnitude of the $\partial B_r/\partial t$ values tend to go higher along the magnet regions away from the centre for γ = -90^0 compared to the corresponding values at γ = 0^0 in most of the cases considered. As the eddy current loss is proportional to the square of $\partial B_r/\partial t$ values as seen from (2-47) , the average value is of $(\partial B_r/\partial t)^2$ is evaluated for every points along the middle surface of the magnet for each γ at 6 different intervals considered. This helps in making a quantitative assessment of $\partial B_r/\partial t$ variation and also gives an insight to the magnet loss variation with change in γ.

Table 2-2. Consolidation of Average$(\partial B_r/\partial t)^2$ Values at Six Different Intervals when γ =0^0, $+90^0$ and -90^0 with β_M =175^0, 150^0, 125^0 and 100^0.

Table 2-2(a) Average $(\partial B_r/\partial t)^2$ with β_M =170^0, 150^0

	β_M =175^0			β_M= 150^0		
Angle	γ = -90^0	γ = 0^0	γ = $+90^0$	γ = -90^0	γ = 0^0	γ = $+90^0$
0	63240.5	42852.9	47573.7	69726.5	46089.3	53553.5
10	83930.0	62769.0	48645.1	68180.5	70030.8	40501.7
20	66766.7	44145.3	45158.0	66735.4	51776.9	44450.3
30	69704.4	68278.1	41173.9	68858.0	63514.2	43324.4
40	59516.7	75497.4	36920.3	51323.1	88853.3	24146.5
50	74535.4	53429.1	41417.8	57449.1	54401.4	39529.0
Average	69615.6	57828.6	43481.5	63712.1	62444.3	40917.6

Table 2-2 (b) Average $(\partial B_r/\partial t)^2$ with β_M =125^0, 100^0

	β_M =125^0			β_M =100^0		
Angle	γ = -90^0	γ = 0^0	γ =+90^0	γ = -90^0	γ = 0^0	γ = +90^0
0	75620.8	50445.2	53964.6	60257.2	58372.6	20367.7
10	50405.3	75707.1	21132.5	34584.1	72957.2	14013.1
20	69349.0	59996.3	47856.1	83889.7	74443.3	50786.0
30	61850.1	61054.6	32487.8	49653.7	72994.7	25453.0
40	44528.4	101421.5	22644.7	40209.6	107995.9	8812.7
50	56851.4	61800.6	58883.5	63052.1	72281.6	42449.6
Average	59767.5	68404.2	39494.9	55274.4	76507.6	26980.4

To consider the influence of magnet pole arc angle while changing γ in the magnet loss , $\partial B_r/\partial t$ is also evaluated at six different intervals along the middle surface of the magnet with β_M =150^0, 125^0 and 100^0. Table 2-2 consolidates the average $(\partial B_r/\partial t)^2$ values for the cases when γ =0^0, +90^0 and -90^0 with β_M =175^0, 150^0,125^0 and 100^0.

It can be seen from the Table 2-2 that the average values of $(\partial B_r/\partial t)^2$ for the six intervals considered is larger for γ = -90^0 and lowest for γ = +90^0 with β_M =175^0. With β_M =150^0 the trend remains the same, however the gap between the average $(\partial B_r/\partial t)^2$ reduces for γ = -90^0 and = 0^0. For the case with β_M =125^0 the average value of$(\partial B_r/\partial t)^2$ for the six intervals considered is larger for γ = 0^0 and the gap widens further with β_M=100^0. This is because $\partial B_r/\partial t$ values becomes considerably higher along the centre of the magnet pole arc when γ = 0^0 as seen from Fig. 2-22. Also it is worth nothing that the average value of $(\partial B_r/\partial t)^2$ is continuously going lower at deep field weakening (i.e. when γ = +90^0) compared to the corresponding value at γ = 0^0 with reduction in β_M .

These observations indicates that the increase in magnet loss when γ < 0^0 compared to the normal operation at γ = 0^0 reduces with reduction in β_M. Also the reduction in magnet loss when γ > 0^0 compared to the normal operation at γ = 0^0 increases with reduction in β_M.

To cross check these findings 3D magnet loss is evaluated using the analytical method proposed in this chapter for 18-slot 8-pole SPM machine at 4500rpm with a peak phase current of 80A when γ =0^0, +90^0 and -90^0. Total magnet loss is predicted for magnet pole arc angles 175^0, 150^0,125^0 and 100^0. Fig. 2-23 shows difference in magnet loss predicted when γ = +90^0 with respect to corresponding loss value at γ =0^0 and also the difference in magnet loss predicted when γ = 0^0 with respect to corresponding loss value at γ =+90^0 with change in magnet pole arc angle.

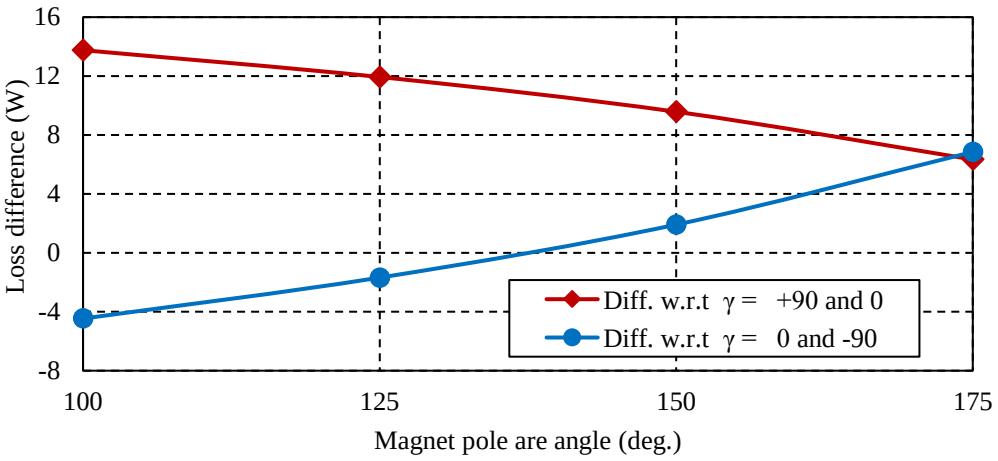

Fig. 2-23. Comparison of difference in magnet loss variation with magnet pole arc angle.

It is seen from the results that the difference in loss obtained aggress very well with loss predicted based on the average $(\partial B_r/\partial t)^2$ values discussed before.

2.9 Conclusion

The 3D analytical method for predicting magnet eddy current loss has been developed and validated by 3D time-stepped transient FEA. The model is computationally efficient and hence suitable for evaluating the variation of eddy current loss in magnet with number of axial and circumferential segmentations. The method considers slotting effect, the field produced by the permanent magnets, flux density variations within the magnet along its radial direction and the magnet curvature effects while predicting the magnet loss.

The accuracy of the results from the developed model justifies the negligence of tangential magnetic field inside the magnet and also the eddy current reaction effect at the operating conditions for the PM machine under study. It is observed that machines with lower magnet pole arc angle incurs lower magnet eddy current loss at deep field weakening conditions when compared to machines with higher pole arc angles.

CHAPTER 3
3D Computationally Efficient Magnet Eddy Current Loss Prediction in SPM Machines using 3D Fourier Method

3.1 Introduction

The method described in the Chapter 2 could be employed to predict the 3D magnet eddy current loss in SPM machines accounting slotting effect at different load conditions [109]. However, the method completely ignores the contribution of circumferential component of flux density in the loss evaluation, hence fails to assess its significance with increase in axial and circumferential number of segmentations.

In Chapter 2 loss computation is carried in out for each forward or backward rotating harmonic in the magnet and the superposition is employed to compute the total magnet loss. Similar technique is used in most of the resistance limited analytical models [22, 53, 54, 59, 69, 91], skin-limited analytical models [63, 64, 77, 118, 119] and harmonic based FE methods [37, 40] assuming no influence of mutual interaction between field harmonics of different order within the magnets. In [60] J. Wang *et al.* pointed out the interaction between different ordered harmonics can result in unequal loss in each magnet piece of a segmented pole. The superposition of harmonics of same spatial order and same frequency but running in opposite direction in the rotor reference frame can lead to erroneous prediction of total magnet loss [35, 120] . Employing the slotting effect subdomain model L. J. Wu *et al.* have shown in [107], the interaction between the harmonics of the different orders can not only affect the distribution of magnet loss to each magnet segment but also can affect the total magnet loss predicted as the sum of loss due to each harmonic field.

The method proposed in Chapter 2 accounts only for the eddy current flow in $\theta - z$ plane, and is not able quantify the current flow in the radial direction

as it does not evaluate the current density component in this direction. This is because the current vector potential assumed only has a radial component circulating in $\theta - z$ plane. Also the method cannot be extended to predict the 3D magnet loss accounting the eddy current reaction which may result from high frequency switching harmonics in the armature current.

Hence a better computationally efficient and also a faster tool is necessary which can address the mutual harmonic interactions, assess the loss contribution of the tangential component of flux density and the loss contribution of radial component of eddy current density while evaluating the total 3D magnet loss.

The method of generalized imaging is proposed in [121] to establish the eddy current source distribution in the form of 3D Fourier series in $x, y, z -$ directions. Using the imaging method, the eddy current sources associated with a harmonic component is distributed sinusoidally within an infinite isotropic 3-dimensional conductor without any boundaries. Ultimately only the coefficients for the sines and cosines needed to be evaluated in loss computation using Fourier expansion in three dimensions.

Since the mathematical description of the imaging series is cumbersome in [121], this chapter establishes the 3D eddy current source distributions in a much more elegant manner from the eddy current boundary conditions and Coulomb gauge imposed on the current vector potential. The proposed method is validated on both 8-pole, 18-slot and 8-pole, 12-slot SPM machines by evaluating its magnet loss with due account of slotting at no load and at peak load conditions and comparing the results with time-stepped 3D FEA. Also the significance of the source components in loss evaluation is established and the loss associated with different source harmonics with increase in number of segmentations is quantified to study the relationship between harmonic wavelength and the segment width in magnet loss reduction.

The main contents of this chapter is published by the author in [C2] and [J2], as detailed in Section 1.8.

3.2 Field Description for Eddy Currents in Rectangular Magnets

If eddy current reaction is neglected, from Faraday's law of induction the distribution of eddy current density J within the PMs at a given time instant can be determined proportional to the rate of change of flux density B with respect to time. This rate of flux density variation can defined as eddy current source distribution represented by S.

Their relation is defined as,

$$\nabla \times J = \sigma S$$

$$S_x = -\frac{\partial B_x}{\partial t}, S_y = -\frac{\partial B_y}{\partial t}, S_z = -\frac{\partial B_z}{\partial t} \tag{3-1}$$

where σ is the magnet conductivity.

According to the continuity law of magnet eddy current density, $\nabla \cdot J = 0$. J may be expressed as the curl of a current vector potential A_i as [122],

$$\nabla \times A_i = J \tag{3-2}$$

Applying the Coulomb gauge $\nabla \cdot A_i = 0$, it can be shown that the current vector potential A_i satisfies:

$$\nabla^2 A_i = -\sigma S \tag{3-3}$$

Fig. 3-1 shows a PM in a SPM machine within which the eddy currents are induced by time-varying 2D magnetic field. The curvature effect of the magnet is neglected and is approximated as rectangular in shape. The circumferential direction of the magnet is indicated as x, its radial direction as y and its axial direction is denoted as z. Thus, the source vector S only has two components $S_x = \partial B_x/\partial t$ and $S_y = \partial B_y/\partial t$. The magnet dimensions in the three directions are denoted as L_x, L_y and L_z respectively.

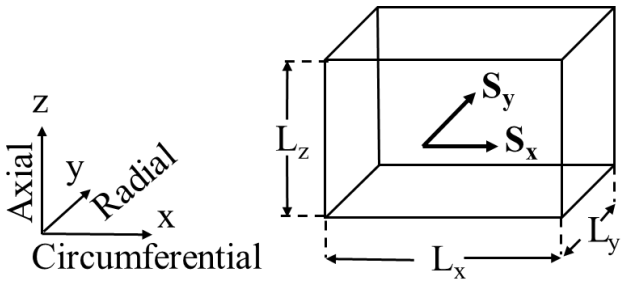

Fig. 3-1. A rectangular PM in a SPM machine, with eddy currents induced by 2D magnetic field.

The conductivity of the PM outside is zero, hence the boundary conditions on the six magnet surfaces, which are defined by, two parallel $x-z$ planes, two $x-y$ planes and also two $y-z$ planes, can be given as:

$$n_v \cdot J = 0 \tag{3-4}$$

where n_v denotes the vector normal to the magnet surfaces.

3.3 Solution to 3D Source Distribution from the Boundary Conditions for a Rectangular Magnet

At a given rotor position, the source distributions, S_x and S_y in a rotor magnet are known and may be expanded into 3D space by 3D Fourier series of the following form:

$$S_x = \sum_{m=1}^{\infty}\sum_{n=1}^{\infty}\sum_{k=1}^{\infty} a_{(m,n,k)} cos\left(mP_{x_1}x + \psi_{x_1}\right) cos\left(nP_{y_1}y + \psi_{y_1}\right) cos\left(kP_{z_1}z + \psi_{z_1}\right) \tag{3-5}$$

$$S_y = \sum_{m=1}^{\infty}\sum_{n=1}^{\infty}\sum_{k=1}^{\infty} b_{(m,n,k)} cos\left(mP_{x_2}x + \psi_{x_2}\right) cos\left(nP_{y_2}y + \psi_{y_2}\right) cos\left(kP_{z_2}z + \psi_{z_2}\right) \tag{3-6}$$

where m, n, k are the harmonic orders in x, y, z directions respectively. $P_{x_1}, P_{y_1}, P_{z_1}, P_{x_2}, P_{y_2}, P_{z_2}$ and the phase angles $\psi_{x_1}, \psi_{y_1}, \psi_{z_1}, \psi_{x_2}, \psi_{y_2}, \psi_{z_2}$ are the parameters to be determined in order to satisfy the physical constraints of

eddy current distributions. $a_{(m,n,k)}$ and $b_{(m,n,k)}$ are the 3D Fourier coefficients to be determined.

The 3D Fourier expansion implies that the source distribution within the magnets is repeated periodically in 3D space although the space of the concern is limited within the magnet defined by its dimensions L_x, L_y and L_z.

Since the sources $S_{x(m,n,k)}$, $S_{y\,(m,n,k)}$ is assumed distributed sinusoidally, then according to the operations in (3-1) and (3-3) , it is reasonable to assume the resultant field of A_x, A_y and J_x, J_y, J_z are also sinusoidal in form having harmonic of order (m, n, k).

Thus,

$$A_{ix} = \sum_{m=1}^{\infty}\sum_{n=1}^{\infty}\sum_{k=1}^{\infty} c_{(m,n,k)} cos\left(mP_{x_1}x + \psi_{x_1}\right) cos\left(nP_{y_1}y + \psi_{y_1}\right) cos\left(kP_{z_1}z + \psi_{z_1}\right) \quad (3\text{-}7)$$

$$A_{iy} = \sum_{m=1}^{\infty}\sum_{n=1}^{\infty}\sum_{k=1}^{\infty} d_{(m,n,k)} cos\left(mP_{x_2}x + \psi_{x_2}\right) cos\left(nP_{y_2}y + \psi_{y_2}\right) cos\left(kP_{z_2}z + \psi_{z_2}\right) \quad (3\text{-}8)$$

where $c_{(m,n,k)}$ and $d_{(m,n,k)}$ are the Fourier coefficients associated with $(m, n, k)^{\text{th}}$ harmonic for the current vector potential. Consequently J_x, J_y, J_z can be derived from (3-2) as,

$$J_x = \sum_{m=1}^{\infty}\sum_{n=1}^{\infty}\sum_{k=1}^{\infty} e_{(m,n,k)} cos\left(mP_{x_2}x + \psi_{x_2}\right) cos\left(nP_{y_2}y + \psi_{y_2}\right) sin\left(kP_{z_2}z + \psi_{z_2}\right) \quad (3\text{-}9)$$

$$J_y = \sum_{m=1}^{\infty}\sum_{n=1}^{\infty}\sum_{k=1}^{\infty} h_{(m,n,k)} cos\left(mP_{x_1}x + \psi_{x_1}\right) cos\left(nP_{y_1}y + \psi_{y_1}\right) sin\left(kP_{z_1}z + \psi_{z_1}\right) \quad (3\text{-}10)$$

$$J_z = \sum_{m=1}^{\infty}\sum_{n=1}^{\infty}\sum_{k=1}^{\infty} \begin{matrix} q_{1_{(m,n,k)}} sin\left(mP_{x_2}x + \psi_{x_2}\right) cos\left(nP_{y_2}y + \psi_{y_2}\right) cos\left(kP_{z_2}z + \psi_{z_2}\right) \\ + q_{2_{(m,n,k)}} cos\left(mP_{x_1}x + \psi_{x_1}\right) sin\left(nP_{y_1}y + \psi_{y_1}\right) cos\left(kP_{z_1}z + \psi_{z_1}\right) \end{matrix} \quad (3\text{-}11)$$

where, $e_{(m,n,k)}$, $h_{(m,n,k)}$, $q_{1_{(m,n,k)}}$, and $q_{2_{(m,n,k)}}$ are the coefficients associated with $(m,n,k)^{\text{th}}$ harmonic for the eddy current densities which are derived from $a_{(m,n,k)}$ and $b_{(m,n,k)}$ after the operations in (3-2) and (3-3).

From the boundary condition given in (3-4) the normal component of the current density need to be zero along all the six surfaces of the magnet as shown in Fig. 3-2.

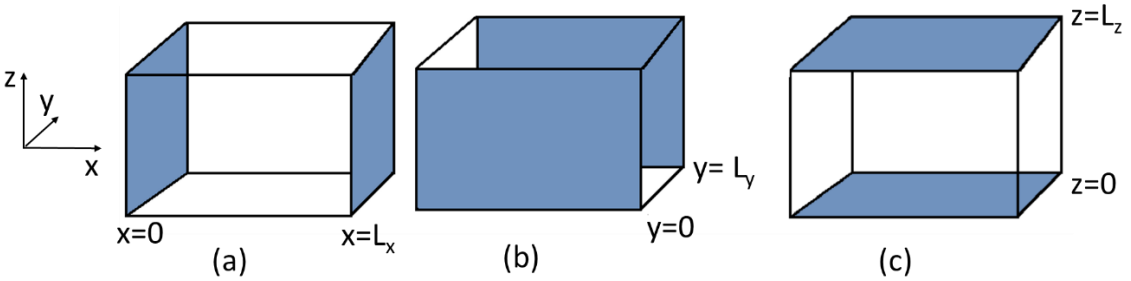

Fig. 3-2. Magnet surfaces (a) $= 0$ *and* $x = L_x$, (b) $y = 0$ *and* $y = L_y$, (c) $z = 0$ *and* $z = L_z$.

For the surfaces defined by $x = 0$ and $x = L_x$, as shown in Fig. 3-2 (a) , the normal current density $J_x = 0$.

From (3-9),

it demands $cos(mP_{x_2}x + \psi_{x_2}) = 0$ at $x = 0$ and $x = L_x$.

Hence, $P_{x_2} = \frac{\pi}{L_x}$ *and* $\psi_{x_2} = \frac{\pi}{2}$.

For the surfaces defined by $y = 0$ and $y = L_y$, as shown in Fig. 3-2 (b) , the normal current density $J_y = 0$.

From (3-10),

it demands $cos(nP_{y_1}x + \psi_{x_1}) = 0$ at $y = 0$ and $y = L_y$.

Hence, $P_{y_1} = \frac{\pi}{L_y}$ *and* $\psi_{y_1} = \frac{\pi}{2}$.

And finally for the surfaces defined by $z = 0$ and $z = L_z$, as shown in Fig. 3-2 (c) , the normal current density $J_z = 0$.

From (3-11),

it demands $cos(nP_{z_1}z + \psi_{z_1}) = 0$ and $cos(kP_{z_2}z + \psi_{z_2}) = 0$ at $z = 0$ and $z = L_z$. Hence, $P_{z_1} = \frac{\pi}{L_z}$ *and* $\psi_{z_1} = \frac{\pi}{2}$ also $P_{z_2} = \frac{\pi}{L_z}$ *and* $\psi_{z_2} = \frac{\pi}{2}$.

Now from the Coulomb gauge $\nabla \cdot A_i = 0$ imposed over the magnet volume, as the PM is insulated on all its surfaces it needs to be satisfied along all its surfaces too.

Hence,

$$\sum_{m=1}^{\infty}\sum_{n=1}^{\infty}\sum_{k=1}^{\infty}\begin{Bmatrix} c^1_{(m,n,k)}sin(mP_{x_1}x + \psi_{x_1})cos(nP_{y_1}y + \psi_{y_1})cos(kP_{z_1}z + \psi_{z_1}) \\ +d^1_{(m,n,k)}cos(mP_{x_2}x + \psi_{x_2})sin(nP_{y_2}y + \psi_{y_2})cos(kP_{z_2}z + \psi_{z_2}) \end{Bmatrix} = 0 \quad (3\text{-}12)$$

At $x = 0$ and $x = L_x$, (3-12) demands :

$sin(nP_{x_1}x + \psi_x) = 0$, which leads to $P_{x_1} = \frac{\pi}{L_x}$ and $\psi_{x_1} = 0$.

Similarly, at $y = 0$ and $y = L_y$, (3-12) demands:

$sin(nP_{y_2}y + \psi_y) = 0$, which leads to $P_{y_2} = \frac{\pi}{L_y}$ and $\psi_{y_2} = 0$.

Substituting the values of $P_{x_1}, P_{y_1}, P_{z_1}, P_{x_2}, P_{y_2}, P_{z_2}$ and the phase angles $\psi_{x_1}, \psi_{y_1}, \psi_{z_1}, \psi_{x_2}, \psi_{y_2}, \psi_{z_2}$ in (3-5) and (3-6) gives,

$$S_x = \sum_{m=1}^{\infty}\sum_{n=1}^{\infty}\sum_{k=1}^{\infty} a_{(m,n,k)}\, cos\left(m\frac{\pi}{L_x}x\right) sin\left(n\frac{\pi}{L_y}y\right) sin(k\frac{\pi}{L_z}z) \quad (3\text{-}13)$$

$$S_y = \sum_{m=1}^{\infty}\sum_{n=1}^{\infty}\sum_{k=1}^{\infty} b_{(m,n,k)}\, sin\left(m\frac{\pi}{L_x}x\right) cos\left(n\frac{\pi}{L_y}y\right) sin(k\frac{\pi}{L_z}z) \quad (3\text{-}14)$$

As proved using the generalized imaging technique in [121], it can be observed from (3-13) and (3-14) that :

1) The sources have been mirrored across the normal boundary.

2) The sources have become inverted mirror image across the tangential boundary.

From the imaging technique[121] it is proved that physical boundaries of the magnet can be removed; extra (image) sources can be placed in the positions symmetrical with respect to the boundary faces of the permanent magnet. This is explained in detail in Appendix A.

Hence the sources S_x , S_y can be observed to be repeating itself at every $2L_x$, $2L_y$, $2L_z$. This allows to compute the source harmonic components within a magnet employing 3D FFT for a given distribution of S_x , S_y. Thus $a_{(m,n,k)}$ and $b_{(m,n,k)}$ can be evaluated, which is detailed in Section 3.5. The relation for the A_{ix} , A_{iy}, J_x , J_y and J_z can also be obtained in the same manner after substitution as below.

$$A_{ix} = \sum_{m=1}^{\infty}\sum_{n=1}^{\infty}\sum_{k=1}^{\infty} c_{(m,n,k)}\, cos\left(m\frac{\pi}{L_x}x\right) sin\left(n\frac{\pi}{L_y}y\right) sin(k\frac{\pi}{L_z}z) \tag{3-15}$$

$$A_{iy} = \sum_{m=1}^{\infty}\sum_{n=1}^{\infty}\sum_{k=1}^{\infty} d_{(m,n,k)}\, sin\left(m\frac{\pi}{L_x}x\right) cos\left(n\frac{\pi}{L_y}y\right) sin(k\frac{\pi}{L_z}z) \tag{3-16}$$

Also J_x , J_y and J_z after substitution as,

$$J_x = \sum_{m=1}^{\infty}\sum_{n=1}^{\infty}\sum_{k=1}^{\infty} e_{(m,n,k)}\, sin\left(m\frac{\pi}{L_x}x\right) cos\left(n\frac{\pi}{L_y}y\right) cos\left(k\frac{\pi}{L_z}z\right) \tag{3-17}$$

$$J_y = \sum_{m=1}^{\infty}\sum_{n=1}^{\infty}\sum_{k=1}^{\infty} h_{(m,n,k)}\, cos\left(m\frac{\pi}{L_x}x\right) sin\left(n\frac{\pi}{L_y}y\right) cos\left(k\frac{\pi}{L_z}z\right) \tag{3-18}$$

$$J_z = \sum_{m=1}^{\infty}\sum_{n=1}^{\infty}\sum_{k=1}^{\infty} \begin{matrix} q_{1(m,n,k)}\, cos\left(m\frac{\pi}{L_x}x\right) cos\left(n\frac{\pi}{L_y}y\right) sin\left(k\frac{\pi}{L_z}z\right) \\ + q_{2(m,n,k)}\, cos\left(m\frac{\pi}{L_x}x\right) cos\left(n\frac{\pi}{L_y}y\right) sin\left(k\frac{\pi}{L_z}z\right) \end{matrix} \tag{3-19}$$

Combining $q_{1_{(m,n,k)}}$ and $q_{2_{(m,n,k)}}$ as $q_{(m,n,k)}$, J_z becomes,

$$J_z = \sum_{m=1}^{\infty}\sum_{n=1}^{\infty}\sum_{k=1}^{\infty} q_{(m,n,k)} \cos\left(m\frac{\pi}{L_x}x\right)\cos\left(n\frac{\pi}{L_y}y\right)\sin\left(k\frac{\pi}{L_z}z\right) \tag{3-20}$$

The coefficients $c_{(m,n,k)}$, $d_{(m,n,k)}$, $e_{(m,n,k)}$, $h_{(m,n,k)}$, $h_{(m,n,k)}$ and $q_{(m,n,k)}$ area derived in the subsequent sections.

3.4 Evaluation of Coefficients from the Variable Separation Method and Prediction of Total Magnet Loss.

Expanding the Poisson equation in (3-3),

$$\frac{\partial^2}{\partial x^2}+\frac{\partial^2}{\partial y^2}+\frac{\partial^2}{\partial z^2}\left(A_{ix}\vec{\imath}+A_{iy}\vec{\jmath}\right) = -\sigma\left(S_x\vec{\imath}+S_y\vec{\jmath}\right) \tag{3-21}$$

Hence,

$$\frac{\partial^2 A_{ix}}{\partial x^2}+\frac{\partial^2 A_{ix}}{\partial y^2}+\frac{\partial^2 A_{ix}}{\partial z^2} = -\sigma S_x \tag{3-22}$$

$$\frac{\partial^2 A_{iy}}{\partial x^2}+\frac{\partial^2 A_{iy}}{\partial y^2}+\frac{\partial^2 A_{iy}}{\partial z^2} = -\sigma S_y \tag{3-23}$$

After substituting for A_x in (3-22),

$$\frac{\partial^2 A_{ix}}{\partial x^2} = -\left(m\frac{\pi}{L_x}\right)^2 A_{ix} \tag{3-24}$$

$$\frac{\partial^2 A_{ix}}{\partial y^2} = -\left(n\frac{\pi}{L_y}\right)^2 A_{ix} \tag{3-25}$$

$$\frac{\partial^2 A_{ix}}{\partial z^2} = -\left(k\frac{\pi}{L_z}\right)^2 A_{ix} \tag{3-26}$$

Hence (3-23) becomes,

$$-\left[\left(m\frac{\pi}{L_x}\right)^2+\left(n\frac{\pi}{L_y}\right)^2+\left(k\frac{\pi}{L_z}\right)^2\right]A_{ix}=-\sigma S_x \tag{3-27}$$

thus

$$c_{(m,n,k)}=\sigma\frac{a_{(m,n,k)}}{\left(m\frac{\pi}{L_x}\right)^2+\left(n\frac{\pi}{L_y}\right)^2+\left(k\frac{\pi}{L_z}\right)^2} \tag{3-28}$$

After substituting for A_y in (3-23),

$$\frac{\partial^2 A_{iy}}{\partial x^2}=-\left(m\frac{\pi}{L_x}\right)^2 A_{iy} \tag{3-29}$$

$$\frac{\partial^2 A_{iy}}{\partial y^2}=-\left(n\frac{\pi}{L_y}\right)^2 A_{iy} \tag{3-30}$$

$$\frac{\partial^2 A_{iy}}{\partial z^2}=-\left(k\frac{\pi}{L_z}\right)^2 A_{iy} \tag{3-31}$$

Hence (3-23) becomes,

$$-\left[\left(m\frac{\pi}{L_x}\right)^2+\left(n\frac{\pi}{L_y}\right)^2+\left(k\frac{\pi}{L_z}\right)^2\right]A_{iy}=-\sigma S_y \tag{3-32}$$

thus

$$d_{(m,n,k)}=\sigma\frac{b_{(m,n,k)}}{\left(m\frac{\pi}{L_x}\right)^2+\left(n\frac{\pi}{L_y}\right)^2+\left(k\frac{\pi}{L_z}\right)^2} \tag{3-33}$$

Substituting $c_{(m,n,k)}$ and $d_{(m,n,k)}$ in (3-2) for evaluating the current densities, $e_{(m,n,k)}$, $h_{(m,n,k)}$, $q_{1(m,n,k)}$ and $q_{2(m,n,k)}$ can be obtained as below.

$$e_{(m,n,k)}=\sigma\cdot\frac{-b_{(m,n,k)}(k\frac{\pi}{L_z})}{M^2} \tag{3-34}$$

$$h_{(m,n,k)}=\sigma\cdot\frac{a_{(m,n,k)}(k\frac{\pi}{L_z})}{M^2} \tag{3-35}$$

$$q_{(m,n,k)} = \sigma \cdot \frac{b_{(m,n,k)}\left(m\frac{\pi}{L_x}\right)) - a_{(m,n,k)}(n\frac{\pi}{L_y})}{M^2} \tag{3-36}$$

where,

$$M = \left[\left(m\frac{\pi}{L_x}\right)^2 + \left(n\frac{\pi}{L_y}\right)^2 + \left(k\frac{\pi}{L_z}\right)^2\right] \tag{3-37}$$

Once the eddy current distribution is known the total magnet eddy current loss at a given time instant can be evaluated as the sum of the losses associated with each harmonic component. Applying orthogonality principle, the total magnet loss can be evaluated as [122, 123]:

$$\begin{aligned} P_{eddy} &= \sum_{m=1}^{\infty}\sum_{n=1}^{\infty}\sum_{k=1}^{\infty} P_{(m,n,k)} \\ &= \sum_{m=1}^{\infty}\sum_{n=1}^{\infty}\sum_{k=1}^{\infty}\frac{1}{8}\int_0^{2L_x}\int_0^{2L_y}\int_0^{2L_z}\frac{1}{\sigma}\cdot\left[J_{x(m,n,k)}{}^2 + J_{y(m,n,k)}{}^2 + J_{z(m,n,k)}{}^2\right]dxdydz \\ &= \sum_{m=1}^{\infty}\sum_{n=1}^{\infty}\sum_{k=1}^{\infty}\left\{p_{1(m,n,k)} + p_{2(m,n,k)} + p_{3(m,n,k)} + p_{4(m,n,k)} + p_{5(m,n,k)}\right\} \end{aligned} \tag{3-38}$$

where,

$$p_{1(m,n,k)} = b_{(m,n,k)}{}^2 \cdot \left[\frac{\left(k\frac{\pi}{L_z}\right)}{M^2}\right]^2 \cdot \frac{\sigma L_x L_y L_z}{8} \tag{3-39}$$

$$p_{2(m,n,k)} = a_{(m,n,k)}{}^2 \cdot \left[\frac{\left(k\frac{\pi}{L_z}\right)}{M^2}\right]^2 \cdot \frac{\sigma L_x L_y L_z}{8} \tag{3-40}$$

$$p_{3(m,n,k)} = b_{(m,n,k)}{}^2 \cdot \left[\frac{\left(m\frac{\pi}{L_x}\right)}{M^2}\right]^2 \cdot \frac{\sigma L_x L_y L_z}{8} \tag{3-41}$$

$$p_{4(m,n,k)} = a_{(m,n,k)}{}^2 \cdot \left[\frac{\left(n\frac{\pi}{L_y}\right)}{M^2}\right]^2 \cdot \frac{\sigma L_x L_y L_z}{8} \tag{3-42}$$

$$p_{5(m,n,k)} = -2a_{(m,n,k)}b_{(m,n,k)} \cdot \left(m\frac{\pi}{L_x}\right)\left(n\frac{\pi}{L_y}\right) \cdot [\frac{1}{M^2}]^2 \cdot \frac{\sigma L_x L_y L_z}{8} \quad (3\text{-}43)$$

The above results show that the eddy current distribution and eddy current loss are evaluated based on the coefficients of 3D-Fourier series expansion of eddy current sources and hence the method is termed as 3D-Fourier method.

3.5 Method of Implementation

The process of computing 3D eddy current distribution and eddy current loss in the PMs using the proposed 3D-Fourier method is illustrated as a flowchart shown in Fig. 3-3.

The 2-D magnetic field as the source function $S_x = \partial B_\theta/\partial t$ and $S_y = \partial B_r/\partial t$ are obtained using the more accurate subdomain model [85] which accounts for the slotting effect. Alternatively, the magnetic field distribution may also be obtained from 2D-FE in which case complex geometry, heavy magnetic saturation, and eddy current reaction can also be accounted. The method of implementation employing 2D FE results will be explained in the subsequent chapters.

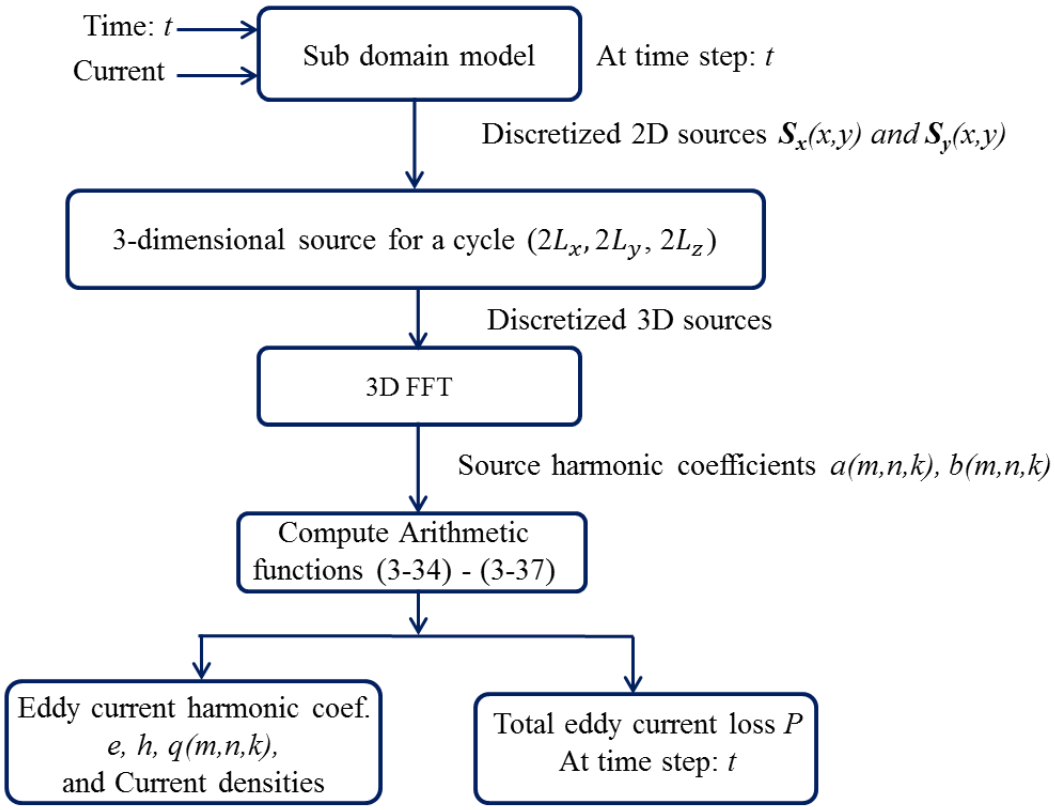

Fig. 3-3. Flow chart illustrating the computation of eddy current distribution and eddy current loss.

It is seen that the periodicity helps in representing the original and image sources as sum of 3D harmonic series in free space. In order to represent that way, the original 2D sources S_x (derived analytically or from 2D FE at each time instant enclosed by the physical magnet boundaries L_x, L_y) is repeated as mirror image in $x-$ direction while it is repeated as inverted image of the original sources along $y-$ direction, For the case with S_y, the original sources are repeated as mirror image in $y-$ direction while it is repeated as inverted image of the original sources along $x-$ direction. This completes the 2D repetition of the sources constrained by the boundaries $2L_x$ and $2L_y$. The original and image sources of S_x and S_y thus formed along two dimensions are again repeated along $z-$ direction till L_z. Finally, this sources and images each enclosed by $2L_x, 2L_y, L_z$ for S_x and $S_y$is repeated again as inverted mirror images along $z-$ direction till $2L_z$. Thus a complete set of sources each for S_x and S_y are formed which will be repeating every $2L_x, 2L_y, 2L_z$ [121]. Now the 3D

FFT of the resultant S_x and S_y can be performed to evaluate $a_{(m,n,k)}$ and $b_{(m,n,k)}$.

Hence , in order to perform FFT of the combined sources, the magnetic field distribution obtained from the subdomain model needed to be discretized in the x, y, z dimensions. Therefore the accuracy of the sources and their resultant eddy current field depends on the harmonic numbers (m, n, k) that are considered in the calculations, which, in turn, determines the number of samples of the magnetic field in the $x, y, z -$ directions in the magnet region which are used while performing 3DFFT.

To account for the all the high order space harmonics caused by a winding configuration, slotting and step change of the image sources across the boundaries, the number of discretization samples should be sufficiently large. The sample numbers are preferred to be chosen as the integer power of 2 to speed up the discrete FFT. It is observed from the loss calculation using different number of samples that the magnet loss converges to sufficient accuracy with 64× 16 × 32 samples for the SPM machines considered in this chapter. When calculating the eddy current loss at the rated current and the maximum speed with 2 axial segments and no circumferential segments for the machine under study in this chapter, the relative differences of the results with 64× 16 × 32 samples and 64 × 64 × 64 samples, compared with the results with 128 × 128 × 128 samples, are 0.22% and 0.09%, respectively. However, the time of computations was about 10 seconds for 64 × 16 × 32 samples and is increased to 47 and 225 seconds with 64 × 64 × 64 and 128 × 128 × 128 samples respectively. This shows the usage of more samples may results only in marginal improvement of accuracy at the expense of time consumed.

The eddy current distribution is calculated at each time step. Because time varying eddy current densities usually repeat 6 times in a fundamental electric period, it is necessary to calculate the eddy current loss at least for one sixth or one twelfth of the electrical period to obtain the average value.

To evaluate the magnet loss with axial and circumferential segmentation, the losses are evaluated for each circumferential segments separately and the total magnet loss is computed as the sum of these losses multiplied with number of axial segmentations. For example, for the machine having n_c circumferential segments and n_a axial segments in a magnet as shown in Fig. 2-3, the eddy current loss is evaluated for each circumferential segment separately employing the segment dimensions in the proposed method . The total loss per magnet is evaluated as the sum of the loss from the n_c tangential segments multiplied with the number of axial segmentation n_a. The loss variations among the axial segments placed over the same circumferential segment is not being considered as the source field is considered essentially 2D, hence it has no variation along the axial direction. This rapid evaluation the eddy current loss variations with axial and circumferential segmentation will enable the designer to optimise the magnet segmentation pattern, hence have a better control over the loss among the magnets.

3.6 Finite Element Validation

3.6.1 Machine Topology and Design Parameters

The proposed method is applied to an 18-slot 8-pole SPM machine for evaluation of the eddy current loss in the rotor permanent magnets. The subdomain model [84] employed here to generate the eddy current sources can deal with both overlapping and non-overlapping type of double layer windings. The 8-pole, 18-slot SPM machine considered for predicting eddy current loss in the magnets uses an overlapping type of winding as shown in Fig. 3-4. The key physical parameters and specifications of the machine are listed in Table 3-1. The 8-pole,18-slot machine employs winding design features to reduce the space harmonics and hence the rotor eddy current loss [115] , while retaining the merits of fractional slot per pole machine topology.

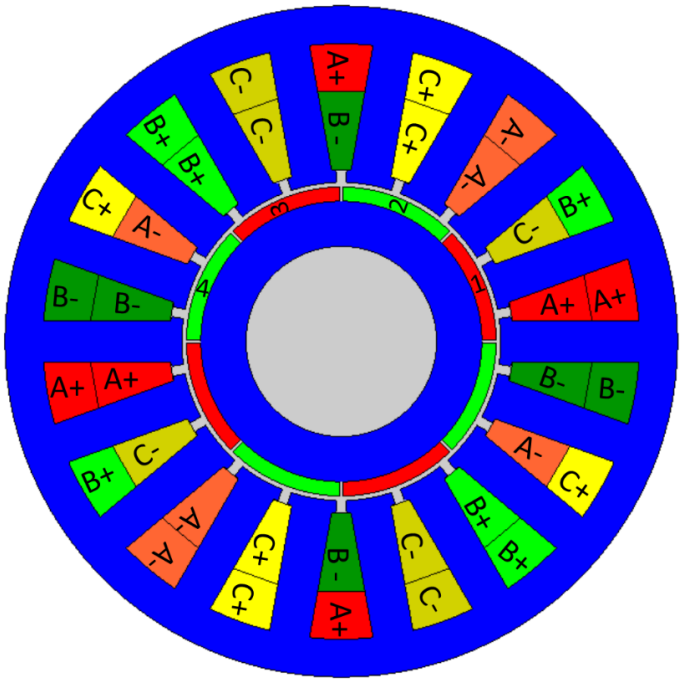

Fig. 3-4. Cross-sectional schematic of 8-pole, 18-slot SPM machine.

Table 3-1. Key Physical Parameters and Specifications of 8 pole-18 slot SPM Machine.

Parameter	Unit	Value
Stator outer radius	mm	70.59
Motor stack length	mm	118
Rotor radius	mm	32.5
Magnet thickness	mm	3.0
Magnet pole arc	elec.deg	175
Slot opening	mm	2.03
Slot opening depth	mm	2.375
Slot depth	mm	29.15
Teeth width	mm	8.5
Shaft radius	mm	20.0
No. of turns per coil	-	6
Magnet remanent flux density	T	1.1
Magnet resistivity	Ohm. m	$1.8\text{x}10^{-6}$
Maximum speed	rpm	4500
Rated speed	rpm	2100
Rated current	A	39

Major difference in the SPM machine topology considered in this chapter with that discussed in the previous chapter is the magnet pole arc angle of 175^0 to account for the curvature effect while performing 3D finite element validation. This could capture any error in the predicted results because of the curvature effect which is neglected in the 3D- Fourier method proposed here.

3.6.2 2D Finite Element Source Validation

The eddy currents and the associated loss are evaluated when the machine is operated at a peak phase current of 55A at 4500rpm. This is because the aim of this chapter is to validate the proposed method on the SPM machine at the worst operating conditions. The presence of the d–axis current results in field weakening conditions and can reduce the magnet loss due to harmonic interactions of magnetic fields associated with slotting and armature currents as described in Chapter 2. Also the core saturation may reduce because of d-axis current and hence the robustness of the proposed method cannot be critically assessed. Hence magnet loss is evaluated considering only the q–axis value for the current.

2D magnetic field within the magnet considering slotting is obtained from the subdomain model [85]. The radial and circumferential flux density variations are evaluated from the magnetic field as described in Chapter 2. As the slotting effect model neglects the material saturation it is necessary to have a comparison for the magnetic field variation with the results obtained from 2D FEA at the given operating conditions before proceeding to the eddy current calculations.

Fig. 3-5 compares the analytically and 2D FE predicted flux density component variations with angular position at a given time instant of $\omega_r t = 1.25^0$ (mech.) for Magnet–1 along its mean radius when the machine operates at the peak load conditions mentioned above.

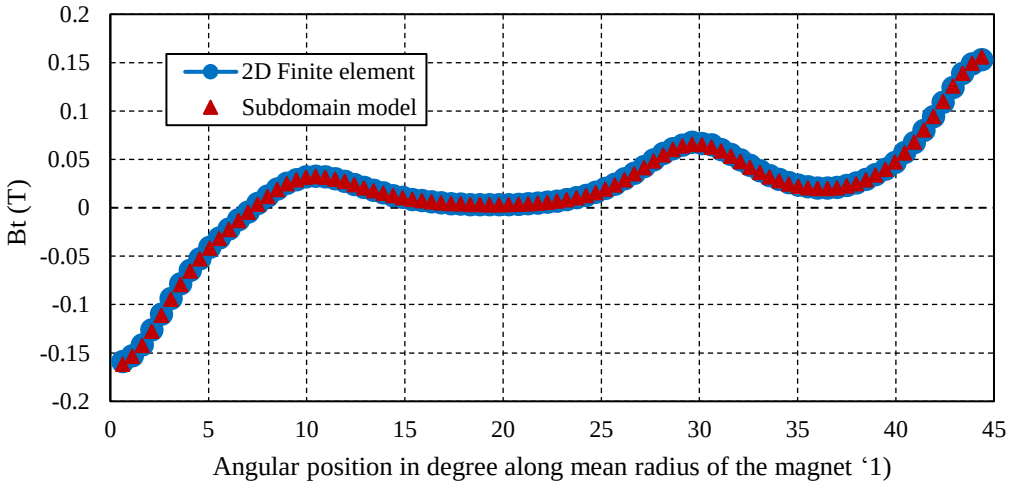

(a) Circumferential flux density component (B_t) variation

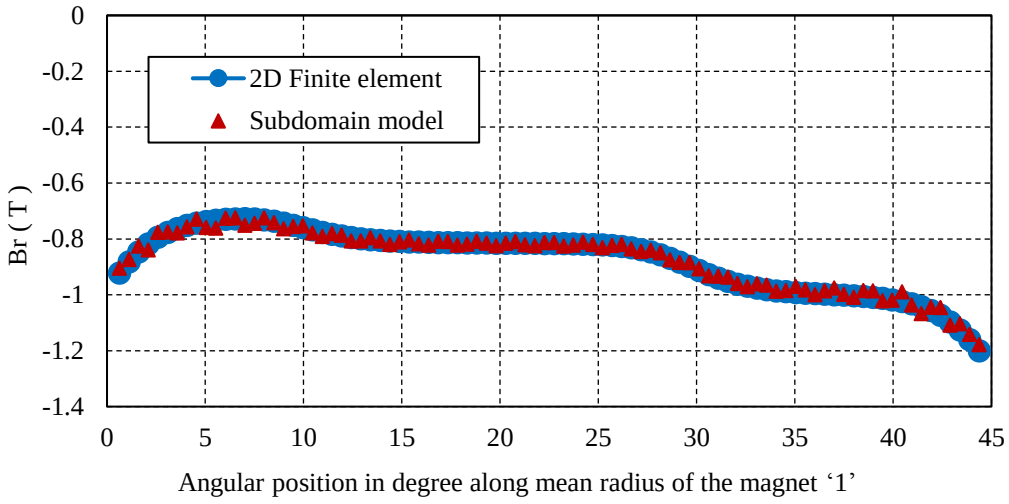

(b) Radial flux density component (B_r) variation

Fig. 3-5.Comparison of flux density components from subdomain model and 2D-FE along the mean radius of Magnet –1 at $\omega_r t = 1.25^0$.

The analytically and 2D FE predicted eddy current source variations with angular position at the same time instant along the mean radius of Magnet –1 is compared in Fig. 3-6.

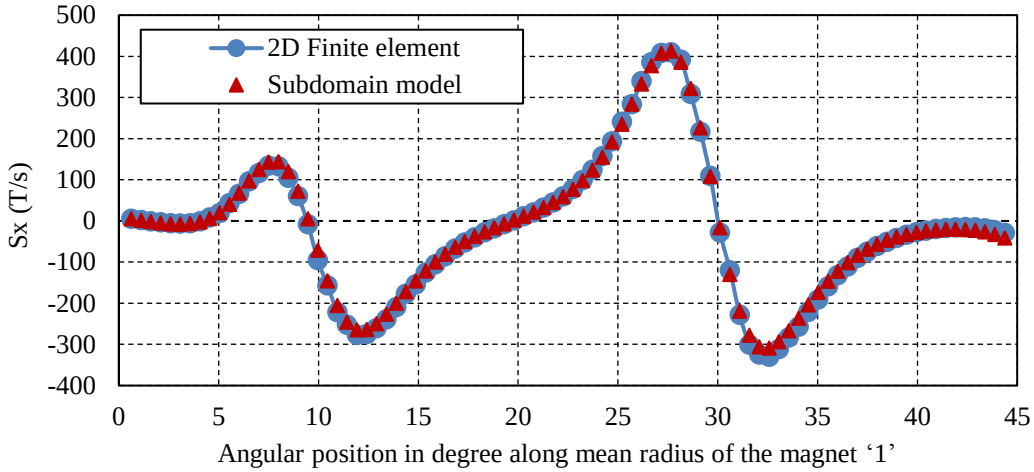

(a) Comparison of circumferential component (S_x) variation.

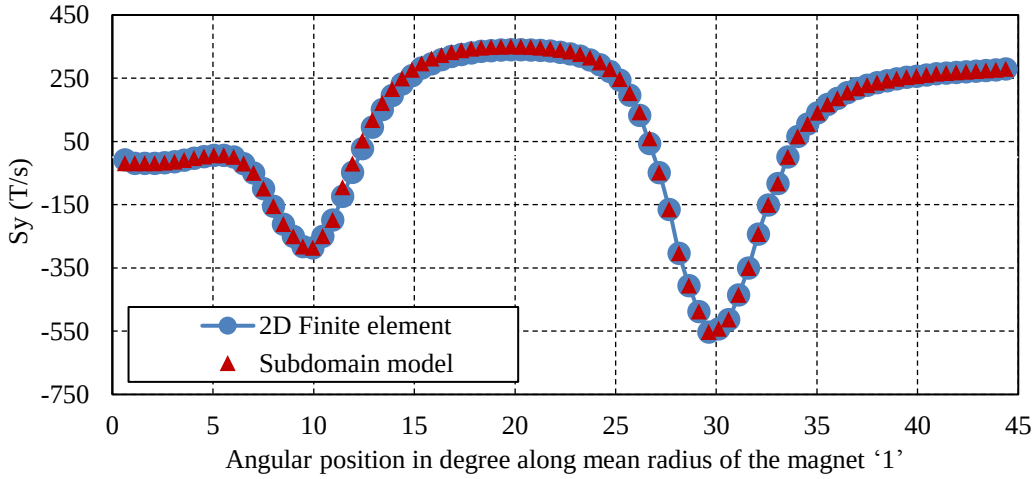

(b) Comparison of radial component (S_y) variation.

Fig. 3-6. Comparison of source components from subdomain model and 2D-FE at mean radius of Magnet –1 at $\omega_r t = 1.25^0$.

As can be seen, S_x and S_y predicted by the subdomain model considering slotting effect has shown good accuracy compared with those predicted by the 2D transient FE analysis at the peak load conditions.

3.6.3 Comparison of 3D Eddy Current Distribution and Magnet Eddy Current Loss with 3D FEAs

A 3D FE model of the machine, as shown in Fig. 3-7 has been built to predict the 3D eddy current distribution and resultant eddy current loss induced in the magnets. Since the 8-pole, 18-slot SPM machine employs fractional slot per pole topology, circumferential symmetry exits only over 180 mechanical

degrees. Thus, as in Chapter 2 a quarter of the machine need only to be modelled in 3D FEAs accounting both the circumferential and axial symmetries.

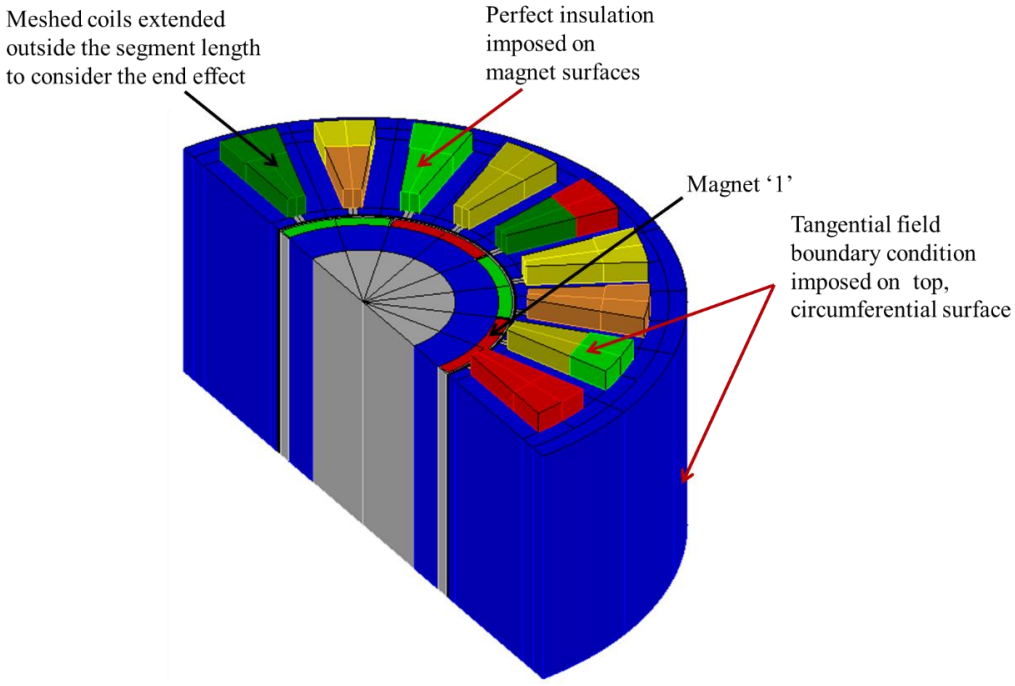

Fig. 3-7. 3D-FE model of 8-pole, 18-slot SPM based on symmetry.

The meshed coils are extended in contrast to 3D-FE geometry in Chapter 2 along the axial direction to consider the winding end effect. Tangential boundary conditions are imposed on this extended surface. A perfect insulation boundary conditions are applied to the axial and circumferential end surfaces of the magnets to insulate the segments from each other. In addition, the conductivity of the rotor iron core is not considered to avoid the eddy current flow in them. In practice, segmented pieces are glued together by high temperature epoxy which acts as insulator. The meshing along magnet is increased to fine level, especially along the z–direction for the best accuracy in the 3D magnet loss prediction. For example, for loss evaluation without any axial segments within the magnet, the number of divisions along the z–directions considered is 70, while it becomes 14 when the when the axial segments reach 12.

3-phase sinusoidal currents of 55 peak is injected in the machine phases via the electrical circuit as described in Chapter 2. The 3D machine model is operating with only *q*-axis current assuming no field weakening as simulated in the subdomain model.

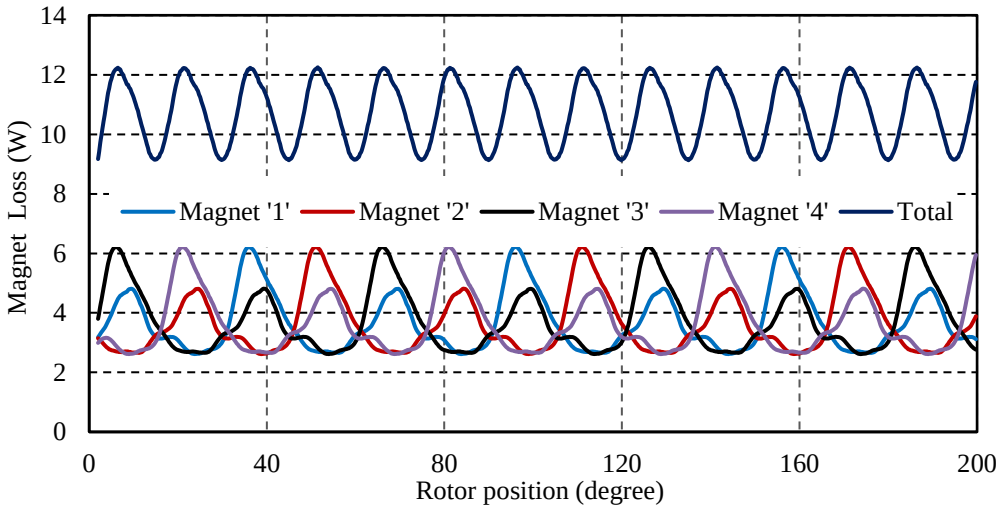

Fig. 3-8. Instantaneous magnet loss variation for magnets 1 to 4 and their total obtained from the proposed 3D-Fourier method when suppled with 55A(peak); the number of axial segments =2 and circumferential segments =1.

Fig. 3-8 compares the instantaneous loss computed from the proposed 3D Fourier method for the first four magnets and their total when the machine is having 2 axial segments and no further circumferential segments when excited at peak current conditions at 4500 rpm.

The magnet loss is observed to be repeating at every 1/6th fundamental frequency, and hence the losses evaluation is repeated over this time span and averaged to predict the magnet loss[121, 122].

Magnet loss evaluation is carried out in 3D FE at the same segments mentioned previously. Fig. 3-9 compares analytically and 3D FE predicted instantaneous total eddy current loss variations with rotor position when the machine operates at the peak load condition with each magnet per pole segmented into 2 pieces axially and no circumferential segmentations. Fig. 3-10 and Fig. 3-11 compares the analytically and 3D FE predicted variations of

z–and x–components of the current density w.r.t magnet position (x) at $z = 0.75L_z, y = 0.5L_y$ in Magnet–1 under the previously mentioned conditions respectively.

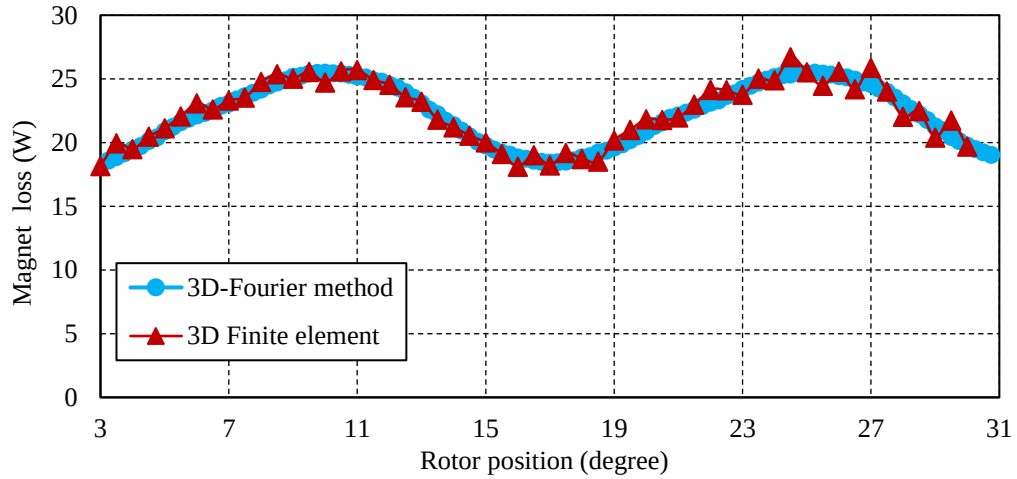

Fig. 3-9. Loss comparison from the proposed 3D analytical method and 3D- FEA when suppled with 55A(peak); the number of axial segments =2 and circumferential segments =1.

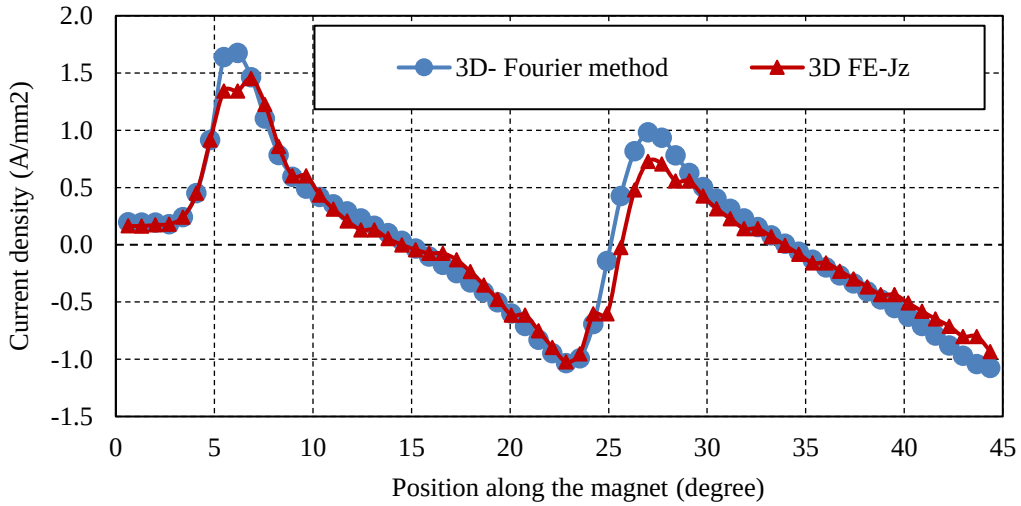

Fig. 3-10. Comparison from the z –component of current density from the proposed 3D analytical method and 3D- FEA when suppled with 55A(peak); the number of axial segments =2 and circumferential segments =1.

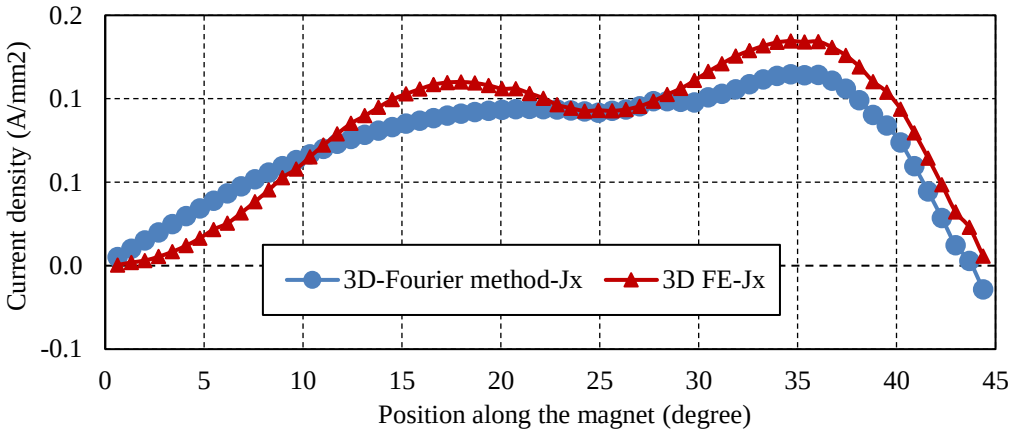

Fig. 3-11. Comparison from the x –component of current density from the proposed 3D analytical method and 3D- FEA when suppled with 55A(peak); the number of axial segments =2 and circumferential segments =1.

It is seen that good agreement between the analytical and 3D FE predicted instantaneous values are observed albeit few minor mismatches which may be attributed to the curvature, the end winding effects and the core saturation which are neglected in the proposed method.

Fig. 3-12 compares analytically and 3D FE predicted z–component eddy current density distributions at $\omega_r t = 1.25^0$on the middle surface of Magnet–1 (defined by, $y = 0.5L_y, 0 < x < L_x, 0.5\,L_z < z < L_z$), when the machine operates at the maximum speed of 4500 rpm and at the peak phase current of 55A. The magnet per pole is segmented into 2 pieces axially and with no circumferential segmentation at these conditions.

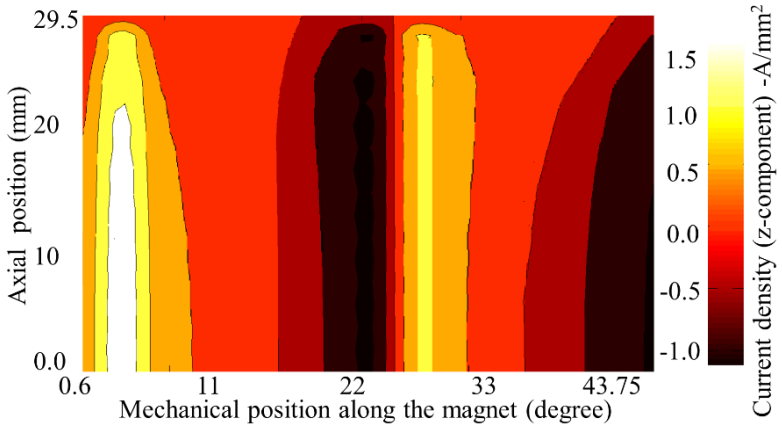

(a) Current density (J_z) distribution from 3D-Fourier method.

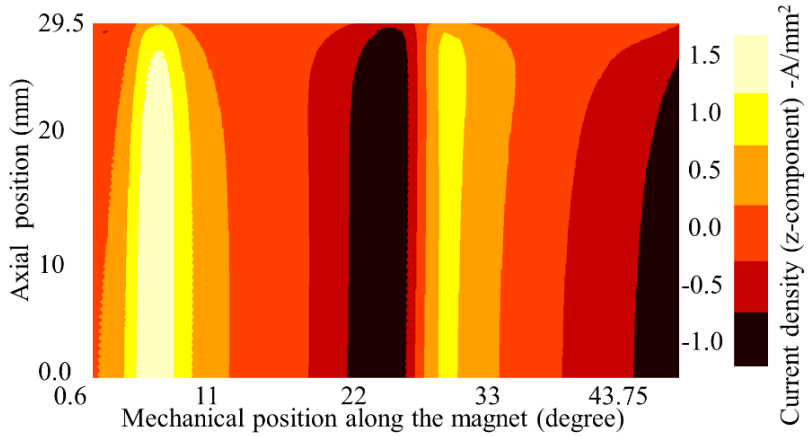

(b) Current density (J_z) distribution from 3D-FE method.

Fig. 3-12. Comparison of z–component of current density (J_z) distribution from 3D analytical and 3D-FE method along the magnet surface defined by its mean radius ($y = 0.5L_y, 0 < x < L_x, 0.5\,L_z < z < L_z$) .

While Fig. 3-13 compares analytically and 3D FE predicted x–omponent eddy current density distributions at $\omega_r t = 1.25^0$ on the middle surface of Magnet– 1 at the same operating conditions.

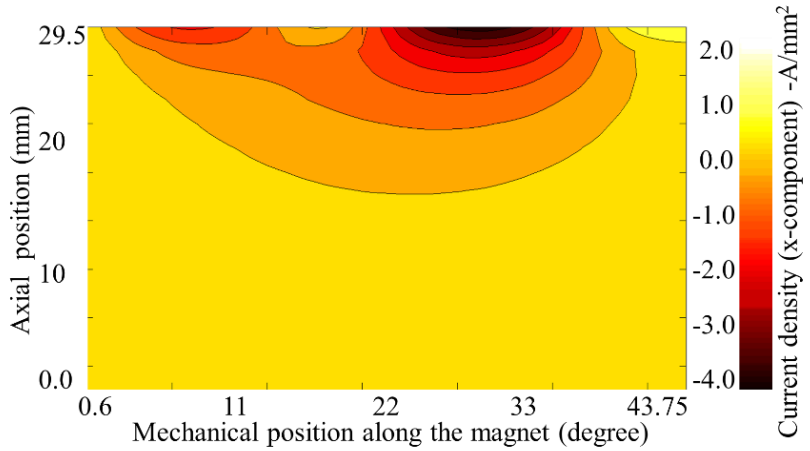

(a) Current density (J_x) distribution from 3D-Fourier method.

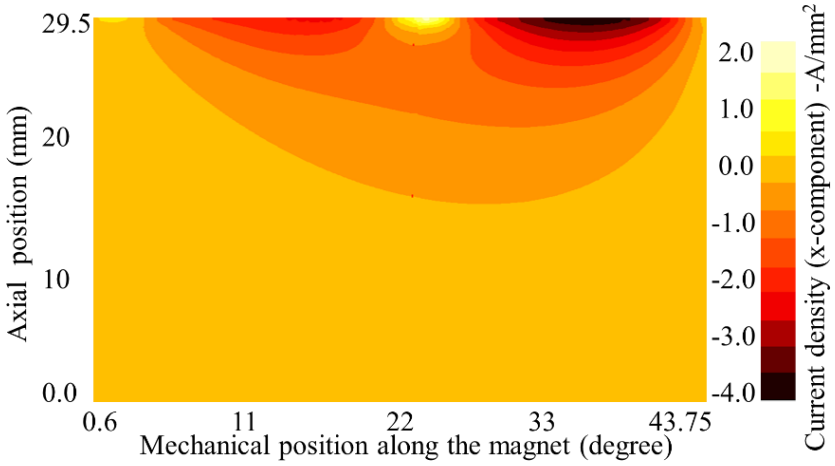

(b) Current density (J_x) distribution from 3D-FE method.

Fig. 3-13. Comparison of x–component of current density (J_x) distribution from 3D analytical and 3D-FE method along the magnet surface defined by its mean radius ($y = 0.5L_y, 0 < x < L_x, 0.5 L_z < z < L_z$).

It is seen from the above figures that the eddy current distributions predicted by the proposed analytical method shows good agreement with the 3D-FE results.

The magnet loss prediction is repeated with increases in axial and circumferential number of segmentations both at peak current conditions at 4500 rpm using the proposed analytical method and 3D-FEA. The same is repeated at no load conditions as well. Fig. 3-14 compares analytically and 3D FE predicted eddy current losses at peak current with increase in axial and circumferential number of segments. While Fig. 3-15 compares analytically and 3D FE predicted eddy current losses at no load with increase in axial and circumferential number of segments.

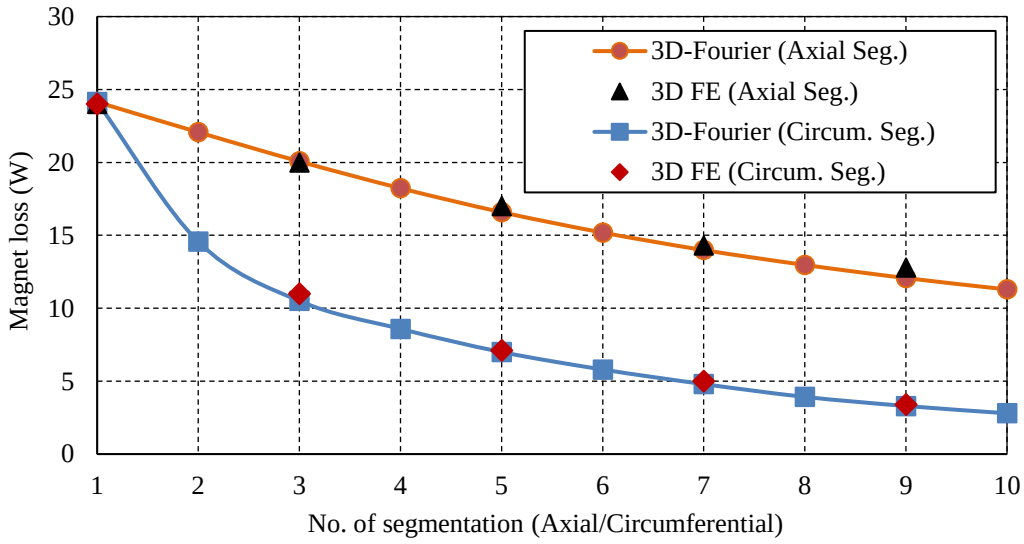

Fig. 3-14. Comparison of magnet loss in 8-pole, 18-slot SPM with increase in axial and circumferential number of segmentations at peak current (4500 rpm).

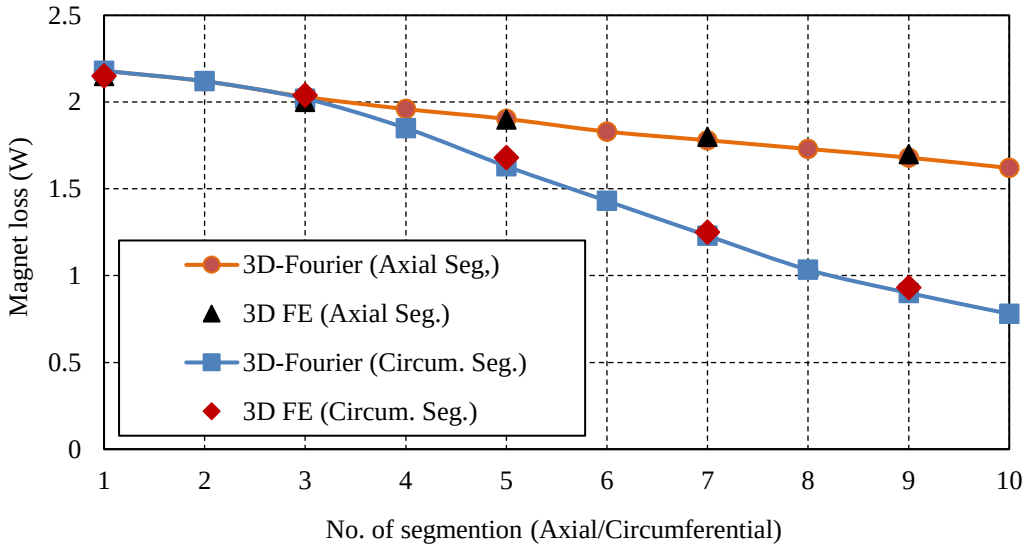

Fig. 3-15.Comparison of magnet loss in 8-pole, 18-slot SPM with increase in axial and circumferential number of segmentations at no load (4500 rpm).

It can be seen that in all cases, good agreements are obtained between the 3D FE and analytical results.

3.7 Computational Efficiency of the Proposed Method

Since the calculations are performed in 3-dimensional space for each harmonic, matrix operations are used to facilitate efficient calculations. When the magnetic field within the magnets are sampled with 64 × 16 × 32 points in the $x-y-z$ directions, the harmonic orders (m, n, k) are also accounted up to 64× 16 × 32. The analytical prediction of the magnetic field from the subdomain model takes approximately 18 minutes while the eddy current loss calculation takes only about 10 seconds on a 64 GB RAM desktop computer (3.3 GHz, I7 processor with 6 cores) in Matlab environment. Hence on an average it takes less than 2 minutes per case to compute the 3D eddy current loss including the source evaluation for magnet loss prediction up to 10 axial segmentations [122].

As a comparison, in order to perform 3D time-stepped FEs, apart from the geometry and physical model construction and meshing process, the computation time on the same PC is about 36 hours for the case of non-axial-segmentation and 8.5 hours for the case of 10 axial segmentations.

3.8 Evaluation of Results

3.8.1 Separation of Magnet Loss Based on Source Components

Since the eddy current source within the PM has two components, $\partial B_r/\partial t$ and $\partial B_t/\partial t$, it is insightful to assess the contribution of each towards the magnet loss. Fig. 3-16 shows the contribution of tangential and radial source components (S_x, S_y) of the flux density towards magnet loss, with increase in axial and circumferential number of segmentations when the machine operates in the peak current conditions at 4500 rpm.

It is observed that the contribution of $\partial B_t/\partial t$ towards the magnet loss is less significant, being an order of magnitude lower, compared to the loss contribution due to $\partial B_r/\partial t$ at lower number of magnet segments. This is because the radial component of flux density, B_r, in a magnet is usually dominant, and hence both the rms and peak values of $\partial B_r/\partial t$ are much greater than those of $\partial B_t/\partial t$, as is evident from Fig. 3-6(a) whilst the resultant eddy current loss is proportional to square of the time derivatives.

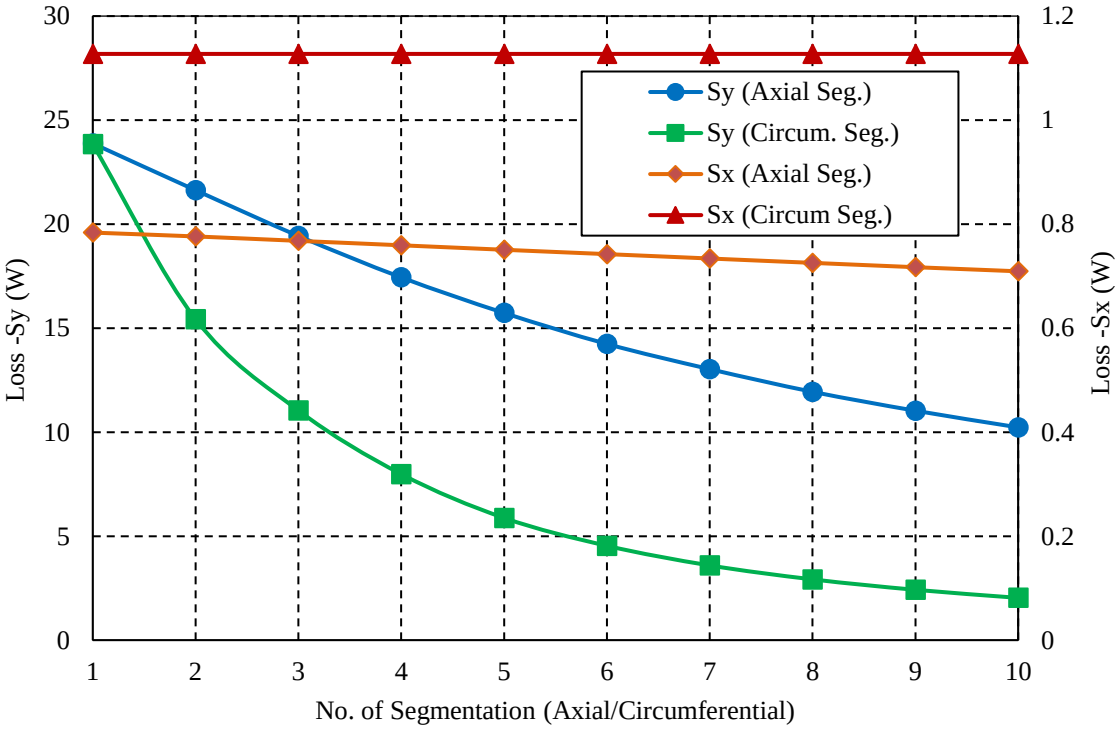

Fig. 3-16. Magnet *loss associated with source components with increase in segmentation (Loss associated with S_y is displayed on primary y axis, while loss associated with S_x is displayed on secondary y axis).*

Further, the reduction of the loss associated with $\partial B_t/\partial t$ is found to decrease very slowly with increase in the axial number of segments [122]. Moreover, the loss associated with $\partial B_t/\partial t$ is found to have no significant variation with the circumferential number of segments. This is because the eddy currents due to $\partial B_t/\partial t$ flows in 2D $y-z$ plane and segmentation along x–direction cannot alter the eddy current circulation path. It is also worth noting that the actual magnet loss in the machine is found to be lower than the sum of the losses due to the time derivatives of the radial and tangential

flux density components as a result of harmonic interaction between them which can be seen from the expression of J_z in (3-20 and 3-36). The results follows that circumferential segmentation is not effective in reducing the eddy current loss associated with $\partial B_t/\partial t$.

3.8.2 Contribution of y-Component of Current Density J_y towards Magnet Loss

Most of the eddy current loss evaluation methods so far discussed in literature fails to assess the contribution of y–component of current density towards the total magnet loss. Fig. 3-17 shows the analytically predicted y–component eddy current density distributions at $\omega_r t = 1.25^0$ on the side surface of Magnet–1 (defined by, $x = 0.5L_x, 0 < y < L_y, 0.5\,L_z < z < L_z$), when the 8-pole, 18-slot machine operates at the peak current conditions mentioned before and with each magnet per pole segmented into 2 pieces axially and with no further circumferential segmentation.

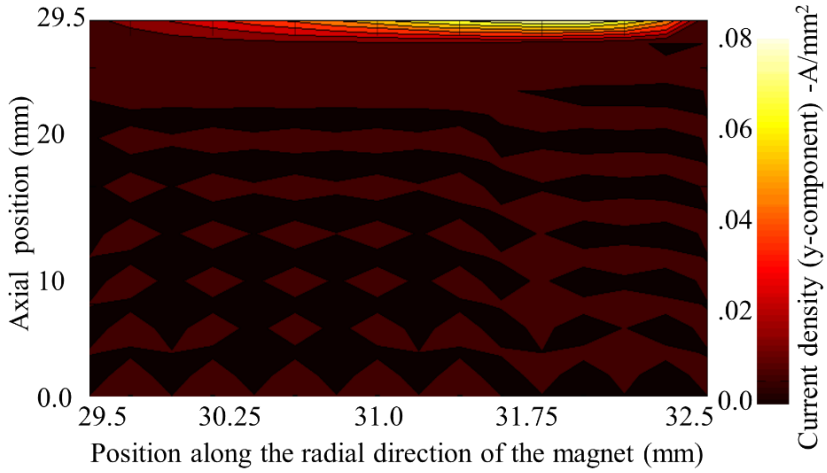

Fig. 3-17. y–component of current density (J_y) distribution from 3D analytical and 3D-FE method along the magnet side surface defined by ($x = 0.5L_x, 0 < y < L_y, 0.5\,L_z < z < L_z$).

It is seen that the y–component of eddy current distribution J_y is two orders of magnitude lower than x–and z–components (J_x, J_z) as seen before in Fig. 3-12 and Fig. 3-13.

The contribution of the y–component of current density towards magnet loss can be evaluated separately as $P_{2(m,n,k)}$ from equation (3-40). The comparison of magnet loss variation with axial and circumferential segmentation contributed by J_y for both the SPM machines is shown in Fig. 3-18.

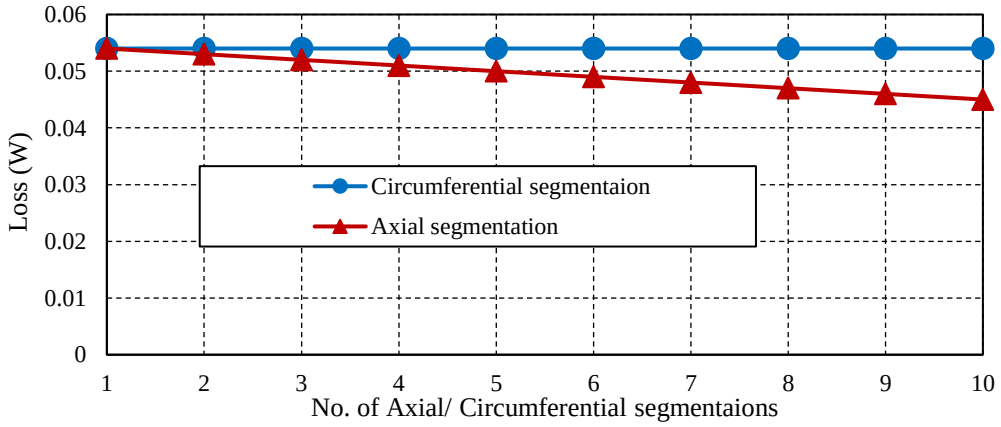

Fig. 3-18. Comparison of magnet loss variation because of J_y with increase in number of axial and circumferential number of segmentations.

It is clear from the figure that the contribution of J_y towards magnet loss is much negligible when compared to the total magnet loss as a result of all the three components. Also it is seen that the magnet loss due to J_y is not affected by the increase in circumferential number of segmentations. This is because J_y is the result of circumferential source component S_x as seen from (3-18, 3-35) and hence its flow is limited to in y– z plane.

3.8.3 Variation of Harmonic Loss with Increase in Number of Segmentation

The analytical solution of source components obtained from the subdomain model allows to evaluate the different harmonic contents present in the eddy currents. The major MMF space harmonics and hence the flux density harmonics associated with winding distribution in SPM machine is identified as 2, 8, 14, 20, 26… rotating in the backward direction and 4, 10, 16, 22, 28…rotating in the forward direction. The MMF harmonic spectrum

illustrating the order and normalized magnitude of the harmonic is shown in Fig. 3-19.

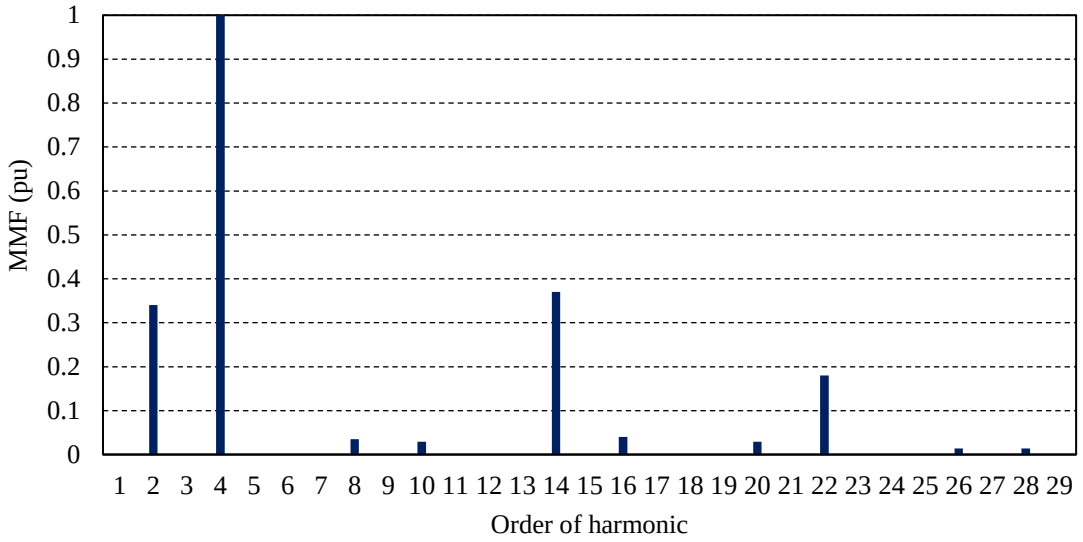

Fig. 3-19. Normalized MMF space harmonic distribution for the 8-pole,18-slot SPM machine.

It is observed that the harmonics in the rotor which are resulting in magnet loss are of the orders $(n_1 p_s + p)$and $(n_2 p_s - p)$ as identified in [60]. Where $n_1 = (qk + 1) = 2, 5, 8\ldots, k = 0,1,2\ldots$ and $n_2 = (qk + 1) =$ 1,4,7…, $k =$ 1,2,3 … Also p_s is the number of pole-pairs associated with the stator winding , p the rotor pole pairs and q the number of phases which is equal to 3. p_s is 2 for the 8-pole, 18-slot machine under study [124].

Hence in the rotor reference the above MMF space harmonics are found to be of the order of 6, 12, 18, 24, 30, 36, 42, 48, 54… in 8-pole, 18-slot SPM machine. The contribution of the forward and the reverse rotating harmonics of the same order towards the flux density variations is accounted together as they interact with each other [60] in loss production. It is observed from the loss computation that the major contributors for the magnet loss among the above harmonics are of the orders 6, 12, 18, 36 and 54 in S_x and S_y .

The instantaneous harmonic loss variation contributed by the major loss harmonics discussed previously in Magnet-1 is shown in Fig. 3-20 . It is clear

from the figure that the loss varies with twice the frequency of the flux density harmonic. This is because the instantaneous loss variation is proportional to the square of the flux density variations as observed in (3-38).

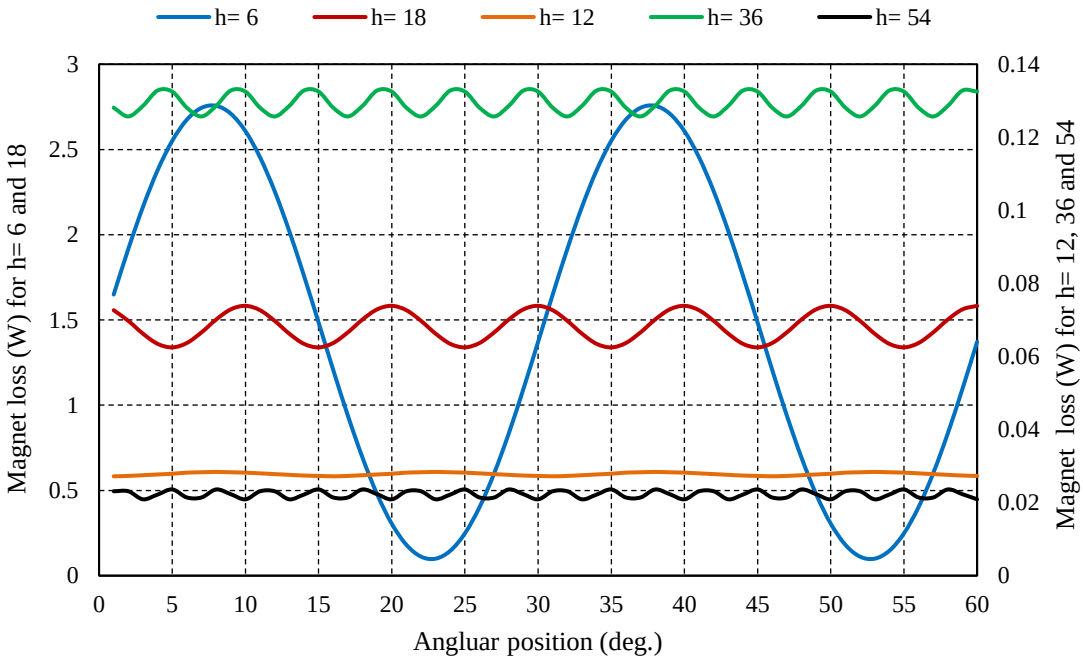

Fig. 3-20. Instantaneous magnet loss variations for all the major harmonics for Magnet-1 under load conditions.

Now, the wavelengths associated with all the major harmonics calculated based on the mean magnet radius (31mm) are tabulated in Table 3-2. This helps in comparing the loss associated with each major harmonic with respect to segment width.

Table 3-2. Wavelength associated with major harmonics.

Harmonic No. (h)	6	12	18	24	36	54
Wavelength -λ_h(mm)	32.46	16.23	10.82	8.12	5.41	3.60

The magnet loss variations for each major harmonic with increase in circumferential of segments is compared in Fig. 3-21. While the magnet loss variations for each major harmonic with increase in axial numbers of segments is compared in Fig. 3-22.

For the purpose of illustration, the segment widths are also given for each number of segmentations.

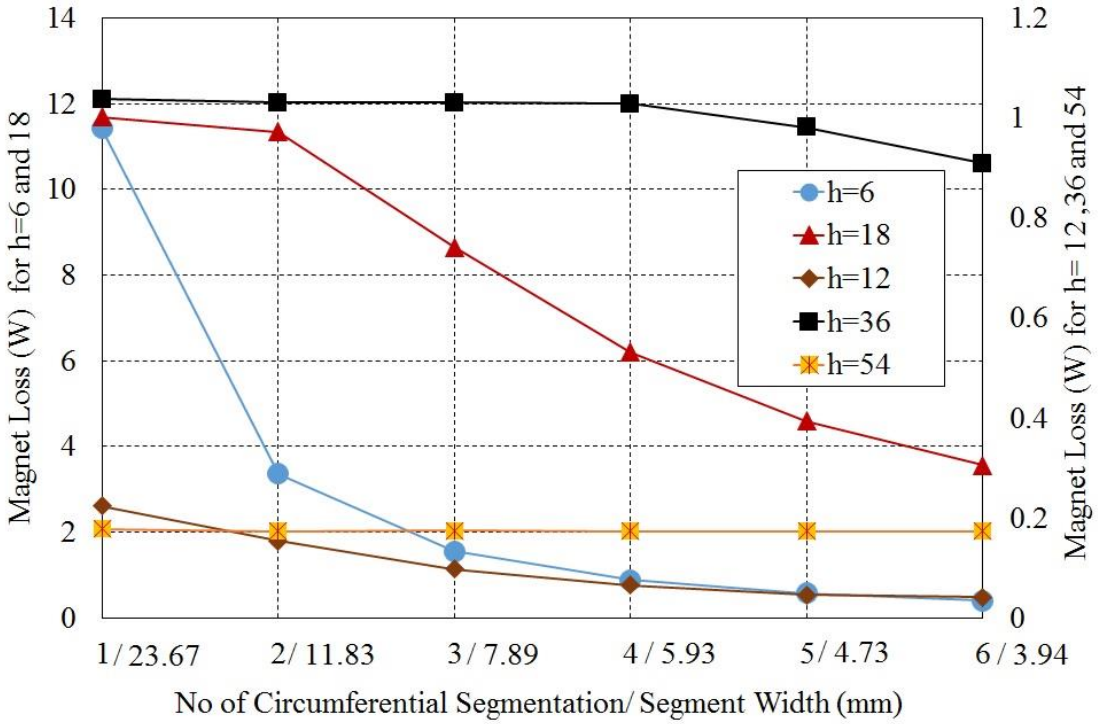

Fig. 3-21. Magnet loss variation of major harmonics with increase in circumferential number of segments when the 8-pole, 18-slot SPM is operating with peak phase current at 4500 rpm.

As can be seen, the 6th and 18th harmonics contribute to ~94 % of the total magnet loss, where the loss contributions from 12, 36 and 54 orders of harmonics are shown in the scale of the secondary y-axis to clearly understand the relationship between the segment widths and the harmonic wavelengths

Given that the circumferential segmentation is effective in reducing the eddy current loss associated with $\partial B_r/\partial t$, it is clear from Fig. 3-21 that those harmonics most affected by the circumferential segmentation have their wavelength (λ_h) greater than the circumferential segment width [93]. Hence magnet loss reduction by circumferential segmentation will be less effective when the harmonic wavelength (λ_h) is lower than circumferential segment width, but becomes effective when the wavelength is greater than

circumferential segment width [122]. For example, the loss associated with the 18th harmonic is reduced at a faster rate when the number of circumferential segments are greater than two as the wavelength (10.82 mm) of the 18th harmonic becomes lower than the segment width (11.83 mm). For the case with the 6th harmonic, its wavelength (32.46 mm) is already lower than the segment width (23.67mm) when the number of circumferential segment is one, hence the associated loss is reduced at a faster rate with any further circumferential segmentations. However, it can be observed that the loss reduction becomes slow with increase in circumferential number of segmentations when the harmonic wavelength is much greater than the segment width. The above phenomenon can be understood by the fact that when a harmonic wavelength is shorter than the segment width, the induced eddy current due to $\partial B_r/\partial t$ which mainly circulates on the $x-z$ plane can return easily within the segment. However, the eddy current return path is hampered when the segment width is shorter than the wavelength, resulting in a greater reduction in eddy current circulation and hence the associated loss.

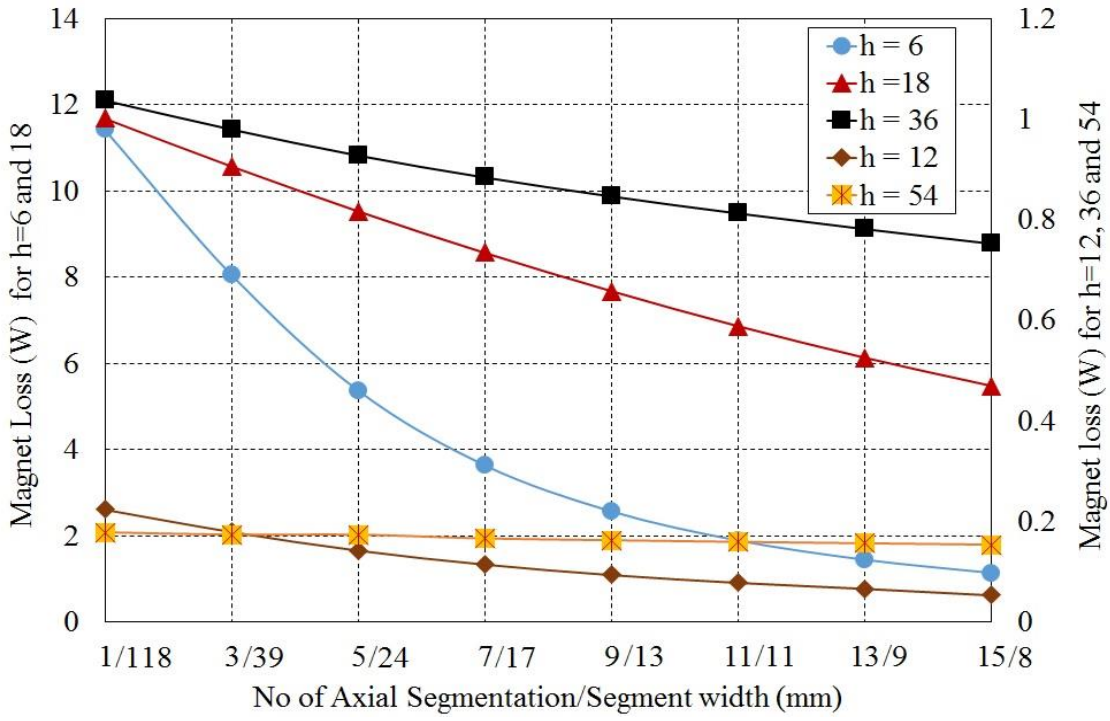

Fig. 3-22. Magnet loss variation of major harmonics with increase in circumferential number of segments when the 8-pole, 18-slot SPM is operating with peak phase current at 4500 rpm.

For the case with axial segmentation it can be observed from Fig. 3-22 that the rate of loss reduction with increase in number of segmentations decreases with increase in harmonic order. Hence the loss associated with the 6^{th} harmonic is reduced at a much faster rate than that of the 54^{th} harmonic (h=54) with increase in the axial number of segmentations. While the circumferential segmentation only affects the eddy current circulation due to $\partial B_r/\partial t$, the axial segmentation breaks both the induced eddy current paths due to $\partial B_r/\partial t$ and $\partial B_t/\partial t$, and hence it is effective for reduction of eddy current losses associated with both the radial and circumferential components. The increase in the axial number of segments will increase the effective resistance of the z –component of the eddy current density, and hence reduces the eddy current losses. Thus, the axial segmentation will be effective in loss reduction even the wavelength of a harmonic is shorter than the axial segment height, as is evident in Fig. 3-22. However, the harmonic loss reduction is observed at a slower pace with increase in axial segmentation number. This is because the magnet segment height is also reduced at a lower rate with increase in axial segmentation number.

Hence it may be preferred to segment the permanent magnet in the circumferential direction so that the width of the segment is lower than the wavelengths of all the dominant harmonics responsible for eddy current loss, followed by axial segmentation which targets those harmonics whose wavelengths is close or greater than the magnet width after the first step. However, segmentations in both directions have to be considered in the context of manufacturing feasibilities and cost.

3.9 Conclusion

An accurate and computationally efficient method of predicting 3D eddy current loss in rotor magnets of SPM machines has been developed considering slotting based on 3D Fourier expansion of time-derivatives of flux density in magnets. The developed method has been validated by 3D FEAs on an 18-slot, 8-pole SPM machine. The method proposed here considers the

harmonic interaction while evaluating the 3D eddy current loss. It is observed that the loss contribution from the tangential component of the magnetic field variation is much lower in comparison to the loss associated with radial field variations. It is observed that the magnet loss associated with circumferential source component can be up to 5% of the total magnet loss. Also the contribution of y–component of current density towards the total magnet loss is observed to be negligible compared to the other two components. The method of axial segmentation is found be better in reducing magnet loss from those harmonics with their wavelength lower than the segment width. The developed method provides an effective tool for assessing eddy current loss and for devising segmentation schemes for the loss reduction.

CHAPTER 4
Prediction of High Frequency 3D Eddy Current Loss in Permanent Magnets of SPM Machines

4.1 Introduction

Most of the SPM machines employed in high power density applications [10, 125] are fed by 3–phase inverter drives with pulse width modulation which can produce high frequency harmonics in the armature currents. The dominant switching harmonics usually occur at the integer multiple of the switching frequencies ranging from a few kHz to a few tens kHz and may also have magnitudes up to a few percent of fundamental depending on the switching frequency and the control strategy employed in these machines [126, 127].

These harmonics not only cause ripples in the generated electromagnetic torque but also can result in eddy current loss in magnets. The eddy currents induced by these high frequency harmonics may not be resistance limited, as the eddy current field reacts with the magnetic field responsible for producing it. As the eddy current losses are proportional to the square of the frequency of the field variations as described in previous chapters, the losses attributed to these switching harmonics may go higher than that produced by the lower order space and time harmonics. Hence its evaluation is necessary to prevent the worst ever operating conditions, which may lead to an excessive temperature rise in the magnets and cause a possible partial demagnetization [128, 129].

There are quite a few FE based [31] and 2D analytical [64, 72, 77, 86, 95] methods reported in literature to predict the magnet eddy current loss at high frequencies with varying degree of accuracy. The reduction in magnet loss with circumferential segmentation can be successfully predicted employing these methods. However as discussed before in Chapter 1, the accuracy of 2D

methods are compromised when the magnet axial length is similar to its other dimensions since the magnet eddy current flow may become predominantly 3D[121]. Also the possibility of increase rather than decrease in magnet loss with increase in axial segmentation [120] cannot be evaluated in 2D.

Most of the computationally efficient 3D methods are reported in literature in evaluating magnet loss at high frequencies [27, 39, 89, 92, 94, 120] ignores slotting effect and also the radial variation of flux density along the magnets. They also discard the field produced by the permanent magnets and are incapable of assessing the loss contribution by the tangential component of the magnetic field at high frequencies. Moreover, these methods neglect the variation of loss among different magnet segments in computing the total eddy current loss.

The 3D-Fourier method proposed in Chapter 3 does not consider 3D eddy current loss in rotor PMs due to high frequency harmonics in the armature phase currents. Hence in this Chapter, a computationally efficient technique for the prediction of high frequency 3D eddy current loss in rotor magnets employing the 3D-fourier method with due account to the eddy current reaction effect is proposed. The proposed method is validated on the 8-pole, 18-slot SPM machine by predicting the eddy current loss in magnets at high frequencies with increase in axial and circumferential segmentations and comparing the results obtained with 3D FEA.

The main contents of this chapter is published by the author in [J3], as detailed in Section 1.8.

4.2 Implementation of 3D-Fourier Method at High Frequencies and Validation of Results

4.2.1 Method of Implementation

The 3D Fourier method is implemented on the 8-pole, 18-slot SPM machine discussed in Chapter 3 to predict the high frequency eddy current loss in the permanent magnets. Also as discussed in the previous chapter, to predict 3D eddy current loss by the proposed 3D Fourier method, the flux density values from the subdomain model or 2D FEA need to be captured to form the source distribution matrix. The method of loss prediction implemented in this chapter employs the flux density information from 2D FEA to obtain the eddy current source values. This is because the subdomain model discussed previously [85] doesn't consider the eddy current reaction effect and hence cannot accurately predict the flux density undulations within the magnet.

Since, the values in each matrix should correspond to the source at a given rotor position in the (r, θ) coordinates attached to the center of the machine, the magnetic flux density values from the 2D FEA are extracted from the mesh grids constructed over the magnets as shown in Fig. 4-2.

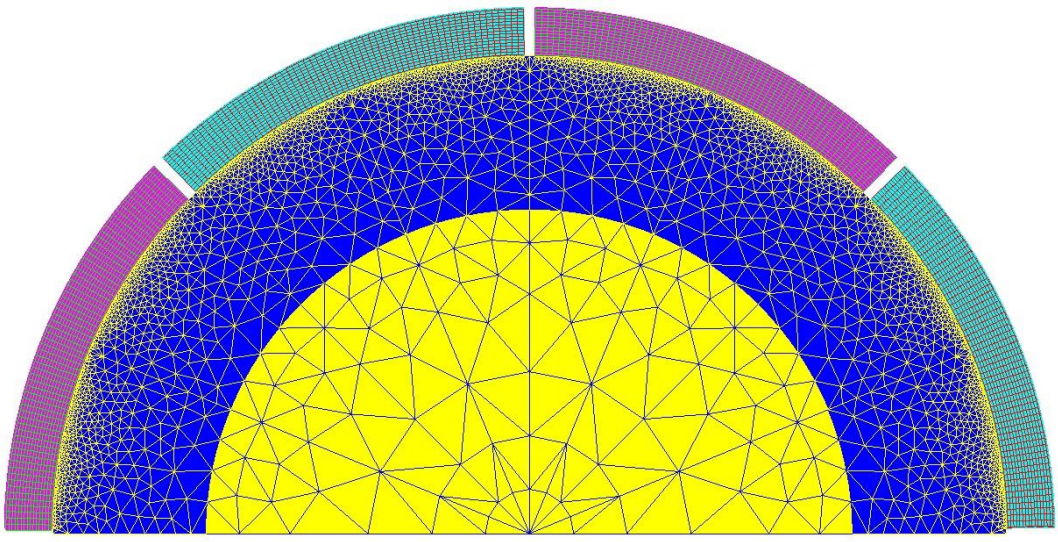

Fig. 4-1. Mesh grids constructed over the 4 magnets based on symmetry.

Considering the machine symmetry, only one half of the machine needs to be modelled in loss evaluation and hence mesh grids are constructed only over the four magnets. Every point of intersection on these mesh forms the r and θ -coordinates of the field information.

For the machine under consideration without any circumferential segmentation, each magnet as shown in Fig. 4-2(a) is discretized into sixty four divisions along the θ–direction and sixteen divisions along the r–direction. This is because the eddy current results evaluated using these discretization has given sufficient accuracy at the reduced computation time in the loss prediction. The number of divisions within a magnet segment may be modified according to the number of circumferential segmentations. For example, the mesh is modified as shown in Fig. 4-2(b) with thirty–two divisions along the θ–direction in the analysis for the case with two circumferential segmentations [130] .

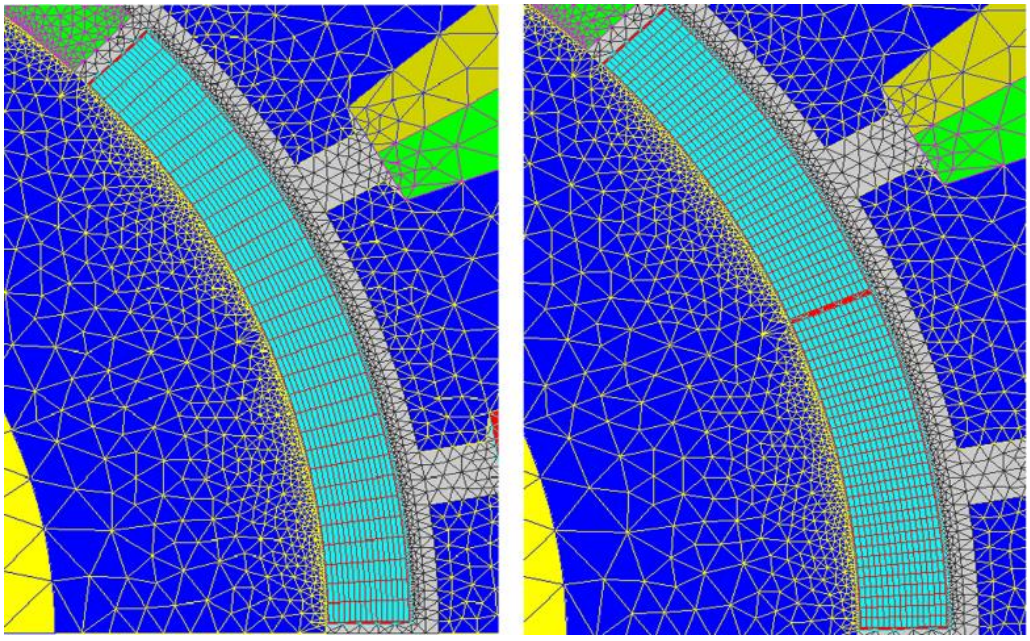

(a) Magnet with circumferential segment = 1 (b) Magnet with circumferential segment = 2

Fig. 4-2. Mesh grids constructed over the magnet-1 based on circumferential segmentations.

The eddy current sources (S_x, S_y) are evaluated from flux density values obtained from two consecutive time intervals of time stepped 2D FEA. The source values are discretized in three dimensions in a volume bounded by $(2L_x, 2L_y, 2L_z)$. The number of discretization in the z–direction is limited to 32 divisions to ensure high accuracy as described in previous chapter. 3D FFT is performed to evaluate the source coefficients described in (3-13) and (3-14) and hence the current density coefficients described in (3-17), (3-18) and (3-20). The eddy current loss in every magnet is calculated at each time step employing (3-38). To consider the effect of slotting in loss prediction, this analysis needed to be repeated for 1/6th cycle of the fundamental current.

As discussed before in Chapter 3, to evaluate the magnet loss variations with axial and circumferential segmentations, the losses are evaluated for each circumferential segment separately and the total magnet loss is computed as the sum of these losses multiplied with number of axial segmentations for the SPM machine. The loss in each axial segment is considered identical as the source field is treated essentially 2D and hence no variation along the axial direction.

The entire process is implemented in Matlab, and it takes around 5 hours to generate the flux density harmonics from 2D FEA and less than 20 seconds to compute the total 3D eddy current loss for all the magnets in a typical PC. Hence on an average for evaluating the loss variation with increase in axial number of segmentation up to 20, it takes around 15 minutes for each case. In contrast it takes more than 6 days for one 3D FEA with no axial segmentation. The whole analysis is performed on a 12 core, 64 GB RAM computer and it takes about a day for the case with 12 axial segmentations in 3D FEA.

4.2.2 Evaluation of Magnet Loss and Comparison of Results with 3D FEA

To predict 3D eddy current loss due to high frequency current harmonics by 3D Fourier method, it is intuitive to form the eddy current source matrix by 2D FEA which accounts the eddy current reaction in NdFeB magnets. The 2D FEA is carried out in CEDRAT FLUX 2D software by injecting 20 kHz sinusoidal currents having a magnitude of 5% of the fundamental peak current of 55A when the machine operates at 4500rpm. The analysis is then repeated with a higher magnet resistivity (increased by a factor of 1000) to evaluate the magnetic field in the magnets when the reaction effect is not accounted for comparison purposes. Magnet loss is evaluated with increase in number of axial segmentations up to 22 for both the cases.

The 3D time-stepped transient FEA is also carried out for the 8-pole,18-slot machine under consideration with 20 kHz frequency harmonic current employing the 2D FE machine model discussed in Chapter 3. Fig. 4-3 compares the magnet loss variations with the number of axial segments predicted from the 3D Fourier method employing the 2D FEA sources with and without considering eddy current reaction along with the magnet loss obtained from the 3D FEA.

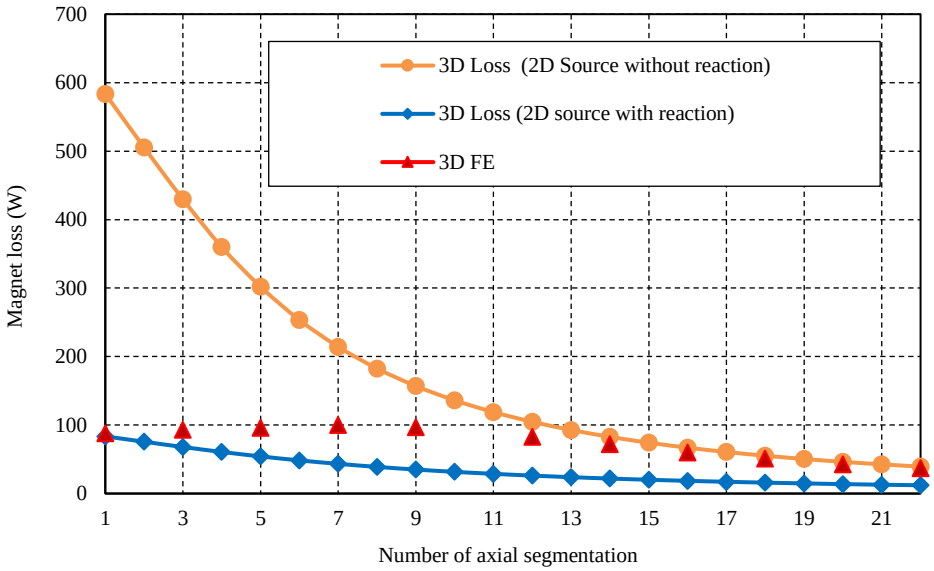

Fig. 4-3. Comparison of magnet loss variations predicted by direct application of 3D Fourier method and 3D FEA with increase in axial number of segmentations (20 kHz).

It is clear from Fig. 4-3 that the results from the direct 3D Fourier method which accounts eddy current reaction in only 2D plane overestimates the eddy current reaction and hence underestimates the magnet loss. It deviates from the actual 3D FEA predicted magnet loss as the number of axial segments increases. In contrast, the results obtained from the 3D Fourier method which employs 2D field without account of eddy current reaction are much higher than the 3D FEA predicted losses when the segmentation number is lower. However, they become closer to the 3D FE results at very high segmentation numbers [130].

4.2.3 Cause of Discrepancy in the Magnet Loss Prediction

To examine the discrepancy in the loss predictions obtained from the direct applications of the 3D Fourier method by employing the 2D FE predicted source fields, $\partial B_r/\partial t$ obtained from 2D FEA with and without considering eddy current reaction is compared with $\partial B_r/\partial t$ obtained from 3D FEA, at different axial positions of the magnet when no axial segmentation is made.

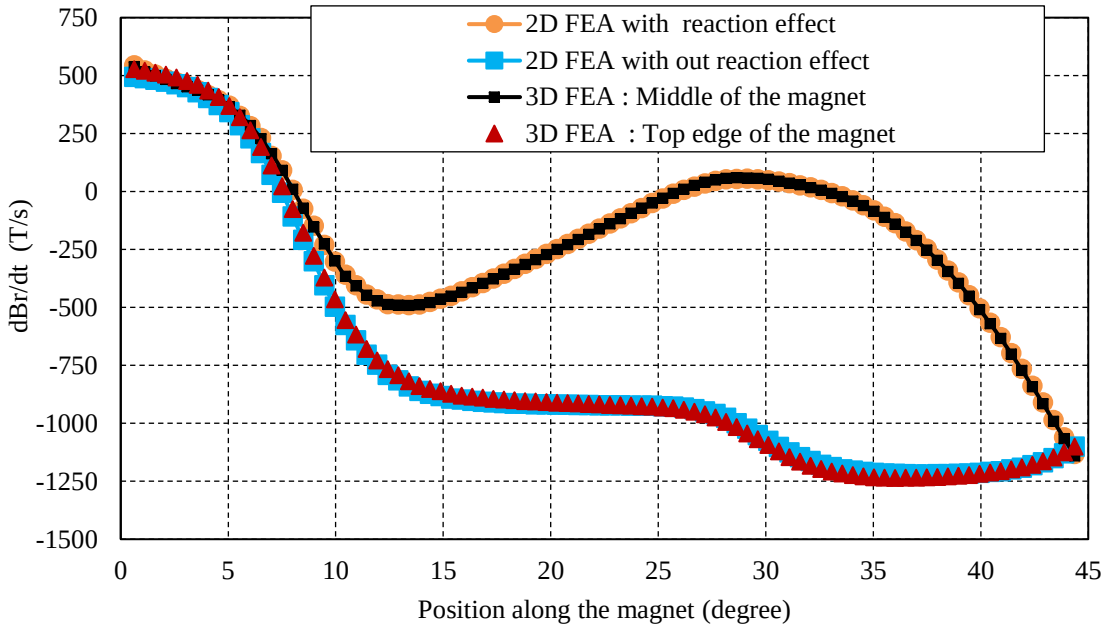

Fig. 4-4. Comparison of $\partial B_r/\partial t$ from 2D FEA (with and without reaction effect) and from 3D FEA along the middle surface of Magnet–1.

Fig. 4-4 compares 3D FE predicted $\partial B_r/\partial t$ variations with x at $\omega_r t = 4^0$ in the middle of Magnet–1 (defined by $z = L_z/2$, $y = L_y/2$, and $0 < x < L_x$) and also on its top edge (defined by $z = L_z$, $y = L_y/2$ and $0 < x < L_x$) with respect to the $\partial B_r/\partial t$ values obtained from 2D FEA with and without considering eddy current reaction.

It is clear from the figure that $\partial B_r/\partial t$ along the middle of the magnet obtained from the 3D FEA matches with those obtained from the 2D FEA which accounts eddy reaction. Whereas the 3D predicted $\partial B_r/\partial t$ values at the top edge of the magnet are very close to the 2D FEA predictions without considering reaction effect. This is because the eddy current reaction is more significant towards the middle of the magnet and it is reduced along the outer edges of the magnet due to skin effect. Thus, $\partial B_r/\partial t$ predicted by 2D FE without eddy current reaction matches closely with the 3D FE prediction at the axial edges. This illustrates the necessity to obtain the field variation along the axial direction in a magnet segment when evaluating the magnet loss at high frequencies.

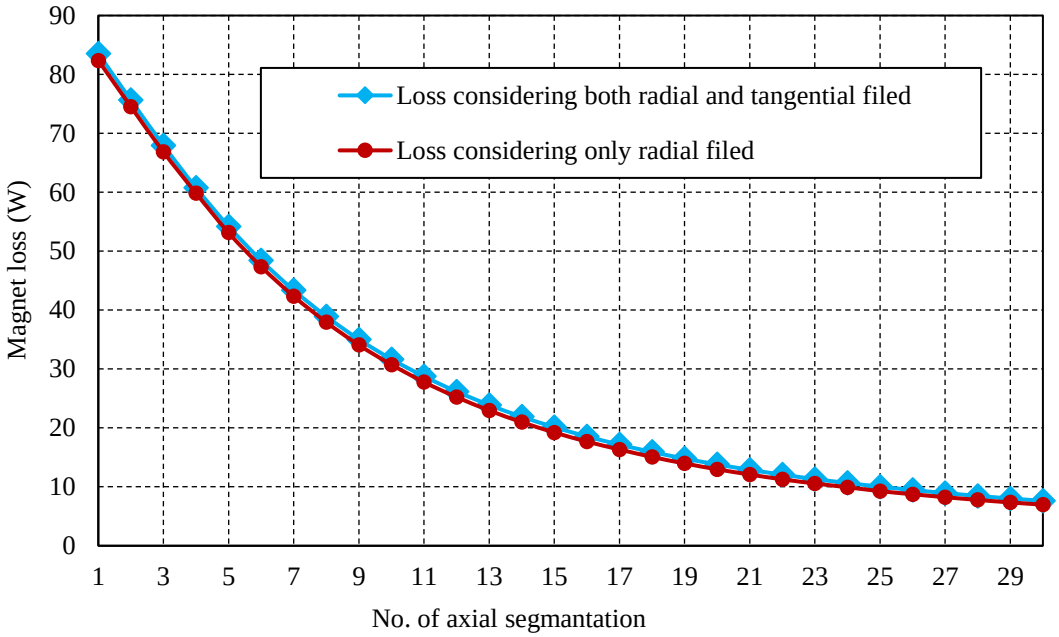

Fig. 4-5. Comparison of magnet loss variations due to radial field only and due to both radial and tangential fields with increase in axial number of segmentations (20 kHz).

Before comparing the variations of $\partial B_t/\partial t$ predicted from 2D FEA along different axial heights with 3D FEA it is insightful to assess its significance on the high frequency magnet loss which is not done so far in the literature. Hence the losses obtained from the 3D Fourier method considering only the radial source field $\partial B_r/\partial t$ is plotted against the loss obtained considering both the radial and tangential source fields in Fig. 4-5. It is clear from the above figure that the effect of the tangential field on high frequency eddy current loss is negligible [130]. Hence its variation along the axial direction can be ignored in high frequency magnet loss prediction.

4.3 Solution to the Diffusion of Eddy Current Sources in the Axial Plane and its Application with 3D Fourier Method

4.3.1 Solution to 2D Diffusion Along the Axial Plane

To circumvent the discrepancy in magnet loss prediction with the direct application of 2D FEA results in the 3D Fourier method a solution to the

diffusion of the eddy current sources along the axial (x, z) and (y, z) planes is essential. As an analytical solution to the 3D diffusion equation throughout the volume of a magnet is difficult to establish, the following assumptions are made to consider the diffusion in 2 dimensions.

(i) The variation of the eddy current sources S_y along the radial direction has been neglected.

(ii) Further, as the contribution towards the loss from the tangential source S_x is much lower than that from S_y as shown in Fig. 4-5, its diffusion along the axial plane is neglected.

These assumptions imply that the diffusion takes place predominantly in the 2D $x - z$ plane.

Assuming that a current density J_s of infinitesimally small thickness is distributed over the stator bore radius, the two dimensional eddy current problem can be formulated in the form of diffusion equation as in [92].

$$\frac{\partial^2 J_z}{\partial x^2} + \frac{\partial^2 J_z}{\partial z^2} - \mu_0 \frac{1}{\rho} \cdot \frac{d}{g} \cdot \frac{\partial J_z}{\partial t} = \mu_0 \frac{1}{\rho} \cdot \frac{d}{g} \cdot \frac{\partial J_s}{\partial t} \tag{4-1}$$

where $d = L_y$, the magnet thickness along the radial direction, g the air gap length and ρ is the resistivity of the magnet material.

Fig. 4-6 shows the general model describing d, g and the current sheet J_s as well as other geometric parameters of the machine.

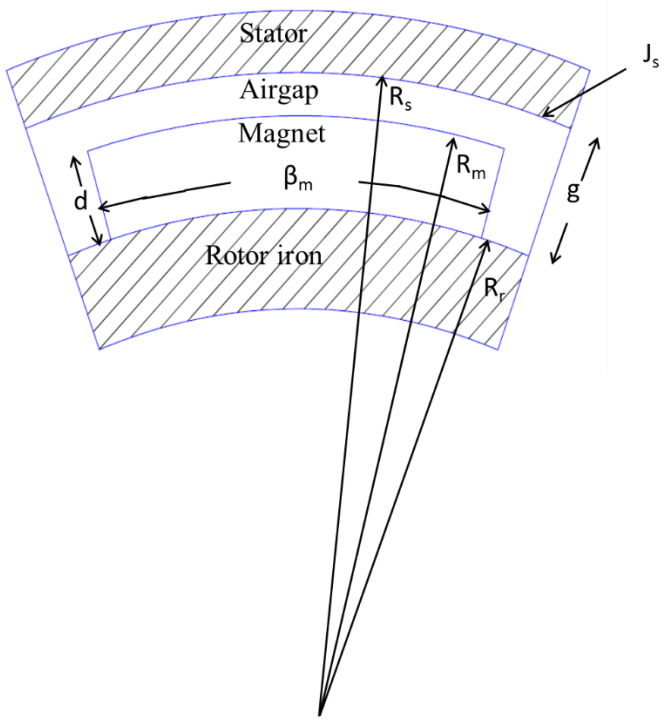

Fig. 4-6. Geometry and parameters of 2D eddy current diffusion model.

The equation (4-1) is derived in [92] from the three basic equations using the simplifying assumption discussed before ,

From Ampere's law,

$$\frac{g}{\mu_0}.\frac{\partial B}{\partial x} = J_s + J_z \tag{4-2}$$

From Ohm's law,

$$\frac{\rho}{d}.\left(\frac{\partial J_z}{\partial x} - \frac{\partial J_x}{\partial z}\right) = \frac{\partial B}{\partial t} \tag{4-3}$$

And also,

$$\nabla.J = 0 \tag{4-4}$$

Combining (4-2) to (4-4) and eliminating B, (4-1) can be obtained.

The source current density J_s distributed over the stator bore radius defined as,

$$J_s = J_m e^{j(\omega_s t - p_r \theta)} \tag{4-5}$$

where $J_m = q/2.(2N_t I_m/\pi R_s)$,

ω_s is the source supply frequency, R_s is the radius of the stator inner bore, N_t , I_m are the number of series turns per phase and the peak phase current respectively. Also q is the number of phases.

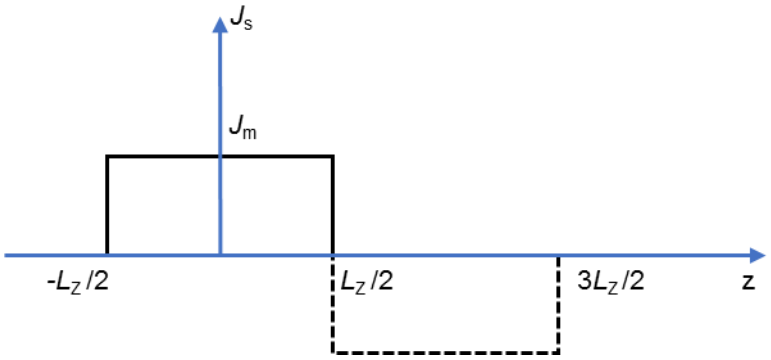

Fig. 4-7. Periodic expansion of source current in axial (z) direction.

J_s can be expressed as Fourier series in the z –direction satisfying the boundary conditions at $z = \pm L_z/2$ to create an alternating source in the axial direction as shown in Fig. 4-7.

Hence,

$$J_s(\theta, z) = \sum_{n=1,3,5\ldots} J_m \cdot \frac{4}{(n\pi)} . \sin\left(\frac{n\pi}{2}\right) . \cos\left(\frac{n\pi}{L_z} . z\right) . e^{j(\omega t - p\theta)} \tag{4-6}$$

The solution to the diffusion equation (4-1) is derived by application of $\nabla . J = 0$ such that,

$$\frac{\partial J_x}{\partial x} + \frac{\partial J_z}{\partial z} = 0. \tag{4-7}$$

And also satisfying the boundary conditions for the circumferential current density J_x given as,

$$J_x\left(x=\frac{-L_x}{2}\right)=J_x\left(x=\frac{L_x}{2}\right)=0. \tag{4-8}$$

The solution for J_z and J_x is derived in [92] .

Now from the Ohms Law applied to the magnet volume (4-3) , the axial field variations of $S_y(x,z)$ can be evaluated as,

$$\frac{\partial B_r(x,z)}{\partial t}=S_y(x,z)=\frac{\rho}{d}.\left(\frac{\partial J_z}{\partial x}-\frac{\partial J_x}{\partial z}\right). \tag{4-9}$$

The solution of the diffusion equation (4-1) evaluating J_z and hence J_x is described in Appendix B.

4.3.2 Implementation of Source Diffusion Along the Axial Plane in 3D Fourier Method

$S_y(x,z)$ evaluated from (4-9) gives eddy current source variation along the axial direction. However, its diffusion in the x and $y-$ directions has been accounted in 2D FEA. To account the axial variation of $S_y(x,y,z)$ when predicting 3D high frequency eddy current loss by employing the 3D Fourier method, $S_y(x,y)$ at given (x,y) obtained from 2D FEA which accounts eddy current reaction is adjusted by the ratio obtained from the analytical solution (4-9) [130].

Hence,

$$\left[S_y(x,y,z)\right]_{F_M}=\left[S_y(x,y)\right]_{2DFE}\times\frac{\left[S_y(x,z)\right]_{As}}{\left[S_y(x,z=0.5L_{zm})\right]_{As}} \tag{4-10}$$

where,

$[S_y(x,y,z)]_{F_M}$ is the source values to be used in the 3D Fourier method, $[S_y(x,y)]_{2DFE}$ is the source value obtained from 2D FE considering eddy current reaction, $[S_y(x,z)]_{As}$ is the source value from the analytical solution (4-9) at a given z and $[S_y(x,z=0.5L_{zm})]_{As}$ is the source value from the analytical solution (4-9) at $z=0.5L_{zm}$, where L_{zm} is the machine axial length.

It is evident that the analytical adjustment given in equation (4-10) is justified for the machines having large axial length, as the source values along the middle of the machine at $z=0.5L_{zm}$ is close to source values from 2D FE ($[S_y(x,y)]_{2DFE}$) accounting eddy current reaction. This is because the reaction effect becomes strongest at the middle of the magnets with larger axial lengths and hence source values are reduced to its minimum values as shown in Fig. 4-4 . However, for the machines designed to have lower axial length, the source values along the middle of the machine may deviate from the source values from 2D FE accounting eddy current reaction effect. Hence for such machines the axial length L_{zm} used to calculate the denominator of (4-10), $[S_y(x,z=0.5L_{zm})]_{As}$ should be sufficiently large such that the values evaluated are equivalent to the 2D FE source values accounting reaction effect. This make sure the skin depth of the higher order frequency considered is much lower than the axial length chosen and hence the $[S_y(x,z=0.5L_{zm})]_{As}$ calculated is equivalent to the 2D FE source values accounting reaction effect [130].

$[S_y(x,z)]_{As}$ obtained analytically at different axial positions ($z=0.99L_z, 0.95L_z, 0.9L_z\ 0.75L_z, 0.5L_z$) when the magnet is segmented axially with one, seven and twenty axial segments when supplied with 20 kHz armature current (5% of fundamental) at 4500 rpm is shown in Fig. 4-8.

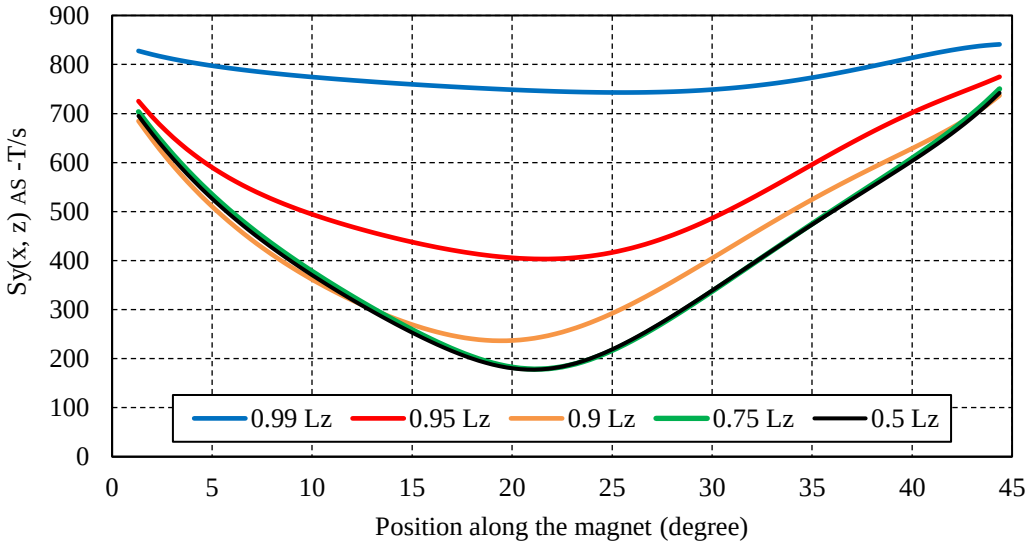

(a) Axial segments =1

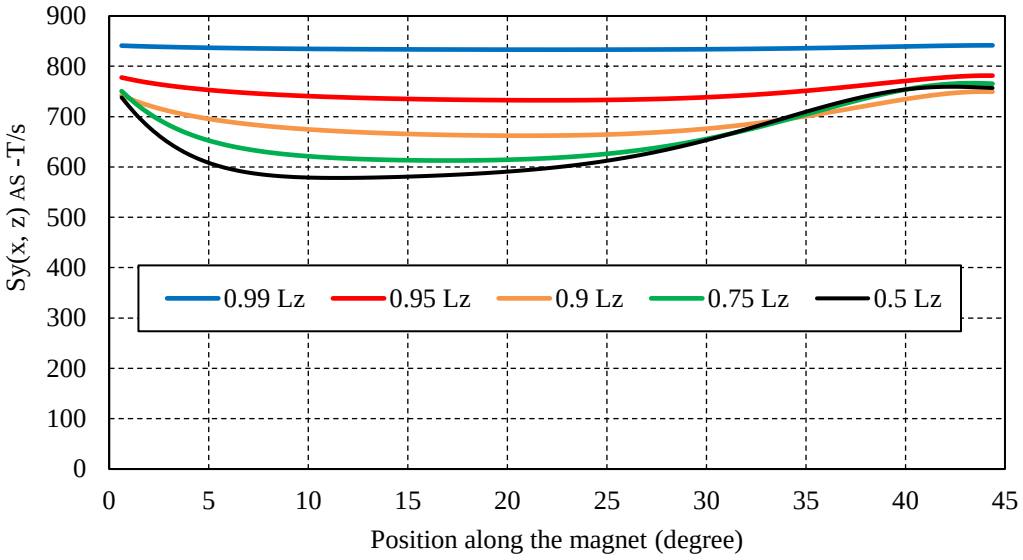

(b) Axial segments =7.

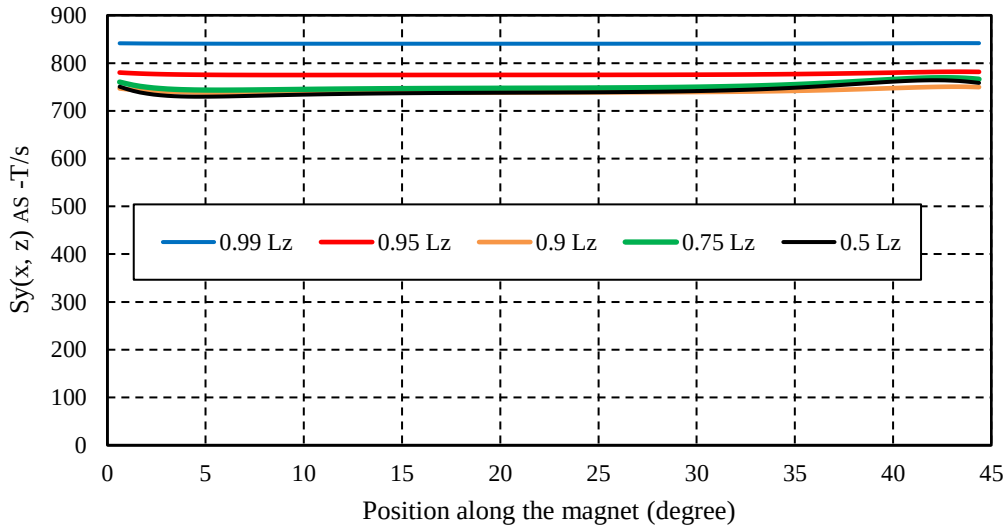

(c) Axial segments =20.

Fig. 4-8. Comparison of analytically predicted flux density variations $[S_y(x,z)]_{As}$ at different axial positions with axial segmentations 1, 7 and 20.

To study the effect of eddy current reaction along the axial direction, $S_y(x,y)$ obtained from 2D FEA accounting eddy current reaction is adjusted using (4-10) under the same load conditions as above with one, seven and twenty axial segments and one circumferential segments. The results obtained at different axial positions ($z = 0.99L_z, 0.95L_z, 0.9L_z\, 0.75L_z, 0.5L_z$) within the magnet axial length of Magnet–1 at $\omega_r t = 4^0$are shown in Fig. 4-9.

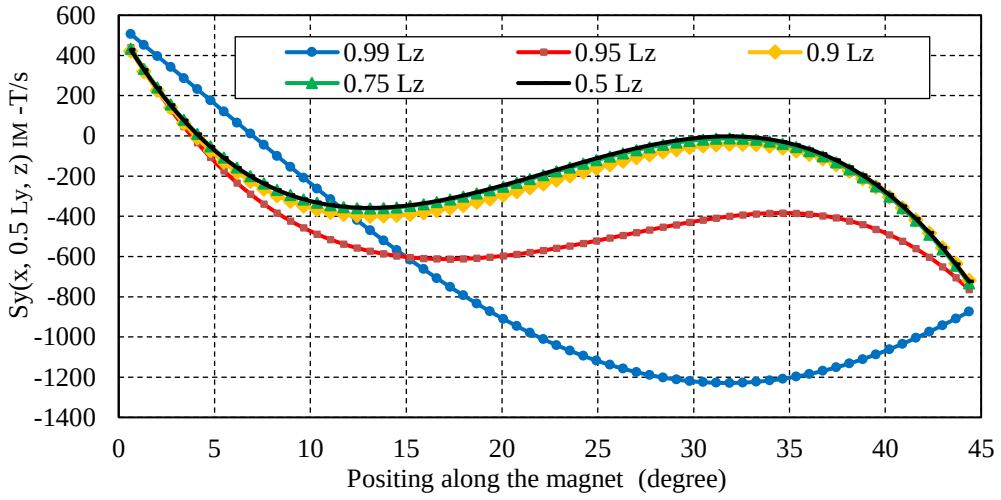

(a) Axial segments = 1.

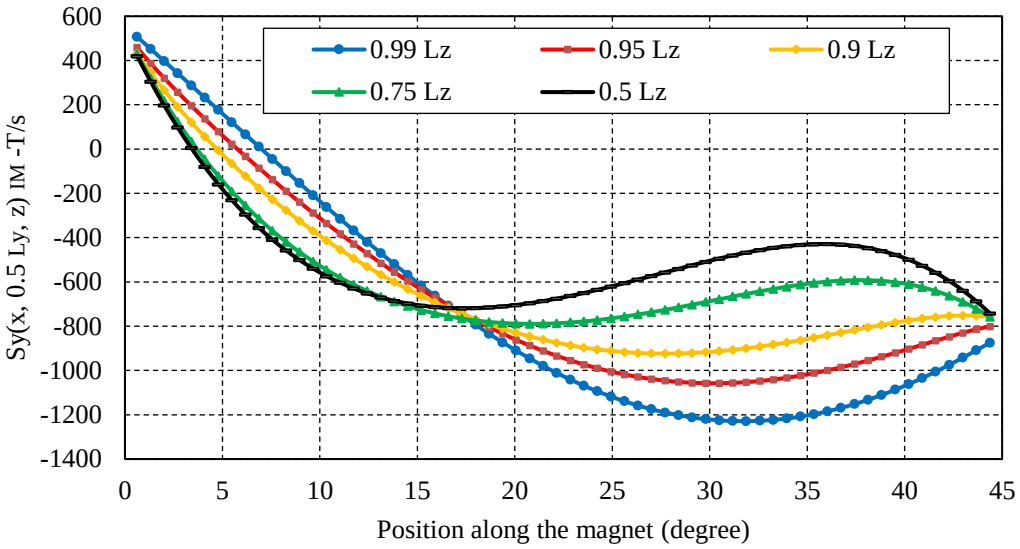

(b) Axial segments = 7.

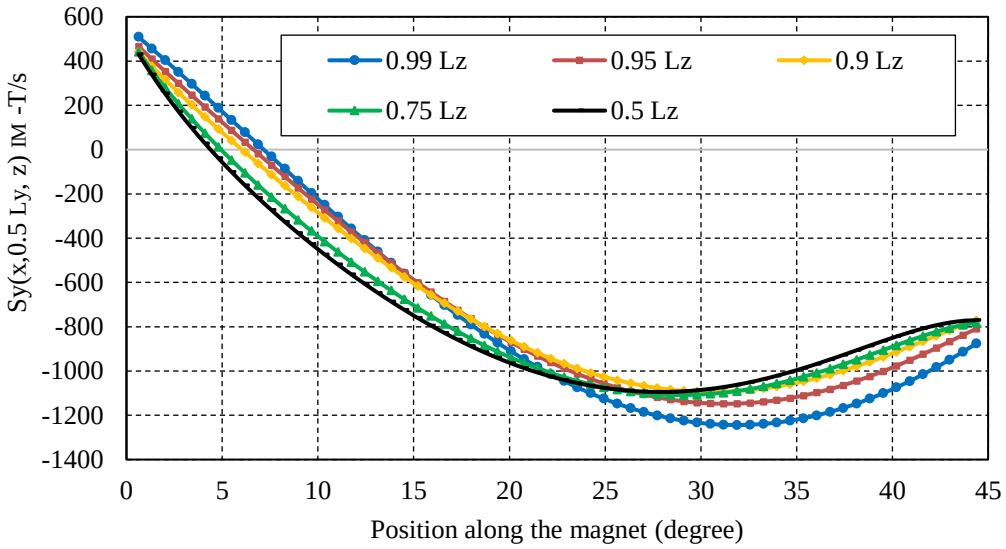

(c) Axial segments = 20.

Fig. 4-9. Comparison of $[S_y(x, 0.5L_y, z)]_{I_M}$ obtained after the adjustment in (4-10) at different axial positions with axial segmentations 1 ,7 and 20.

It can be observed from the figures that for the case with no axial segmentation $S_y(x, z)$ close to the magnet axial edge (z = $0.99\,L_z$) is much greater in magnitude than those at other z – positions. The $S_y(x, z)$ values at z = $0.9L_z$ and $0.75L_z$ are very close to those in the middle (z = $0.5L_z$). When the number of axial segments is seven, $S_y(x, z)$values are more evenly spread along the axial direction and when the number of axial magnet segments reaches

twenty $S_y(x,z)$ variation along the axial direction is reduced considerably, and their values at different z position are close to those at the magnet axial edge. These results are consistent with those obtained from the 3D FEA in Fig. 4-3 where it shows with lower axial segments that the 3D predicted magnet loss is close to the values obtained from the 3D Fourier method which employs 2D FEA considering eddy current reaction, while the 3D FE results at large number of axial segmentations (axial segments above twenty) follows the results from the 3D Fourier method which employs 2D FE ignoring eddy current reaction.

To study the effect of eddy current reaction along the circumferential direction, $S_y(x,y)$ obtained from 2D FEA accounting eddy current reaction for each circumferential segment of Magnet–1 is adjusted using (4-10) under the same load conditions previously mentioned. The results obtained at different axial positions ($z = 0.99L_z, 0.95L_z, 0.9L_z\ 0.75L_z, 0.5L_z$) within the axial length of each of the four circumferential segments of Magnet–1 with only one axial segmentation at $\omega_r t = 4^0$are shown in Fig. 4-10.

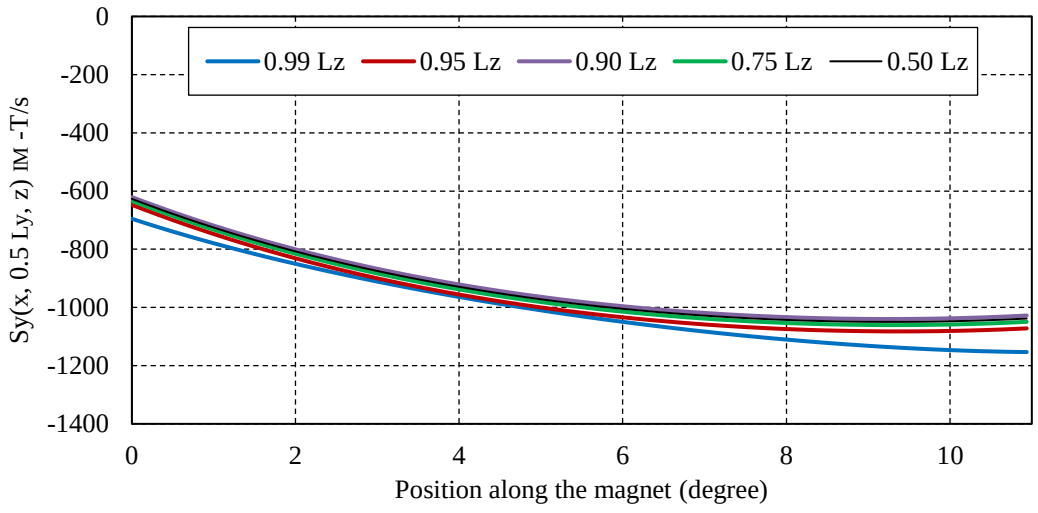

(a) Circumferential Segment–1.

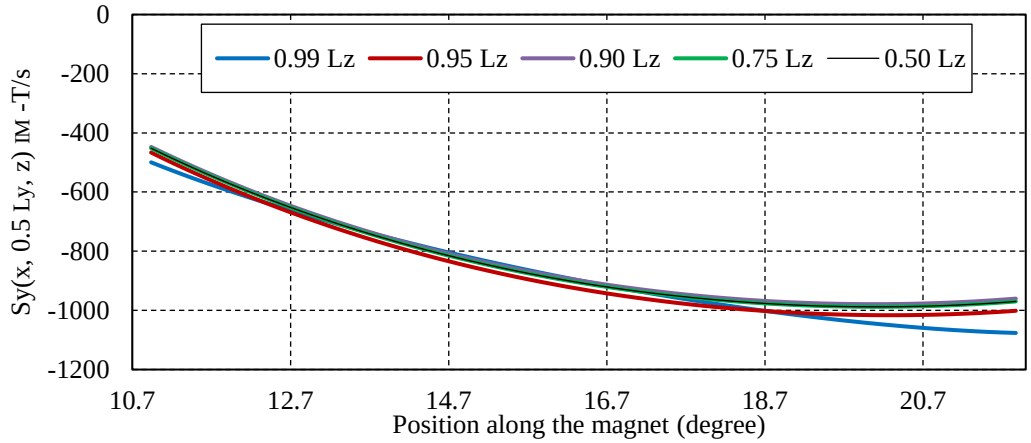

(b) Circumferential segment–2.

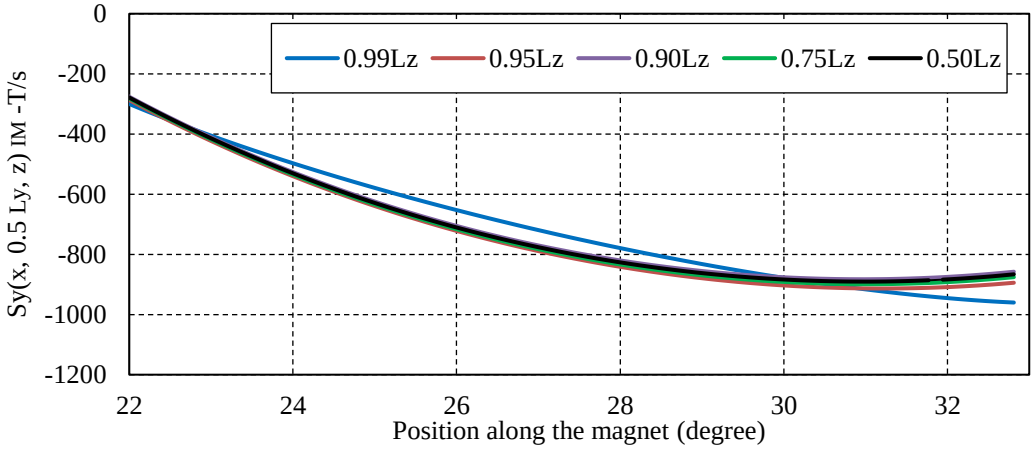

(c) Circumferential segment–3.

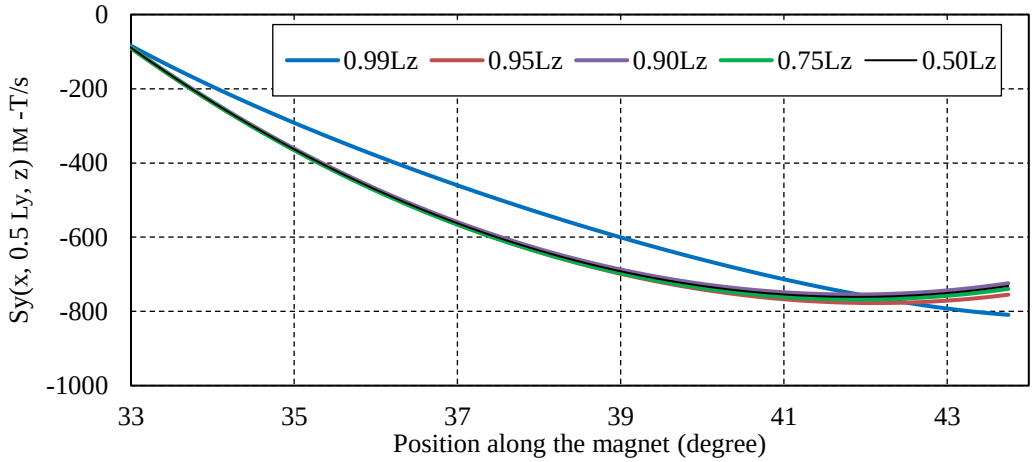

(d) Circumferential segment–4.

Fig. 4-10. Comparison of $[S_y(x, 0.5L_y, z)]_{I_M}$ obtained after the adjustment in (4-10) at different axial positions for the four circumferential segments of Magnet–1.

It is seen that gap between the flux density variations along the middle of the magnet segment and along its the outer edges is reduced with increase in the number of circumferential segmentations. Hence the source distribution becomes more uniform with increase in circumferential segmentation compared to results obtained with increase in axial segmentations.

Since $S_y(x,y)$ evaluated from the 2D FEA includes eddy current diffusion in the radial and circumferential directions, the values evaluated with (4-10) account the diffusion approximately in all 3 dimensions. The whole process of predicting 3D high frequency eddy current loss by the modified 3D Fourier method which accounts for 3D eddy current reaction effect is depicted as a flowchart in Fig. 4-11.

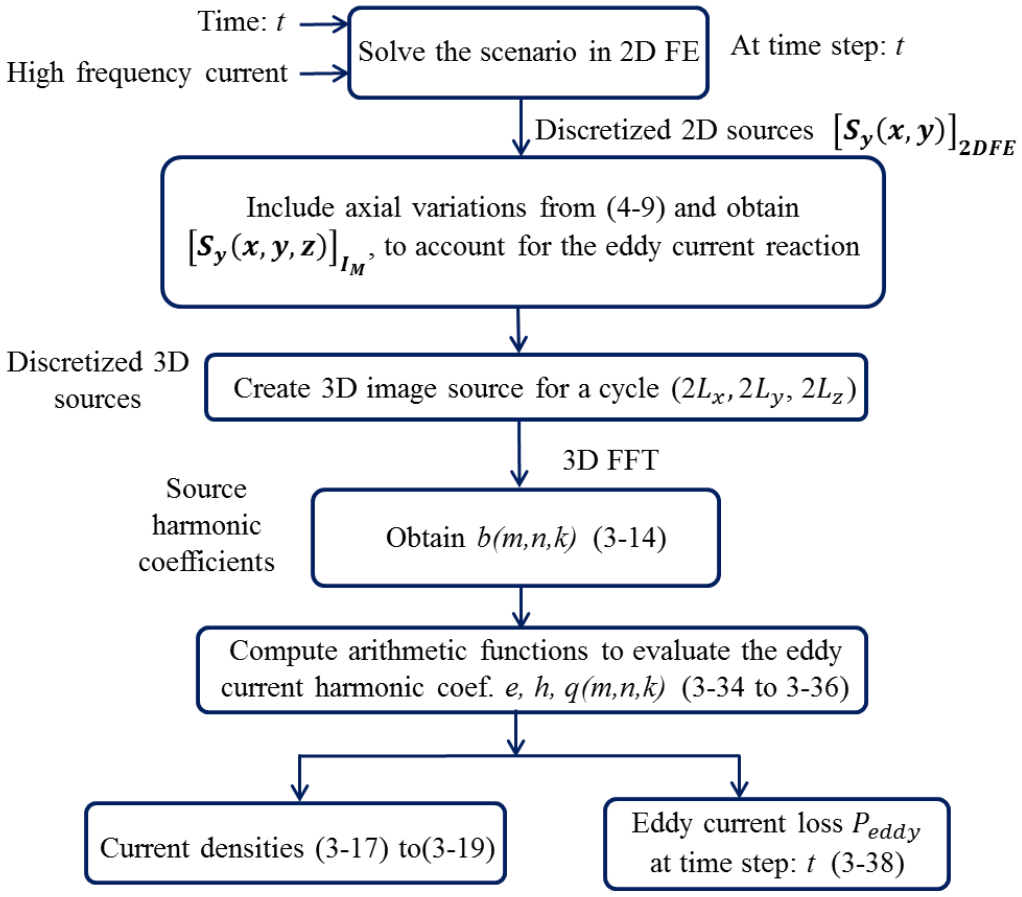

Fig. 4-11. Flowchart illustrating 3D eddy current loss computation at high frequency accounting eddy current reaction effect using modified 3D Fourier method.

4.4 3D Finite Element Validation

The proposed method is implemented by considering axial variation of eddy current sources for both 10 kHz and 20 kHz harmonic contents with 5% of 55A peak fundamental current when the machine operates at a speed of 4500rpm. The analysis is repeated with increase in axial and circumferential number of segmentations.

Fig. 4-12 compares the instantaneous loss computed for the first four magnets and their total when the machine is having seven axial segments and no circumferential segments when excited by 20 kHz harmonic current.

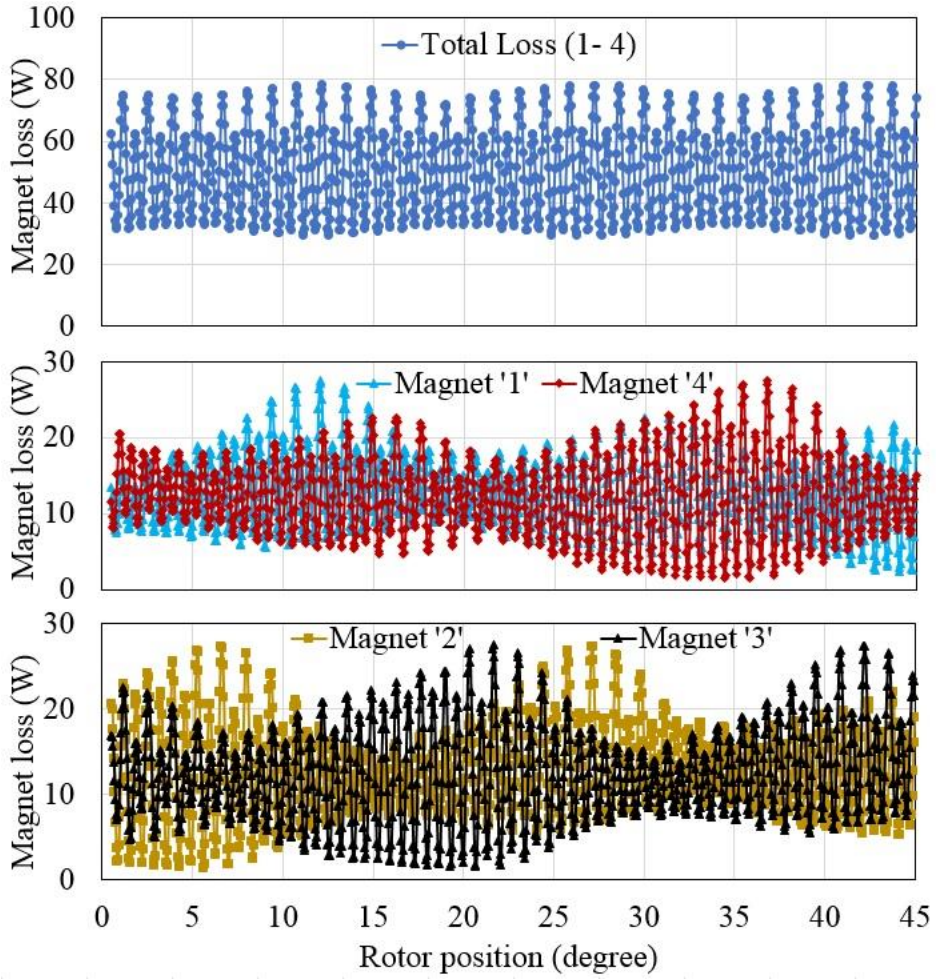

Fig. 4-12. Instantaneous magnet loss variations for Magnets–1 to 4 and their total with rotor position predicted from the proposed method.

The magnet loss is observed to be repeating at every 1/6th fundamental frequency, and hence the losses evaluation is repeated over this time span and averaged to predict the magnet loss [130].

3D FEA is performed at different axial and circumferential segmentations for 20 and 10kHz for validating the results predicted using the proposed method. The predicted loss variations with axial and circumferential number of segments at 20 kHz and 10 kHz are compared with 3D FEA results in Fig. 4-13 and Fig. 4-14 respectively.

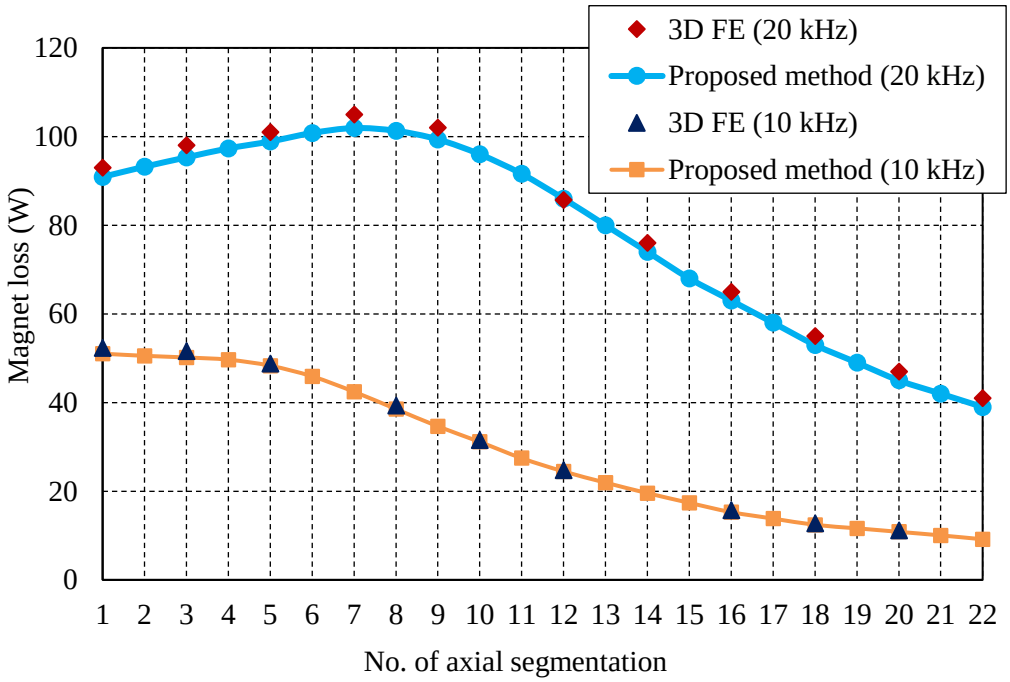

Fig. 4-13. Comparison of loss variations with axial number of segments.

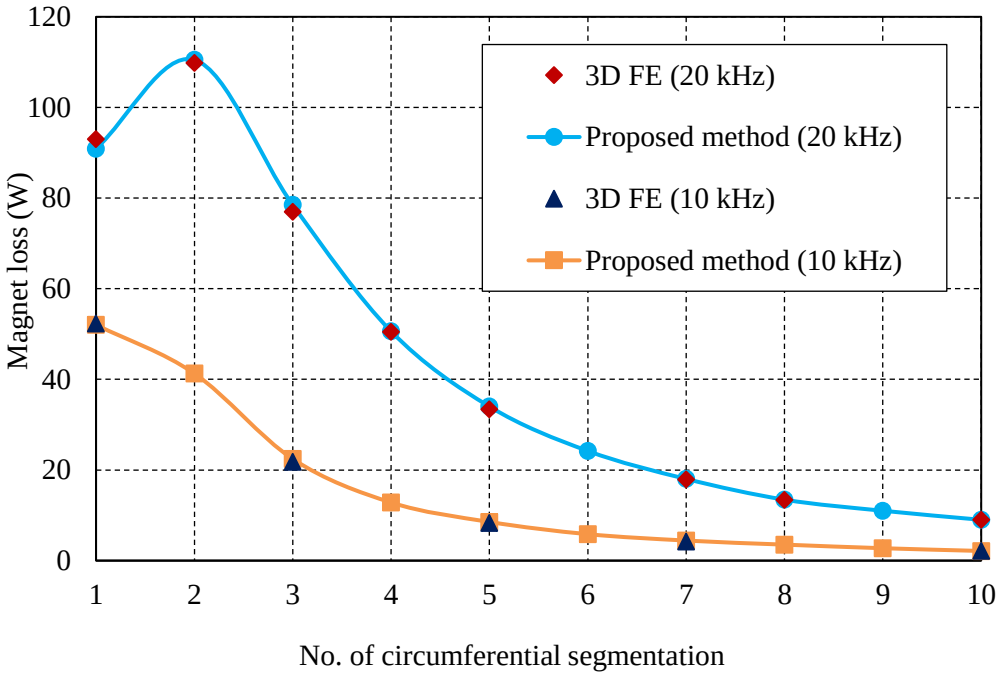

Fig. 4-14. Comparison of loss variations with circumferential number of segments.

It is observed from the results that predicted losses by the proposed method agree well with the 3D FE results.

Fig. 4-15 compares z –component eddy current density distributions evaluated from the proposed method and the 3D FEA at $\omega_r t = 4^0$ on the surface of Magnet–1 defined by $y = 0.5\mathrm{L}_y, 0 < x < \mathrm{L}_x, 0.5\,\mathrm{L}_z < z < \mathrm{L}_z$, when the machine operates at the maximum speed of 4500 rpm and excited by 20 kHz harmonic current. The machine is having seven axial segments and one circumferential segment.

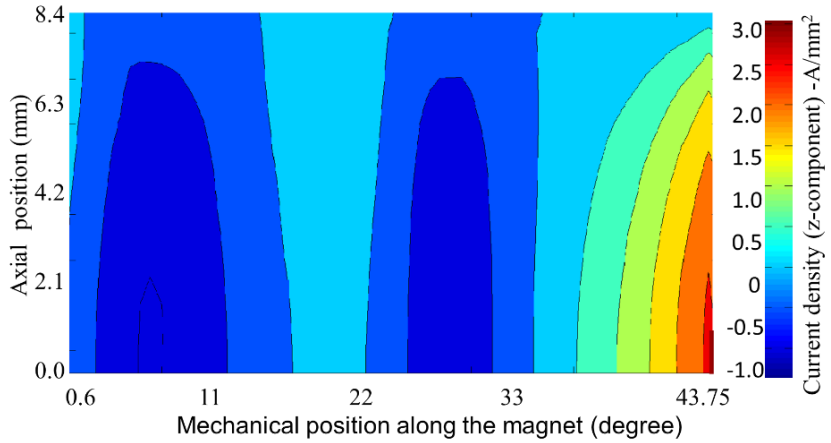

(a) Eddy current density (z- component) distribution predicted by the proposed method.

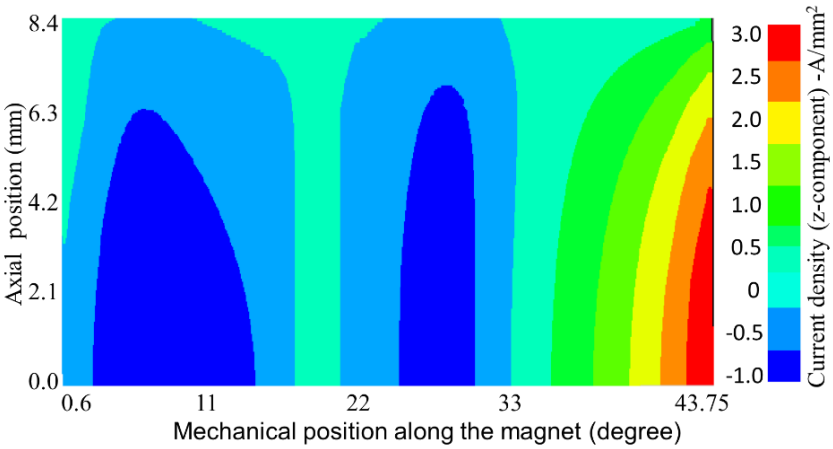

(b) Eddy current density (z- component) distribution predicted by 3D FEA.

Fig. 4-15. Comparison of eddy current density (z- component) distribution predicted by the proposed method and 3D- FE on the middle surface of Magnet–1 at r=31mm when supplied with 20kHz armature current at 4500 rpm.

Fig. 4-16 compares x –component eddy current density distributions evaluated from the proposed method and the 3D FEA at $\omega_r t = 4^0$ on the surface of Magnet–1 defined by $y = 0.5L_y, 0 < x < L_x, 0.5\,L_z < z < L_z$, when the machine operates at the same conditions as above.

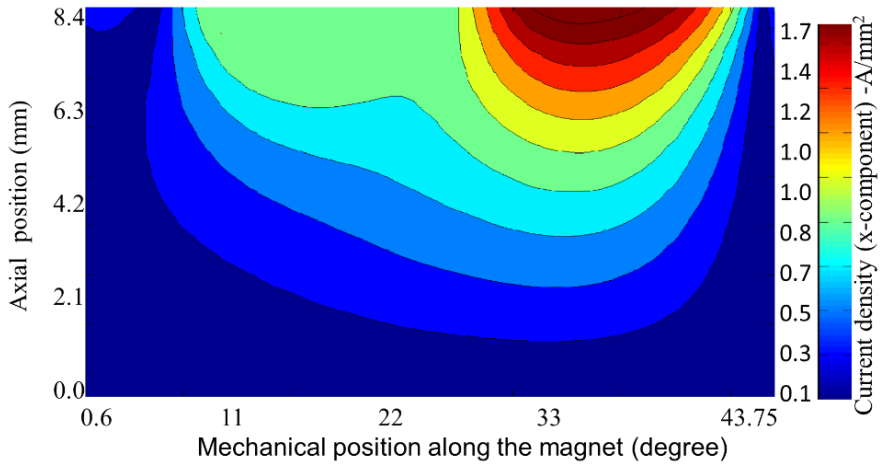

(a) Eddy current density (x-component) distribution predicted by the proposed method

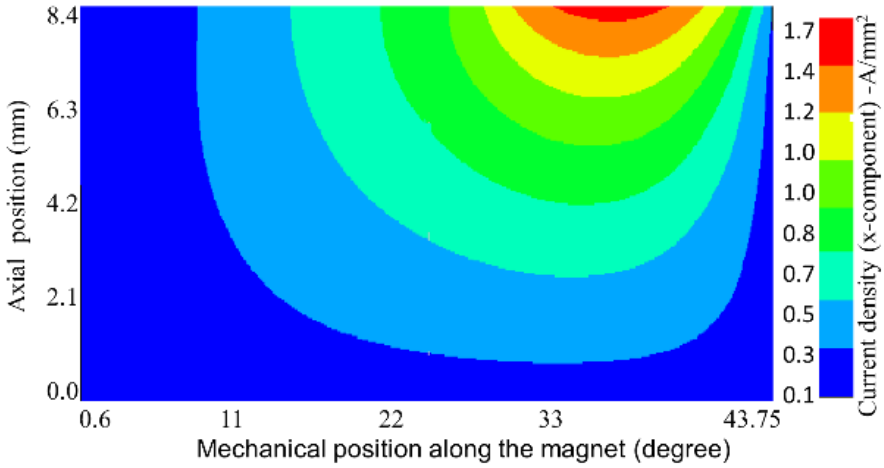

(b) Eddy current density (x- component) distribution predicted by 3D FEA.

Fig. 4-16. Comparison of eddy current density (x- component) distribution predicted by the proposed method and 3D- FE on the middle surface of Magnet–1 at r=31mm when supplied with 20kHz armature current at 4500 rpm.

Fig. 4-17 compares the proposed method and 3D FE predicted variations of z and x components of the current density with x in Magnet–1 ($0 < x < L_x$) at $\omega_r t = 4^0$, $z = 0.5\,L_z$ and $y = 0.5\,L_y$ when magnet per pole is segmented into 7 pieces axially and with no circumferential under the same load conditions.

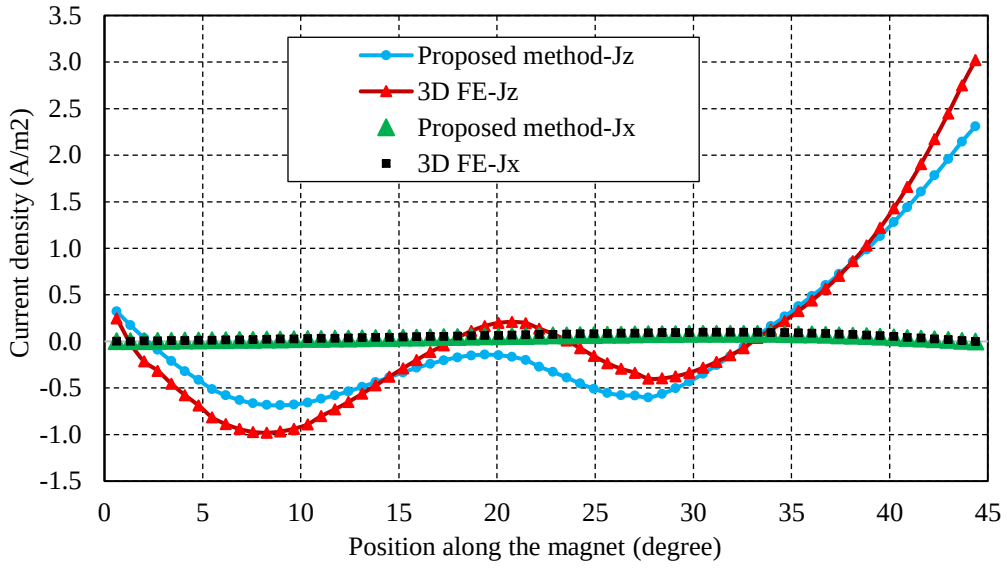

Fig. 4-17. Proposed method and 3D FE predicted variations of z and x-components of eddy current density along the magnet at $\omega_r t = 4^0$, y = 0.5Ly and $L_z = 0.5\ L_z$

All the above results show that the current density distribution predicted by the proposed method follows the 3D FEA predictions at most points in the magnet. The mismatches may be attributed to the curvature effect which is neglected and also the assumptions made in evaluating the axial field variations.

4.5 Discussion on Results

The variation of 3D eddy current loss with increase in axial number of segmentations (anomaly of segmentation) [120, 131] can be explained from the combination of the eddy current reaction effect and the increase in 3D end effects with axial segmentation. Without any axial segmentation, the eddy current reaction effect is strong and consequently a large reduction in the magnetic field inside the magnets, and hence the $S_y(x, y, z)$ is reduced considerably as seen in Fig. 4-9 (a). A smaller number of segmentations would reduce the eddy current reaction field and spreads the $S_y(x, y, z)$ more evenly in the axial segments as seen in Fig. 4-9 (b). This may lead to increase in eddy current loss. However, when the number of segments continues to increase, the eddy currents are forced to return via axial or circumferential ends. This increases the length of the eddy current flow path, and escalates the resistance

to the eddy current flow, and hence reduces the eddy current loss. Under such circumstances, the eddy current density is lower, and hence its reaction field becomes weaker. This results in $S_y(x, y, z)$ more or less uniform in the different axial segments as seen in Fig. 4-9(c).

The eddy current density distributions at $\omega_r t = 4^0$ on the middle surface of Magnet–1 at r = 31mm for one, three, seven, fourteen and twenty one axial segmentations when the machine is excited with 20 kHz armature harmonic and operates under the same condition as previously described are shown in Fig. 4-18.

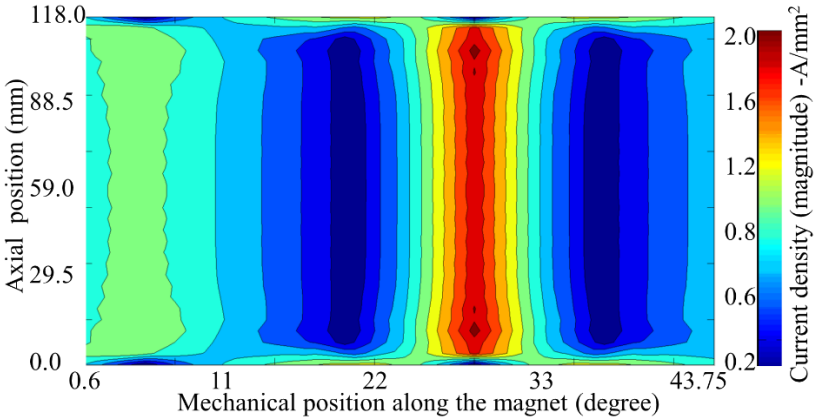

(a) Eddy current density distribution, number of axial segments = 1.

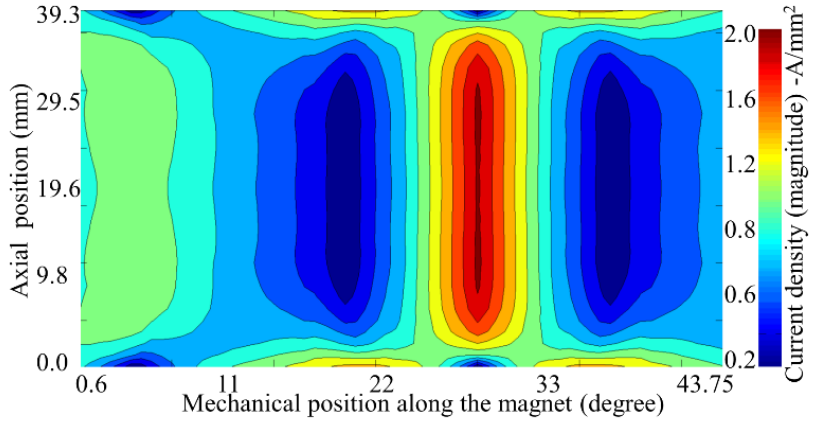

(b) Eddy current density distribution, number of axial segments = 3.

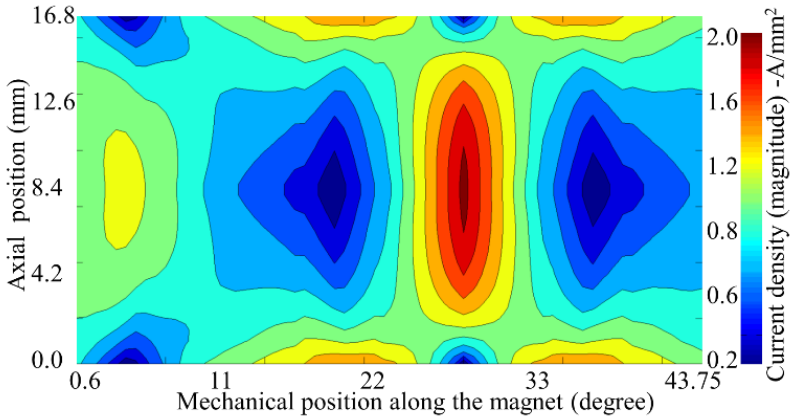

(c) Eddy current density distribution, number of axial segments = 7.

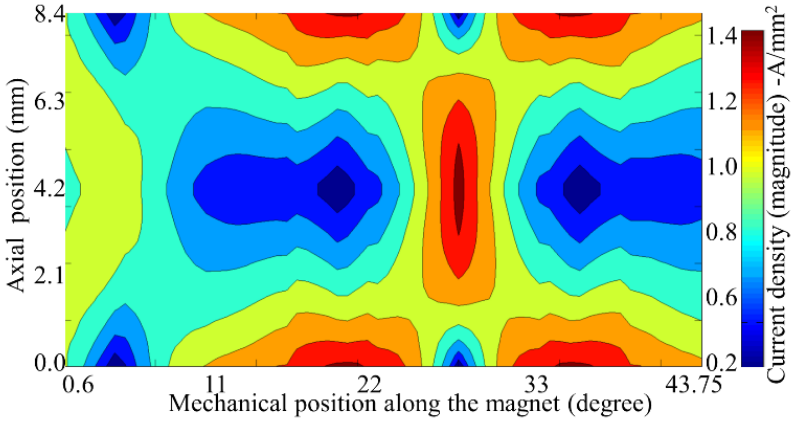

(d) Eddy current density distribution, number of axial segments = 14.

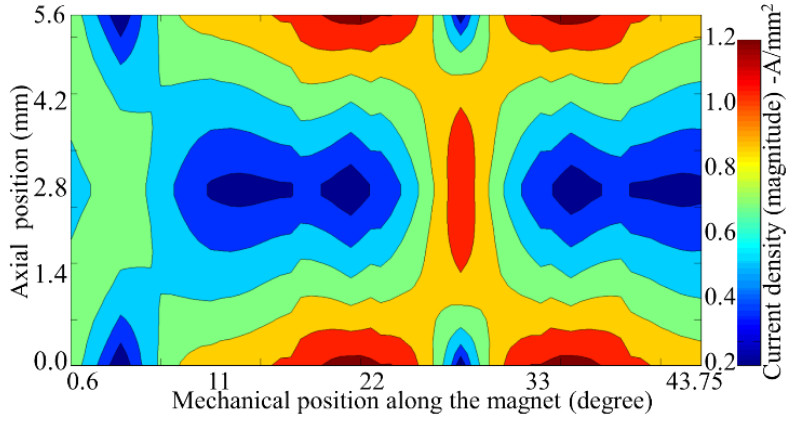

(e) Eddy current density distribution, number of axial segments = 21.

Fig. 4-18. Eddy current density distribution (magnitude) predicted by proposed method on the middle surface of Magnet–1, when number of axial segments = 1, 3,7, 14 and 21.

It can be observed from the figures that the high current density regions are increased when the segmentation number reaches seven as seen Fig. 4-18

(c), resulting in maximum loss. With large number of segmentations, eddy current density distribution becomes more 3-dimentional causing significant reduction in its magnitude as seen in Fig. 4-18 (d) and Fig. 4-18 (e). Thus, the resultant magnet loss is quite low.

For the case with circumferential segmentation a small increase in the number of segmentations itself causes the eddy current sources to spread along the axial direction and hence makes the magnet loss maximum. This is because with increase in circumferential segmentation the segment width decreases faster compared to reduction in its axial height with increase in axial segmentations. It is observed that the gap between the eddy current sources at the axial ends and the middle of the segment is reduced much faster as seen from Fig. 4-10 with further increase in circumferential segmentations, however the return path for the eddy current flow also is largely increased [90] making the eddy current distribution to become more 3-dimentional causing reduction in the magnet loss at increased rates.

4.6 Conclusion

A computationally better efficient technique for predicting high frequency 3D eddy current loss in rotor PMs of SPM machines has been described. It has been shown that the predicted magnet losses from direct application of the 3D-Fourier method which employs 2D FE predicted sources deviate from 3D FE predicated values. The modified method which accounts 3D eddy current diffusion yields more accurate results for magnet loss in the SPM machine.

The developed method accounts for the,

(i) Radial field variation inside the magnet,
(ii) Slotting effect.
(iii) Field produced by the permanent magnet,
(iv) Variation of loss among the magnet segments,
(v) Saturation effects of the lamination material.

It is observed that the contribution of the tangential component of flux density to at high frequency magnet loss is negligible. The proposed method is computationally efficient as it takes about an average of 15 minutes per case in contrast to about 6 days in 3D FE analysis with no axial segmentation.

CHAPTER 5
Experimental Validation of the 3D Fourier Method for SPM Machine

5.1 Introduction

As discussed in Chapter 1, the present day finite element based commercial tools for 2D and 3D analysis of electromagnetic fields have reached a high level of maturity and hence the accuracy of analysis is guaranteed as long as the machine model is correctly formulated. Thus, almost all publications in literature on prediction of eddy current losses in rotor magnets employ 3D FE analysis as a means of validation of the developed computationally efficient methods. From scientific point of view, rotor eddy current loss validation is far from ideal. The challenges for the experimental validation, however, arise from the fact that the amount of rotor eddy current loss is relatively small in a well-designed PM machine, and it cannot be separated from the iron loss and mechanical loss by direct measurements.

However, there are a few publications in the literature describing the methods of rotors loss measurements by rotor temperature measurements. Indirect magnet loss measurement by thermometric method is devised by Z.Q Zhu *et al.* [64] for PM machines based on the rate of temperature rise measured by temperature sensors through low noise slip-rings. A similar method is carried out for rotor loss measurements in [45, 71] for validating analytical and FE based predictions. N. Zhao *et al.* in [31] carried out the temperature measurements every time when the machine stops its operation and hence prevents the friction between the copper rings and brushes. This method avoids the increase in the contact resistance between the brushes and slip rings and hence the measurement accuracy of the magnet temperature is significantly improved. However, the method can only estimate the loss based on the thermal property and geometry of the magnets, and its accuracy is often affected by no-uniform temperature distribution in the magnets as well as the heat exchanges with other regions[132].

There are also a few publications [26, 27, 132, 133] in the literature which measures magnet temperature outside the machine and hence to avoid any contact loss associated with brushes and slip-rings. Test magnets are enclosed in a solenoid coil and the thermal measurements are carried out at different currents and frequencies. These experimental results re-confirm the reduction in magnet loss with increase in segmentations. In [134] K. Yamazaki *et al.* separated the total iron loss from the other machine loss while proposing a reduced eddy current loss rotor and stator shape for concentrated winding IPM machines. D. Liu *et al.* in [135]validated eddy current loss estimation models by experiments separating the rotor loss from the other machine losses. K. Yamazaki *et al.* [136] separated magnet eddy current loss from the other losses by subtracting the loss of the machine with the magnets from that without the magnets employing appropriate control of armature currents and voltages at locked rotor conditions of the SPM machine.

In this chapter the 3D Fourier method proposed in Chapter 3 and 4 is validated by experiments in which the magnet loss is separated from other losses by employing locked rotor tests with and without magnets at reduced armature currents on a 14-pole, 12 –slot PM machine. Also the magnet loss considering all the armature harmonics at the real operating conditions is evaluated by employing the phase currents measured from the experiments at maximum speed conditions in the proposed method.

The main contents of this chapter is discussed by the author briefly in [J1] and is discussed in detail with the magnet loss at real operating conditions in [J8], as mentioned previously in Section 1.8.

5.2 Machine Specifications and Rotor Prototyping

5.2.1 Machine Specifications

The 3D magnet loss prediction technique developed in Chapters 3 and 4 is experimentally validated on a 10kW (peak), 14-pole,12-slot SPM machine designed for EV traction applications [125] . This motor proposes a new design technique for traction machines to achieve high efficiency against a defined driving cycle such as the New European Drive Cycle, while satisfying the required torque–speed operating range and other volumetric and thermal design constraints. The motor is developed for micro-sized vehicle propulsion assuming that two similar motors located at its front and rear shares equally the traction torque [125].

The cross-section of the machine illustrating its winding configuration is shown in Fig. 5-1. The design specifications and the performance indicators at peak and rated torque conditions of the 14-pole,12-slot SPM is shown in Table 5-1 and Table 5-2 respectively.

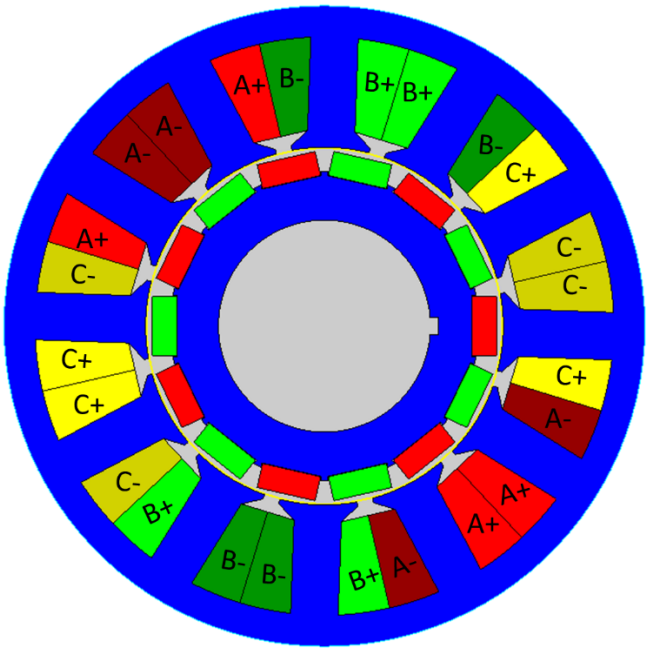

Fig. 5-1. Cross-section of the 14-pole, 12-slot SPM machine.

Table 5-1.Design Specifications of the 10kW, 14-pole, 12-slot SPM

Design parameter	Unit	Value
Stator outer radius	mm	75.58
Motor stack length	mm	122.0
Air-gap length	mm	1.0
Rotor radius	mm	41.19
Shaft radius	mm	25.0
Stator slot depth	mm	26.04
Stator tooth width	mm	11.20
Stator slot opening	mm	3.75
Stator slot opening depth	mm	1.04
Length of magnet	mm	14.0
Width of magnet	mm	5.8
No. of turns per coil	-	8
No. of coils per phase	-	4
Phase resistance	mΩ	0.19
Phase inductance	mH	0.309
Magnet (NdFeB-N35SH) -Br	T	1.22
Max operating temperature (Magnet)	°C	150
Magnet Resistivity	Ω	$1.6x10^{-6}$
Nominal DC link voltage	V	120
Peak power	kW	9.9
Based speed	rpm	1350
Maximum cruise speed	rpm	4500

Table 5-2. Performance Indicators at Rated and Peak Toque Conditions

Performance indicator	Unit	Rated	Peak
Torque	N·m	35.0	70.0
Torque ripple	%	1.03	1.15
Peak phase current	A	79.0	166.0
Current density	A/mm2	5.3	11.3
Copper loss	W	198	857
Iron loss	W	43.6	64.5
Efficiency	%	95.3	91.5
Torque at max. speed (4500 rpm)	N·m	4.7	15

5.2.2 Rotor Prototyping

As the testing of the 14-pole,12-slot SPM is planned to be carried out under locked rotor conditions, two rotors are built one with and the other without rotor magnets. The rotor endings which locks the rotor core on to the shaft are built with reduced outer diameter. This helps in reducing the parasitic iron loss which can occur in it from the leakage flux variations while testing. The adhesive (Loctite 658) applied in between the magnets and the rotor core will provide a thin layer of electrical insulation between the two. There was the presence of a feeble magnetization when magnets were supplied, however they are pasted as such without any further magnetization Therefore, when the motor windings are exited with appropriate current under locked rotor conditions, the magnetic field distributions in the machine are essentially almost the same. The prototyped rotor parts before assembly are shown in Fig. 5-2.

The rotor with rectangular shaped permanent magnets are built with 3 axial segments and no further circumferential segments for each pole. The prototyped rotors with and without magnets assembled is shown in Fig. 5-3 and Fig. 5-4.

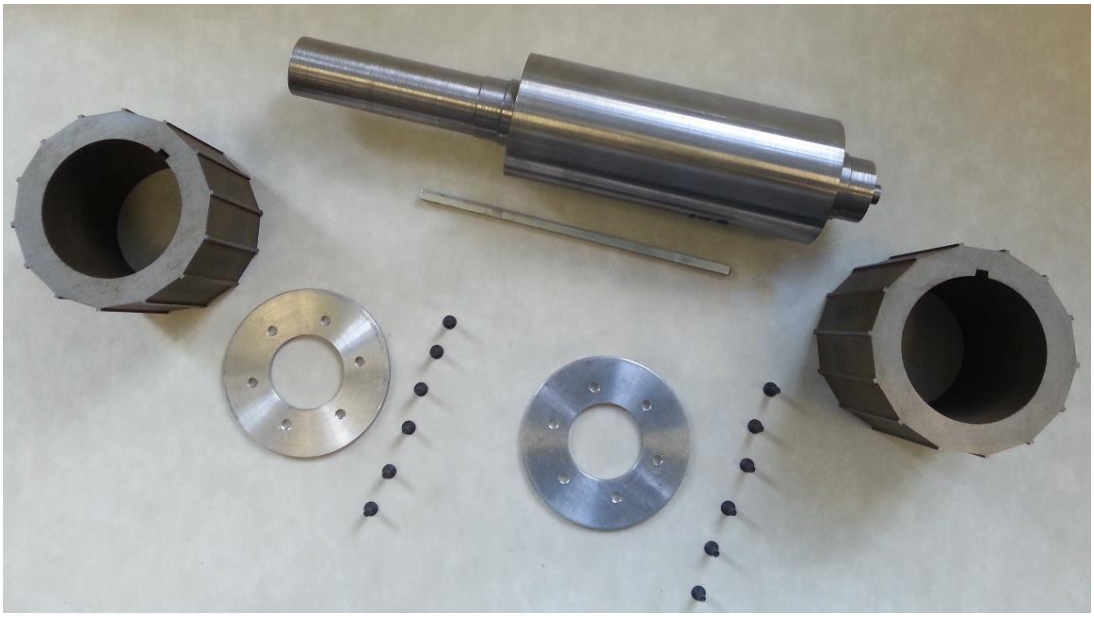

Fig. 5-2. Prototyped rotor parts before assembly.

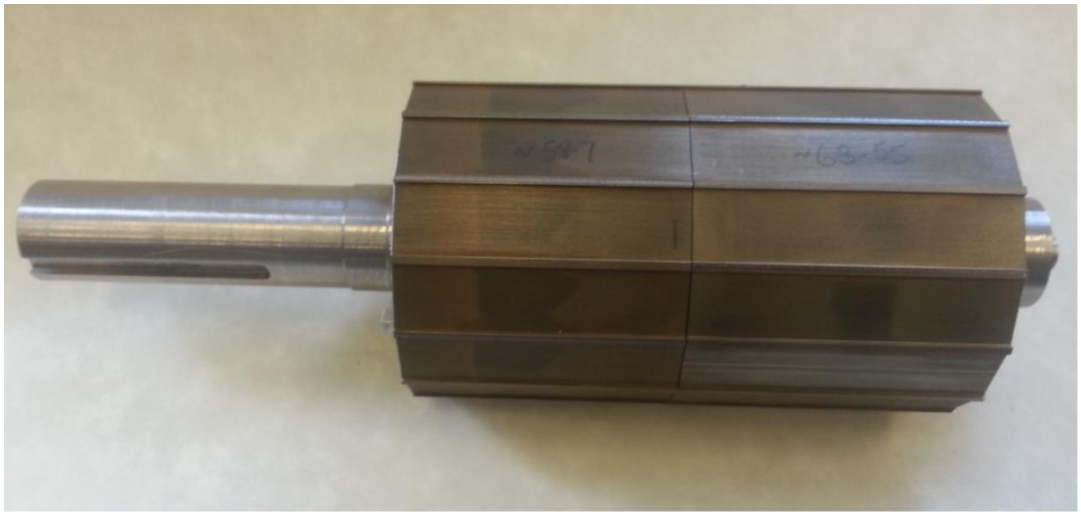

Fig. 5-3. Prototyped rotor without permanent magnets.

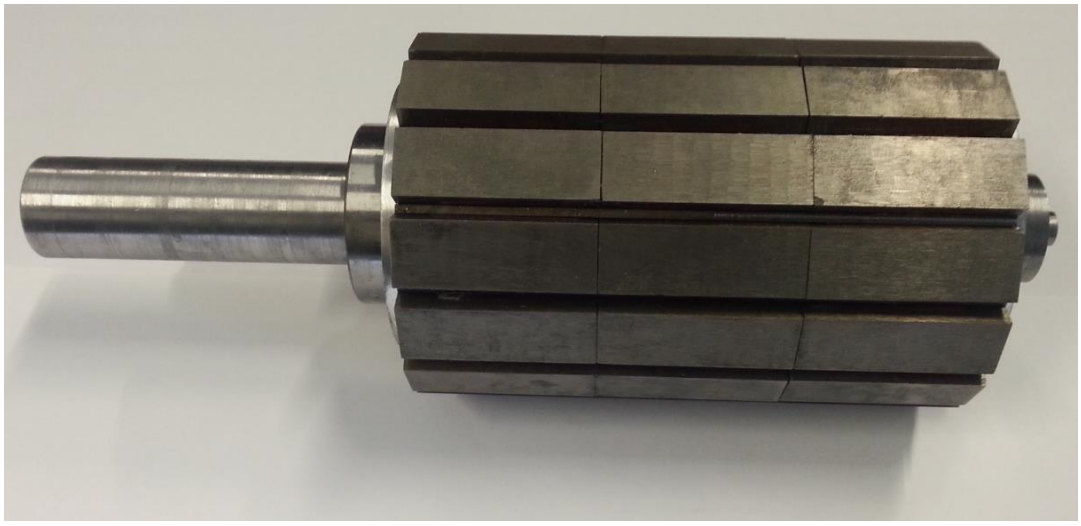

Fig. 5-4. Prototyped rotor with permanent magnets assembled.

The fully assembled SPM machine under locked rotor condition is shown in Fig. 5-5.

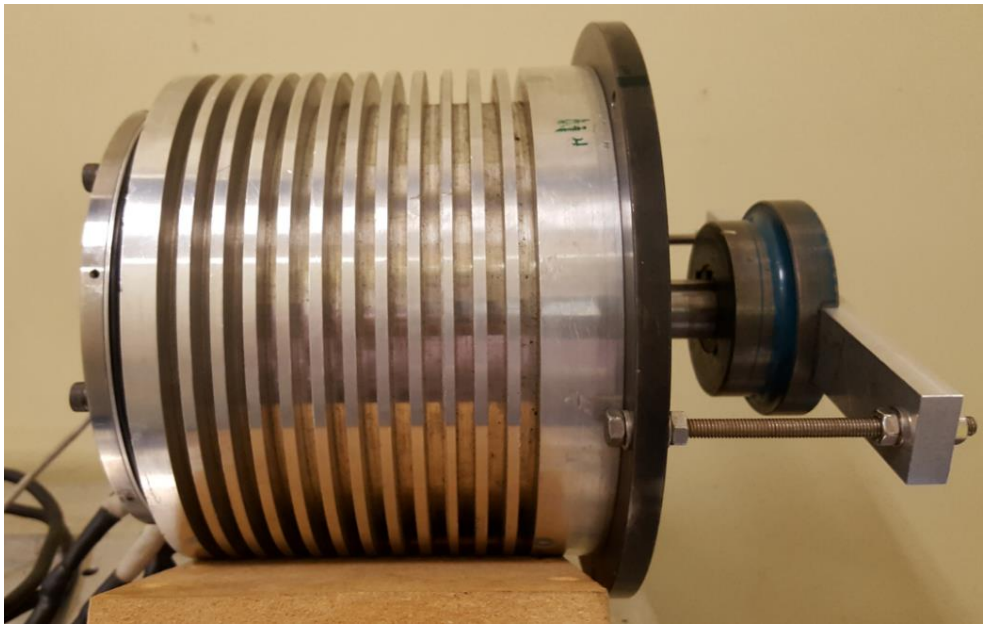

Fig. 5-5. 14-pole, 12-slot SPM machine under locked rotor conditions.

5.3 Test Procedure and Loss Measurements

The schematic of the experimental testing and the measurements is illustrated in Fig. 5-6. Initially the testing was carried at the locked rotor condition with the rotor in which magnets are not assembled.

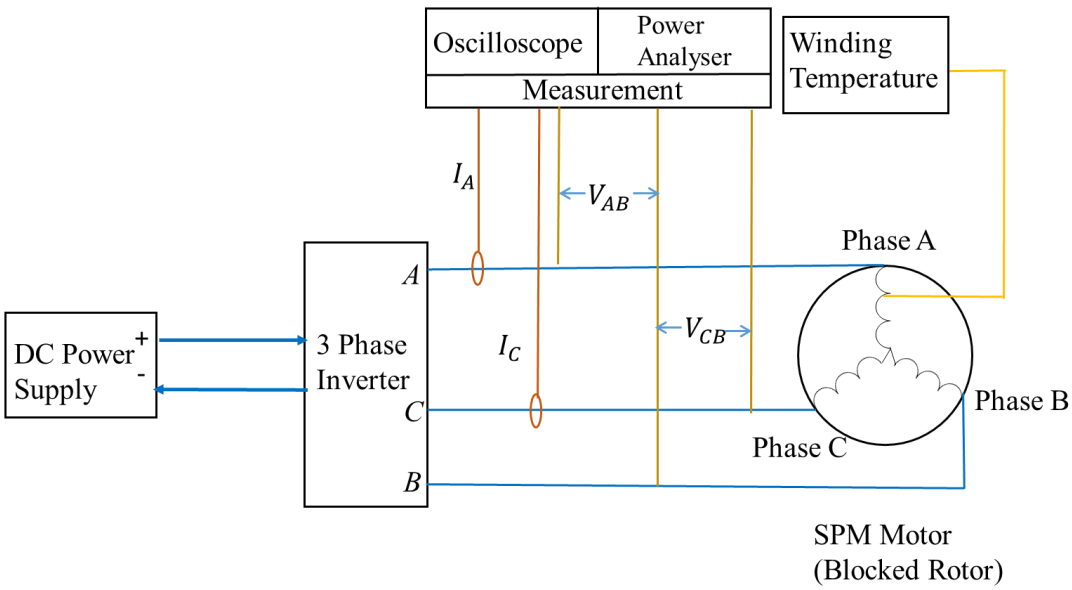

Fig. 5-6. Schematic of the experimental testing and measurement set-up.

The machine windings were supplied with 45A (peak) phase currents at 400Hz. 8kHz switching frequency is implemented for the inverter while generating the 3-phase currents under current feedback control. Measurements were taken at three different angular positions of the rotor each separated by 60^0 (mech.). Theatrically, the magnet loss will be independent of the locked rotor position if the machines are perfectly symmetrical and the air gap is uniform. In reality, these conditions may not be true due to manufacturing tolerance, and hence the measurements at the three positions will yield a more accurate and consistent average.

The experiment was repeated employing the rotor assembled with permanent magnets for the same phase current and the measurements were taken at the same three different rotor positions and also at the same winding temperatures as measured in the previous case without magnets. Winding temperature was maintained same before taking each measurements to make sure the winding copper loss is almost the same throughout the test. For both the tests power input to the machine was measured from the power analyser (YOKAGAVA WT3000) configured in 2 Wattmeter method and phase current waveforms were captured using the oscilloscope (LeCory HDO6054). The test was repeated when the machine windings were supplied with 50A peak phase currents at 400Hz and also with 45A peak phase currents at 450Hz. The whole experimental set-up is shown in Fig. 5-7.

The three different cases with dissimilar phase current and frequency combinations are chosen such that the magnet loss incurred at these conditions are sufficiently large enough for experimental measurements. It is ensured that these three combinations will not result in an excessive temperature rise within the machine at the locked rotor conditions, thus preventing any potential damage. Also the winding temperature rise is kept low as possible thus avoiding rapid variations in the copper loss because of change in electrical resistivity.

The measured power inputs to the machine under locked rotor conditions with and without magnet for the three test cases are listed in Table 5-3 and Table 5-4 respectively. The resultant power input is evaluated as the average of the power input measured at the three different angular positions.

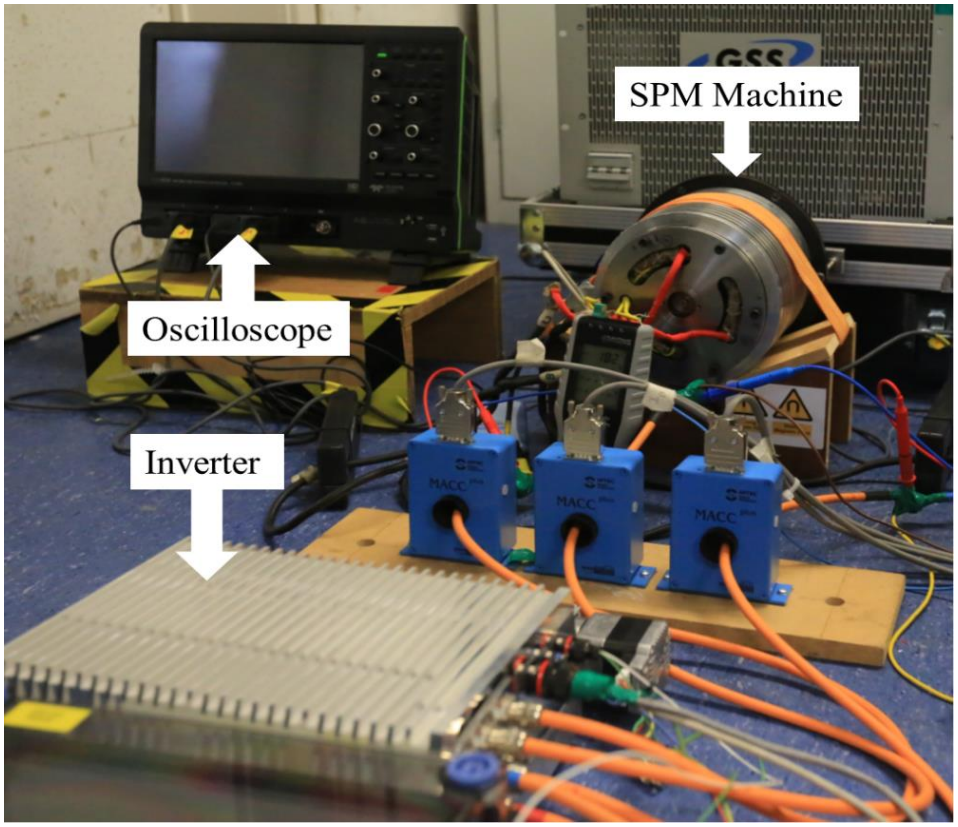

Fig. 5-7. Experimental set-up under for magnet loss measurement.

Table 5-3. Power Input Measured from the Experimental Test without Magnets (P.1, P.2 and P.3 are the Rotor Angular Positions .1,2 and 3).

Case	Frequency	Current (peak)	Temperature			Power			
			P. 1	P.2	P.3	P.1	P.2	P.3	Average
1	400	45	29	30	32	146.17	148.23	147.03	147.14
2	400	50	36	42	33	177.67	175.74	172.38	175.27
3	450	50	39	44	38	198.17	197.37	196.87	197.47

Table 5-4. Power Input Measured from the Experimental Test with Magnets (P.1, P.2 and P.3 are the Rotor Angular Positions.1, 2 and 3).

Case	Frequency	Current (peak)	Temperature			Power			
			P. 1	P.2	P.3	P.1	P.2	P.3	Average
1	400	45	29	34	30	167.24	167.05	167.52	167.27
2	400	50	37	39	38	198.72	199.51	200.87	199.7
3	450	50	34	45	44	227.25	228.42	230.94	228.87

The phase currents captured from the experiments for the three test cases are shown in Fig. 5-8.

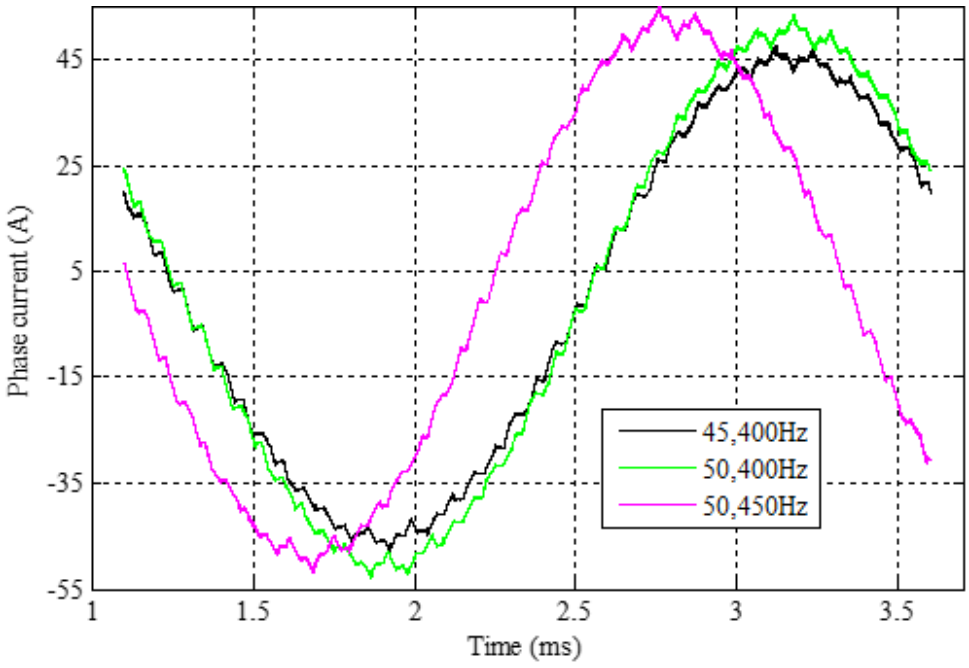

Fig. 5-8. Phase current captured during the experiment for the three test cases with magnets.

It is observed that there is a small difference in the phase currents measured from the two experiments with and without magnets for all the three test cases. The variation in the phase currents captured from the two experiments for the case-2 is shown in Fig. 5-9. Hence a correction towards the copper loss is calculated based on the fundamental value of each phase

currents. This is included in the measured power input for the experiments with magnets. The evaluation of the power input to the machine illustrating this correction is shown in Table 5-5.

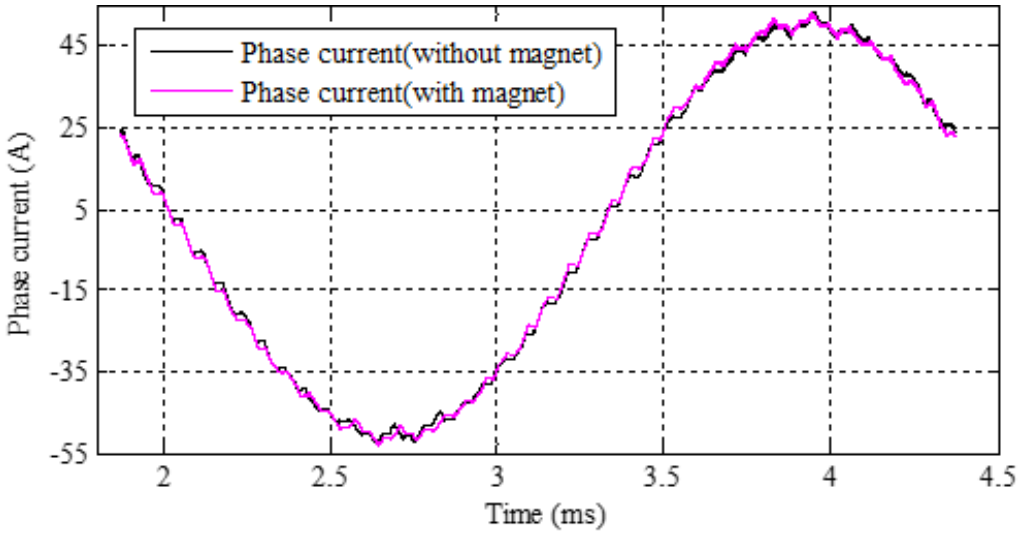

Fig. 5-9. Comparison of phase currents captured from the two experiments for the case.2 (50A,400Hz).

Table 5-5. Correction in Copper Loss for the Minor Variation in the Phase Currents

Test case	Measured power input with magnets (W)	Change in fundamental current with magnets (A)	Correction in Copper loss (W)	Power input with magnets (W) (Corrected)
45A, 400Hz	167.27	0.28	1.03	166.24
50A,400Hz	199.70	0.39	1.67	198.03
50A,450Hz	228.87	0.45	1.81	227.17

For each test without the magnets, the measured input power should be the sum of the iron loss in the stator and rotor cores, and the winding copper loss. For each test with magnets, the measured input power should be the sum of the iron loss in the stator and rotor cores, the winding copper loss and magnet eddy current loss. Since the two tests without and with magnets are performed under the same excitation current and frequency, the iron loss and

copper loss should be almost the same. Therefore, magnet eddy current loss is evaluated from the difference in the power inputs measured from the two tests, with and without magnets after incorporating correction in the copper loss previously described.

Eddy current loss in magnets = W2-W1

where W1 denotes the measured power input without magnets, and W2 denotes the measured power input with magnets after correcting the small difference.

The magnet losses measured for the three test cases performed above are listed in Table 5-6.

Table 5-6.Magnet loss from the power inputs to the SPM with and without magnets for the three different test conditions.

Test case	Power input without magnets (W!)	Power input with magnets (after correction) (W2)	Magnet loss measured (W2-W1)
400Hz, 45A	147.15	166.24	19.09
400Hz, 50A	175.27	198.03	22.77
450Hz, 50A	197.55	227.17	29.61

As it can be seen the magnet loss measured from the experimental case-3 results in the largest magnet loss among all the three cases. This is because both the operating current and frequency are at the largest for this case and hence the eddy current sources (S_x, S_y) can be the largest[137].

5.4 Magnet Loss Prediction from the Proposed - 3D Fourier Method Employing the Experimental Phase Currents

FFT is performed for the one complete cycle to evaluate the harmonic contents present in the measured phase currents for all the three different test conditions. Fig. 5-10 shows the phase current spectrum for the three test cases with magnets. It is observed that the total harmonic distortion (THD) are 3.1, 3.1 and 3.4% respectively for the case 1, 2 and 3 respectively.

(a) 400Hz, 45A

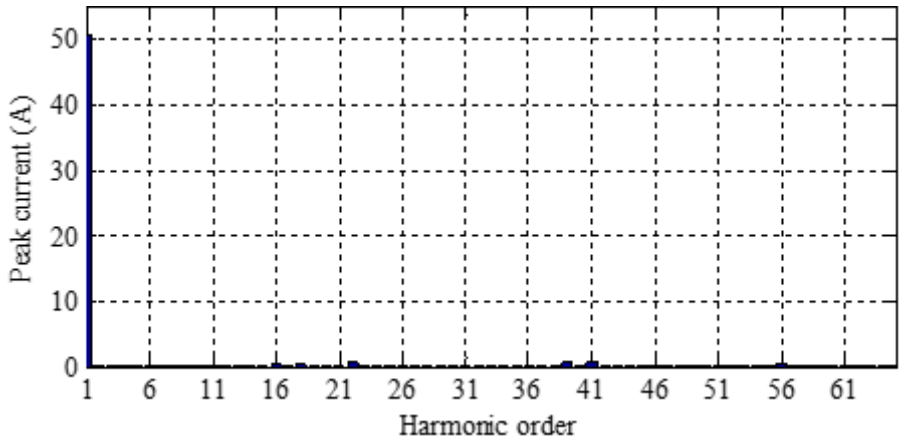

(b) 400Hz, 50A

(c) 450Hz, 50A

Fig. 5-10. Harmonic spectrum of the phase currents captured from the three test cases.

As discussed in Chapter 3 and 4 magnets loss can be predicted for the SPM machine at each test conditions employing the proposed 3D Fourier method using the field information from 2D FEA. Hence before conducting the loss prediction, 2D FEA is performed for every dominant harmonic contents in the respective phase currents. It is worth noting that the phase angle of the higher order harmonics need to be considered with due account to its phase shift with respect to the fundamental while evaluating the flux density information from 2D FEA.

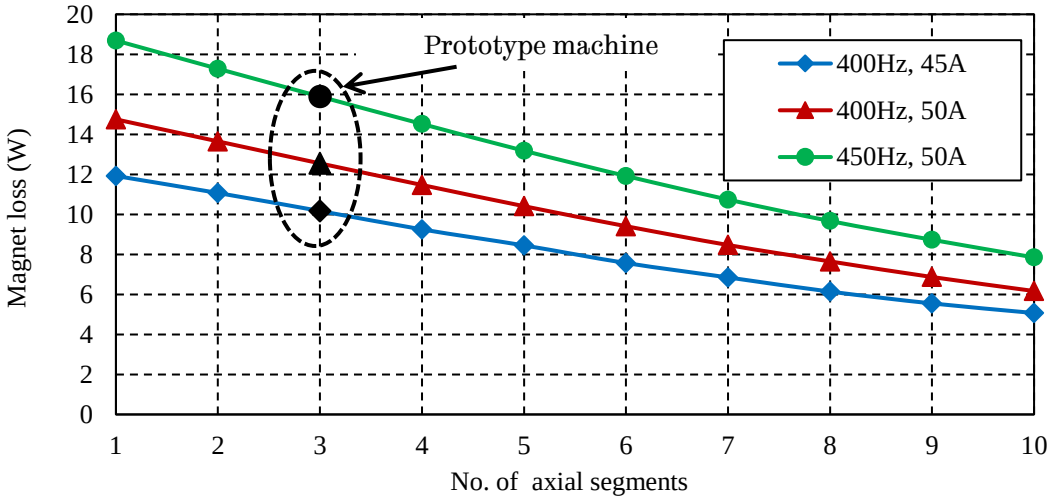

Fig. 5-11. Variation of Fundamental magnet loss with increase in axial segmentations devalued from the 3D Fourier method for the three test cases (The points marked in black indicates the corresponding loss values for the prototype machine).

To implement 3-D loss evaluation in the 3D Fourier method, the flux density values are captured to form a matrix as discussed in Chapter 3 and 4. Hence the magnetic flux density values from the 2D FEA are extracted using mesh grids constructed over the magnets. For the machine under consideration, each magnet attached to the mesh grids discretized into sixty-four divisions along the x– and thirty-two divisions along y– directions. Magnet loss at fundamental frequency is evaluated for the axial segments from 1 to 10 and the results are shown in Fig. 5-11. The points separately marked in black indicate the magnet loss for the prototype machine with 3 axial segments.

It is observed that for all the harmonic contents of frequency above 7200Hz, the eddy current sources are found to have significant variations along the axial plane due to eddy current reaction effect. Hence for evaluating the loss associated with these components axial variations of S_y is incorporated before implementing in the 3D Fourier method as described in the previous chapter. The variation of magnet loss with increase in axial segmentations for the major high frequency harmonics evaluated employing the method proposed in Chapter 4 is shown in Fig. 5-12. The points separately marked in black indicate the magnet loss for the prototype machine with 3 axials segments.

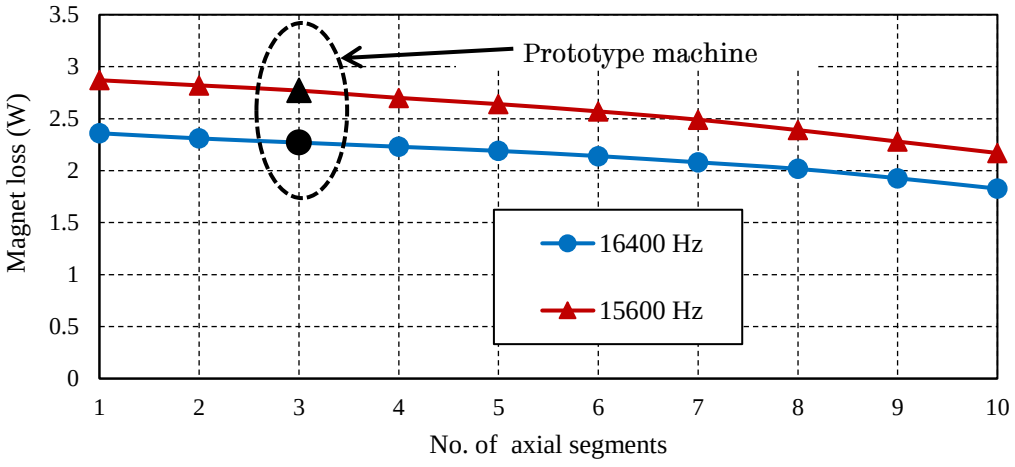

(a) 400Hz (fundamental), 45A.

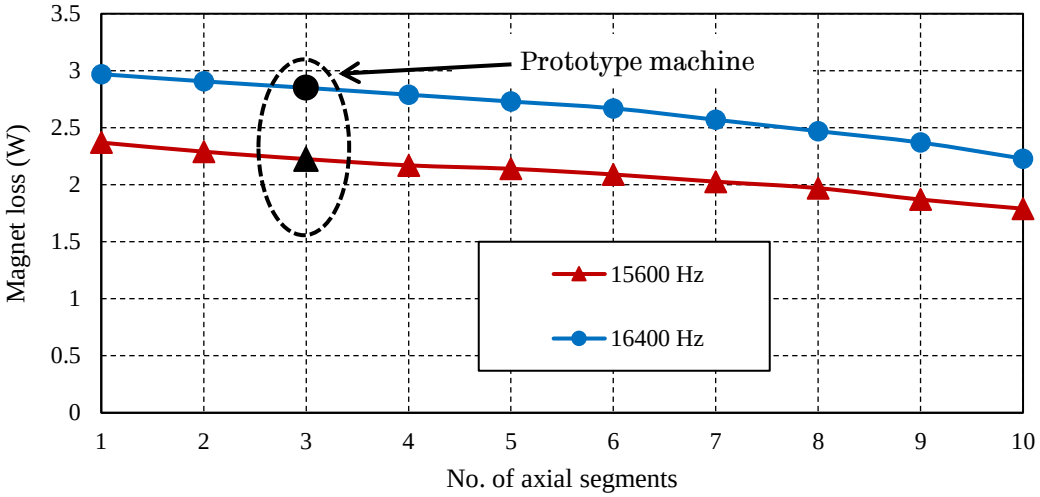

(b) 400Hz (fundamental), 50A.

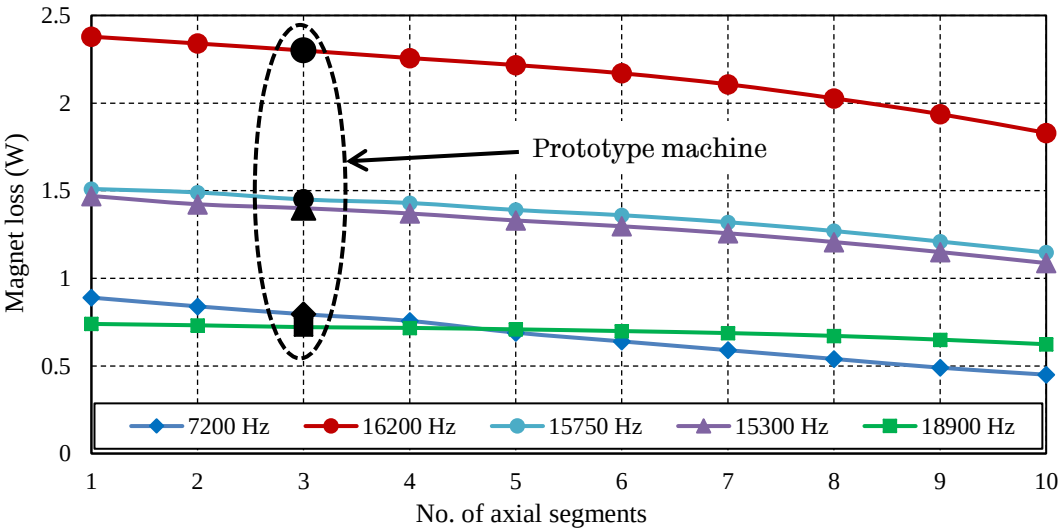

(c) 450Hz (fundamental), 50A.

Fig. 5-12. Loss variation with increase in axial number of segments at high frequencies evaluated accounting the axial variations of eddy current source (The points marked in black indicates the corresponding loss values for the prototype machine).

It is worth noting that the increase in magnet loss with initial increase in axial segmentation is not observed here as for the 8-pole, 18-slot SPM machine [130] in the previous chapter when supplied with high frequency phase current harmonics. This is because the lower circumferential width (L_x =14mm) of the magnet narrows the gap between the eddy current sources along the its middle and the axial edges as described in previous chapter (Fig. 4-10). An increase in axial segmentation again will predominantly increases

only the resistance towards the eddy current flow and thus causing the reduction in magnet eddy current loss. The unsegmented magnet for 8-pole,18-slot SPM machine described in Chapter 4. has a higher circumferential width (L_x = 23.7mm) which makes the axial variation of the eddy current sources more significant, as it is observed from Fig. 4-9 and results in anomaly of segmentation as described in Section 4.5.

The magnet loss is evaluated for the prototype SPM machine at each major harmonic frequency in the phase current for all the test cases employing 3D Fourier method and the results are listed in Table 5-7 and Table 5-8.

As the saturation effect is not significant at the given operating conditions, the total magnet loss under the locked rotor condition can evaluated from the summation of individual harmonic losses.

Table 5-7. Magnet Loss for the Major Harmonic Contents for the Cases 400Hz, 45A and 400Hz, 50A.

Harmonic order	Frequency (Hz)	400Hz ,45A		400Hz, 50A	
		Peak Current (A)	3D Loss (W)	Peak Current (A)	3D Loss (W)
1	400	45.770	10.170	50.470	12.550
16	6400	0.273	0.075	0.330	0.900
18	7200	0.367	0.217	0.450	0.270
19	7600	0.187	0.127	0.220	0.165
22	8800	0.524	0.270	0.640	0.450
24	9600	0.267	0.190	0.280	0.220
36	14000	0.127	0.227	0.184	0.270
39	15600	0.783	2.790	0.720	2.225
41	16400	0.693	2.270	0.820	2.850
56	22400	0.170	0.290	0.340	0.650
62	24800	0.190	0.527	0.220	0.550
64	25600	0.120	0.370	0.125	0.350
Total	-	-	17.523	-	21.450

Table 5-8. Magnet Loss for the Major Harmonic Contents for the Cases 450Hz, 50A.

Harmonic order	Frequency (Hz)	50 A, 450Hz Peak Current (A)	3D Loss (W)
1	450	50.490	15.890
14	6300	0.3422	0.165
16	7200	0.745	0.795
17	7650	0.177	0.063
18	8100	0.188	0.075
19	8550	0.120	0.057
20	9000	0.570	0.527
21	9450	0.417	0.425
22	9900	0.112	0.125
30	13500	0.270	0.527
34	15300	0.572	1.400
35	15750	0.597	1.450
36	16200	0.730	2.300
38	17100	0.350	1.405
42	18900	0.360	0.725
51	22950	0.197	0.620
55	24750	0.147	0.540
70	31500	0.187	0.190
72	32400	0.094	0.175
Total	-	-	27.457

5.5 Magnet Loss Comparison from the Experiments and the 3D Fourier Method

The magnet losses measured from the experiments and predicted by the 3D Fourier method for the three test cases are compared in Table 5-9.

Table 5-9. Comparison of Magnet Loss Measured from the Experiments and Predicted by 3D Fourier method.

Test case	Magnet loss measured (W)	Magnet loss evaluated (W)	Error (%)
400Hz, 45A	19.09	17.52	8.22
400Hz,50A	22.76	21.45	5.76
450Hz, 50A	29.61	27.45	7.28

It is observed that the experimental results agree closely with the results obtained from the proposed 3D method. The difference in measured and predicted losses may be attributed to the end winding effect which is neglected in the proposed prediction method, because of the minor variations in the rotor and stator iron loss and also the saturation levels between the two tests. It is worth nothing the contribution of switching harmonics towards the magnet eddy current loss is significant and is over 40% of the total magnet loss for all the three test cases even though the THD is just over 3%.

Magnet loss is also evaluated from the proposed 3D Fourier method not accounting the axial variation of eddy current sources as explained in the previous chapter. Fig. 5-13 shows the comparison of magnet losses measured from the experiments, evaluated from 2D FE sources not considering eddy current reaction, evaluated from 2D FE sources considering eddy current reaction and the actual 3D loss predicted accounting axial variation of eddy current sources.

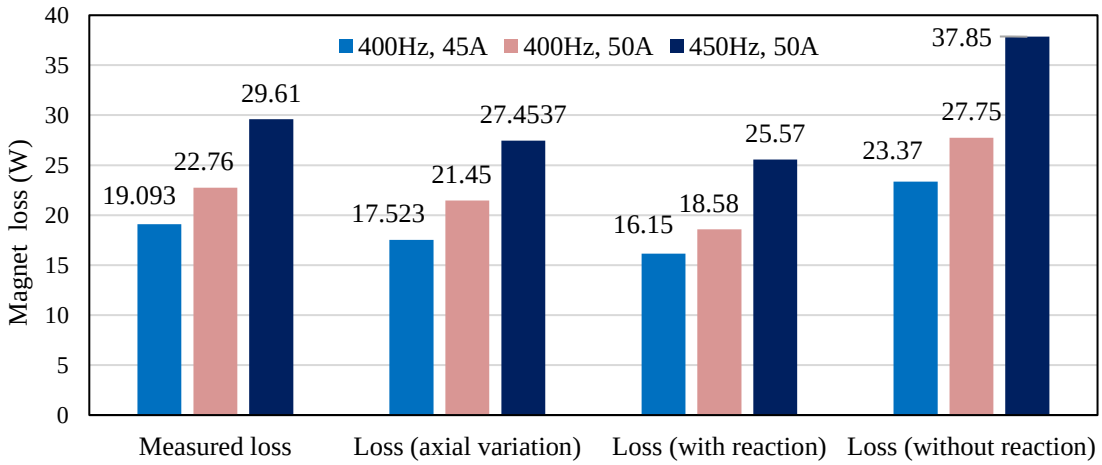

Fig. 5-13. Comparison of magnet loss measured and the loss predicted from proposed 3D Fourier methods.

As described in detail in the previous chapter, it is seen that the losses predicted from 3D Fourier method employing source values from 2D FE not accounting reaction effect for higher frequencies is higher than the measured losses. Also the losses predicted from 3D Fourier method employing source

values from 2D FE accounting reaction effect for higher frequencies over estimates the actual eddy current reaction and hence are lower than the actual measured losses.

5.6 Magnet Loss at the Maximum Speed Conditions of the Machine

As the 3D Fourier method is validated by experiments at the locked rotor conditions, it can be employed to predict the magnet loss at any operating conditions of the SPM machine. Experiments are conducted to validate the performance characteristics of the 14-pole, 12-slot SPM machine [125]. Phase currents are captured and the corresponding torque is measured at various operating conditions of the machine. Likewise, in the magnet loss validation experiments discussed previously, 8kHz switching frequency is employed for the inverter for the performance validation experiments also.

The actual magnet losses in the SPM machine could be significantly higher than those measured from the experiments under the locked rotor conditions as operating currents/frequencies are comparatively larger especially while operating at the peak load conditions. Also the magnet loss varies significantly due to the interaction of forward and backward rotating harmonics under the rotating conditions of the PM machine [107]. Hence losses are need to be predicted at the peak load conditions of the SPM machine which will enable the designer in devising the appropriate axial/circumferential segmentation for reducing it. This otherwise as discussed previously may result in unnecessary temperature increase in the magnets which in the worst case may lead to partial demagnetization [28, 29].

Hence, magnet loss is predicted by employing the phase currents captured when the machine is delivering 7 kW power (15 Nm) at 4500 rpm. This particular operating point is chosen as it corresponds to the maximum cruise speed of the electric vehicle on which the particular SPM machine is mounted [125]. The magnet loss is expected to be much larger at this operating

conditions because of maximum variations in flux density values. The phase current recorded at the above operating conditions of the machine for one full cycle is shown in Fig. 5-14. At this operating conditions the phase current demand to the inverter was 74.5A ($I_q = 35A, I_d = -65.75A$).

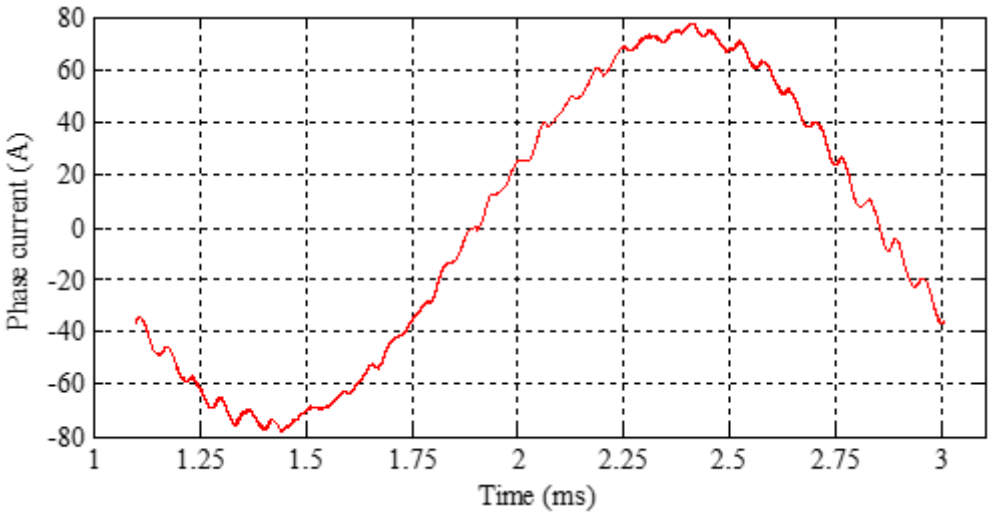

Fig. 5-14. Phase current captured for a cycle when the 14-pole,12-slot SPM machine is operating at maximum cruise speed (4500 rpm) and also while delivering 7kW power.

FFT is performed to evaluate the different harmonic contents in the phase currents obtained at real operating conditions. THD for the phase current is observed as 4.5%.

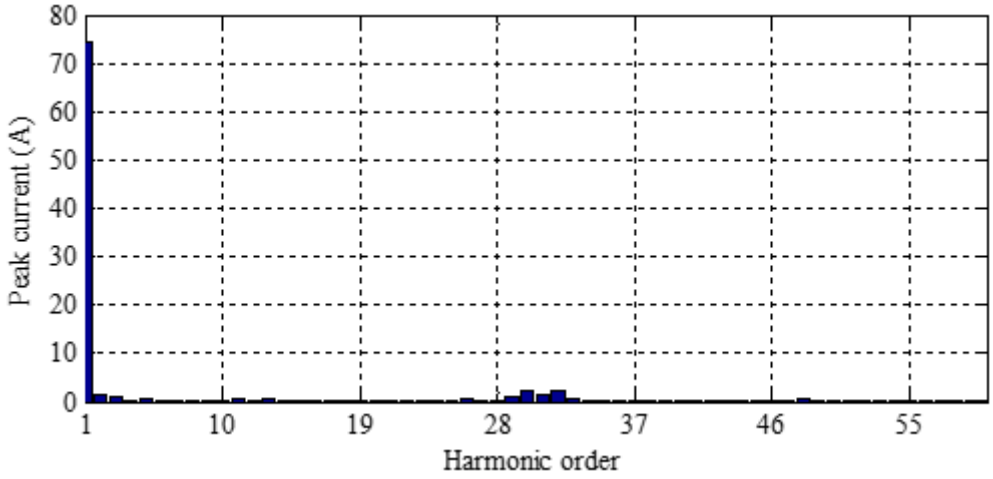

Fig. 5-15. Harmonic spectrum of the phase current captured at the maximum cruise speed.

Fig. 5-15 shows the phase current spectrum for the phase current at maximum cruise speed conditions.

Magnet loss is predicted for each major harmonic frequency content available in the phase current captured. Fig. 5-16 shows the variation of the magnet losses associated with the fundamental component of the phase current with increase in axial number of segments predicted by the 3D Fourier method.

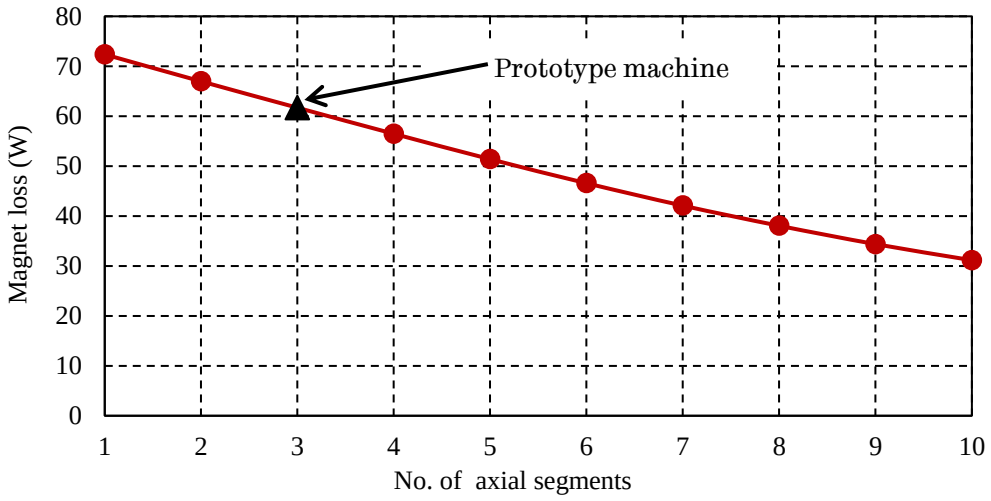

Fig. 5-16. Comparison of 3D magnet loss under maximum speed conditions with increase in axial number of segments (The points marked in black indicates the corresponding loss values for the prototype SPM machine).

The points separately marked in black indicate the magnet loss for the prototype machine with 3 axials segments. As discussed previously for the case with experiments for magnet loss validations the 3D magnet loss in this case also is evaluated employing the axial source variations for all those higher order source harmonics which are affected by eddy current reaction effect.

Predicted magnet losses associated with all the significant harmonics evaluated for the previously mentioned operating conditions is consolidated in the Table 5-10. As the core saturation associated with phase current is not

significant in the SPM machine for the operating conditions considered, the superposition is employed to evaluate the total magnet eddy current loss.

Table 5-10.Magnet Loss for the Major Harmonic Contents for Operation at Max. Speed.

Harmonic order	Frequency (Hz)	Peak Current (A)	3D Loss (W)
1	525	74.29	61.69
2	1050	1.07	0.18
3	1575	0.69	0.15
5	2625	0.42	0.16
11	5775	0.48	0.45
13	6825	0.51	0.62
17	8925	0.57	0.67
26	13650	0.37	0.32
29	15225	0.72	1.57
30	15750	1.67	15.27
31	16275	0.87	3.57
32	16800	1.57	15.79
33	17325	0.49	0.97
43	22575	0.27	1.17
48	25200	0.39	1.37
57	29925	0.19	0.85
60	31500	0.25	1.07
Total	-	-	105.87

It can be see seen that the magnet loss associated with the peak torque conditions is 105.87 W at the maximum cruise speed conditions. Also the table above shows that the loss associated with higher order harmonics is close to 41.37% of the total loss at the operating conditions specified. Hence it is clear that the loss associated with the switching harmonics is significant and cannot be neglected while predicting the total magnet loss at the real operating conditions of the machine. For example, the amplitude of the 16800Hz harmonic is about 2.12% of the fundamental but it incurs 25.59% of the loss associated with the fundamental.

A 3D model of the 14-pole, 12-slot SPM machine is constructed in CEDRAT-FLUX 3D as described in Chapter 3. 3D transient FE analysis is carried out at employing the phase current given in Fig. 5-14 accounting all the major

harmonics together in the phase currents for the SPM machine. Analysis is carried out for 60 angular divisions along 1/6th of an electrical cycle and the results are averaged to predict the 3D eddy current loss within the magnets. It is observed the total magnet loss predicted by 3D FEA at this condition is 101.57W.

The similarity of the results obtained justifies the method of superposition applied to the loss associated with individual harmonics while predicting the total magnet loss. The miss match in the results can be attributed to the saturation of the core material as a result of increased phase currents in the SPM machine. The difference in results can also be the attributed to the lower number of angular divisions considered in 3D FEA for each cycle of higher order harmonics for reducing the enormous increase in the computation time.

5.7 Circumferential Segmentation for the Further Reduction in Magnet Loss

The increased magnet loss at the real operating conditions suggests the designer to further segment the magnets and thus reduce the total eddy current loss. As the contribution of higher order harmonics is significant and also from Fig. 5-12 that a minor increase in the number of axial segments (from 3, which is the existing) will result only in a little reduction in this contribution, axial segmentation is not preferred for the further reduction of magnet loss. This is because a minor increase in axial segmentation cannot result in a major increase in the length of return path and hence resistance towards the eddy current flow. For the high frequency harmonics causing eddy current reaction effect, a minor reduction in magnet segment width along the circumferential direction results in large reduction in eddy current reaction effect causing more or less uniform distribution of eddy current source components along its axial direction (as seen in Chapter 4 for the 8-pole, 18-slot SPM machine). However, the reduction in segment width can also result in a rapid increase in the length of return path for the eddy currents via

the circumferential ends causing a large increase in the resistance towards its flow. Hence the circumferential segmentation makes the eddy current flow more 3-dimensional causing a faster reduction in magnet loss [90, 130]. The faster increase in return path for the eddy currents with increase in circumferential segmentation can be attributed to the larger axial length of the magnet segments in the prototyped 14-pole,12-slot SPM machine.

Now, it can be observed from Fig. 5-17 that the MMF space harmonics of the order 1, 5, 7, 11, 13, 17, 19, 23, 29, 31… etc. exists in the 14-pole, 12-slot SPM.

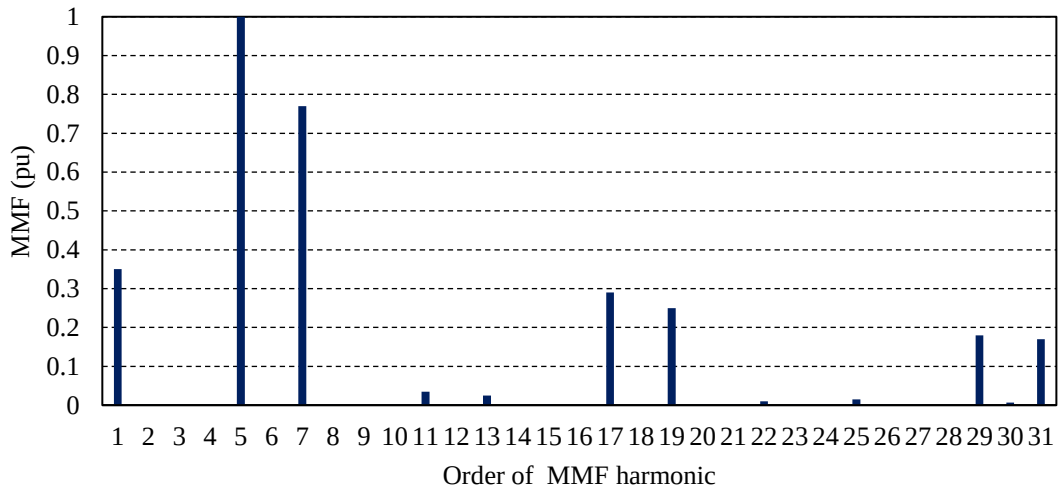

Fig. 5-17. Normalized MMF space harmonic distribution for the 8-pole,18-slot SPM machine.

Loss analysis employing subdomain model in 3D Fourier method predicts 6, 12, 24, 36… order harmonics in the rotor resulting in magnet eddy current loss as shown in Fig. 5-18. Hence for the loss associated with the fundamental phase current, as explained in Chapter 3 a minor increase in number of circumferential segmentation makes the wavelength ($\lambda_h = 20.04$mm) of the dominant 12th harmonic [124] within the magnet go much higher than the segment width (unsegmented width L_x =14.0mm). Consequently a larger reduction in the magnet loss [122] can be expected. Thus circumferential segmentation is preferred for further reduction in magnet loss.

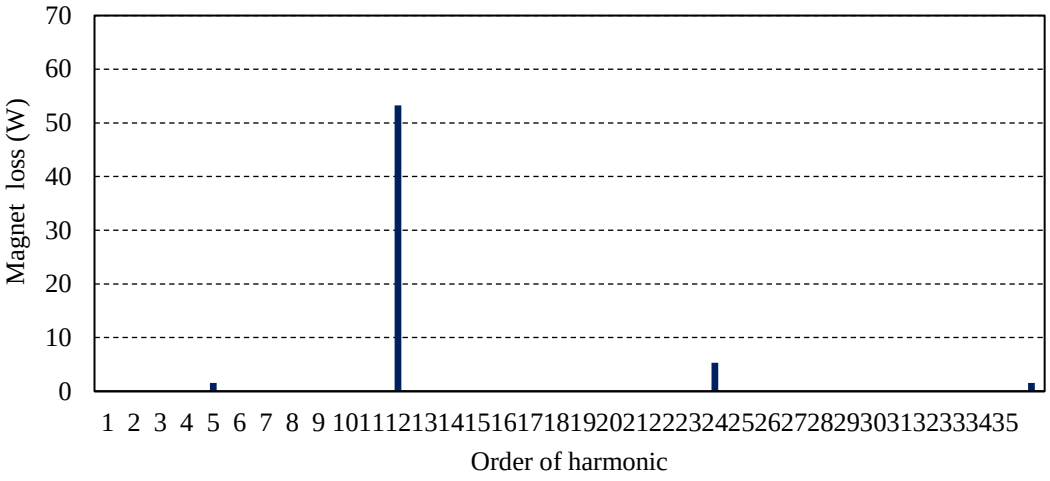

Fig. 5-18. Magnet loss associated with major fundamental MMF space harmonics in the 8-pole,18-slot SPM machine at maximum cruise speed.

Hence, for example an increase in the magnet segments to four along the circumferential direction and keeping the same 3 axial segments as before has resulted in the reduction of total magnet loss to 20.59W at the maximum cruise speed conditions of the PM machine. Also it is observed that the magnet loss associated with the fundamental and higher order harmonics are 10.17W and 10.42W respectively.

As discussed previously, the result proves the method of circumferential segmentation has significantly reduced the total magnet loss associated with both the fundamental and higher order harmonics.

5.8 Conclusion

The proposed 3D Fourier method is experimentally validated on 14-pole, 12-slot SPM machine. It is observed that the contribution of the switching harmonics in the phase currents can become significant and can be even close to 50% of total eddy current loss at maximum speed conditions of PM machine. The accuracy of the results proves the superposition method can be employed to predict the total magnet loss associated with all the phase current harmonics in SPM machines. The method of circumferential segmentation is

preferred for the reduction of the total magnet loss when the loss associated with higher order harmonics are significant.

CHAPTER 6
3D Computationally Efficient Magnet Eddy Current Loss Prediction in IPM Machines

6.1 Introduction

In the previous chapters so far, the methods to predict 3D magnet loss in SPM machines, accounting both low and high frequency armature harmonics is discussed. However, high power density IPM machines are also increasingly being used in a variety of applications, including high speed manufacturing [1], power generation [138], hybrid and electric tractions [11, 139-141], aerospace [142] and ship propulsion [143]. These PM machines can be operated over a broad range of speeds when compared to SPM machines by employing flux weakening control [144-146].

As discussed with SPM machines previously, at higher speeds in IPM machines with concentrated windings, also produce increased electromagnetic field variations which are associated with space harmonics from stator winding distribution in addition to slotting and also time harmonics from the armature currents [25, 134, 147, 148]. While the pole shoes may prevent these harmonics from penetrating in to the magnets in IPM machines, the presence of flux barriers and the saturations of the silicon steel laminations will allow them eventually entering the magnets and cause eddy current loss.

The highly nonlinear nature of the rotor core and the complicated boundary conditions makes a complete analytical estimation of the magnet loss almost impossible in IPM machines. However a few analytical insight can be derived on the magnet loss based on which the design parameters can be altered for reducing them [149, 150]. The much simplified theoretical estimation of magnet loss proposed to evaluate the eddy currents associated with carrier harmonics in IPM machines approximates an uniform source field along the magnets [90, 131]. Also another simplified analytical estimation

of permanent magnet loss proposed in [96, 97, 151], ignores the saturation effects of silicon steel laminations and neglects any field variation along its radial direction. This approximation deviates from the real flux density distribution in magnets significantly and results in poor accuracy in loss estimation. Hence numerical analysis [42, 147] becomes indispensable in accurately estimating the loss in the permanent magnets for such machines.

There are a few reduced order 2D-3D numerical methods proposed to overcome the computational burden involved in direct 3D finite element calculations [39, 103, 104]. The method described in [104] evaluates the magnet loss at each frequency of interest in 3D FEA by employing differential permeability derived from 2D FEA calculations. Whereas the method proposed by T . Okitsu *et al.* [103] models only the permanent magnet in 3D FEA and inputs the magneto-static field obtained from 2D FEA for loss evaluation. Magnet loss evaluation at each frequency of concern separately considering average differential permeability, may also fail to consider the effective magnetic saturation of the silicon steel laminations arising out of all the armature harmonics in the machine.

To elude the computational burden of 3D FEA completely in PM loss evaluation, the method proposed by Z. Peng *et al.* in [102] predicts the resistance-limited eddy current loss analytically from the magnetic field derived from few magneto-static computations. This method approximates the 3D end effects of eddy currents by considering rectangular loops of varying perimeter along the axial plane, and hence predicts the eddy current distribution within the magnets at reduced accuracy. Moreover, it fails to assess the contribution of magnet loss associated with the tangential component of the magnetic field

The 3D Fourier method proposed in Chapter 3. can be extended to evaluate the resistance limited eddy current distribution which satisfies its natural boundary condition for the magnets in IPM machines. As the analytical

solution for the eddy current diffusion is difficult to be derived for IPM machine based on the supply current distribution along the stator bore as explained in Chapter 4, the solution to magnet loss accounting high frequency harmonics in the armature current is derived in an alternate way in this chapter. Also the combined loss evaluation associated with fundamental and the carrier frequency harmonics in the armature currents is evaluated by employing the frozen permeability concept to account for the stator and rotor iron core saturation. The proposed method is validated on the 8-pole, 18-slot IPM machine by predicting the eddy current loss in magnets at low and high frequencies with increase in axial and tangential segmentations and comparing the results obtained with 3D FEA.

The main contents of this chapter is published by the author in [J4], as detailed in Section 1.8.

Implementation of 3D Fourier Method for IPM Machines

6.1.1 Machine Topology and Design Parameters

Without loss of generality, the 3D Fourier method is implemented on the 8-pole, 18-slot IPM machine [152] employing V-shaped NdFeB magnets. The machine topology benefits from low-space harmonics [115] and, hence, low eddy current loss, improved reluctance torque and less demagnetization risk. The machine is designed for EV traction applications and has been optimized for maximum energy efficiency over the combined drive cycles of the Artemis Urban Driving Cycle (Artemis) and the New European Driving cycle (NEDC) while satisfying the machine torque, speed specifications as well as volumetric, electrical, thermal and mechanical design limits [125, 153, 154]. The cross section of the IPM machine illustrating its winding pattern is shown in Fig. 6-1. For the analysis, the rotor position is defined as 0° when the centre of Magnet –1 and Magnet–2 is aligned horizontally, as shown in Fig. 6-1.

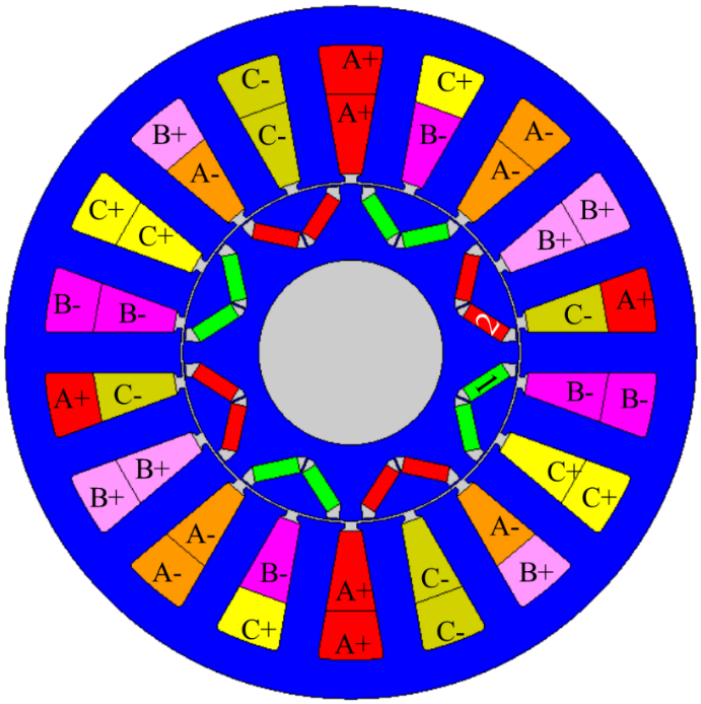

Fig. 6-1. Cross sectional schematic of 8-pole,18-slot IPM machine.

The key specifications and geometric parameters of the machine are listed in Table 6-1.

Table 6-1. 8-pole, 18-slot IPM Specifications and Key Dimensions

Parameter	Unit	Value
Base speed	rpm	1350
Maximum Speed	rpm	4500
Peak torque below and at base speed	Nm	70
Continuous torque below and at base speed	Nm	35.5
Maximum Current Limit	A	170
Nominal DC link voltage	V	120
Stator outside diameter	mm	150
Stator bore diameter	mm	73.9
Rotor outside diameter	mm	72.9
Magnet width	mm	3.5
Magnet length	mm	10
Stack length	mm	118
Slot opening	mm	2.5
Shaft diameter	mm	40
No. of turns per coil	-	6
Magnet Resistivity	Ω.m	$1.8\text{x}10^{-6}$

6.1.2 Implementation of 2D FEA Results in 3D Fourier Method for IPM Machines

As discussed in Chapter 4, to implement loss evaluation in the proposed method, the flux density values need to be captured from 2D FE and has to be in the form a matrix. Unlike the case with SPM machines as discussed in Chapter 4. where the magnet field orientations are referred w.r.t the global r–θ co-ordinate system, the orientation of field associated with each magnet is different for the case with IPM machines. Hence the values in each matrix should correspond to the source at a location given by the local x-y coordinates attached separately to every magnet. Thus the magnetic flux density values from the 2D FEA are extracted using a mesh grid constructed over the magnets as shown in Fig. 6-2.

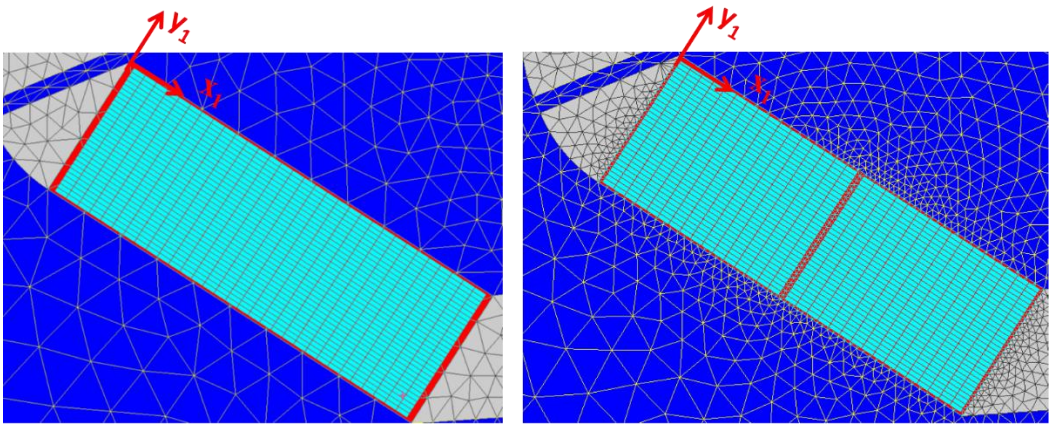

(a) Tangential segments=1 (b) Tangential segments =2.

Fig. 6-2. Mesh grids constructed over the magnets and are attached to separate coordinate system at $\omega t = 0$ position.

Considering the machine symmetry, only one half of the machine needs to be modelled in loss evaluation and hence mesh grids are constructed only over the eight magnets. As explained before in Chapter 4, every point of intersection on this mesh forms the x– and y– coordinates of the field information.

For the machine under consideration without any segmentation in the x–direction, each magnet as shown in Fig. 6-2 (a) is discretized into thirty-two divisions along the x and y– directions. The number of divisions within a magnet segment may be modified according to the number of tangential (in the x– direction) segmentations. For example, the mesh is modified as shown in Fig. 6-2 (b) with sixteen divisions along the x –directions in the analysis for the case with two tangential segmentations.

However, since the flux density values (B_{x_1}, B_{y_1}) captured are referred in the stationary (x_1, y_1) coordinates attached to the magnets at the initial rotor position, the values needed to be transformed to the co-ordinate system which rotates with the magnets as shown in Fig. 6-3.

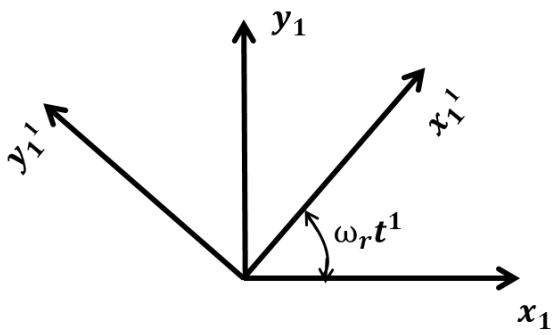

Fig. 6-3. Rotor coordinate system (x_{r1}, y_{r1}) displaced at an angle $\omega_r t$ w.r.t the stationary system(x_1, y_1).

This ensures the eddy current sources ($S_{x_1} = \partial B_{x_1}/\partial t\,, S_{y_1} = \partial B_{y_1}/\partial t$) seen by the magnets are referred in the rotor coordinate system. Hence the flux density values $(B_{x_{r1}}\,, B_{y_{r1}})$ at an angular position $\omega_r t$ with respect to the rotating co-ordinate system (x_{r1}, y_{r1}) attached to the magnets at time t can be calculated as,

$$B_{x_{r1}} = B_{x_1}\cos(\omega_r t) - B_{y_1}\sin(\omega_r t) \tag{6-1}$$

$$B_{y_{r1}} = B_{x_1}\sin(\omega_r t) + B_{y_1}\cos(\omega_r t) \tag{6-2}$$

As in explained in Chapter 3 and 4. the eddy current sources ($S_x = \partial B_x/\partial t\,, S_y = \partial B_y/\partial t$) are evaluated from flux density values obtained from two consecutive time intervals. Also the source values are discretized together with their images [121] in three dimensions in each magnet bounded by $(2L_x, 2L_y, 2L_z)$. For the machine under consideration 32 divisions are considered for the unsegmented magnet length (L_z) along the axial direction. 3D FFT is performed to evaluate the source coefficients and hence the eddy current density coefficients. The eddy current loss in every magnet is calculated at each time step and the analysis are repeated for 1/6th electrical cycle to predict the average loss [155].

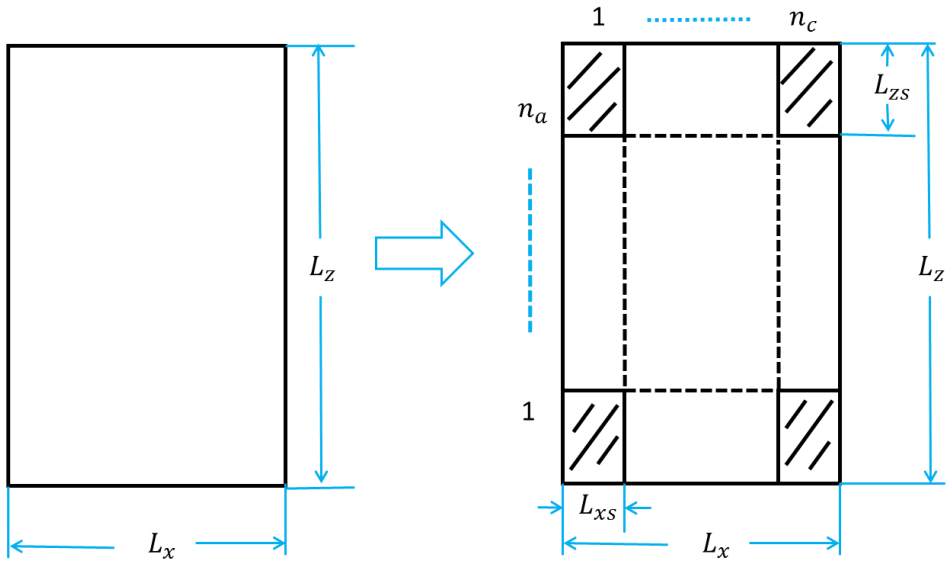

Fig. 6-4. Segmentation of the magnet in axial and tangential direction.

The method of implementation with axial and tangential segmentations can be followed as explained for SPM machines in Chapter.3. For example, for the IPM machine having n_c tangential segments and n_a axial segments in a magnet as shown in Fig. 6-4 , eddy current loss is evaluated for each tangential segment separately employing its dimensions (L_{xs}, L_y, L_{zs}). The total loss per magnet is evaluated as the sum of the loss from the n_c tangential segments multiplied with the number of axial segmentation n_a.

This way of evaluation quantifies the loss in each magnet segment of the IPM machine, which will enable the designer to optimize the number of magnet segments, and hence to control the loss distribution among them.

6.2 3D Finite Element Validation

A 3D FE model of the machine as shown in Fig. 6-5 has been built to predict the 3D eddy current distribution and resultant eddy current loss induced in the magnets.

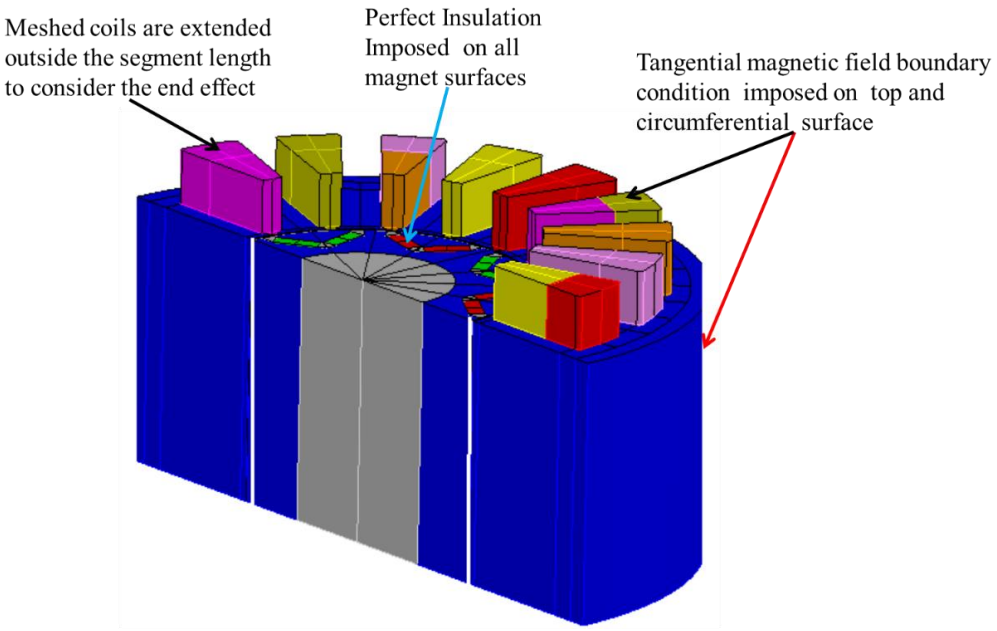

Fig. 6-5. 3D-FE model of 8-pole, 18-slot IPM based on symmetry.

Since the machine employs fractional slot per pole topology, circumferential symmetry exits only over 180 mechanical degrees. Thus, a quarter of the machine has to be modelled in 3D FEAs. Tangential magnetic field boundary condition is imposed on the circumferential surface. The meshed coils are extended in axial directions to consider the end effect. Tangential boundary conditions are imposed on this extended surface. In addition, perfect insulation boundaries are applied to the end surfaces of the magnets. As explained previously in Chapter 3. the meshing along magnet is increased to fine level, especially along the z–direction for the best accuracy in the 3D magnet loss prediction.

Magnet loss are evaluated at the maximum speed of the machine ($N = 4500\ rpm$), when the armature current is 61.17 (RMS), having a flux weakening angle $\gamma = 73.27^0$. Under such operating conditions the effect of eddy current reaction is negligible and hence the magnet loss is considered resistance limited. This is verified from the magnet loss obtained from the 3D Fourier method employing the source values from 2D FE with and without eddy current reactions. The loss evaluation is conducted employing both 3D

Fourier method and 3D FEA with increase in axial segmentations at one and two tangential segments.

The predicted loss variations by 3D Fourier method and 3D FE with number of axial segments with no further tangential segments at the load conditions mentioned before are compared in Fig. 6-6.

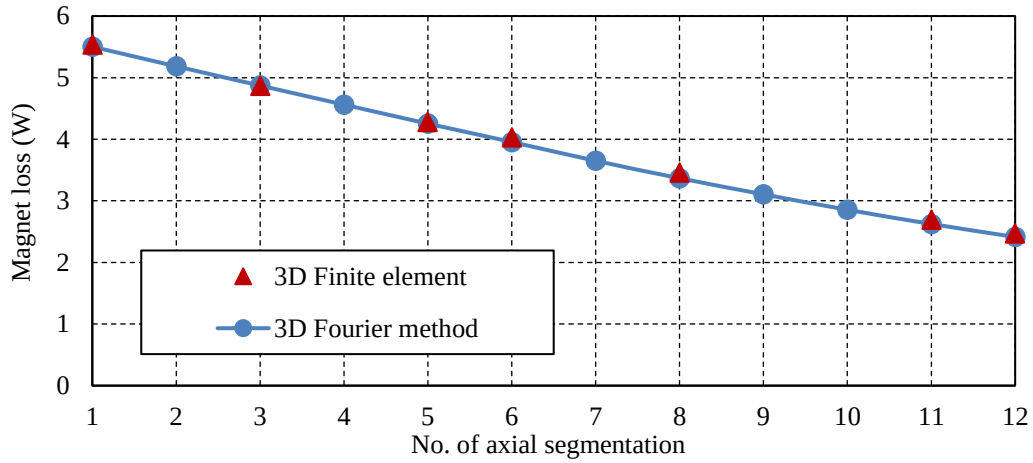

Fig. 6-6. Comparison of eddy current loss variations with axial number of segments (tangential segments = 1).

Fig. 6-7 compares the predicted loss variations by 3D Fourier method and 3D FE with number of axial segments when the number of tangential segments are increased to 2.

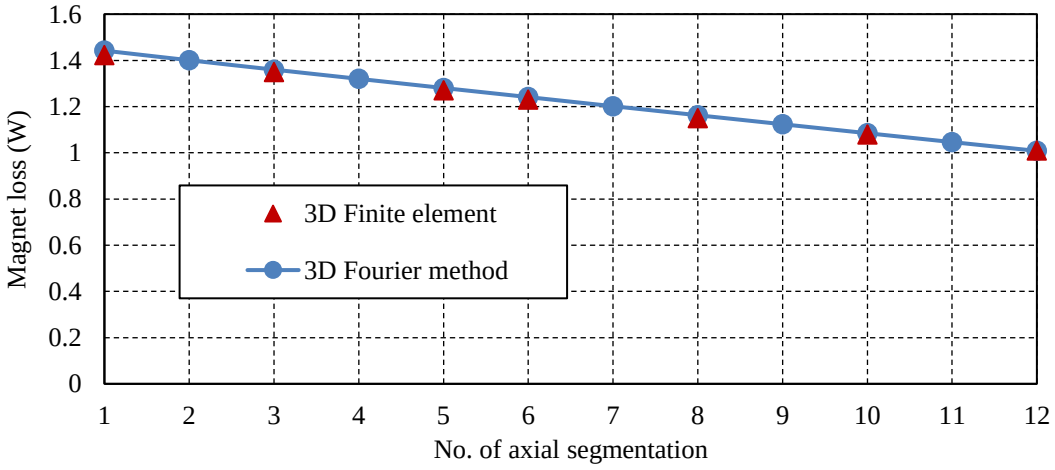

Fig. 6-7. Comparison of eddy current loss variations with axial number of segments (tangential segments = 2).

It can be observed that the magnet loss evaluated from the 3D Fourier method matches very well with the 3D FEA results with increase in the number of axial segmentations.

The instantaneous variations of the total magnet loss with rotor position predicted by the 3D Fourier method and by 3D FEA for the case with eight axial segments and no tangential segmentation are compared in Fig. 6-8.

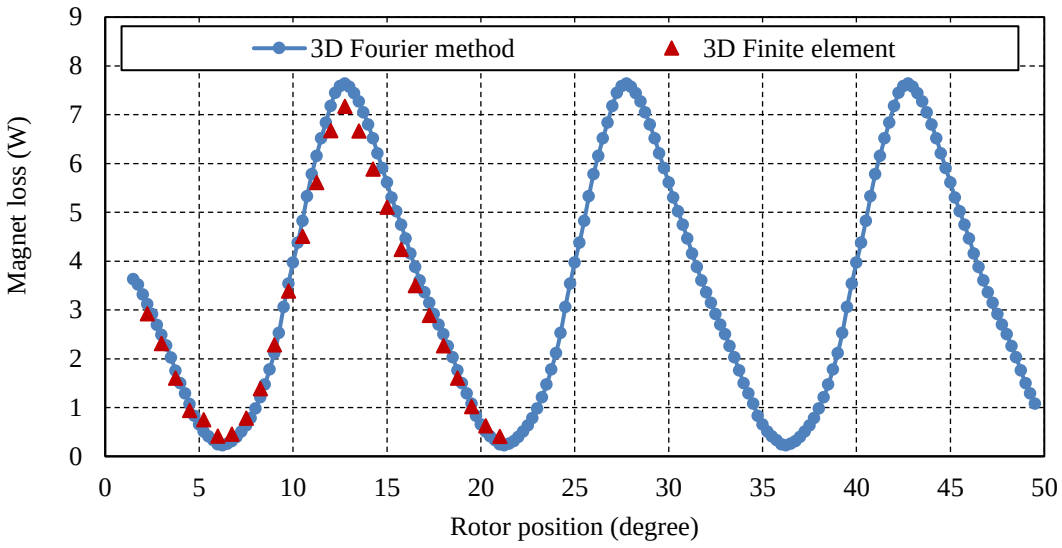

Fig. 6-8. Comparison of instantaneous loss variation from 3D Fourier method and 3D FEA.

It is clear from the figure that that the loss predicted by the 3D Fourier method follows very well with the 3D FEA results. The slight difference from the 3D FE simulation with the proposed method may be attributed to the winding end effect which is neglected in the 3D Fourier method.

The $z-$ component of eddy current density evaluated from the 3D Fourier method is compared with that obtained from 3D FEA along the outer surface of Magnet–1 defined by $y = L_y$ (3mm) for the case with eight axial segments and no tangential segmentation in Fig. 6-9 at $\omega_r t = 12^0$. Fig. 6-10 compare the $x-$component of the eddy current density evaluated from the 3D Fourier method with that obtained from 3D FEA under the same conditions. Fig. 6-11 compares the variation of $z-$ and $x-$ components of the current density along

the $x-$ position predicted from the 3D Fourier method and 3D FEA at $z = 0.85L_z$ under previously stated operating conditions.

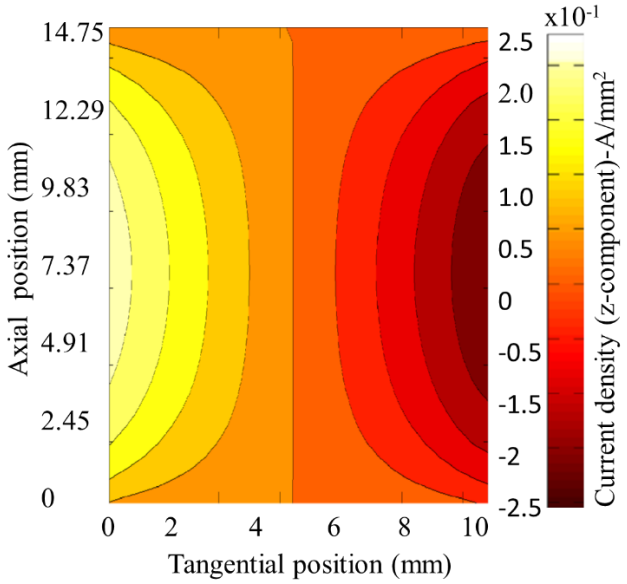

(a) $z-$component of eddy current distribution predicted from 3D Fourier method.

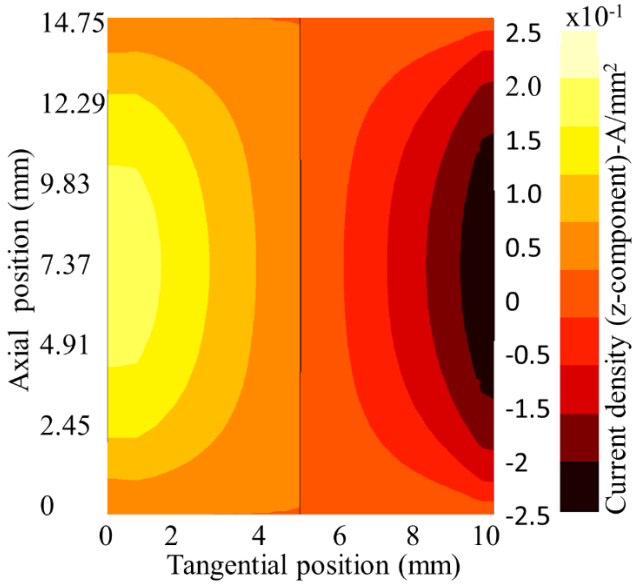

(b) $z-$component of eddy current distribution predicted from 3D FEA.

Fig. 6-9. Comparison of $z-$component eddy current distribution obtained from 3D Fourier method and 3D FEA on the outer surface of Magnet -1 at $\omega_r t = 12^0$.

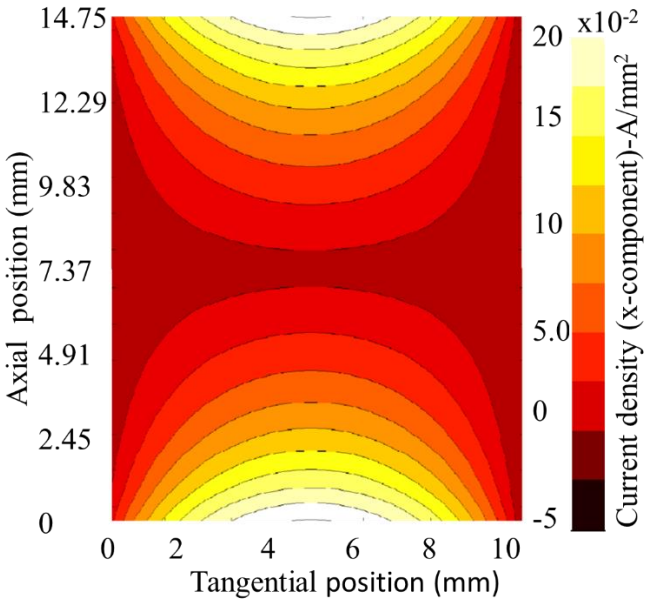

(a) x −component of eddy current distribution predicted from 3D Fourier method.

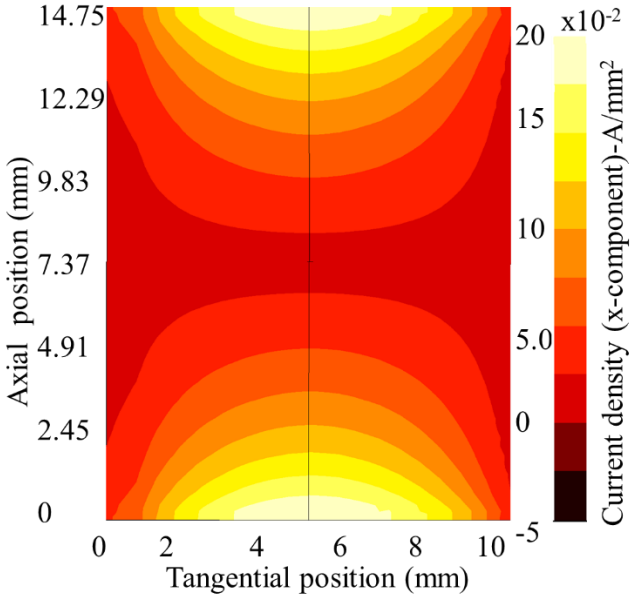

(b) x −component of eddy current distribution predicted from 3D FEA.

Fig. 6-10. Comparison of x-component eddy current distribution obtained from 3D Fourier method and 3D FEA on the outer surface of Magnet -1 at $\omega_r t = 12^0$.

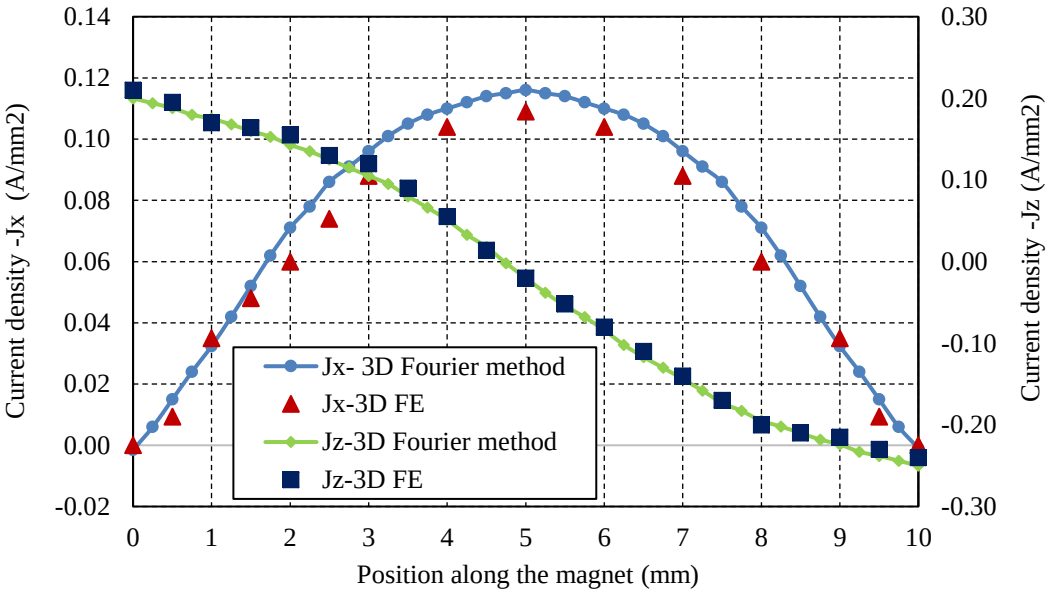

Fig. 6-11. Variations of x– and z–components of eddy current density predicted from 3D FEA and 3D Fourier method along x position at $\omega_r t = 12^0, y = 0{,}5\ L_y$ and $z = 0.85\ L_z$.

It can be observed that the eddy current density distribution evaluated from the 3D Fourier method matches with the 3D FEA results. This ensures the accuracy of the proposed method.

6.3 Computational Efficiency of the Proposed Method

Since the calculations are performed in 3-dimensional space for each harmonic, matrix operations are used to facilitate efficient calculations as employed for SPM machines. The entire process is implemented in Matlab, and it takes around 60 minutes to generate the flux density harmonics from 2D FEA and less than 30 seconds to compute the total 3D eddy current loss for all the magnets in a typical 3.3 GHz, 64GB PC. Hence on an average for evaluating the loss variation with increase in axial number of segmentation up to 12, it takes around 5 minutes for each case.

As a comparison, in order to perform 3D time-stepped FEs, apart from the geometry and physical model construction and meshing process, the computation time on the same PC is more than 7 days for one 3D FE analysis with no axial segmentation and about a day for the case with 10 axial

segmentations. The increased 3D FE computation time associated with IPM machines is because of its highly non-linear nature of the core laminations at the given operating conditions.

6.4 Magnet Loss at High Frequency Accounting Eddy Current Reaction Effect

To predict the magnet loss due to high frequency harmonics in the armature current where the effect of eddy current reaction becomes significant, 2D FEA results which account the reaction effect is employed in the proposed method. However, it is observed from the Chapter 4. that the field variations employed in the 3D Fourier method from 2D FEA overestimates the eddy current reaction effect when the axial length of a magnet segment is relatively larger and hence the magnet loss evaluated will be lower than the actual.

This is because the reaction field obtained from the 2D FEA does not account the axial variation of eddy current sources due to reaction field as explained with SPM machines in Chapter 4. Also it is observed that the skin effect forces the eddy current to be concentrated around the magnet axial end surfaces and its values are reduced at the center of the magnet.

The method applied for the SPM machines in predicting the axial source variations from the solution to the diffusion equation involving the high frequency armature current is nearly impossible in IPM machines because of its inherent nonlinearities. However, a solution to the diffusion of the flux density/eddy current sources along the axial $(x-z),(y-z)$ planes are essential for accurate prediction of magnet eddy current loss.

The diffusion of the 'y' component of flux density $B_y(x,y_1)$ at a given 'y_1' along the '$x-z$' plane can be expressed as,

$$\frac{\partial^2 B_y(x,y_1,z)}{\partial x^2}+\frac{\partial^2 B_y(x,y_1,z)}{\partial z^2}=j\omega\mu\sigma B_y(x,y_1,z) \tag{6-3}$$

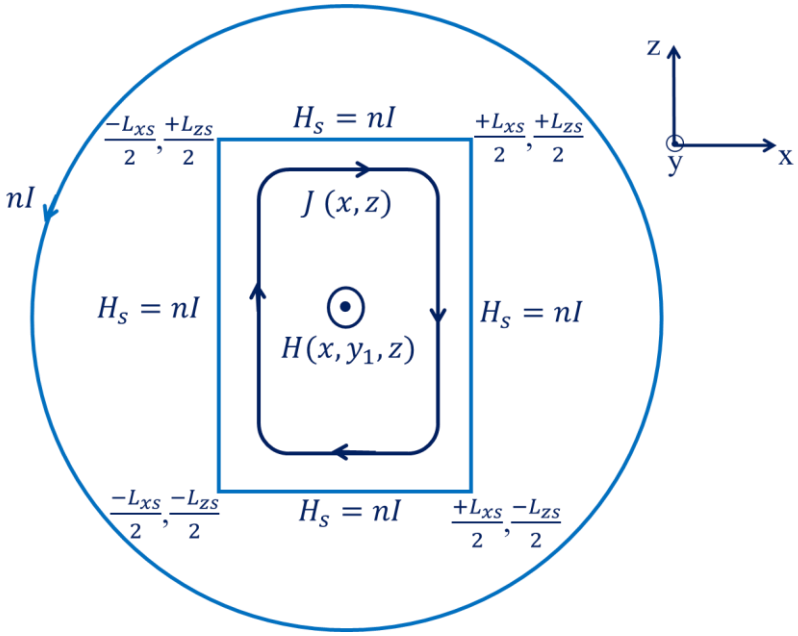

Fig. 6-12. Magnet in the infinite –length exiting coil.

Fig. 6-12 shows a rectangular magnet in an infinite length exiting coil, illustrating the problem when the field variation along the y–axis is neglected.

Solution to (6-3) can be obtained as the magnet being exposed in a uniform source field of H_s and hence the field along its edges will be equal to the applied field. Since $B_s = \mu H_s$, the variation of flux density $B_y(x, z, y_1)$ for any segmentation can be evaluated as in [90],

$$B_y(x,z,y_1) = \frac{\cosh(\gamma x)}{\cosh\left(\gamma \frac{L_{xs}}{2}\right)} B_{y_1}(x,y_1) + \frac{8\frac{L_{xs}}{2}\gamma^2}{\pi^2} B_{y_1}(x,y_1) \times \sum_{m=1}^{\infty} \frac{(-1)^m \lambda_m \cosh(\beta_m z)}{(2m+1)^2 \beta_m^2 \cosh\left(\beta_m \frac{L_{zs}}{2}\right)} \cos(\lambda_m x) \quad (6\text{-}4)$$

where $\gamma = \frac{1+j}{\delta}$,

$\lambda_m = (2m+1)\frac{\pi}{2L_{xs}}$,

$\beta_m = \sqrt{\lambda_m{}^2 + \gamma^2}$ and δ (skin depth)$= \sqrt{\frac{2}{\mu\omega\sigma}}$.

Also $-\frac{L_{zs}}{2} \leq z \leq +\frac{L_{zs}}{2}$, and $-\frac{L_{xs}}{2} \leq x \leq +\frac{L_{xs}}{2}$

A similar variation of $B_x(x, y_1, z)$ with axial position z can be derived. To assess the significance of S_x at high frequency in loss evaluation, its contribution to the magnet loss is predicted and compared with the contribution associated with S_y in Fig. 6-13 . The loss is predicted applying the results from 2D FEA considering eddy current reaction. The loss comparison is conducted at 20 kHz harmonics, assuming 5% amplitude of the fundamental current considered in section 6.2 when the machine operates at 4500 rpm.

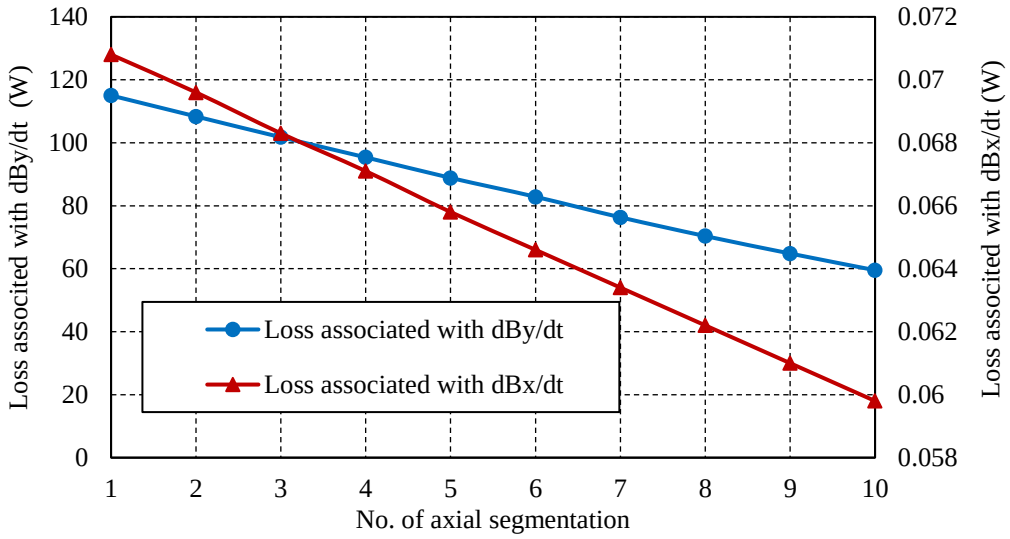

Fig. 6-13. Comparison of loss variations associated with S_y and S_x at 20 kHz.

The results show that the loss associated with S_x is nearly 3 orders of magnitude lower and hence negligible.

Hence, $S_y(x, y, z)$ alone forms the source for eddy current loss in the permanent magnets. So $B_y(x, y)$ values obtained from 2D FEA considering reaction effect is adjusted by the ratio given in (6-4) at a given axial position z for the evaluation of $S_y(x, y, z)$ before application in the 3D Fourier method.

hence for a given y_1,

$$\left[B_y(x,y_1,z)\right]_{F_M} = \left[B_y(x,y_1)\right]_{2DFE} \times \frac{\left[B_y(x,y_1,z)\right]_{As}}{\left[B_y(x,y_1,z=0.5L_z)\right]_{As}} \quad (6\text{-}5)$$

where,

$\left[B_y(x,y_1,z)\right]_{F_M}$ are the adjusted magnetic flux density values for 3D Fourier method, $\left[B_y(x,y_1)\right]_{2DFE}$ are the flux density values from 2D FE considering reaction, $\left[B_y(x,y_1,z)\right]_{As}$ are the flux density values derived from (6-4) for any segmentation and $\left[B_y(x,y_1,z=0.5L_z)\right]_{As}$ are the flux density values derived from (6-4) for $(-\frac{L_{xs}}{2} \leq x^1 \leq +\frac{L_{xs}}{2}$ and at $z^1 = 0)$ with no axial segmentation. The maximum values of the flux density along the axial direction after adjustment is limited to values from 2D FEA without considering eddy current reaction.

Since $B_y(x,y)$ evaluated from the 2D FEA includes its variation in the radial direction, the values evaluated with (6-5) also includes the variation along the radial direction, at the approximation of same rate as that in the $x-z$ plane.

To validate the proposed method, loss evaluation is conducted at 20 kHz harmonics, with an armature current of 3.0585(RMS), having a flux weakening angle $\gamma = 73.27^0$ when the machine is running at 4500rpm. This current is 5% amplitude of the fundamental current considered in section 6.2. The loss evaluation is conducted employing both the proposed method and 3D FEA with increase in axial segmentations at one and two tangential segments. The results are also obtained from the 3D Fourier method based on 2D FEA source data with and without accounting eddy current reaction for comparison.

Fig. 6-14 and Fig. 6-15 compares the magnet loss predicted with increase in axial segmentations by the proposed method, 3D FEA and 3D Fourier method based on 2D FEA source data with and without accounting eddy current

reaction when number of tangential segments is equal to one and two respectively.

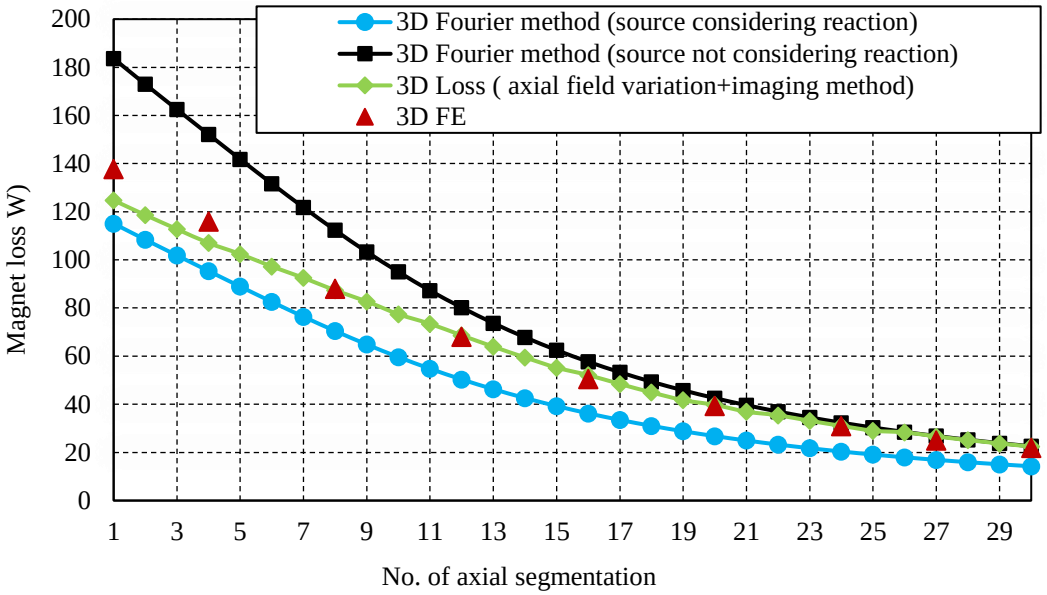

Fig. 6-14. Comparison of loss variations with increase in axial number of segmentations, tangential segment =1 (20 kHz).

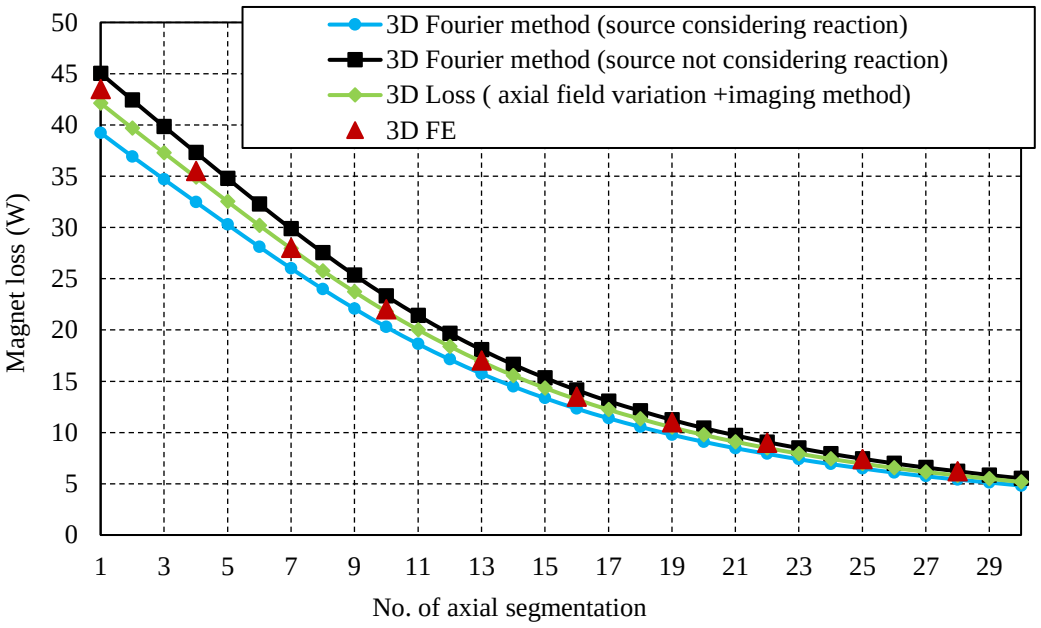

Fig. 6-15. Comparison of loss variations with increase in axial number of segmentations, tangential segment =2 (20 kHz).

The results show that the loss evaluated from the proposed method has good agreement with 3D FE results. It can be observed that there is a slight

miss match especially when tangential segments=1, at lower axial segmentation numbers which can be attributed to the simplifications made in solving the diffusion equation (6-3) as the saturation effect of steel laminations is neglected. The difference in loss prediction with 3D FE results reduces with increase in axial segmentation as with reduction in segment width the source variation tends to become more or less uniform and go close to 2D FE source data not accounting eddy current reaction as discussed in Chapter 4.

6.5 Combined Magnet Loss Evaluation Considering all the Armature Harmonics

Magnet losses for an IPM machine associated with the fundamental component and high frequency pulse width modulation (PWM) harmonics are evaluated separately so far. It is intuitive to assume that the total loss can be evaluated as the sum of these individual losses associated with each harmonic. This method of evaluating the total magnet loss is described in Chapter.5 for SPM machines.

However, for the IPM machine under the operating conditions specified, it is observed that the loss evaluated from the summation of harmonic losses predicted separately is lower than the actual magnet loss which results with all the harmonics together in the supply current.

6.5.1 Cause of Discrepancy in Total Magnet Loss and Solution by Frozen Permeability Method

It is observed that the difference in magnet loss predicted is because of core saturation. When the high frequency harmonic current is excited separately, the core saturation level is much low, and hence the magnets buried in the rotor core are better shielded from the alternating field of the armature reaction, and the resultant loss is lower. Hence, more accurate magnet loss evaluation demands all the current harmonics to be treated together. While all the lower order harmonics for which the induced eddy current is resistance

limited may be treated together, the presence of high frequency harmonics in the armature currents may result in significant eddy current reaction in magnets as explained previously and the variation of the associated eddy current sources along the axial plane for each of them need to evaluated separately. This demands the magnet loss evaluation separately for all the higher order source harmonics influenced by skin effect.

The same dilemma exists for 3D FE prediction of eddy current loss due to a combination of low and high frequency current harmonics. In order to predict high frequency, eddy current loss accurately, the mesh size and time step have to be sufficiently small whereas the simulation time duration has to be sufficiently longer, at least one sixth of the fundamental period. Consequently, the computation time and required memory size will be enormous.

The reason for discrepancy in the total magnet loss with the summation of the harmonic loss evaluated separately arise from the highly nonlinear nature of the interior permanents magnet machines [96]. The machine laminations are operating mainly on the nonlinear region of the B-H curve, as shown in Fig. 6-16.

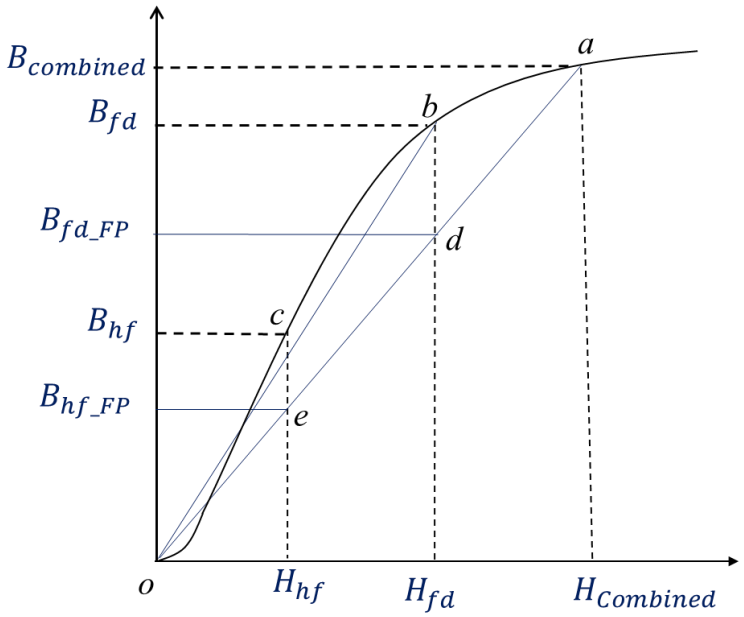

Fig. 6-16. Illustration of the frozen permeability for magnet loss considering harmonics.

This can result in permeability variation with the amplitude of the armature current (or field intensity H). It can be seen from Fig. 6-16 that the sum of the fundamental excitation H_{fd} and the high frequency harmonic excitation H_{hf} will result in an increase in flux density from B_{hf} to $B_{combined}$. However the flux density associated with combined field, $B_{combined}$ is not equal to the superposition of those associated with the fundamental and harmonic excitations. Hence, $B_{combined} < B_{fd} + B_{hf}$. Consequently, time-varying flux density experienced by the magnets is a non-linear function of the excitation current, and hence the principle of superposition is no longer valid.

To circumvent this problem the frozen permeability concept [156, 157] may be employed. If the apparent relative permeability is fixed at a specific value $\mu_{combined}$, given by slope of the line 'oeda' as shown in Fig. 6-16 , the resultant B-H relationship is a straight line with a slope of $\mu_{combined}$. Therefore, the working points under the fundamental and harmonic excitations are points "*d*" and "*e*", respectively, where the flux densities are B_{fd_FP} and B_{hf_FP}. In this case, $B_{combined} = B_{fd\_FP} + B_{hf\_FP}$., which implies the principle of superposition is applicable with the frozen permeability concept.

6.5.2 Method of Implementation of Frozen Permeability for Magnet Loss Prediction

In order to separate the loss associated with different harmonics using the concept of frozen permeability, a sequence of dedicated processes for 1/6th electrical period as illustrated in the Fig. 6-17.

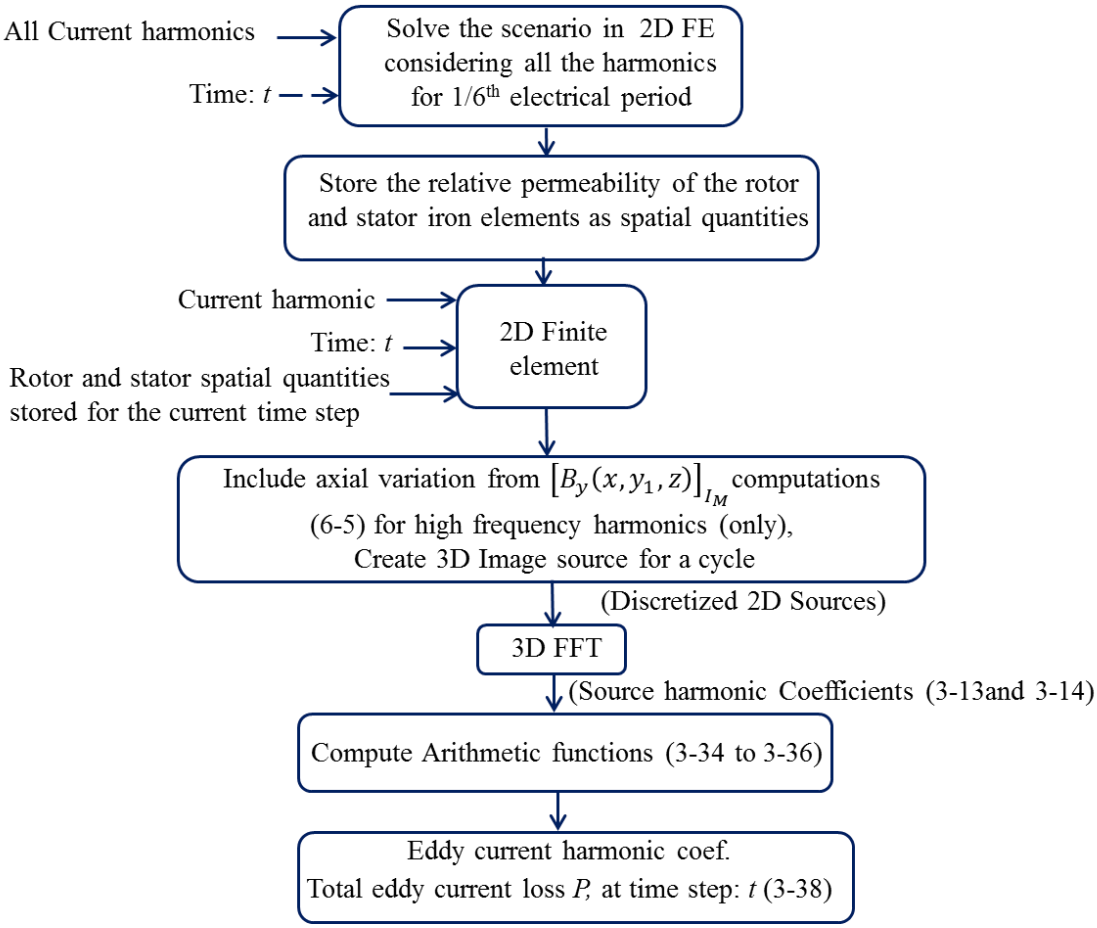

Fig. 6-17. Flow chart showing the magnet loss evaluation at a specific harmonic employing frozen permeability.

First, time-stepped 2D FEA is performed for the machine over 1/6 of an electrical cycle with all the significant low frequency current harmonics in the armature current. The size of the time-step should be sufficiently small to consider the highest frequency harmonics. At each time step or each rotor position, relative permeability of each element in the stator and rotor cores are stored as spatial quantities. Thereafter, the magnetic properties for the stator and rotor cores are updated from the original B-H curves to the spatial

quantities at every time step. Subsequently, 2D FE is performed with each armature harmonic content with the stored spatial quantities at every time step to obtain the eddy current source data to be used in the 3D Fourier method.

6.5.3 3D FE Validation of the Method Proposed

The 3D eddy current loss in the magnets of the 18-slot, 8-pole IPM machine is evaluated by applying the frozen permeability concept when it operates at 4500rpm and is excited with the fundamental current and the high frequency switching harmonics. The dominant switching harmonics usually occur at the integer multiple of the switching frequencies ranging from a few kHz to a few tens kHz and may also have magnitudes up to a few percent of the fundamental depending on the switching frequency and the control strategy employed as discussed in Chapter 5. 20kHz and 10kHz switching frequency harmonics with each 5% amplitude (of the fundamental) together with the fundament over 1/6th electrical cycle as shown in Fig. 6-18 is considered in predicting the total eddy current loss.

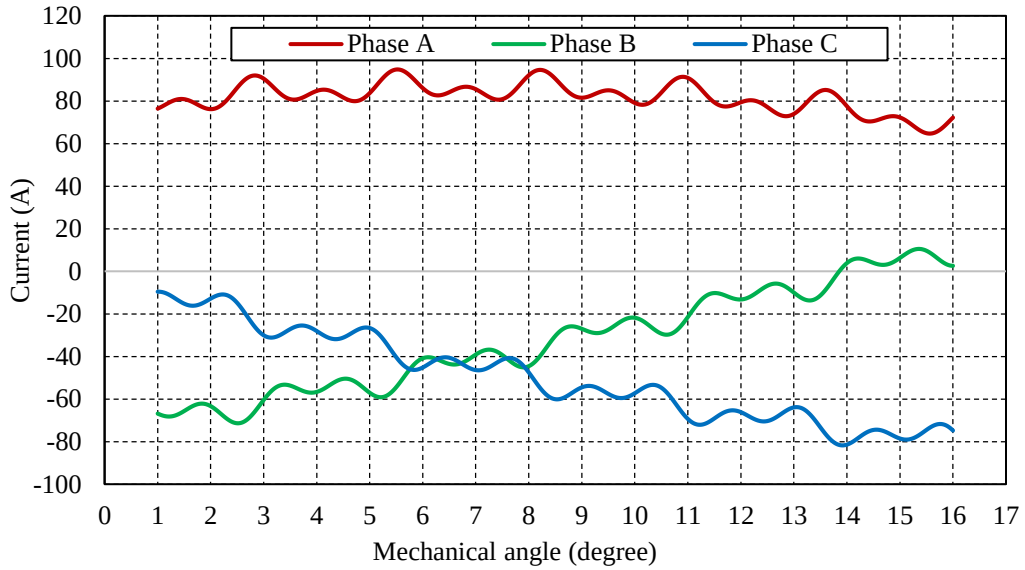

Fig. 6-18. Armature current considering all harmonics applied for 1/6th electrical cycle.

A higher percentage is deliberately chosen such that the predicted magnet loss is noticeable and could replicate the worst ever operating conditions. The

same amplitude is selected for the loss comparison in both cases (20kHz and 10kHz) to see the effect of eddy current reaction at multiples of switching frequencies.

The loss prediction is conducted employing frozen permeability at the fundamental and at both the harmonics with increase in axial segments up to 30 at one tangential segment. Fig. 6-19 illustrates the relative permeability contour frozen for the rotor and stator laminations of the IPM machine at $\omega_r t = 3.8^0$ when the it operates with phase currents shown in Fig. 6-18 at 4500 rpm.

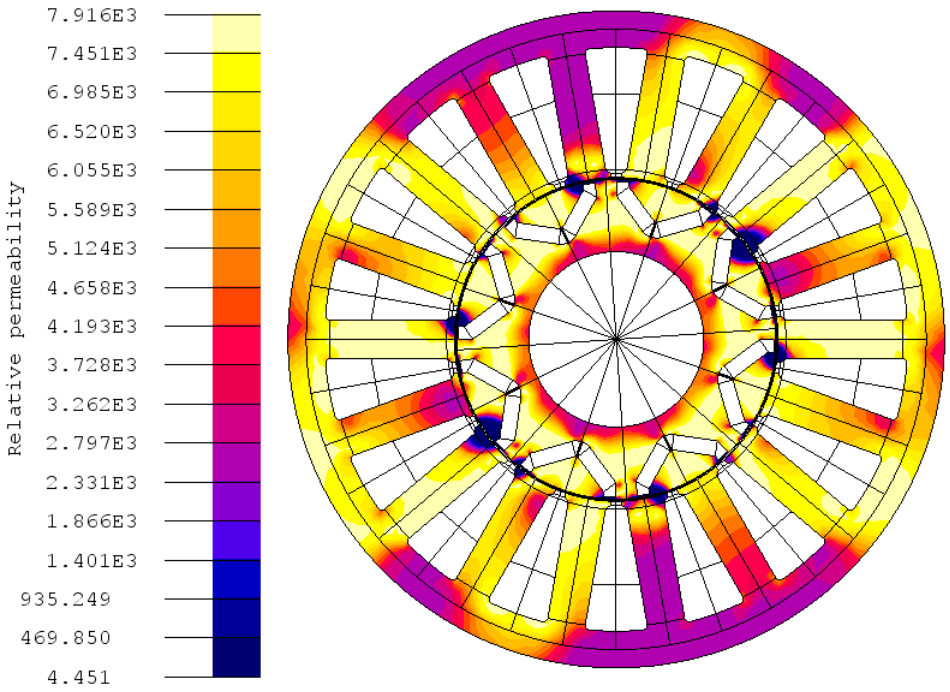

Fig. 6-19. Frozen permeability along the machine laminations at $\omega_r t = 3.8^0$ when the IPM operates at 4500 rpm with fundamental and high frequency harmonics.

The loss evaluation is also performed in 3D FEA with all the harmonics with increase in axial segmentation. The variations of magnet loss associated with different harmonics and the total loss evaluated are compared with 3D FEA predictions in Fig. 6-20.

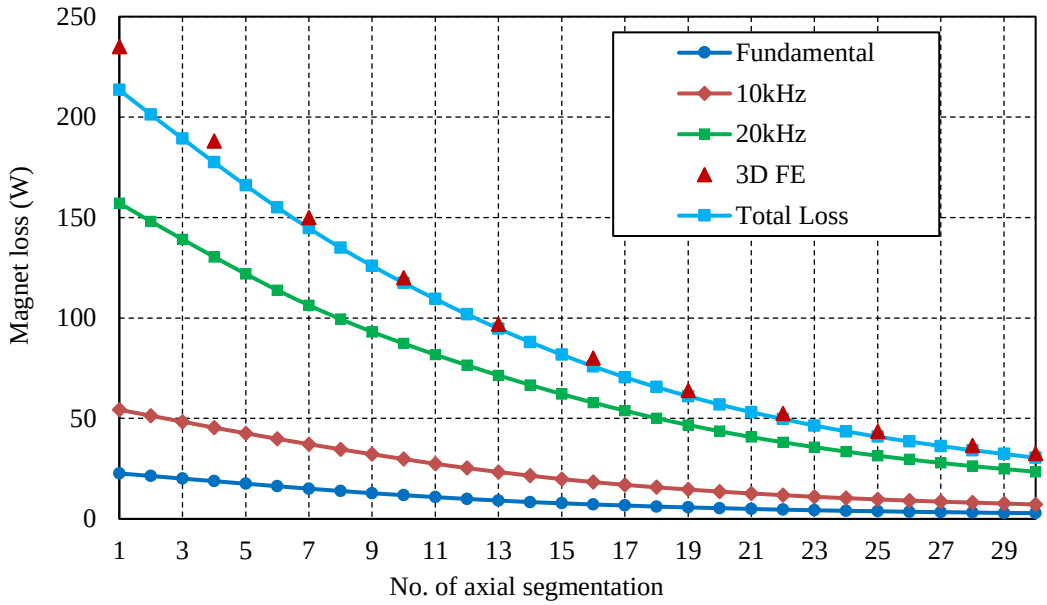

Fig. 6-20. Variations of magnet losses with number of axial segments evaluated at different harmonics employing frozen permeability (number of tangential segment = 1).

It is clear from the results that the loss associated with different harmonics add together to form the total magnet loss. Further, the results from the figure shows that the loss at each harmonic evaluated by employing frozen permeability is greater than the loss evaluated at the same harmonic frequency evaluated previously in section 6.2 and 6.5 when magnetic saturation under a given operating condition is not appropriately accounted. This is because with the presence of the fundamental current, the saturation level in the rotor core is much high, and hence its shielding effect to high frequency field harmonics is reduced.

It should also be noted that while the eddy current loss associated with the fundamental component is quite low, the losses associated with the PWM frequency harmonics are much greater even the harmonic current magnitude is only 5% of the fundamental. The losses associated with high frequency current harmonics need to be accurately predicted and reduced so as to ensure the rotor temperature is not excessive.

6.5.4 Computational Efficiency in High Frequency Loss Prediction

For loss evaluation at each harmonic employing frozen permeability it takes around 9 hours to generate the flux density harmonics from the 2D FEA and less than 30 seconds to compute the total 3D eddy current loss for all the magnets in a typical PC with configuration discussed previously. Hence on an average for evaluating the loss variation with number of axial segments up to 30, it takes around 18 minutes for each case, in contrast to more than 10 days usually required for one 3D FE analysis with no axial segmentation.

6.6 Conclusion

A method for predicting 3D magnet eddy current loss in the rotors of IPM machines has been developed in this chapter based on the 3D Fourier method considering source variations from 2D FEA. The results obtained by accounting axial source variation in the 3D Fourier method gave more accurate results for magnet loss at high frequencies when eddy current reaction is significant in IPM machine. The actual loss in the machine due to all the armature current harmonics is established by evaluating each harmonic loss separately by employing frozen permeability. The results obtained show insignificance of the tangential source component in eddy current loss. The developed technique provides a computationally efficient tool for assessing the eddy current loss in the rotor magnets and for minimizing its impact on the machine performance.

CHAPTER 7
Estimation of 3D Eddy Current Loss in Retaining Sleeve of SPM Machines

7.1 Introduction

The method of loss estimation in the magnets of SPM and IPM machines are discussed in detail in the previous chapters. However, rotors in SPM machines especially used in high speed applications are often reinforced with retaining sleeves over the permanent magnets to provide them with a firm mechanical support [158-160], and thus preventing them from flying out when subject to a possible adhesive failure at high centrifugal forces and also at high temperatures. These sleeve materials can be manufactured with less conductive glass or fibrous carbon, however a more conductive stainless steel or Inconel are preferred because of their better mechanical properties at high temperatures and reduced manufacturing cost.

The conducting sleeves may provide shielding [161, 162] to very high frequency harmonics from penetrating into magnets, however may suffer eddy current loss within it. Like permanent magnets, the low frequency eddy current loss can also be more prominent in sleeves for the machines with concentrated or modular winding configurations. As discussed in Chapter 1 the loss at low frequency can be attributed to the harmonics associated with slotting, higher armature currents and spatial winding distributions. Different structures are suggested in literature for reducing the sleeve losses[159, 163] however the less complicated hollow tube structure with axial segmentation is preferred in most of the cases. An accurate estimation of sleeve loss enables the designer to take necessary steps in limiting the excessive eddy current loss and hence the temperature rise in the rotor and the magnets, and thus helps in increasing the reliability and efficiency of the SPM machines.

There are only a few publications reported in literature to evaluate 2D eddy current loss in retaining sleeve for permanent magnet machines some of which are discussed in Chapter 1. The 2D analytical methods reported in [56, 64, 164] ignores the loss associated with slotting effect, and approximates the armature currents by an infinitely thin current sheet distributed across the stator bore as discussed previously in Chapter 1. The 2D relative permeance models proposed in [18] fails to represent the flux density undulations due to slotting with sufficient accuracy, hence provides erroneous results in rotor loss evaluation [69]. However, the more accurate subdomain models [80, 83, 84] are employed to estimate the retaining sleeve loss with better accuracy [165]. The methods described in [64] and [164] considers the reaction effect of eddy currents while evaluating the loss associated with retaining sleeve. As discussed in previous chapters 2D predictions analytically or by numerical analysis would not provide accurate results if the end effect of eddy current circulation is significant.

In order to account the end effect in eddy current distribution, 3D analysis is required for predicting eddy current loss in the retaining sleeve. Unlike the loss estimations in permanent magnets which may need only a part of the machine to be modelled in 3D FEA based on the axial and circumferential symmetry, the 3D FEA of the relating sleeve demands the solution to the half of the machine model considering only its axial symmetry in $r-\theta$ plane. This along with finer meshing requirements can result in enormous computation time and also much higher memory requirements in storing the results obtained while evaluating the loss associated with the retaining sleeve. The introduction of axial segmentation in reducing the sleeve loss makes the 3D – analysis indispensable. M.R. Shah *et al.* developed 2.5-D FEA in [166] to reduce the computation time in elevating the sleeve loss considering axial segmentation. However, this method is complicated to implement and is still time consuming.

The 3D Fourier method proposed in Chapter 3 to evaluate the resistance limited eddy current distribution in rotor permanent magnets of a SPM machine. While the same concept is applicable to evaluation of eddy current loss in the retaining sleeves, the boundary condition along the θ-direction, and hence the analytical solution need to be treated differently.

This Chapter paper proposes 3D Fourier method for predicting the resistance limited eddy current loss in the sleeve accounting its boundary conditions. The proposed technique is validated on an 8-pole, 18 slot SPM machine by predicting the sleeve loss and comparing the results with those obtained from 3D FEA. The eddy current loss at high frequencies is evaluated by applying the proposed method with flux density variation derived along the axial plane from the solution to the eddy current diffusion.

The method of sleeve loss prediction developed in this chapter is published by the author in [C3] and discussed in detail in [C4], as mentioned previously in Section 1.8.

Eddy Current Source Evaluation in the Retaining Sleeve from Subdomain Model

Chapter 2 describes the evaluation of eddy current sources in the magnets from the more accurate subdomain model [84, 85]. The same machine model is employed here to evaluate the flux density variations in the sleeve region for the 3D eddy current loss prediction considering the effect of slotting.

Since in the subdomain model, the sleeve is considered to be equivalent to the air gap with relative permeability, $\mu_r = 1$ as shown in Fig. 7-1, the solution to the flux density equation derived for the air gap region can also be directly applied to the sleeve region.

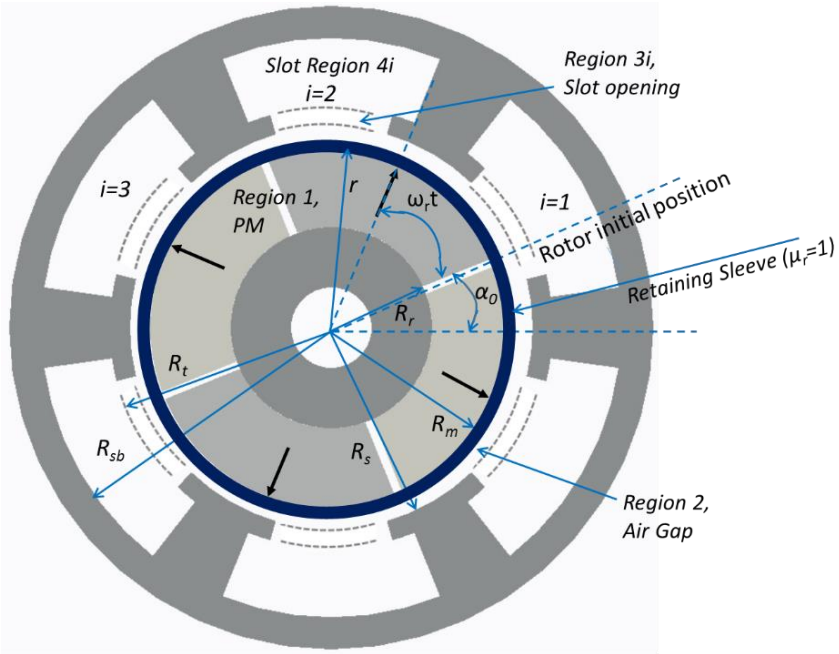

Fig. 7-1. Machine geometry for subdomain model illustrating retaining sleeve, other regions and symbols.

Hence the radial and the tangential component of flux density (B_{sl_r} and B_{sl_t} respectively) within the sleeve region can be expressed at a radial distance 'r' in the rotor reference as [84, 85],

$$B_{sl\_r} = \sum_k -(A_2 C_{1kr} + B_2 C_{2kr}) \sin(k\theta_r + k\omega_r t) + \sum_k (C_2 C_{1kr} + D_2 C_{2kr}) \cos(k\theta_r + k\omega_r t) \quad (7\text{-}1)$$

$$B_{sl\_t} = \sum_k -(A_2 C_{1kr} - B_2 C_{2kr}) \cos(k\theta_r + k\omega_r t) - \sum_k (C_2 C_{1kr} - D_2 C_{2kr}) \sin(k\theta_r + k\omega_r t) \quad (7\text{-}2)$$

where

$$C_{1kr} = k/r \,.\, (r/R_s)^k \quad (7\text{-}3)$$

$$\text{and } C_{2kr} = k/r \,.\, (r/R_m)^{-k} \quad (7\text{-}4)$$

As shown in [165] coefficients which accounts for the slotting effect viz. A_2, B_2, C_2 and D_2 varies with rotor position and can be expressed as Fourier series.

The time variations for radial and tangential component of flux density can be derived from the magnetic vector potential A_{z2} (Ref. Chapter 2) as,

$$\frac{\partial B_{sl\_r}}{\partial t} = \frac{\partial}{\partial t}\left(\frac{1}{r}\frac{\partial A_{z2}}{\partial \alpha}\right) \tag{7-5}$$

$$\frac{\partial B_{sl\_r}}{\partial t} = \frac{\partial}{\partial t}\left(-\frac{\partial A_{z2}}{\partial r}\right) \tag{7-6}$$

Accommodating the Fourier expansion of A_2, B_2, C_2 and D_2 the time variations for the flux density can be expressed as the sum of harmonics as,

$$\begin{aligned}\frac{\partial B_{sl\_r}}{\partial t} &= \sum_k \sum_l -C_{1kr}\begin{bmatrix} a_{1b}(k+lp)\,\omega_r \cos(k\theta_r + (k+lp)\omega_r t + \psi_{1b}) \\ +a_{1f}\,(k-lp)\omega_r \cos\left(k\theta_r + (k-lp)\omega_r t + \psi_{1f}\right)\end{bmatrix} \\ &+ \sum_k \sum_l -C_{2kr}\begin{bmatrix} a_{2b}(k+lp)\omega_r \cos(k\theta_r + (k+lp)\omega_r t + \psi_{2b}) \\ +a_{2f}\,(k-lp)\omega_r \cos\left(k\theta_r + (k-lp)\omega_r t + \psi_{2f}\right)\end{bmatrix}\end{aligned} \tag{7-7}$$

$$\begin{aligned}\frac{\partial B_{sl\_t}}{\partial t} &= \sum_k \sum_l C_{3kr}\begin{bmatrix} a_{1b}(k+lp)\omega_r \sin(k\theta_r + (k+lp)\omega_r t + \psi_{1b}) \\ +a_{1f}\,(k-lp)\omega_r \sin\left(k\theta_r + (k-lp)\omega_r t + \psi_{1f}\right)\end{bmatrix} \\ &+ \sum_k \sum_l C_{4kr}\begin{bmatrix} a_{2b}\,(k+lp)\omega_r \sin(k\theta_r + (k+lp)\omega_r t + \psi_{2b}) \\ +a_{2f}\,(k-lp)\omega_r \sin\left(k\theta_r + (k-lp)\omega_r t + \psi_{2f}\right)\end{bmatrix}\end{aligned} \tag{7-8}$$

where,

$$C_{3kr} = k.r^{k-1}/{R_s}^k \tag{7-9}$$

$$\text{and } C_{4kr} = -k.r^{-k-1}/{R_m}^{-k} \tag{7-10}$$

The Fourier series expansion of the coefficients A_2, B_2, C_2 and D_2 and the definition of the simplified coefficients $a_{1b}, a_{1f}, a_{2b}, a_{2f}$ and their corresponding phase angles $\psi_{1b}, \psi_{1f}, \psi_{2b}, \psi_{1f}$ is given in Appendix C.

The definition of other coefficients and variables in (7.1) to (7.10) is given in Chapter 2. The harmonic relations for the eddy current sources are established to evaluate the contribution of different harmonics towards the 3D eddy current loss in the retaining sleeve.

7.2 3D Fourier Technique Proposed to the Retaining Sleeve and Loss Formulation

Neglecting the curvature effect for relatively thin retaining sleeve wrapped over the permanent magnets, it can be unrolled along the circumferential x–direction as thin film of metal of length equal to its circumference as shown in Fig. 7-2.

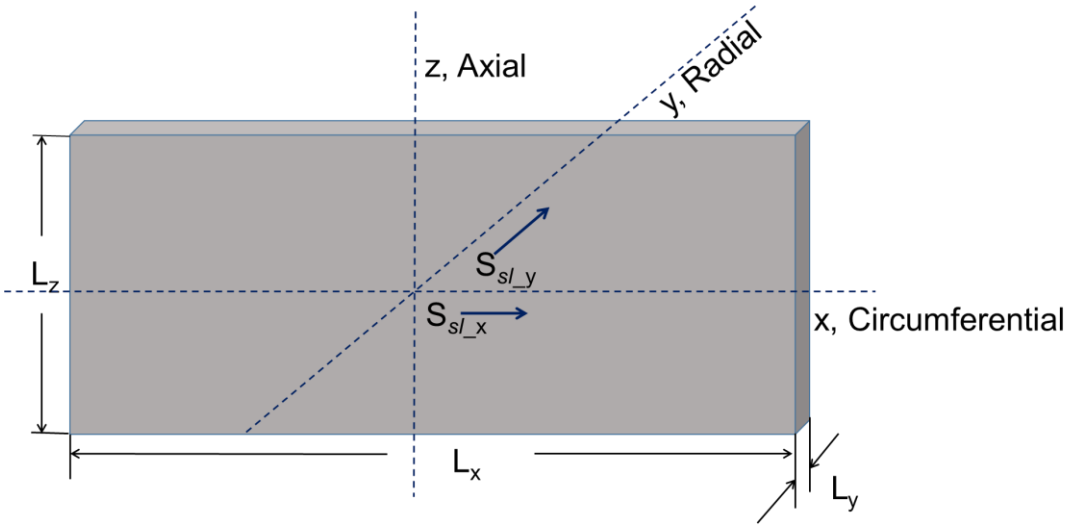

Fig. 7-2. Unrolled retaining sleeve in the form of a rectangular segment with sources in x–and y–directions.

It is evident from Chapter 3 that for a thin rectangular segment without any curvature, 3D Fourier method can be applied directly. It has been established from the imaging method[121] that across the normal boundary the sources are mirrored, while it has become an inverted mirror image across

the tangential boundaries. However, along the x–direction, the boundary conditions for the retaining sleeve is determined by the repetition of the unrolled segment for every 360^0.While the image sources along the y–direction will be repeated in the same way as it was repeated for the case with PMs in Chapter 3.

Hence the eddy current source distribution in the sleeve S_{sl} ($S_{sl\_x} = \partial B_{sl\_t}/\partial t$, $S_{sl\_y} = \partial B_{sl\_r}/\partial t$) is found to be repeating itself with every L_x, $2L_y, 2L_z$. This allows to represent the sources in the sleeve as 3D Fourier series satisfying its boundary conditions as [167],

$$S_{sl\_x} = \sum_{m=1}^{\infty}\sum_{n=1}^{\infty}\sum_{k=1}^{\infty} a_{sl(m,n,k)} sin\left(m\frac{2\pi}{L_x}\right) sin\left(n\frac{\pi}{L_y}y\right) sin\left(k\frac{\pi}{L_z}z\right) \tag{7-11}$$

$$S_{sl\_y} = \sum_{m=1}^{\infty}\sum_{n=1}^{\infty}\sum_{k=1}^{\infty} b_{sl(m,n,k)} sin\left(m\frac{2\pi}{L_x}x\right) cos\left(n\frac{\pi}{L_y}y\right) sin\left(k\frac{\pi}{L_z}z\right) \tag{7-12}$$

where m, n, k are the harmonic orders in x, y, z directions respectively. The coefficients $a_{sl(m,n,k)}$ and $b_{sl(m,n,k)}$ can be evaluated from Fourier expansion of the sources, considering the boundary enveloped by the size of four rectangular segments each having the volume of the retaining sleeve.

For each harmonic of $S_{sl\_x(m,n,k)}$ and $S_{sl\_y(m,n,k)}$, the source is distributed sinusoidally within an isotropic 3D infinite space. The solution of the current vector potential in the sleeve ($A_{i\_sl} = (A_{sl\_x}, A_{sl\_y})$ which satisfy Poisson's equation,

$$\nabla^2 A_{i\_sl} = -\sigma S_{sl} \tag{7-13}$$

after applying Coulomb gauge $\nabla \cdot A_{i\_sl} = 0$,with the source distribution (S_{sl_x} , S_{sl_y}) in (7.11) and (7.12) are given by

$$A_{i\_sl\_x} = \sum_{m=1}^{\infty}\sum_{n=1}^{\infty}\sum_{k=1}^{\infty} c_{sl(m,n,k)} sin\left(m\frac{2\pi}{L_x}x\right) sin\left(n\frac{\pi}{L_y}y\right) sin\left(k\frac{\pi}{L_z}z\right) \quad (7\text{-}14)$$

$$A_{i\_sl\_y} = \sum_{m=1}^{\infty}\sum_{n=1}^{\infty}\sum_{k=1}^{\infty} d_{sl(m,n,k)} sin\left(m\frac{2\pi}{L_x}x\right) cos\left(n\frac{\pi}{L_y}y\right) sin\left(k\frac{\pi}{L_z}z\right) \quad (7\text{-}15)$$

where $c_{sl(m,n,k)}$ and $d_{sl(m,n,k)}$ are Fourier coefficients associated with (n, m, k)th harmonic . Consequently the eddy current density in the sleeve ($J_{sl} = J_{sl\_x}, J_{sl\_y}, J_{sl\_z}$) can be derived from

$$\nabla \times A_{sl} = J_{sl} \quad (7\text{-}16)$$

as,

$$J_{sl\_x} = \sum_{m=1}^{\infty}\sum_{n=1}^{\infty}\sum_{k=1}^{\infty} e_{sl(m,n,k)} sin\left(m\frac{2\pi}{L_x}x\right) cos\left(n\frac{\pi}{L_y}y\right) cos\left(k\frac{\pi}{L_z}z\right) \quad (7\text{-}17)$$

$$J_{sl\_y} = \sum_{m=1}^{\infty}\sum_{n=1}^{\infty}\sum_{k=1}^{\infty} h_{sl(m,n,k)} sin\left(m\frac{2\pi}{L_x}x\right) sin\left(n\frac{\pi}{L_y}y\right) cos\left(k\frac{\pi}{L_z}z\right) \quad (7\text{-}18)$$

$$J_{sl\_z} = \sum_{m=1}^{\infty}\sum_{n=1}^{\infty}\sum_{k=1}^{\infty} \begin{matrix} q_{sl1(m,n,k)} cos\left(m\frac{2\pi}{L_x}x\right) cos\left(n\frac{\pi}{L_y}y\right) sin\left(k\frac{\pi}{L_z}z\right) \\ -q_{sl2(m,n,k)} sin\left(m\frac{2\pi}{L_x}x\right) cos\left(n\frac{\pi}{L_y}y\right) sin\left(k\frac{\pi}{L_z}z\right) \end{matrix} \quad (7\text{-}19)$$

where, $e_{sl(m,n,k)}$, $h_{sl(m,n,k)}$, $q_{sl1(m,n,k)}$, and $q_{sl1(m,n,k)}$ are the Fourier coefficients associated with (n, m, k)th harmonic for the eddy current densities which are derived from $a_{sl(m,n,k)}$ and $b_{sl(m,n,k)}$ after the operations defined in (7.13) and (7.16).

The coefficients, $c_{sl(m,n,k)}$, $d_{sl(m,n,k)}$, $e_{sl(m,n,k)}$, $h_{sl(m,n,k)}$, $q_{sl1(m,n,k)}$, $q_{sl1(m,n,k)}$for the current vector potential and eddy current densities

are all arithmetic functions of the harmonic order and sleeve dimensions can be derived in the same manner as described in Chapter 3, they are defined as below,

$$\text{Let} \quad M\_sl^2 = (m\frac{2\pi}{L_x})^2 + (n\frac{\pi}{L_y})^2 + (k\frac{\pi}{L_z})^2 \tag{7-20}$$

$$c_{sl(m,n,k)} = \sigma \cdot \frac{a_{sl(m,n,k)}}{M\_sl^2} \tag{7-21}$$

$$d_{sl(m,n,k)} = \sigma \cdot \frac{b_{sl(m,n,k)}}{M\_sl^2} \tag{7-22}$$

$$e_{sl(m,n,k)} = \sigma \cdot \frac{-b_{sl(m,n,k)}(k\frac{\pi}{L_z})}{M\_sl^2} \tag{7-23}$$

$$h_{sl(m,n,k)} = \sigma \cdot \frac{a_{sl(m,n,k)}(k\frac{\pi}{L_z})}{M\_sl^2} \tag{7-24}$$

$$q_{sl1(m,n,k)} = \sigma \cdot \frac{b_{sl(m,n,k)}\left(m\frac{2\pi}{L_x}\right)}{M\_sl^2} \tag{7-25}$$

$$q_{sl2(m,n,k)} = \sigma \cdot \frac{-a_{sl(m,n,k)}(n\frac{\pi}{L_y})}{M\_sl^2} \tag{7-26}$$

Since each harmonic is found to be orthogonal, the total sleeve eddy current loss a particular time instant can be evaluated as the sum of the loss associated with each harmonic as,

$$\begin{aligned} P_{sl\_eddy} &= \sum_{m=1}^{\infty}\sum_{n=1}^{\infty}\sum_{k=1}^{\infty}\frac{1}{4}\int_0^{L_x}\int_0^{2L_y}\int_0^{2L_z} \begin{matrix} J_{sl\_x(m,n,k)}{}^2 \\ +J_{sl\_y(m,n,k)}{}^2 \\ +J_{sl\_z(m,n,k)}{}^2 \end{matrix} dxdydz \\ &= \sum_{m=1}^{\infty}\sum_{n=1}^{\infty}\sum_{k=1}^{\infty}\left\{p_{s1(m,n,k)} + p_{s2(m,n,k)} + p_{s3(m,n,k)} + p_{s4(m,n,k)} + p_{s5(m,n,k)}\right\} \end{aligned} \tag{7-27}$$

where,

$$p_{s1(m,n,k)} = b_{sl(m,n,k)}{}^2 \cdot \left[\frac{\left(k\frac{\pi}{L_z}\right)}{M\_sl^2}\right]^2 \cdot \frac{\sigma L_x L_y L_z}{8} \tag{7-28}$$

$$p_{s2(m,n,k)} = a_{sl(m,n,k)}{}^2 \cdot \left[\frac{\left(k\frac{\pi}{L_z}\right)}{M\_sl^2}\right]^2 \cdot \frac{\sigma L_x L_y L_z}{8} \tag{7-29}$$

$$p_{s3(m,n,k)} = b_{sl(m,n,k)}{}^2 \cdot \left[\frac{\left(m\frac{2\pi}{L_x}\right)}{M\_sl^2}\right]^2 \cdot \frac{\sigma L_x L_y L_z}{8} \tag{7-30}$$

$$p_{s4(m,n,k)} = a_{sl(m,n,k)}{}^2 \cdot \left[\frac{\left(n\frac{\pi}{L_y}\right)}{M\_sl^2}\right]^2 \cdot \frac{\sigma L_x L_y L_z}{8} \tag{7-31}$$

$$p_{s5(m,n,k)} = -2a_{sl(m,n,k)}b_{sl(m,n,k)} \cdot \left(m\frac{2\pi}{L_x}\right)\left(n\frac{\pi}{L_y}\right) \cdot \left[\frac{1}{M\_sl^2}\right]^2 \cdot \frac{\sigma L_x L_y L_z}{8} \tag{7-32}$$

It is worth noting that the coefficients defined in the equations (7-20) to (7-32) are different from the corresponding coefficients defined in Chapter 3 as the source equation (7-11) and (7-12) defined for the sleeve is different when compared to the permanent magnets.

7.3 Process of Implementation of the Proposed Method

It is seen from the previous section that the periodicity helps in representing the original and image sources as sum of 3D harmonic series in free space. So as to represent that way, the original 2D sources S_{sl_x} (derived analytically or from 2D FE at each time instant) is repeated as inverted image sources along $y-$direction. However, for the case with S_{sl_y}, the original sources are repeated as mirror image along $y-$direction. This completes the 2D repetition of the sources constrained by the boundaries L_x and $2L_y$. The original and image sources of S_{sl_x} and S_{sl_y} thus formed along two

dimensions are again repeated along $z-$ direction till L_z. Finally, this sources and images each enclosed by $L_x, 2L_y, L_z$ for S_{sl_x} and $S_{sl_y}$is repeated again as inverted mirror images along $z-$ direction till $2L_z$. Thus a complete set of sources each for S_{sl_x} and S_{sl_y} are formed which will be repeating every $L_x, 2L_y, 2L_z$ [121]. Now the 3D FFT of the resultant S_{sl_x} and S_{sl_y} can be performed to evaluated $a_{sl(m,n,k)}$ and $b_{sl(m,n,k)}$.

As described for the permanent magnets in previous chapters the accuracy of loss computation is highly dependent on the number of divisions considered along the 2D sleeve while evaluating the flux density variations employing either analytical or 2D FE models. For example, for the 8-pole, 18-slot SPM machine considered in this chapter, 512 divisions are made along the circumferential direction and 8 divisions are made along the radial direction while evaluating the source information. As described previously, in order to perform FFT of the sources, the magnetic field distribution obtained are needed to be further discretized in 3D. 32 divisions are considered along the axial direction of the sleeve for good computational accuracy. Considering repetition of the sources for the case with retaining sleeve, the FFT needed to be performed for the discretized sources enclosed within a volume whose boundaries are defined by $L_x, 2L_y, 2L_z$. This is the major difference for the sleeve loss evaluation when compared to the loss prediction in permanent magnets where the FFT is performed considering the boundaries defined by $2L_x, 2L_y, 2L_z$.

As for the permanent magnets, it is necessary to calculate the eddy current loss at least for one sixth of the electrical period to obtain the average value of the 3D sleeve eddy current loss. To evaluate the magnet loss variation with n_a number of axial segmentations as shown in Fig. 7-3, the losses are evaluated for only one axial segment and the total loss is computed by multiplying the result with the number of axial segments.

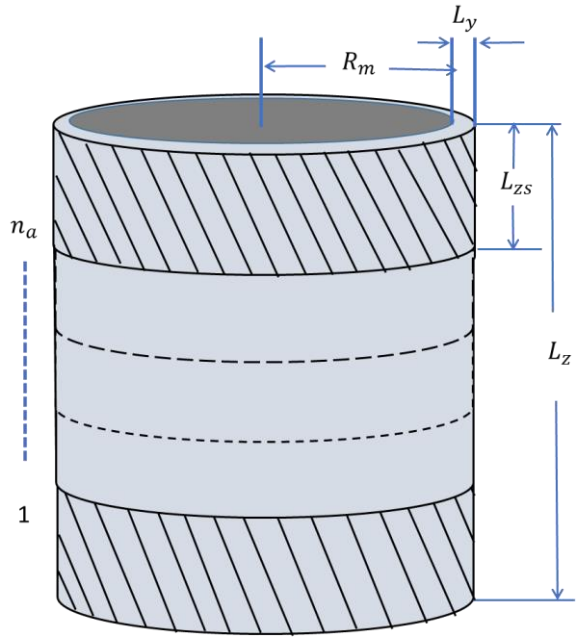

Fig. 7-3. Axial segmentation for the retaining sleeve.

The loss evaluation for the axial segments at different axial positions is not being conducted separately as the source field is essentially 2D, hence the sleeve loss will not have any variation among different axial segments.

7.4 Finite Element Validation

The proposed method is applied the 18-slot 8-pole SPM machine described in Chapter 3 and 4, for the eddy current loss prediction in the retaining sleeve. The sleeve thickness is considered to be 0.4 mm along the radial direction and manufactured with Inconel with a resistivity of 1.25 x10^{-6} Ω m. For validation purpose the eddy currents are evaluated when the machine is operated at the load conditions with a peak phase current of 55A at 4500rpm. This is the same load conditions employed for validation of 3D Fourier method in Chapter 3.

7.4.1 2D FEA for Source Validation

As the source information is derived from the subdomain model [85], which neglects the magnetic saturation in the machine, it is insightful to have a comparison for the magnetic field variation with the results obtained from

2D finite element analysis (FEA). Hence the source components derived analytically are compared with the 2D time stepped finite elements values.

Fig. 7-4 compares the analytically and 2D FE predicted flux density components with angular position at a given time instant of $\omega_r t = 1.5^0$ for the sleeve when the machine operates at the peak load conditions. Fig. 7-5 compares the analytically and 2D FE predicted eddy current source components with angular position at a given time instant of $\omega_r t = 1.5^0$ (elec.) for the sleeve when the machine operates at the peak load conditions.

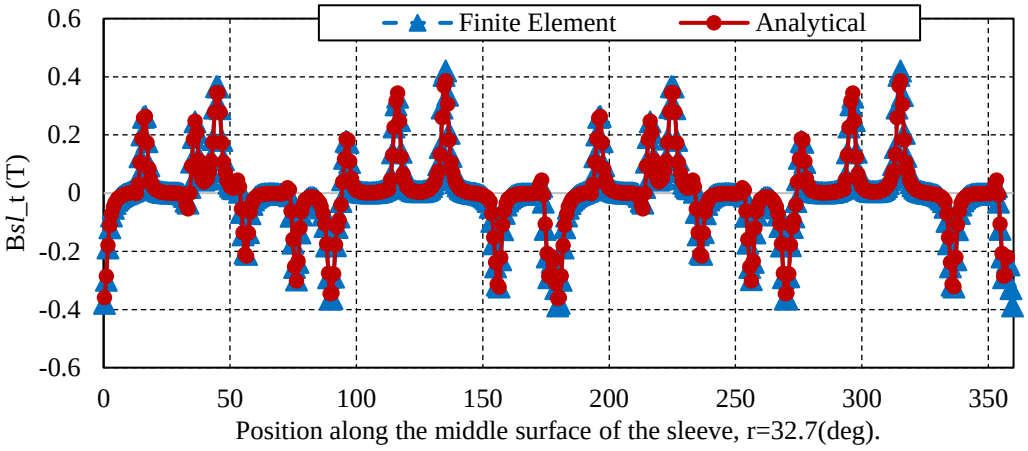

(c) Circumferential flux density component (B_{sl_t}) variation

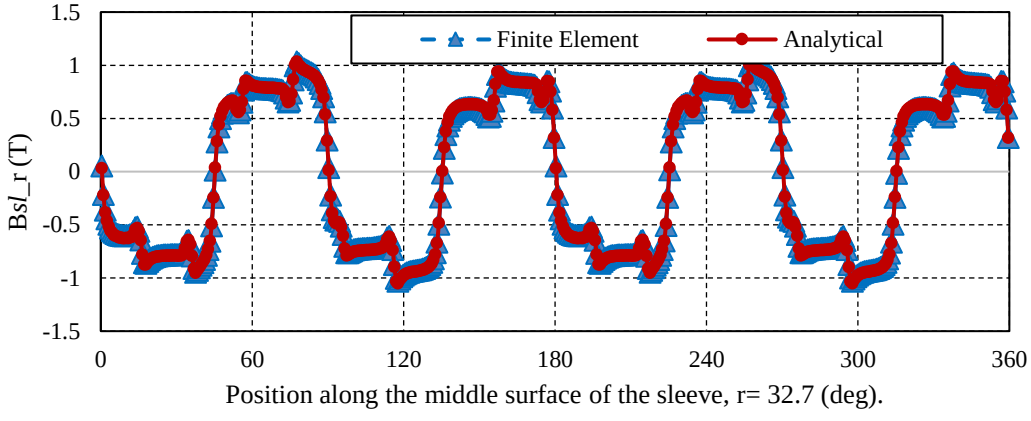

(d) Radial flux density component (B_{sl_r}) variation

Fig. 7-4. Comparison of flux density components from subdomain model and 2D-FE along the mean radius of the sleeve at $\omega_r t = 1.5^0$.

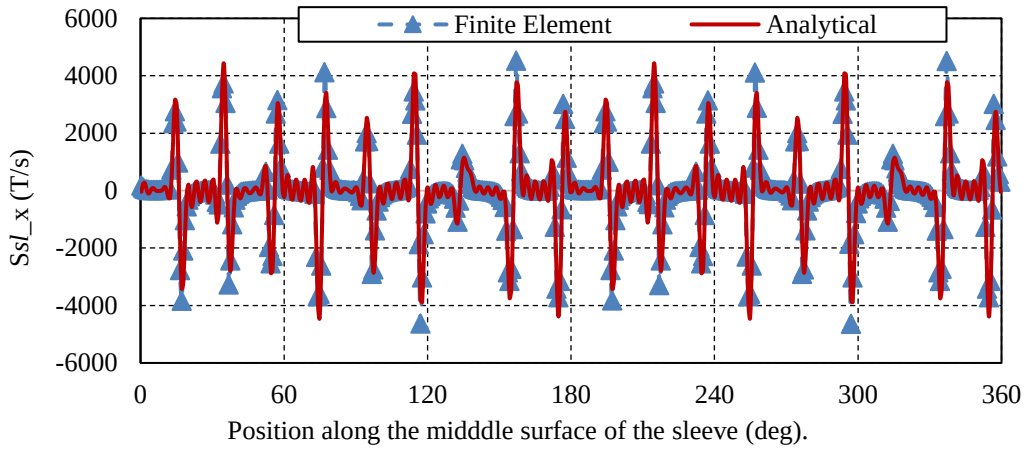

(a) Comparison of circumferential component (S_{sl_x}) variation.

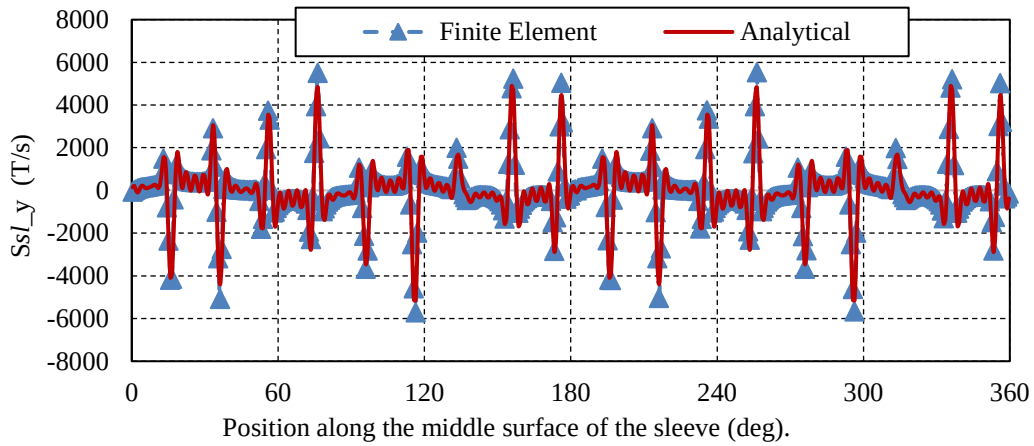

(b) Comparison of radial component (S_{sl_y}) variation.

Fig. 7-5. Comparison of source components from subdomain model and 2D FE at mean radius of the retaining sleeve at $\omega_r t = 1.5^0$.

It can be seen that the analytical predictions agree very well with those obtained from the 2D FEAs. This ensures the accuracy of the source of excitation of the eddy current distribution to be analytically predicted by the proposed method.

7.4.2 3D Finite Element Validation of the Proposed Method

The eddy current loss in the retaining sleeve evaluated by the proposed method is validated using the 3D finite element model as shown in Fig. 7-6.

Considering the axial symmetry, only a half of the machine has to be modelled in 3D FEAs. This increases the computation time compared to the magnet loss evaluation for the same machine as described in Chapter 3 and 4. Tangential magnetic field boundary condition is imposed on the two end surfaces perpendicular to the axial direction. Hence the 3D end effect of the magnetic field distribution is neglected in the analysis. This is to save the 3D computation time which is already much higher as explained in Section 7.7. Also the fine meshing is employed along the axial and circumferential direction which largely increases the computation time. In addition, perfect insulation boundaries are applied to the end surfaces of the retaining sleeve. 3-phase sinusoidal currents of 55 peak is injected in the machine phases via the electrical circuit as described in Chapter 1 while the machine is operating at 4500 rpm. The 3D machine model is operating with only q-axis current assuming no field weakening as simulated in the subdomain model.

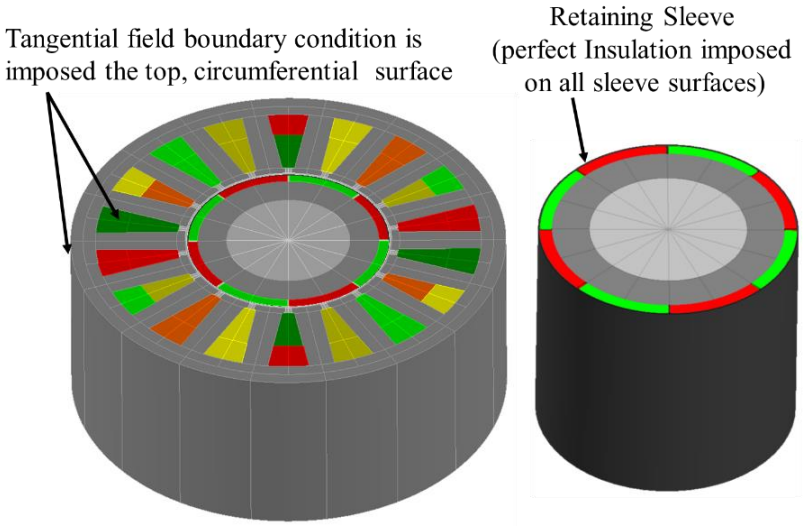

Fig. 7-6. 3D FE model based on axial symmetry.

Sleeve loss evaluation is carried out employing the proposed 3D Fourier method and also 3D FE when operating with seven axial segments at previously mentioned load conditions. Fig. 7-7 compares analytically and 3D FE predicted $z-$component eddy current density distributions at $\omega t = 1.5^0$ on the half surface given by the mean radius of the sleeve at r =32.7mm (defined

by, $y = 0.5\,L_y, 0 < x < L_x, 0.5\,L_z < z < L_z$), when the machine operates at the load conditions mentioned previously. Fig. 7-8 compares analytically and 3D FE predicted x–component eddy current density distributions at same surface and at the same time instant and load conditions.

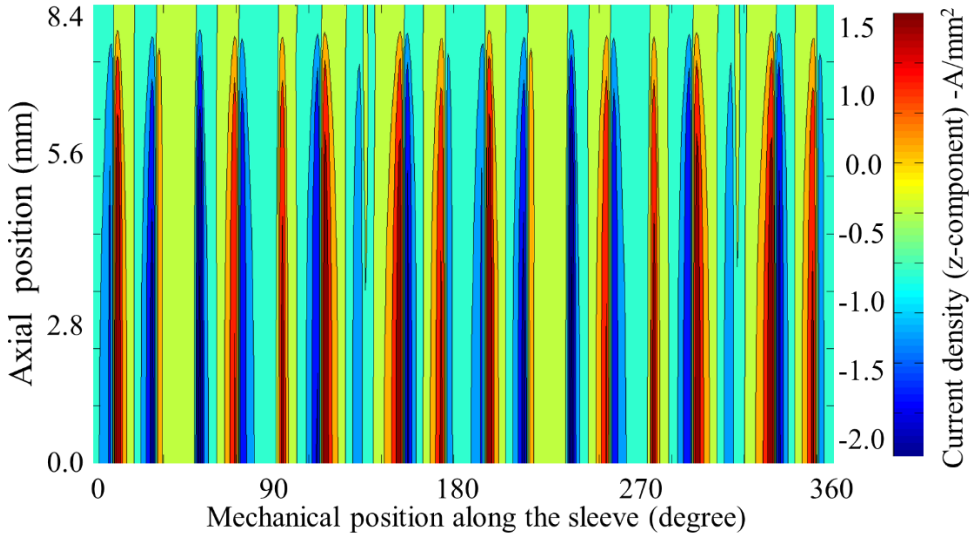

(a) Current density (J_{sl_z}) distribution from 3D-Fourier method

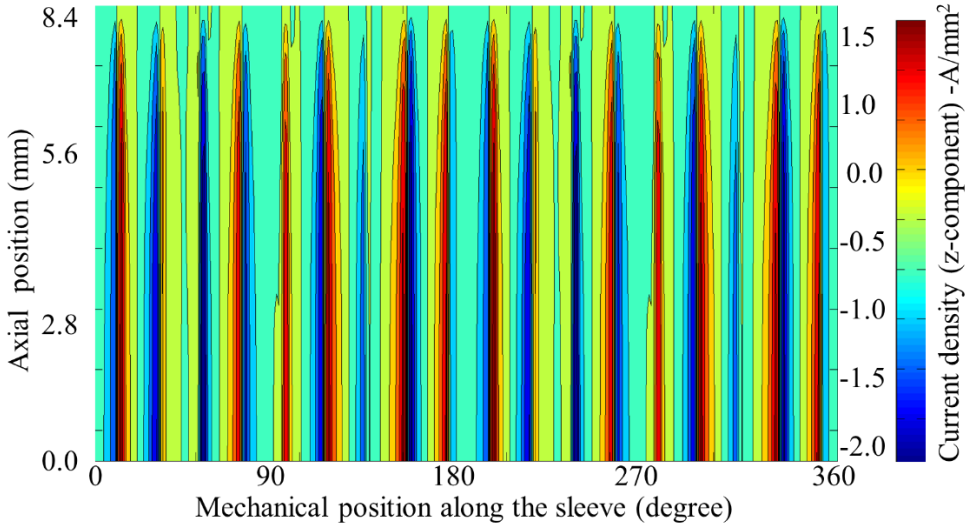

(b) Current density (J_{sl_z}) distribution from 3D-FE method

Fig. 7-7. Comparison of z–component of current density (J_{sl_z}) distribution from 3D analytical and 3D-FE method along the magnet surface defined by its mean radius (r = 32.7 mm, $0 < x < L_x, 0.5\,L_z < z < L_z$).

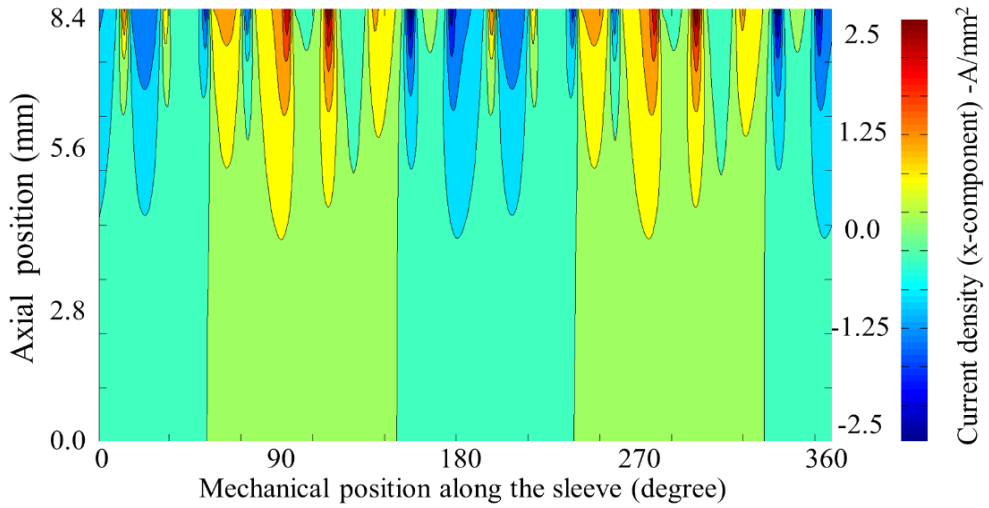

(a) Current density (J_{sl_x}) distribution from 3D-Fourier method.

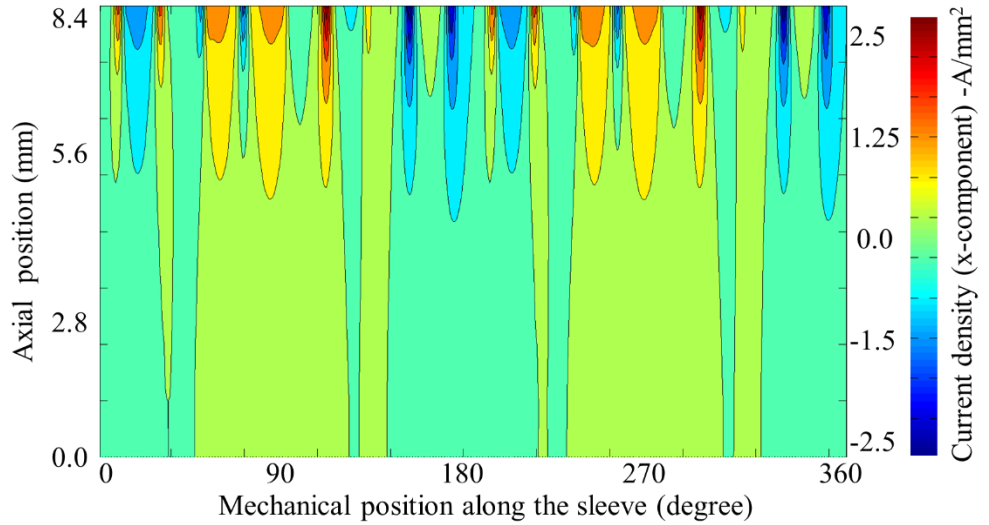

(b) Current density (J_{sl_x}) distribution from 3D-FE method.

Fig. 7-8. Comparison of x-component of current density (J_{sl_x}) distribution from 3D analytical and 3D-FE method along the magnet surface defined by its mean radius (r = 32.7 mm, $0 < x < L_x$,$0.5\ L_z < z < L_z$).

Fig. 7-9. compares the variation of z-and x-components of the current density along the sleeve position($0 < x < L_x$) predicted analytically and from 3D FEA at axial height = 12.65mm and at $y = 0.5\ L_y$ for the above mentioned operating conditions

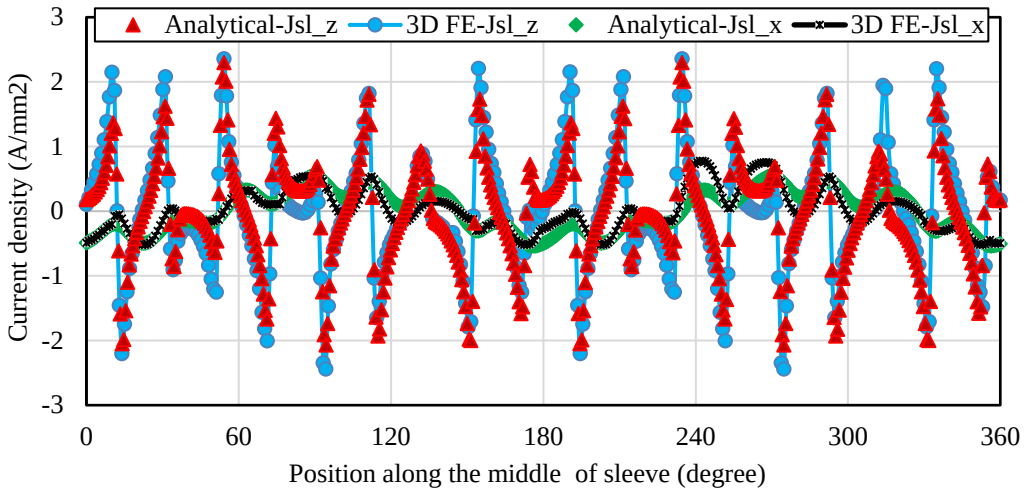

Fig. 7-9. Comparison of analytically and 3D EF predicted variations of $z-$ and $x-$components of eddy current density along $x-$ positions at $\omega_r t = 1.5^0$, $y = 0.5L_y$ and L_z = 12.65mm.

Good agreement between the two can be observed albeit few minor mismatches mostly in the $x-$component of current density which may be attributed to the curvature and the end winding effect which is neglected in the analytical method.

The magnet loss prediction is repeated with increase in axial number of segmentations at peak current conditions and at 4500 rpm using the proposed analytical method and 3D-FEA. The same is repeated also at no load conditions of the machine. The comparison of results obtained at no load from the proposed 3D Fourier method for the sleeve, 3D FEA and 2D FEA with increase in axial segmentation is shown in Fig. 7-10.

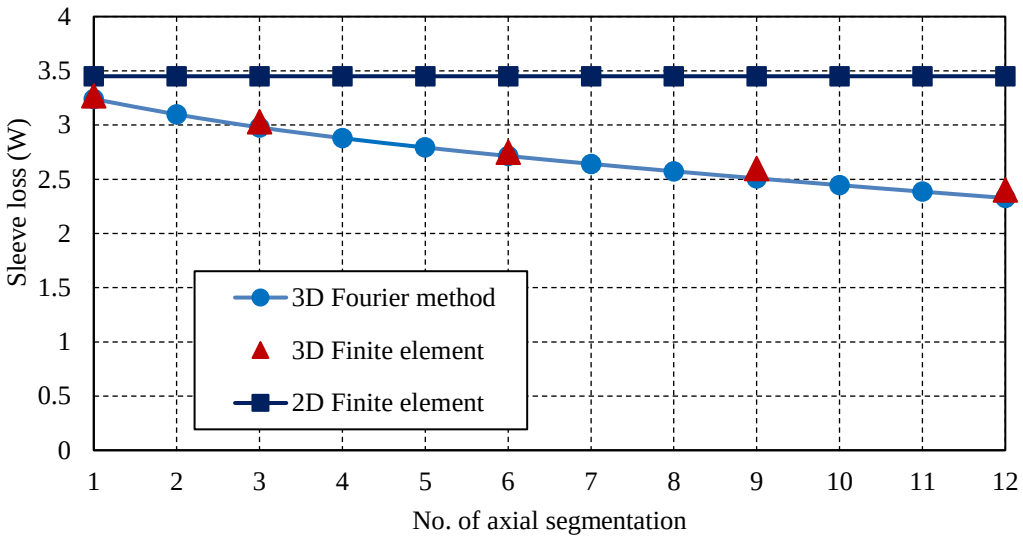

Fig. 7-10. Comparison of sleeve loss variations at no load with axial number of segments.

The variation of loss evaluated with the 3D imaging method, 3D FEA and 2D FEA at peak load conditions with increase in axial segmentation is shown in Fig. 7-11.

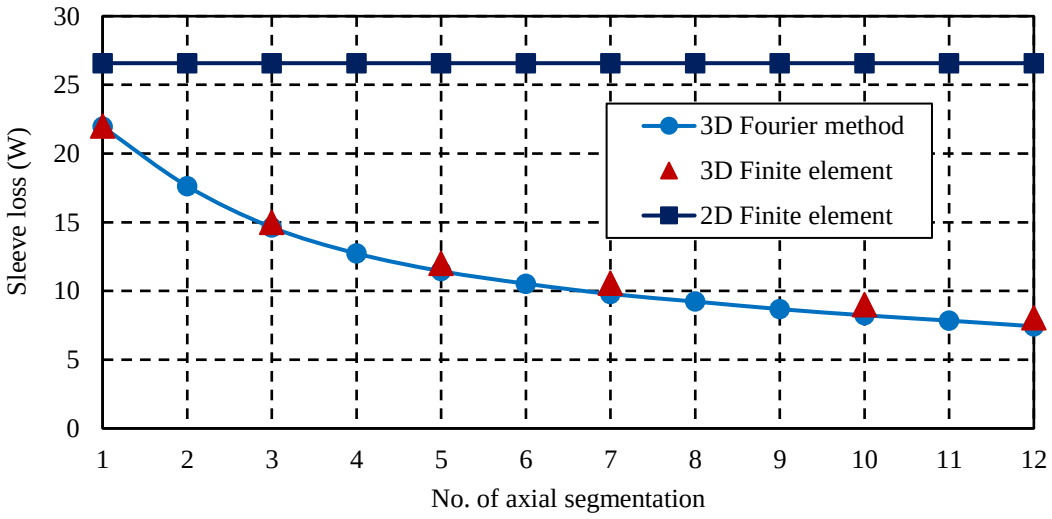

Fig. 7-11. Comparison of sleeve loss variations at peak load with axial number of segments.

It can be observed that the sleeve loss evaluated from the 3D imaging method matches very well with the 3D FEA results, while significant error occurs with 2D FEA with increase in the number of axial segmentations. Fig.

7-12 shows the instantaneous loss variation computed from the imaging method and its comparison with the 3D FEA with seven axial segments.

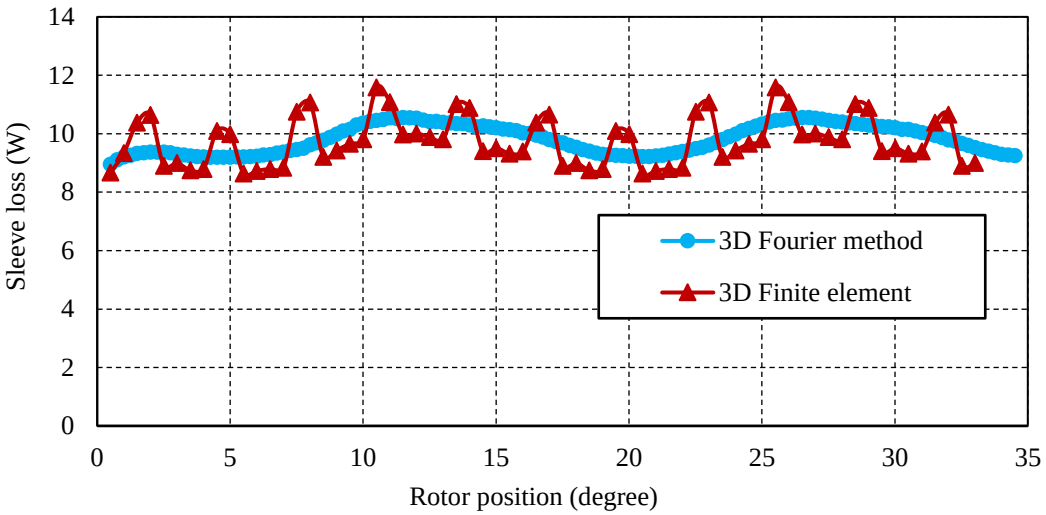

Fig. 7-12. Instantaneous variation of sleeve loss with time at peak load.

The results show that the eddy current loss in the retaining sleeve evaluated from the proposed method closely follows the 3D finite element calculations which exhibit small chattering and may be attributable to numerical computation errors.

The analytical solution of source components from the subdomain model allows to evaluate the different harmonic contents present in the eddy currents. As seen in Chapter 3 for the permanent magnets, it is observed that the major contributors for the sleeve loss are the harmonics of the orders 6, 18, 36 and 54. The variation of sleeve loss for each of these harmonics with increase in axial number of segmentation is shown in Fig. 7-13.

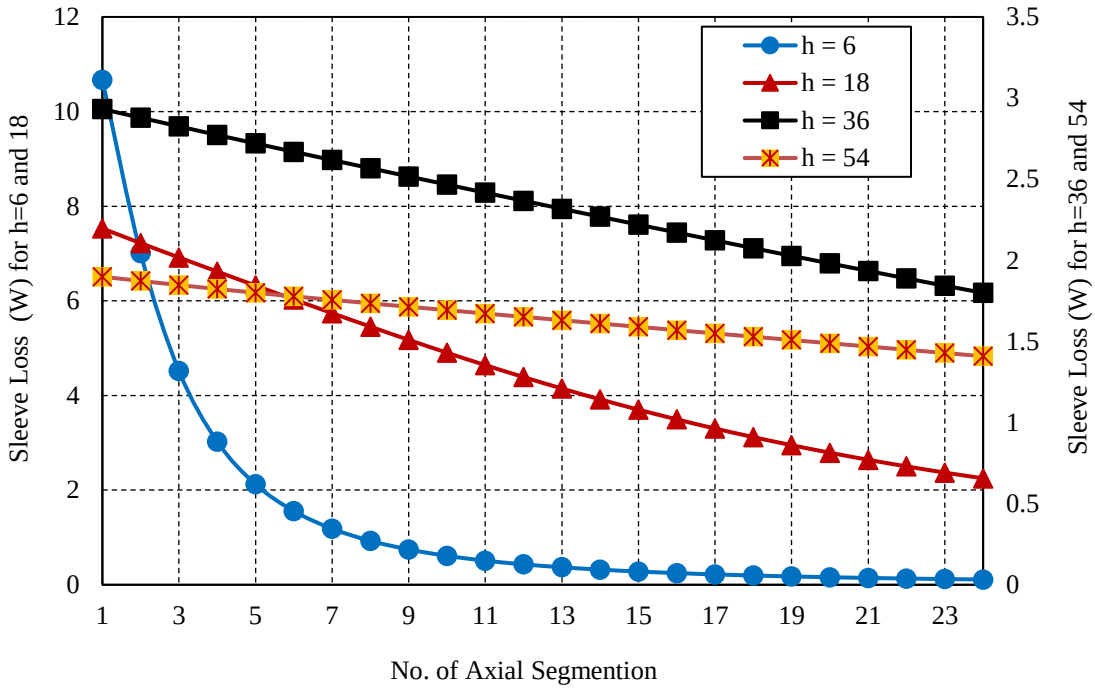

Fig. 7-13. Magnet loss variation of major harmonics with increase in axial number of segments when the 8-pole, 18-slot machine is operating with peak phase current at 4500 rpm.

It is clear from the figure that the rate of loss reduction with increase in number of segmentation decreases with increase in harmonic order. The same phenomenon is experienced with harmonic loss variation with increase in axial segmentations in Chapter 3. This is because the end effect is more pronounced for the lower order harmonics (harmonics with longer wave lengths) and it reduces with increase in the harmonic order.

7.5 Sleeve Loss Prediction at High Frequencies Considering Eddy Current Reaction Effect

The resistance limited eddy current assumption is valid in typical magnets and sleeve materials for frequency below ~2kHz. When the frequency of a field harmonic is greater than 2kHz, eddy current reaction effect become more pronounce.

As for the permanent magnets in Chapter 4, 5 and 6, to predict the eddy current loss in sleeves due to high frequency harmonics in the armature

current, 2D FEA results which account the eddy current reaction may be employed in the imaging method. As described in the previous chapters, the field variations within the sleeve employed in the proposed 3D Fourier method from 2D FEA overestimates the eddy current reaction effect and hence results in underestimation of sleeve loss evaluated. This is because skin effect forces the eddy current sources to be concentrated around the sleeve edges and its values are reduced at the center of the retaining sleeve. An inaccurate estimation of sleeve eddy current loss may result in underestimation of magnet operating temperatures, which in turn can increase the risk of partial demagnetization. Therefore, the axial variation of eddy current sources becomes necessary in accurate estimation of sleeve eddy current loss.

To Circumvent this problem a solution to the diffusion of the eddy current sources along the axial $(x-z)$ is derived in Chapter 4 for permanent magnets in SPM machines. For the case with retaining sleeve also the variation of the eddy currents along the axial plane can be expressed using the similar diffusion equation in terms of current density distribution J_s as shown in Fig. 7-14.

$$\frac{\partial^2 J_{sl\_z}}{\partial x^2}+\frac{\partial^2 J_{sl\_z}}{\partial z^2}-\mu_0\frac{1}{\rho}.\frac{d}{g}.\frac{\partial J_{sl\_z}}{\partial t}=\mu_0\frac{1}{\rho}.\frac{t_s}{g}.\frac{\partial J_s}{\partial t} \tag{7-33}$$

This is because,

1) As the thickness of the retaining sleeve is much smaller, the variation of the time derivative flux density S_{sl_y} along the radial direction can be neglected.
2) The contribution towards the loss from the tangential source variation S_{sl_x} is ~3 orders of magnitude lower than S_{sl_y}. The results are obtained when the SPM machine is supplied with 2.75 A peak (5% of the fundamental current employed for resistance limited loss prediction described previously) at 20kHz while operating at 4500 rpm. This is shown in Fig. 7-15.

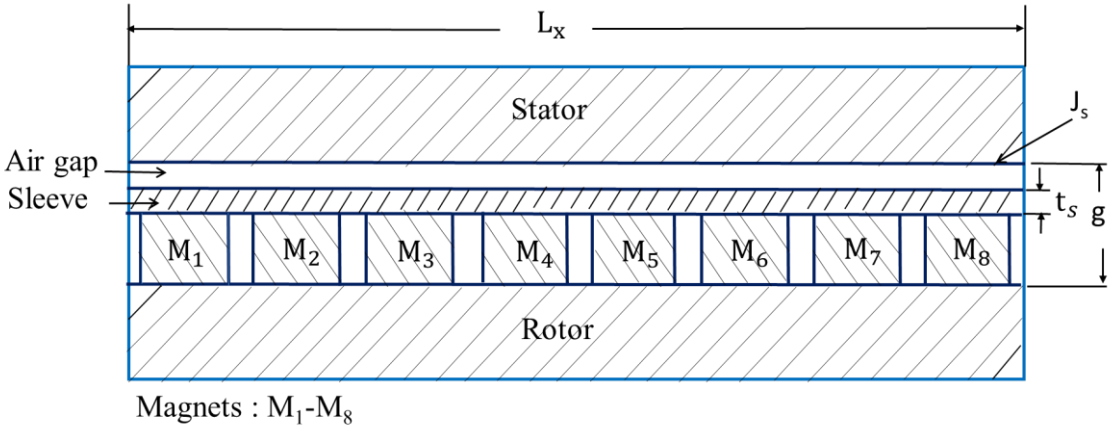

Fig. 7-14. Geometry and parameters of 2D eddy current diffusion model neglecting all curvatures.

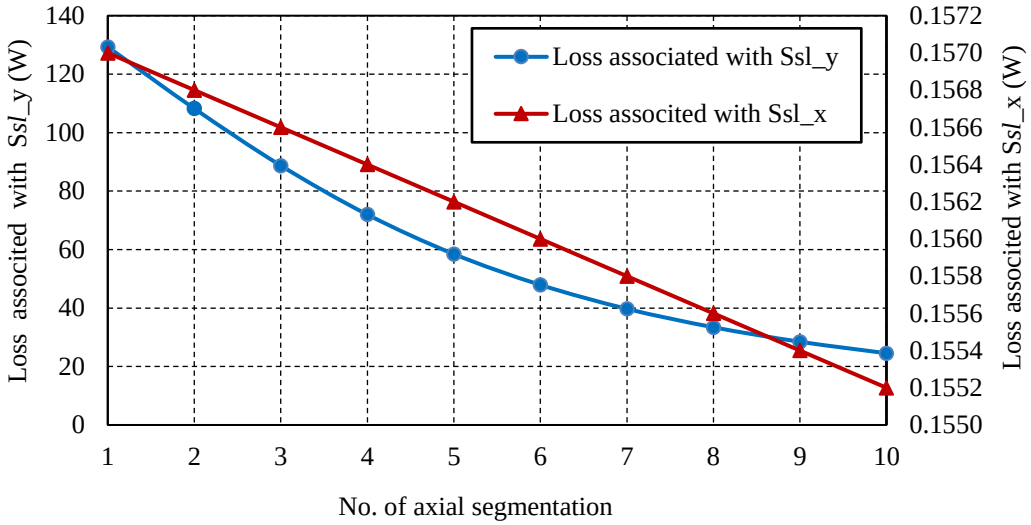

Fig. 7-15. Comparison of sleeve loss associated with source components when supplied with 2.75A peak phase current at 20Khz while the machine is operating at 4500 rpm.

The solution to Poisson's equation (7-33) is obtained for magnets satisfying its boundary conditions in in [92]. For the retaining sleeve of length L_x, an analytical solution can be derived in the similar manner by applying the eddy current density continuity law $\nabla . J_{sl} = 0$, and also forcing the tangential current J_{sl_x} to be zero at $x = \pm\frac{L_x}{2}$, such that

$$J_{sl\_x}(\mathrm{x} = -L_x/2) = J_{sl\_x}(\mathrm{x} = L_x/2) = 0.$$

where J_{sl_x} can be obtained as ,

$$J_{sl\_x} = -\int \frac{\partial J_{sl\_z}}{\partial z} dx \tag{7-34}$$

Applying Ohm's law for J_{sl_x} and J_{sl_z} along $\theta - z$ plane, the S_{sl_y} variations along the axial plane can be evaluated as,

$$S_{sl\_y}(x,z) = \frac{\rho}{L_y}.\left(\frac{\partial J_{sl\_z}}{\partial x} - \frac{\partial J_{sl\_x}}{\partial z}\right) \tag{7-35}$$

The solution of the diffusion equation (7-33) evaluating J_z and hence J_x is described in the Appendix B.

7.6 Method of Sleeve Loss Implementation and 3D FE Validation at High Frequencies

For implementing the high frequency loss evaluation in retaining sleeve, $[S_{sl\_y}(x,y)]_{2DFE}$ variations in the circumferential direction obtained from 2D FEA is adjusted by the ratio obtained from the analytical solution (7-35) to establish its variation along the axial direction. This relation is same as that for the magnets (4-10) as described in Chapter 4.

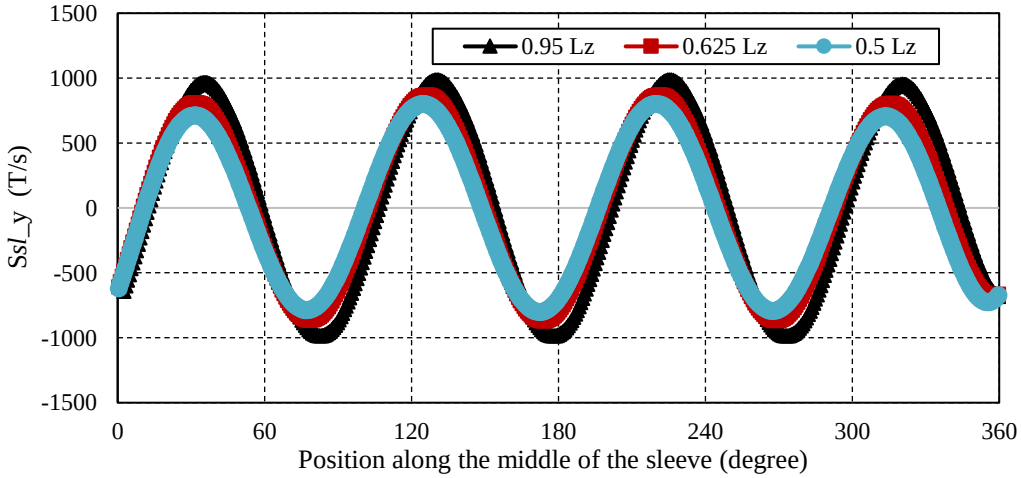

Fig. 7-16. Comparison of $S_{sl\_y}(x, 0.5y, z)$ at different axial positions evaluated from (7-35) at $\omega_r t = 1.5^0$(Number of axial segments =1).

The analytical solution given in (7-35) can be used to evaluate $S_{sl\_y}(x, y)$ for any time instant as shown in Fig. 7-16. However in implementing of the 2D FE source variations along the discretized volume of the sleeve it is sufficient to consider only the RMS values of these source variations evaluated analytically rather than the instantaneous values.

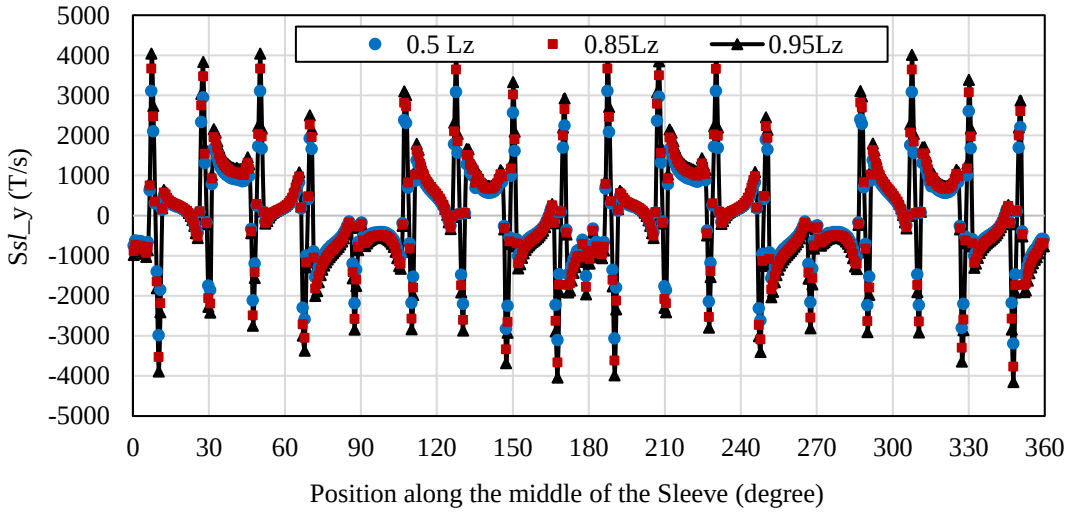

(a) Axial segments =1.

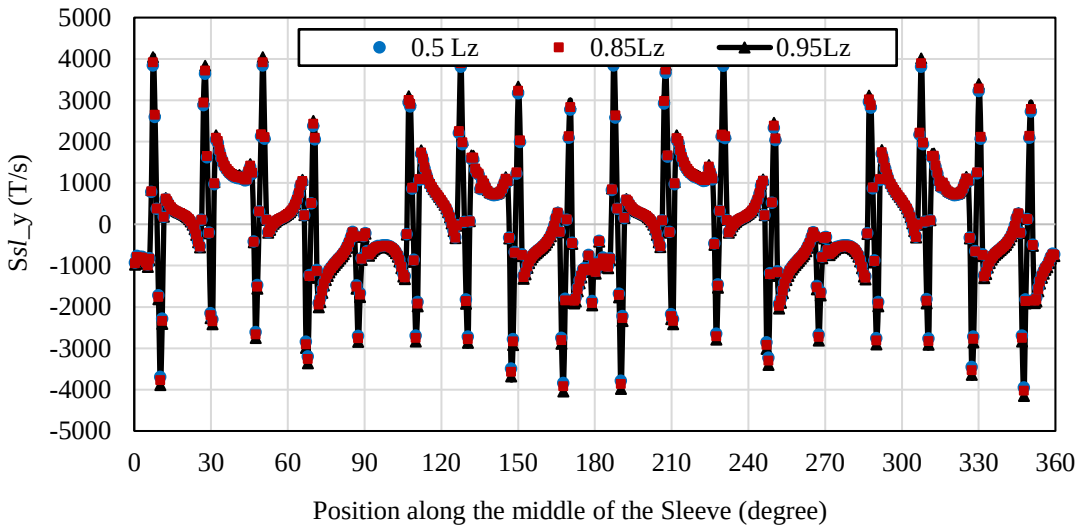

(b) Axial segments= 10.

Fig. 7-17. Comparison of $S_{sl\_y}(x, 0.5y, z)$ at different axial positions evaluated after the axial adjustment at $\omega_r t = 1.5^0$.

The axially adjusted 2D FE source variation $S_{yl}(x,y)$ employing (4.10) at $\omega_r t = 1.5^0$ at different axial positions ($z = 0.95L_z, 0.85L_z, 0.5L_z$) for the sleeve with one and ten axial segmentation is shown in Fig. 7-17 when the machine operates at 4500 rpm with 2.75A (5% of the rated) harmonic current at 20kHz.

As seen with the permanent magnets at high frequencies in Chapter 4, it is also observed that the axial source variations along the middle of the sleeve segment approaches the values at the edges as the number of axial segments are increased from one to ten. The whole process of implementation considering all the armature harmonics is demonstrated in the flow chart as shown in Fig. 7-18.

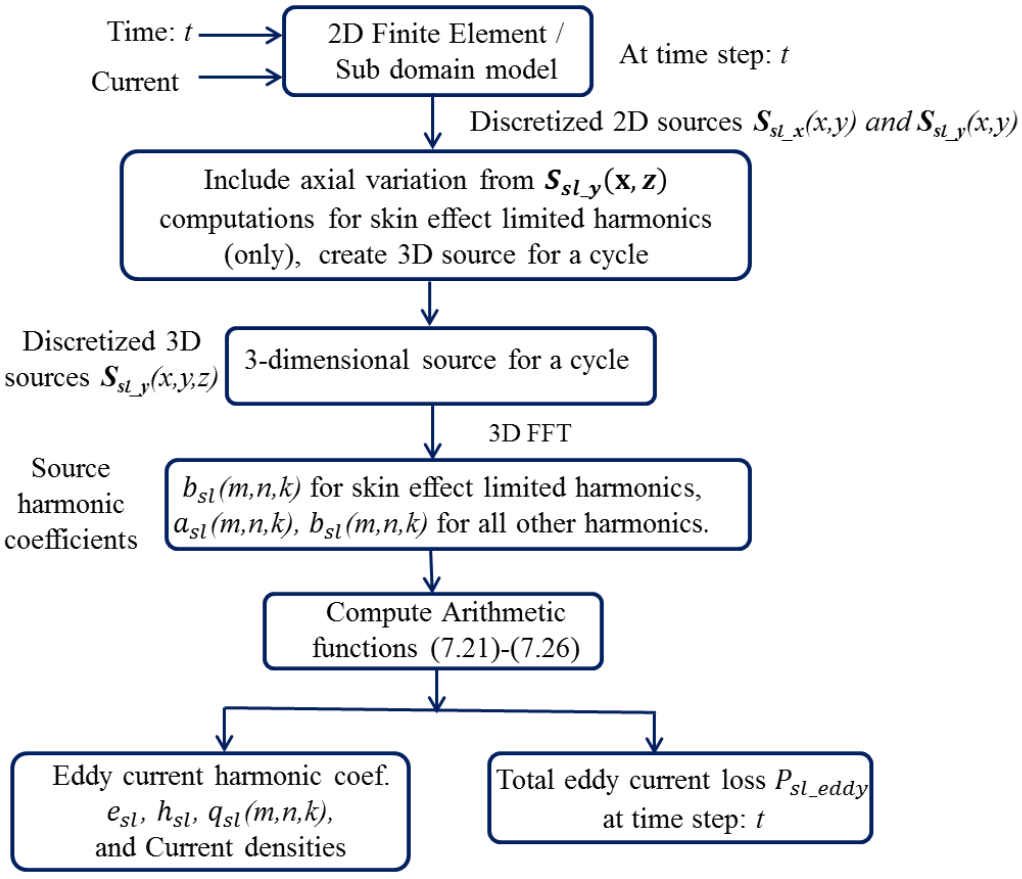

Fig. 7-18. Flow chart illustrating the prediction of sleeve loss at all frequencies.

The 3D imaging method is implemented to predict eddy current loss at 20 and 10 kHz with $S_{sl\_y}(x,y)$ variation along the axial direction under the same operating condition (4500 rpm) and current magnitude (2.75A peak) as

previously stated, and the results are also obtained by employing the imaging method with source values obtained directly from 2D FEA with and without considering eddy current reaction. To verify the results 3D FEAs are conducted for prediction of eddy current losses at the same frequencies and operating condition.

Variations of sleeve loss predicted with different number of axial segmentations at 20 kHz and 10 kHz, and their comparison with 3D FEA results are shown in Fig. 7-19. For the sake of discussion, the predicted loss variations by the 3D Fourier method which employs 2D FEA field sources with and without account of eddy current reaction are also shown.

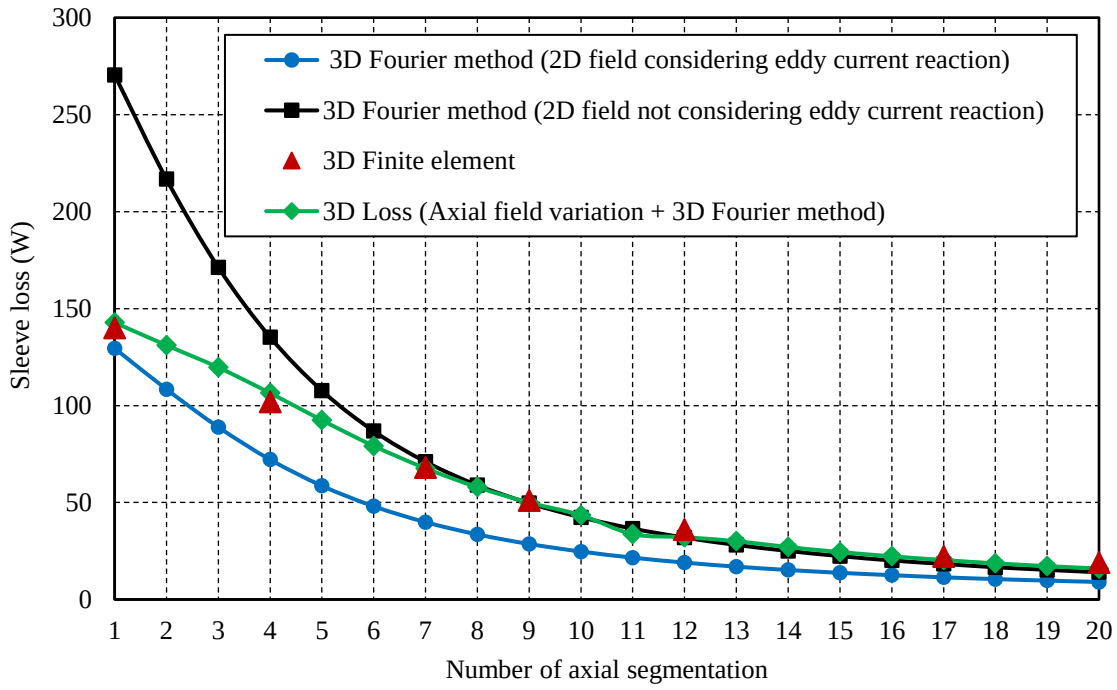

(a) Loss variations at 20kHz

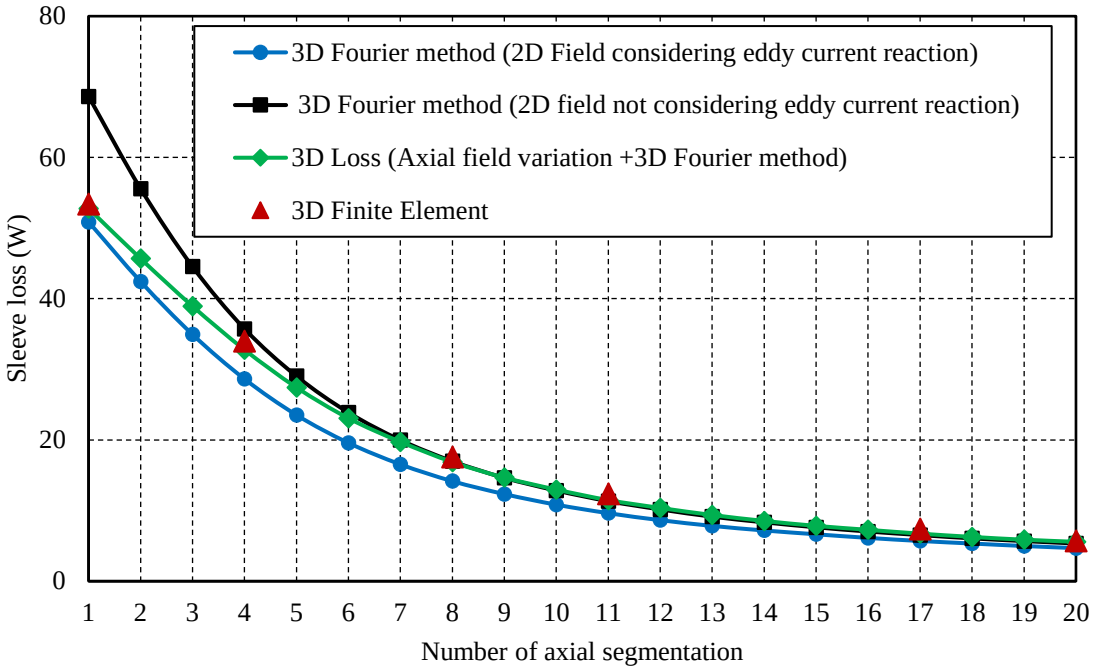

(b) Loss variations at 10kHz

Fig. 7-19. Comparison of sleeve loss variation with axial number of segments at 10 and 20 kHz when supplied with 2.75 peak phase current at 4500 rpm.

It is evident that the losses predicted from the proposed method agree well with the 3D FE results. It is worth noting that results obtained from the imaging method with 2D FE source data without considering eddy current reaction are much higher than the 3D FE predicted values when the segmentation number is lower, however they become closer to the 3D FE results at very high segmentation numbers. This is because with a large number of axial segments, the eddy current flow is significantly curtailed and hence its reaction becomes weak. In contrast, the predicted losses by the image method with 2D FE source data which account the eddy current reactions is lower than the 3D FE results because the eddy current reaction by 2D FE is overestimated.

It is important to note that while the loss in the sleeve associated with the 55A peak fundamental current at the maximum speed of 4500 rpm is comparatively low, the loss at 10 kHz or 20 kHz even with 5% of the fundamental is significantly higher when the number of axial segmentation is

low. This illustrates the need for carefully assessing the loss in the rotor due to high frequency current harmonics which are likely to be present due to inverter switching and current tracking error as explained in Chapter 5.

7.7 Computational Efficiency of the Proposed Method

The entire process is implemented in Matlab, and it takes around 90 minutes to generate the flux density harmonic information from the subdomain model and less than 30 seconds to compute the total 3D eddy current loss in the sleeve in a typical PC. Hence on an average for evaluating the sleeve loss variation with increase in axial number of segmentations up to 12, it takes around 8 minutes for each case, in contrast more than 7 days is usually required for one 3D FE analysis with no axial segmentation and almost 1.5 days for the case with 10 axial segmentations. The large increase in computation time can be attributed to the half the machine geometry and also the fine meshing employed for the sleeve in the 3D FE computations.

Also the high frequency loss evaluation can be conducted with an average time span of about 20 minutes for each case while the 3D FEA needs more than 10 days to complete the simulation for the axially unsegmented sleeve in the machine. As with the permanent magnets discussed in previous chapters, the whole analysis is performed on a 12 core, 64 GB RAM computer.

7.8 Conclusion

A computationally better efficient method for predicting resistance limited 3D retaining sleeve eddy current loss of SPM machines has been developed based on 3D Fourier method. The proposed method considers (1) slotting effect, (2) radial and tangential field variations inside the sleeve and also (3) the interaction of the different source harmonics. High frequency eddy current loss prediction in the sleeve is carried out by employing the proposed, with 2D FE predicted source distributions modified by accounting diffusion

in the axial direction. The developed method considers the axial variation of the magnetic field along the sleeve and also the field variations along the radial directions. It is observed that the sleeve loss contributed by the tangential component is quite negligible at high frequencies when compared to the radial field.

As discussed in Chapter 5, for SPM machines, magnetic saturation is usually not significant, and hence the total eddy current loss in the sleeve can be obtained by sum of the eddy current loss associated with each frequency component.

CHAPTER 8
Demagnetization Assessment of Permanent Magnet Machines and Post Fault Performance Prediction

8.1 Introduction

It can be understood from the discussions in the previous chapter's that 3D eddy current loss in permanent magnets are more prominent at higher speeds where the magnetic field variations are at the increased rates. Hence the permanent magnets in those machines which are operated on an extensive range of speed in the constant power region employing field weakening control [144, 168] significantly suffer eddy current losses which may, in turn, lead to increase in their operating temperatures. The overall machine temperature can increase during continuous operations at higher speeds since the machine iron loss surges at deep field weakening conditions, also as only a part of the armature current is being utilized for generating the useful torque while the rest of the current is required for controlling the main flux to limit the voltage, causing large copper loss.

The increase in temperature can shift the operating point of each magnet segment of the PM machine to a lower BH curve with an increased knee point flux density value consistent to its new operating temperature. Also the magnet flux density may be further pushed towards the vicinity of the knee point with the introduction of d-axis current to control the air-gap flux at deep field weakening operation [168]. These both conditions together can increase the risk of partial irreversible demagnetization. Hence especially the IPM machines which are inherently required to be operated over an extensive range of speed are to be designed with adequate demagnetization withstand capability at its extreme operating temperature and at its maximum speed when field weakening control is employed [169-172] .

The risk of irreversible demagnetization in IPM machines operating at increased magnet temperatures can be intensified further in the event of a transient short circuit at field weakening conditions [30]. Under the event of a sudden short circuit due to the inverter failure while functioning at its peak torque, the transient phase currents in the machine can be much higher than its maximum designed rating and the resultant large d-axis current may cause partial demagnetization [173]. The extent of demagnetization is dependent on the magnet working temperature under such operating conditions. A more serious event may be occurring if the inverter loses its synchronization with the back EMF of machine, resulting into an opposite voltage being applied at the terminals and evolving a sudden surge of phase currents. Hence a comprehensive partial demagnetization assessment at the worst ever operating condition is necessary at the design stage of the PM machine to understand and to minimize its impact.

There exist a number of partial demagnetization models in the literature for assessing the risk of irreversible demagnetization in PM machines. The models described in [128] and [174] are intended to diagnose partial demagnetization in a PM machine based on the torque spectra and the magnetic circuit characteristics, respectively, under an event leading to partial irreversible demagnetization. While the consequence of the partial demagnetization can be quantified by these two approaches, the pattern of demagnetization and their causes are not analysed. H. Xiong *et al.* [175] analyses the asymmetrical demagnetization pattern due to inhomogeneity in various magnet samples using a C-core test fixture, however fails to provide any insight on how these varying properties really affect the demagnetization behaviour inside an electrical machine under the harsh working conditions. A rough estimate of the demagnetizing current while designing an SPM machines is given in [176] approximating almost the same magnetic field in the magnets and also in the slot opening regions. An analytical approach to assess the partial demagnetization by superposing the armature reaction fields in the magnets for a quasi-Halbach magnetized tubular PM machine is

developed by J. Wang *et al.* in [177]. However, the analytical approach is not applicable to IPM machines which have complex rotor geometry and high level of magnetic saturation.

Demagnetization assessment for numerous IPM rotor types is carried out by K. Ki-Chan *et al.* employing average flux density distribution in different magnet segments at various load angles in [178]. However, this approach does not accommodate the direction of flux density with respect to the direction of magnetization, hence leading to incorrect results for partial irreversible demagnetization. The partial demagnetization is predicted in all these models when the magnet operating point along the B-H curve goes below the knee point flux density. However, they are incapable of predicting the extent of partial demagnetization since the magnets are not totally demagnetized even if they operate below their knee points. Consequently, these methods cannot be used to predict the post demagnetization performance of a PM machine.

To address this issue, a number of demagnetization models have been proposed in literature which can track the history of partial demagnetization, hence, enabling a means for predicting the machine post demagnetization performance. S. Ruoho *et al.* [179] compares a number of simplified demagnetization models for an overheated and overloaded SPM machine. The most promising model among them capable of tracking history-dependent hysteresis accounts for both the magnitude and direction of magnetization of permanent magnet. However, the method fails to describe the Nd–Fe–B magnet behaviour precisely. A model reported by K. Gyu-Hong *et al.* in [180] accounts for the change in remanent flux density of the magnet elements when they operate below the Knee point. Y. Zhilichev in [181] employed recoil lines to predict the magnetization vector when the magnet operating points have fallen below the knee of the demagnetization B-H curve. This method is incorporated in [29] and [28] to estimate the combined effect of temperature and the demagnetization in PM machines. However, these models are not

validated with experiments to predict the results on post-demagnetization performance.

Under different stator turn fault conditions demagnetization assessment of an IPM machine is performed in [182] and [183], and also owing to a controller limited fault current is estimated in [129] by updating the magnet elements with new remanence values following partial irreversible demagnetization. The post-fault performance of the machine is assessed and also verified by experiments with limited accuracy. A similar concept is used to assess PM demagnetization under diverse fault conditions in [184] and [185] for a distributed wound IPM machine, but no experimental validation on the post-fault performance is given. Post demagnetization assessment under fault conditions is used in [186] to investigate the role of flux leakage paths in demagnetization pattern for both fractional and distributed winding PMSM.

Demagnetization assessment of permanent magnet brushless machines employing fractional-slot winding configuration under worst case faults, and its comparison with distributed wound PM machines is reported by V. I. Patel *et al.* [173] . It is observed that compared to fractional-slot PM synchronous machines, the distributed wound PM synchronous machines have symmetrical and uniform demagnetization in all magnets. Although it is observed that some of the magnets in fractional-slot PM synchronous machines are more demagnetized compared to distributed wound PM synchronous machines, the overall partial demagnetization of the machine is more in distributed wound PM synchronous machines. The method predicts the resultant back EMF post partial demagnetization to be symmetrical in distributed wound PM synchronous machines, however fails to estimate its values. This is because, this method is incapable to evaluate a continuous demagnetization procedure as the remanence of each permanent magnet element is not updated in the event of partial demagnetization and its new value is not incorporated in the subsequent step of the transient analysis. This can result in the overestimation of the extent of partial demagnetization as

the short circuit current in an event of fault is not being reduced after each step subsequently following demagnetization.

To date the worst case demagnetization scenario has not been comprehensively assessed for IPM machines. Also in addition, the post demagnetization performance so far estimated in the literature is mostly confined to the study of change in machine back EMFs and the reduction in torque after an event of partial demagnetization has not been quantified extensively. Also the increase in the phase currents post demagnetization to generate the rated/ peak torque is not quantified.

Therefore, this chapter provides a comprehensive assessment to the risk of partial irreversible demagnetization for the IPM machines under an event of symmetrical faults by employing a continuous demagnetization model and to predict the machine post fault performance. The results obtained are compared with the method described in [173]. The performance of the IPM machine after a drive failure, causing the loss of synchronization of the applied voltage with the machine, is evaluated as the worst case failure. The results from the FE model are also validated by experiments in which the machine has lost its synchronization when operating at high speed with excessive current in the deep field weakening.

The main contents of this chapter is published by the author in [J5], as detailed in Section 1.8.

8.2 Continuous Demagnetization Analysis using 2D FEA

As discussed previously, in order to assess the continuous demagnetization, it is essential to track the flux density in the direction of magnetization for every magnet element in the FE model of a PM machine distinctly with respect to the knee point flux density at a specified operating temperature. In the presence of armature reaction field, if the flux density of any magnet element evaluated has gone below the knee point flux density as

shown in Fig. 8-1, it will be operated on a new BH curve with reduced remanent flux density [180].

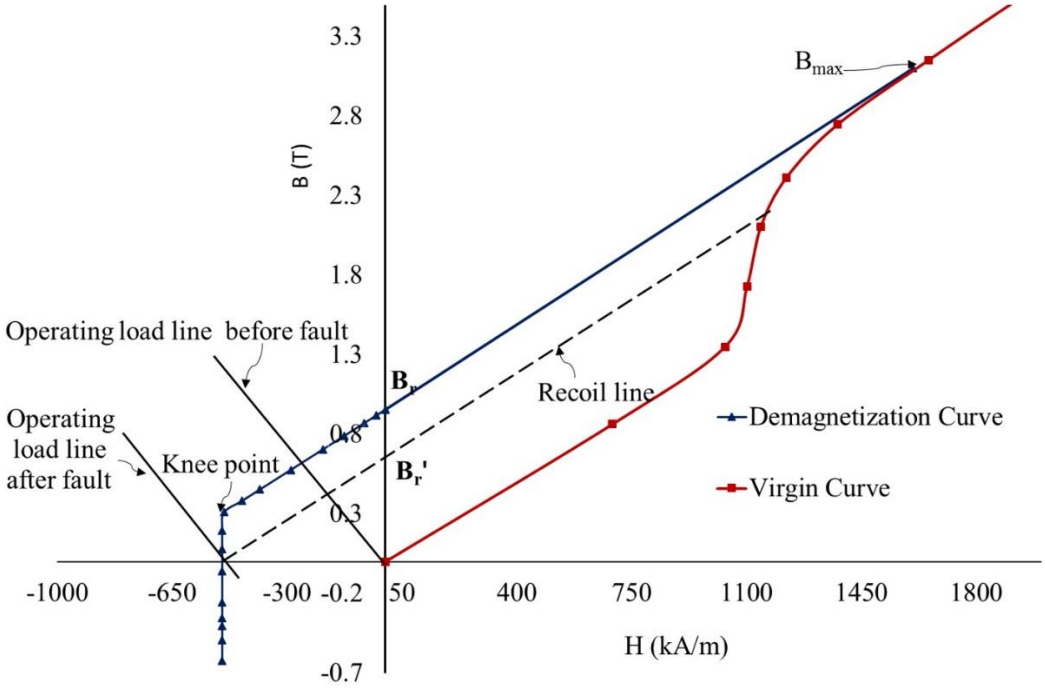

Fig. 8-1. Demagnetization B-H curve with virgin curve for the material L35EHT at 180° C explaining partial demagnetization.

The new B-H curve for operation is denoted as the dotted line in Fig. 8-1, and is determined by the recoil line and its intersection with the vertical axis. This demands the model to keep the history of partial irreversible demagnetization for every element of the magnets and to reassign its magnetization levels in an efficient way to assess the demagnetization levels and to estimate the machine performance under extreme or fault conditions.

The approach employed in this chapter uses B-H curves in the second and the third quadrant to consider partial demagnetization, while the virgin curve of the magnets shown in Fig. 8-1 is used to determine the initial material magnetization in the absence of external fields [187]. Sintered Neodymium-Iron-Boron (NdFeB) magnets of grade N35EH with its B-H characteristics [188] shown in Fig. 8-2 is used for demagnetization study in this chapter.

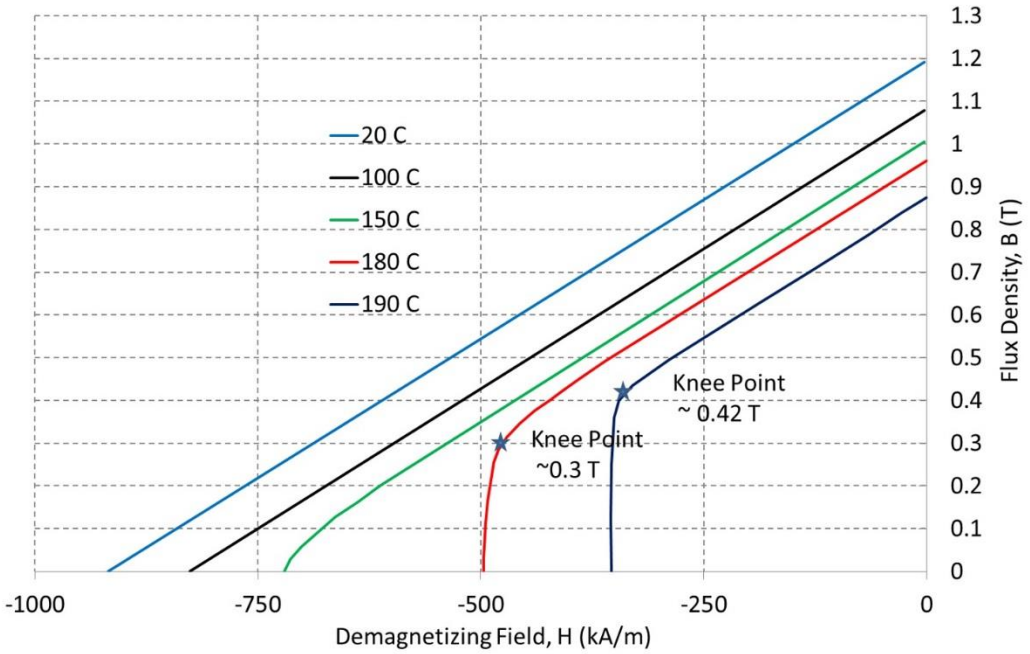

Fig. 8-2. Demagnetization characteristics of N35EH magnet.

To start with the demagnetization analysis, flux density components, for every magnet element need to be referred to the global XY coordinate system based on their angle of magnetization. For example in an IPM machine these components, $B_{mag}X_{Pn}$ and $B_{mag}Y_{Pn}$ are denoted in the XY coordinate system as shown in Fig. 8-3 for each magnet element. They are evaluated individually based on their angle of magnetization θ_P as,

$$B_{mag}X_{Pn} = B_{max}cos\theta_P \tag{8-1}$$

$$B_{mag}Y_{Pn} = B_{max}sin\theta_P \tag{8-2}$$

where B_{max} is the saturation flux density achieved during magnetization of the magnet, which is the flux density value at the intersection of the B-H curve with the virgin curve as shown in Fig. 8-1 and the subscript 'n' denotes the n^{th} element of the P^{th} magnet.

As an example, the decomposition of B_{max} for the n^{th} magnet element in the P^{th} magnet (P =1 and 2) of an IPM machine is shown in Fig. 8-3 . The

magnetization of each magnet element is calculated as in (8-1), (8-2) and the slope of BH curve is decided by the recoil permeability of the magnets.

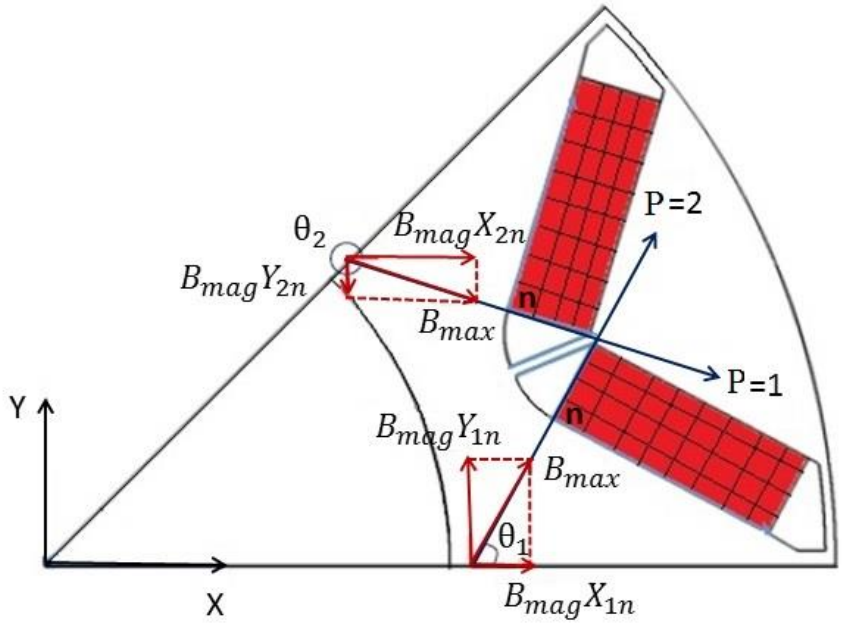

Fig. 8-3. Decomposition of element flux density of a magnet in the direction of magnetization.

After the first step of the transient FE analysis the flux density B_{Pn} observed in the direction of magnetization for each element n of the P^{th} magnet is decomposed in to the X-Y components given by,

$$B_{demag}X_{Pn} = B_{Pn}cos\theta_P \tag{8-3}$$

$$B_{demag}Y_{Pn} = B_{Pn}sin\theta_P \tag{8-4}$$

The B-H curve model for each magnet element is updated and also stored based on the flux density values calculated by (8-3) and (8-4). This process repeats in every transient step of the analysis, thus maintaining the information regarding the minimum flux density observed for every element of the magnets during its course of operation. If the flux density in a magnet element during a transient step is above the knee point of the material B-H curve for a given temperature, the remanence defined for the magnet element will not be changed. If, however, the flux density is below the knee point, the

B-H curve of the element for the subsequent step will be redefined by plotting a recoil line generated from the new minimum flux density as shown in Fig. 8-1 . This calculation is repeated for every element, and hence different elements of a magnet might be operating on different magnetization levels following an event of uneven partial demagnetization. The new value of the minimum flux density calculated in the X and Y directions is updated and stored for all those elements which have their flux density gone below their previously updated value before proceeding for the following step [189]. The whole process of demagnetization analysis is illustrated in the flow chart shown in Fig. 8-4 .

To evaluate the extent of partial demagnetization after operation, the magnitude of the minimum value of the flux density achieved in the n^{th} element of P^{th} magnet along the direction of magnetization can be calculated as,

$$B(min)_n = B_{demag} X_n cos\theta_P + B_{demag} Y_n sin\theta_P \tag{8-5}$$

It is evident that partial demagnetization is said to have occurred if this value has gone below 0.3T at 180°C and 0.42T at 190°C, as shown in Fig. 8-2 . These values can be identified as the knee point flux densities for the corresponding BH curves, as the curves change their slope from the product of relative permeability of the magnet material and the permeability of the free space ($\mu_r \mu_0$) to a much higher value at them. By assessing the minimum flux density in each element of every magnet, the percentage of the demagnetization of the magnet can be evaluated for a particular temperature of operation. This method can be extended to any operating temperature by providing corresponding temperature dependent B-H curves for the magnet under consideration.

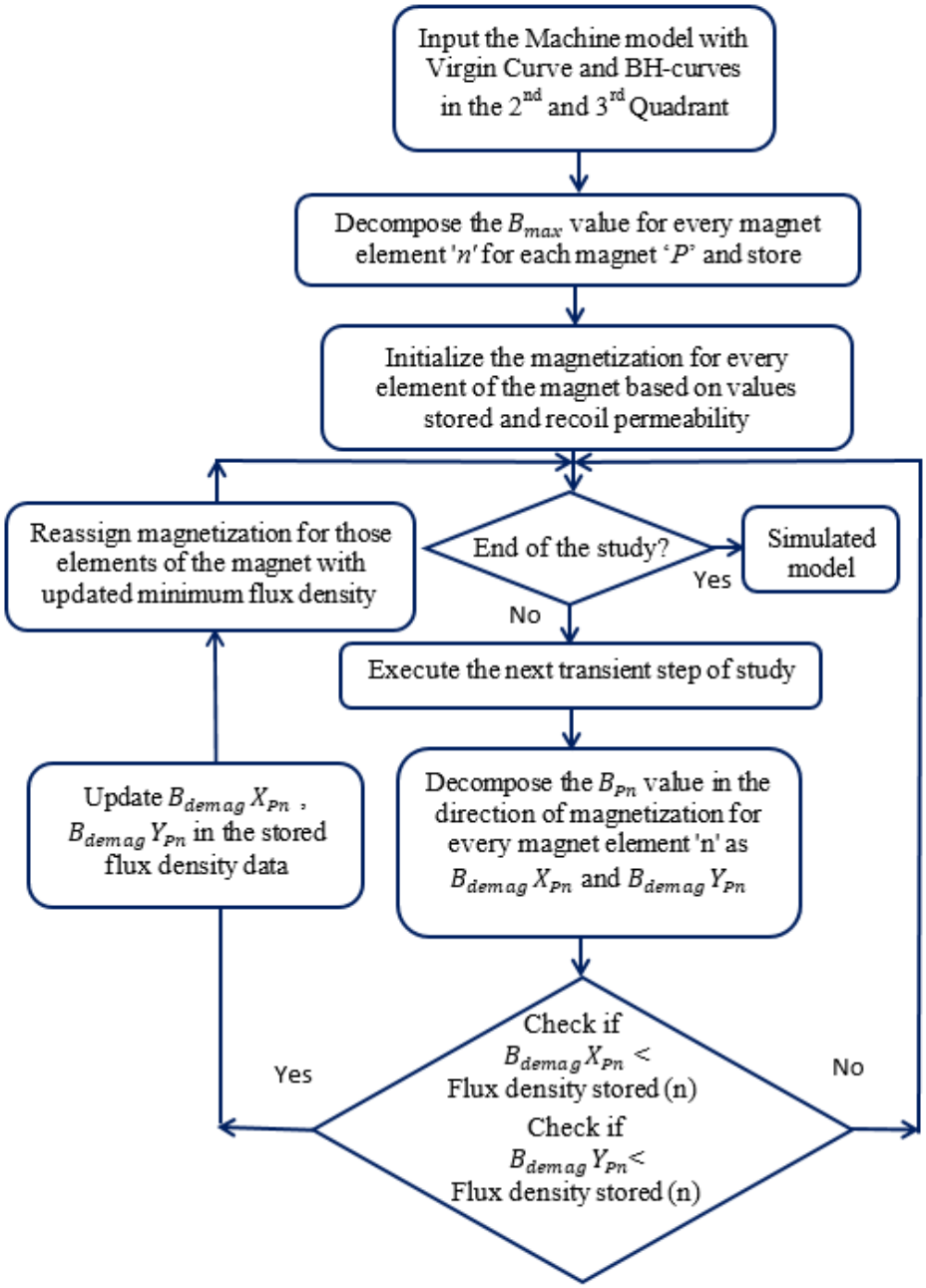

Fig. 8-4. Flow chart of partial– demagnetization analysis of proposed model.

8.3 Demagnetization Assessment in IPM Machines

Without loss of generality, a 6-phase, fractional slot IPM machine with 8-pole, 18- slot combination devolved as part of the FP7 CASTOR project [190] is considered for demagnetization studies. The machine is developed to enhance

drivetrain availability and to improve safety in traction application [169]. Enhanced availability is inherently assured for this machine [191], as loss of one 3-phase system will not lead to a complete loss of traction power. The machine design is optimized to achieve best possible torque production at the base speed whilst minimizing the losses over the representative driving cycle. i.e., New European Driving Cycle (NEDC) as per the procedure described in [192] and/or [193]. The cross-section of the IPM machine is shown in Fig. 8-5. For the machine under consideration, the machine enclosure is designed to carry cooling medium, i.e., water around the housing in a sealed environment for better thermal management.

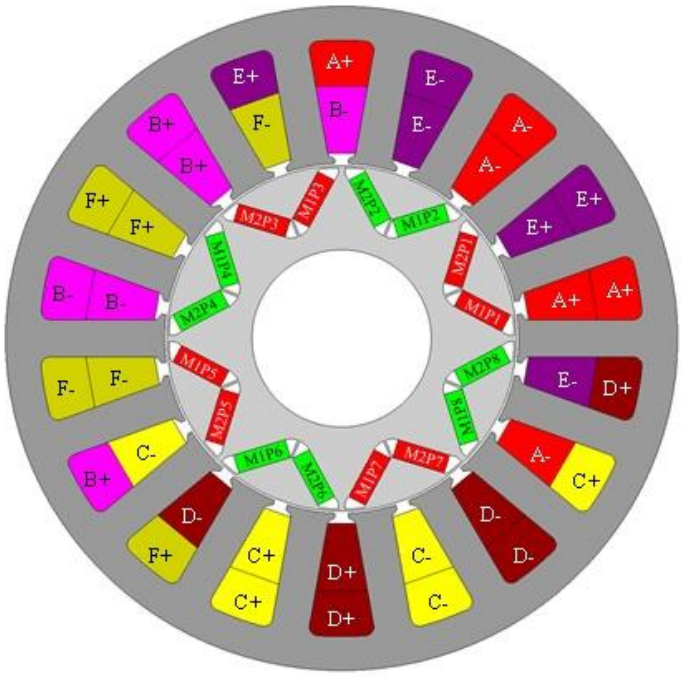

Fig. 8-5. Cross-section of 6-phase, 8-pole, 18-slot, IPM machine.

The machine winding comprises of three series connected coils wired around the neighbouring teeth with polarity as indicated by "+" and "-" and phases are denoted as A, B, C, D, E, and F. The magnets in the IPM are shown in green and red as specified by M_iP_j, where i = 1, 2 denotes i^{th} magnet of the j^{th} rotor pole (j = 1 to 8). The phase shift between the two set of A-B-C and D-E-F windings is 20° electrical, which is achieved by 13 slot-shifts [194]. The design

parameters of the IPM machine and the performance at the peak and the rated torque with magnet properties at 150°C is tabulated in Table 8-1 and Table 8-2 respectively.

Table 8-1. Design Parameters of IPM Machine under Consideration

Design parameter	Unit	Value
Stator outer radius	mm	75.0
Motor stack length	mm	150.0
Air-gap length	mm	0.5
Rotor radius	mm	39.0
Shaft radius	mm	20.0
Stator slot depth	mm	27.82
Stator tooth width	mm	8.38
Stator slot opening	mm	3.0
Stator slot opening depth	mm	1.0
Length of magnet	mm	4.2
Width of magnet per pole	mm	24.0
Magnet pole arc	°elec.	120
Magnet pole cap depth	mm	10
No of turns per coil	-	10
No. of coils per phase	-	3
Magnet mass (NdFeB)	kg	0.9
Post and bridge thickness	mm	0.5

Table 8-2. Performance Indicators of the Machine under Consideration

Performance indicator	Unit	Value	
		Rated	Peak
Torque	N·m	75.0	140.0
Torque ripple	%	2.4	5.0
Speed	rpm	2800	2800
Peak phase current	A	79.5	205.0
Current density	A/mm2	10.4	26.9
Copper loss	W	1004	6677
Iron loss – Stator	W	159	257
Iron loss – Rotor	W	28	47
Magnet eddy current loss	W	11	72
Efficiency	%	94.8	85.3
Energy efficiency over the NEDC	%	94.9	

The 2D transient FEA of the machine is carried out using the commercial FE software (Opera 2D) in which the partial demagnetization model described in section 8.2 is implemented. M270-35A electrical steel is used for

constructing both laminations of the stator and the rotor. For demagnetization analysis, magnet working temperature of 180°C is considered.

The demagnetization study in this chapter focuses on the fault conditions, listed in Table 8-3 , which are most critical with respect to partial irreversible demagnetization. Faults F1 to F6 are short circuit faults while F7 to F12 considers the worse scenarios when the voltage vector has erroneous 180 electrical degree offset with respect to the back EMF due to faults in the position sensor and/or the controller.

Table 8-3. Fault Conditions under Consideration

	Fault	Pre-fault operation	Torque (N·m)	Speed (rpm)
F1	6-phase short-circuit	Rated torque	75	2800
F2	6-phase short-circuit	Peak torque	140	2800
F3	3-phase short-circuit	Rated torque	75	2800
F4	3-phase short-circuit	Peak torque	140	2800
F5	6-phase short circuit	Rated power	19.1	11000
F6	6-phase short circuit	Peak Power	27.8	11000
F7	6-phase voltage reversal	Rated torque	75	2800
F8	6-phase voltage reversal	Peak torque	140	2800
F9	3-phase voltage reversal	Rated torque	75	2800
F10	3-phase voltage reversal	Peak torque	140	2800
F11	6-phase voltage reversal	Rated power	19.1	11000
F12	6-phase voltage reversal	Peak power	27.8	11000

For 2-D transient FEA, the current sources are connected in parallel with the switches which can be turned on at a specific rotor position with regard to the line to line voltage at its peak or zero value when a short circuit occurs as shown in Fig. 8-6. For considering the voltage reversal fault due to controller losing synchronization, voltage sources are connected in parallel to the current sources disconnected with switches which can be turned on in sequence without affecting each other as shown in Fig. 8-7. These voltage sources are two set of 3 phase sources similar to current sources having an

amplitude of 184.75V (184.75= 320/ √3, 320 is the line to line voltage =dc supply voltage). The phase shift for these voltage sources can be set precisely w.r.t the phase of generated back EMFs.

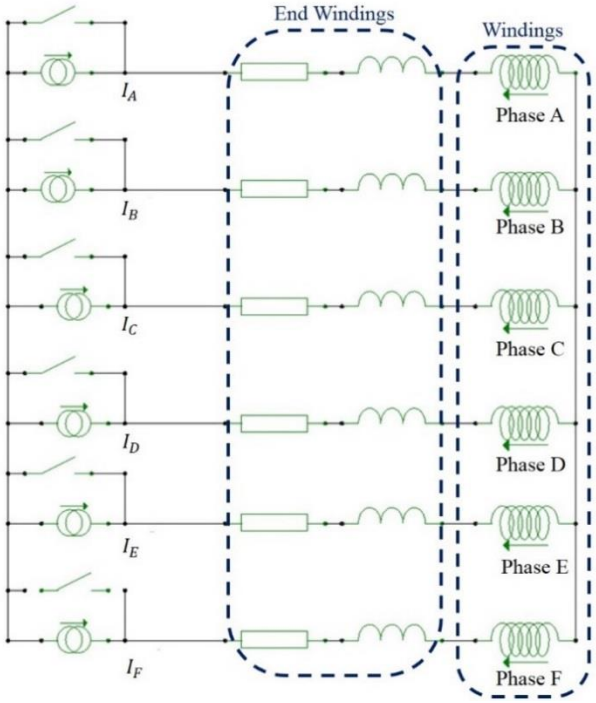

Fig. 8-6. Circuit model for creating short circuit fault (F1 to F6) in 2-D transient FEA.

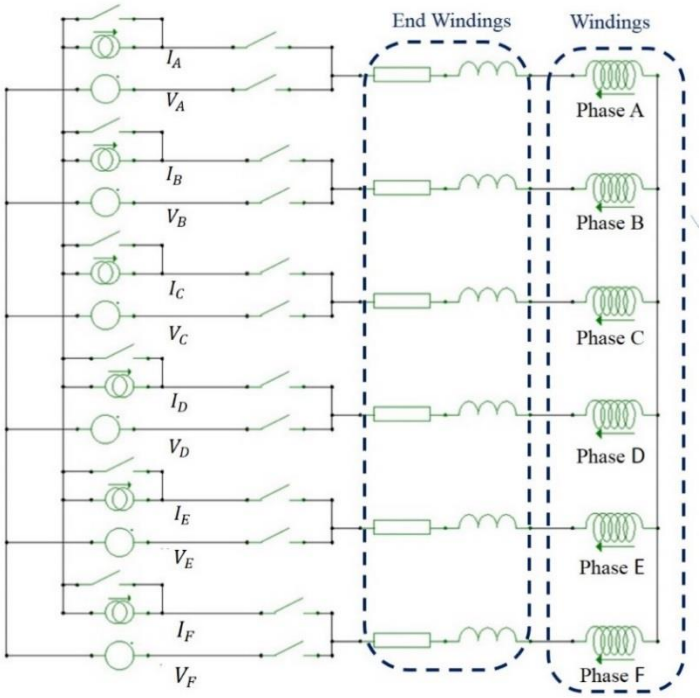

Fig. 8-7. Circuit model for creating voltage reversal fault (F7 to F12) in 2-D transient FEA.

8.3.1 Demagnetization Assessment for Short Circuit Faults

The 2-D transient FEA is carried out enabling demagnetization model at the pre-fault operating conditions listed in Table 8-3 for the faults F1 to F6. The circuit shown in Fig. 8-6 is employed for this purpose. The short circuit is enabled at the instant when the line-line voltage reaches its maximum. The transient behaviour of the machine is observed as shown in Fig. 8-8 under fault condition F1 with pre-fault operation at the rated torque and speed.

Fig. 8-8 shows the phase currents, torque and the *d*-*q* axis currents during transient. As can be seen, the peak demagnetization occurs at rotor position 242^0 mechanical. For better insight on the *d*-and *q*-axis current behaviour during the fault F1, Fig. 8-9 plots the current trajectory in the *d*-*q* axis plane. As can be seen when the fault transient progress, the trajectory of the *d*-*q* axis currents passes through the peak demagnetizing current, identified by an arrow. The steady-state short circuit current is marked at the centre of the curve. It is observed from the FEA that the transient response is independent on the instant of the short circuit [173] as the initial condition for the post-fault transient is decided by the pre-fault *d*-and *q*-axis currents, also the peak *d*-axis current coincides with peak demagnetizing current. Similar transients are observed for all the other short circuit faults which are under consideration.

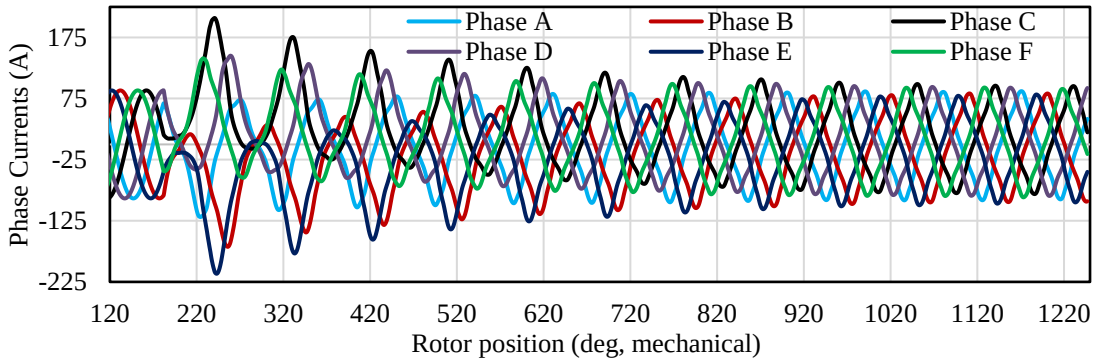

(a) Phase currents during transient

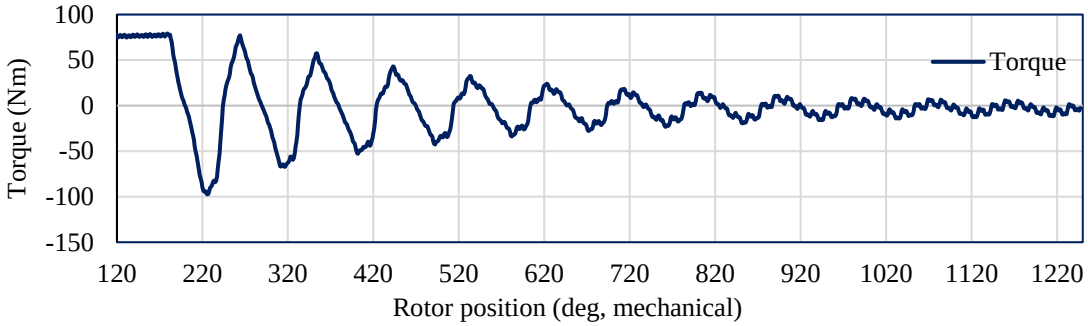

(b) Torque during transient

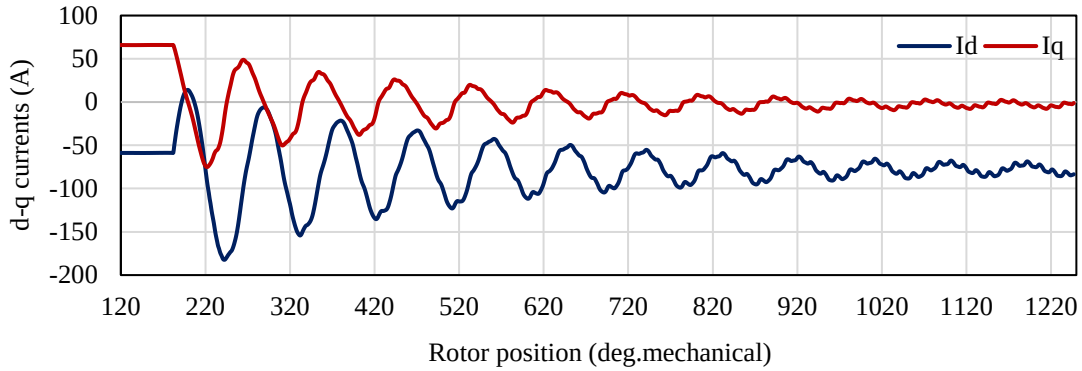

(c) *d-q* axis currents during transient

Fig. 8-8. Transient response of 18-slot,8-pole IPM machine under 6 –phase short circuit (F1).

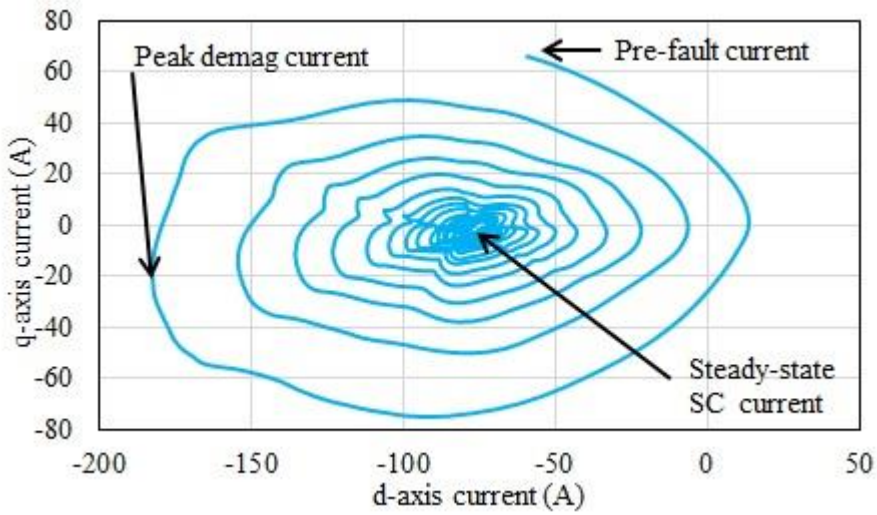

Fig. 8-9. Current trajectory for the 18-slot,8-pole IPM machine under 6 –phase short circuit (F1) at rated torque operations.

Short circuit analysis (F1 to F6) is repeated in 2-D transient FEA without enabling the demagnetization model for the comparison purpose. Table 8-4 (a) compares the maximum phase currents, peak demagnetizing currents (*d*- axis currents) and the steady state short circuit current for short circuits under

rated load conditions (F1, F3 and F5) obtained by the continuous demagnetization (proposed) method with the method which doesn't consider continuous demagnetization as described in [173]. A similar comparison is made for short circuits faults under the peak load condition (F2, F4 and F6) in Table 8-4 (b).

Table 8-4. Comparison of Currents for Old Method and Proposed Method for Faults F1 to F6

Table 8-4 (a). Comparison of Currents under Rated Load Conditions (F1, F3 and F5)

	F1		F3		F5	
Current Max (A)	Old method	Proposed method	Old method	Proposed method	Old method	Proposed method
Phase	215.6	212	201.6	198	134.5	134.5
d-axis	-193.7	-184	-201.6	-200	-122.3	-122.3
Steady-state	-79.5	-74.85	-79.5	-75.2	-79.5	-79.5

Table 8-4 (b). Comparison of Currents under Peak Load Conditions (F2, F4 and F6)

	F2		F4		F6	
Current Max (A)	Old method	Proposed method	Old method	Proposed method	Old method	Proposed method
Phase	245.8	236	225.5	224	136.1	136.1
d-axis	-227.3	-235	-254.7	-236	-120.3	-120.3
Steady-state	-79.5	-72.3	-79.5	-73.3	-79.5	-79.5

It can be seen that the steady state short circuit currents are reduced as a result of partial demagnetization compared to the method reported in [173] where post-fault performance analysis is not possible and the steady-state short circuit currents are computed by FE assuming all the magnets are not demagnetized. It is also observed that peak phase currents are slightly reduced in the continuous demagnetization method compared to the method reported in [173].

Table 8-5 compares the percentage of partial demagnetization in all the magnets calculated from the continuous demagnetization during faults, F1 to F6. If flux density in a magnet element is below the knee point when a post-fault steady-state is reached, this element is considered to be partially demagnetized, although its remanence may still be close to that without demagnetization. The variation in percentage demagnetization among the magnets indicates the non-uniform demagnetization due to the presence of lower order MMF space harmonics in the fractional-slot PM machine.

Table 8-5. Comparison of the Percentage Partial Demagnetized Areas Observed in all Magnets under Short Circuit Fault Conditions (F1 to F6)

	F1	F2	F3	F4	F5	F6
M1P1	10.2	15.3	8.4	17.1	0.1	0.2
M1P2	8.2	10.2	6.2	15.0	0.0	0.1
M2P1	68.1	85.6	12.2	27.3	0.0	0.0
M2P2	75.4	87.7	10.1	20.4	0.1	0.0
M1P3	45.2	67.4	12.3	25.2	0.1	0.0
M2P3	50.2	55.3	9.1	17.0	0.0	0.1
M1P4	6.0	7.2	7.3	12.1	0.2	0.1
M2P4	5.2	5.2	2.4	7.3	0.0	0.0
M1P5	72.4	93.2	20.6	72.4	0.0	0.0
M2P5	80.5	97.2	16.3	64.4	0.0	0.1
M1P6	8.4	16.2	12.2	22.1	0.0	0.0
M2P6	9.2	12.2	6.1	14.0	0.0	0.1
M1P7	5.4	7.3	4.3	13.2	0.0	0.0
M2P7	5.2	8.1	4.2	11.4	0.0	0.0
M1P8	68.3	82.2	11.1	23.1	0.1	0.2
M2P8	72.4	89.1	7.0	16.7	0.2	0.0
Overall percentage	36.8	46.2	9.3	23.7	0.0	0.0

Table 8-6 compares the average value of the minimum flux density in the partially demagnetized regions of all the magnets during short circuit faults, F1 to F6. It is clear from Table 8-5 and Table 8-6 that the faults F5 and F6 has not resulted in any partial demagnetization of the IPM machine and hence the post fault performance of the machine will not get affected.

Table 8-6. Comparison of the Average Minimum Flux density (T) in the Partially Demagnetized Regions of all Magnets under Short Circuit Fault Conditions

	F1	F2	F3	F4	F5	F6
M1P1	0.27	0.25	0.28	0.27	0.34	0.37
M1P2	0.26	0.24	0.28	0.19	0.36	0.38
M2P1	0.24	0.22	0.26	0.20	0.37	0.38
M2P2	0.20	0.15	0.23	0.14	0.34	0.36
M1P3	0.18	0.07	0.16	0.05	0.34	0.38
M2P3	0.27	0.24	0.27	0.26	0.37	0.38
M1P4	0.27	0.26	0.28	0.29	0.35	0.46
M2P4	0.26	0.25	0.27	0.25	0.43	0.44
M1P5	0.22	0.17	0.27	0.16	0.34	0.38
M2P5	0.18	0.08	0.14	0.06	0.34	0.38
M1P6	0.28	0.25	0.28	0.27	0.37	0.40
M2P6	0.29	0.22	0.29	0.28	0.40	0.43
M1P7	0.28	0.24	0.27	0.28	0.38	0.41
M2P7	0.29	0.23	0.27	0.26	0.39	0.42
M1P8	0.20	0.18	0.27	0.26	0.39	0.37
M2P8	0.24	0.24	0.27	0.27	0.30	0.38
Overall minimum average	0.25	0.20	0.26	0.22	0.36	0.39

The demagnetized 2-D FEA model obtained after the short circuit faults F1 to F6 are operated at the respective speeds to evaluate the percentage reduction in back EMF compared to the healthy machine. Also the pre-fault currents are applied to the respective models to evaluate the reduction in rated and peak torque after partial demagnetization. Accounting the post-fault operation at 150^0C, machine pre-fault currents are increased manually in the demagnetized models to evaluate the increased currents which are capable of developing the rated and the peak torques.

Table 8-7 gives the post demagnetization assessment in terms of reduction in back EMF and the reduction in the rated and the peak torque in percentage for the faults F1 to F6. Due to presence of sub-MMF harmonics in the fractional slot PM machine as shown in Fig. 8-10 [169, 173], partial demagnetization in

each pole is slightly different. Hence, the reduction of the back EMF varies in a narrow range for the faults F1 to F4. It can be seen that the machine performance is not affected by short circuit faults F5 and F6 while it is most affected in F2.

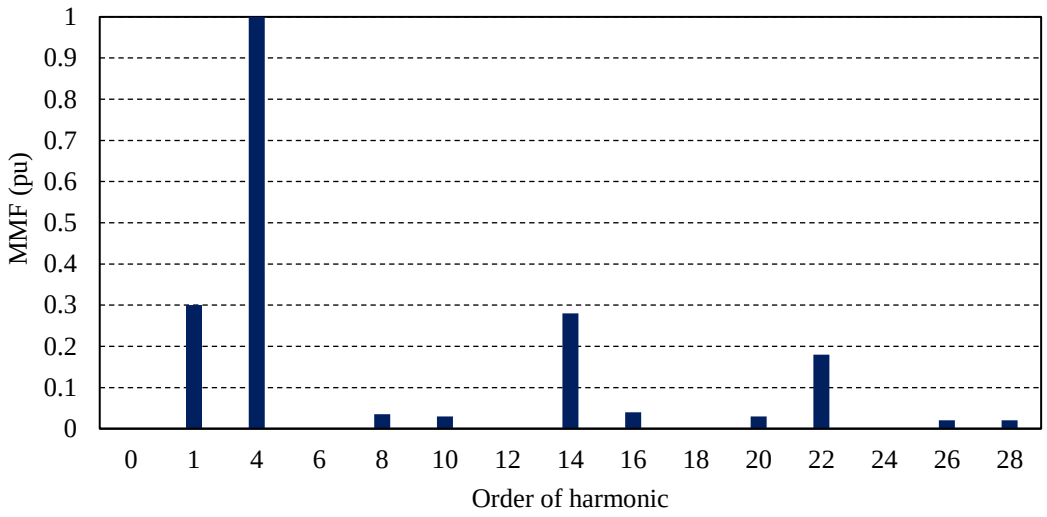

Fig. 8-10. Normalized MMF space harmonic distribution for the 8-pole,18-slot IPM machine.

Table 8-7. Post Demagnetization Assessment Faults F1 to F6

Fault	% Reduction in back EMF	% Reduction in Torque	
		Rated	Peak
F1	1.85 to 1.96	0.91	1.49
F2	4.06 to 5.38	2.43	3.6
F3	0.42 to 0.58	0.21	0.42
F4	3.07 to 4.75	1.9	2.57
F5	0	0	0
F6	0	0	0

Fig. 8-11 compares the increase in current to generate the rated and the peak torque after the short circuit faults F1 to F6. As the faults F5 and F6 have not caused any partial demagnetization the rated and the peak currents are not affected as indicated in the figure with a doted horizontal line.

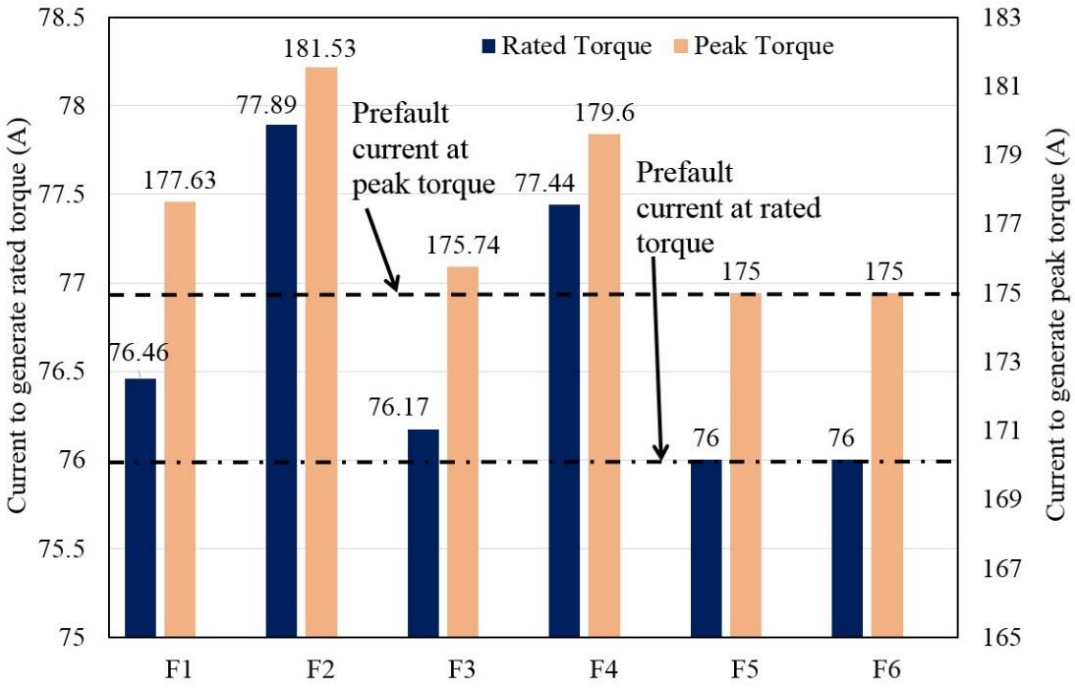

Fig. 8-11. Comparison of post fault current when magnet properties at 150°C for generating rated and peak torque (Faults F1 to F6).

Fig. 8-12(a) and Fig. 8-12(b) shows the comparison of the demagnetized regions in the magnets for the worst affected faults F2 and F4, reinstating the uneven distributions of partially demagnetized areas.

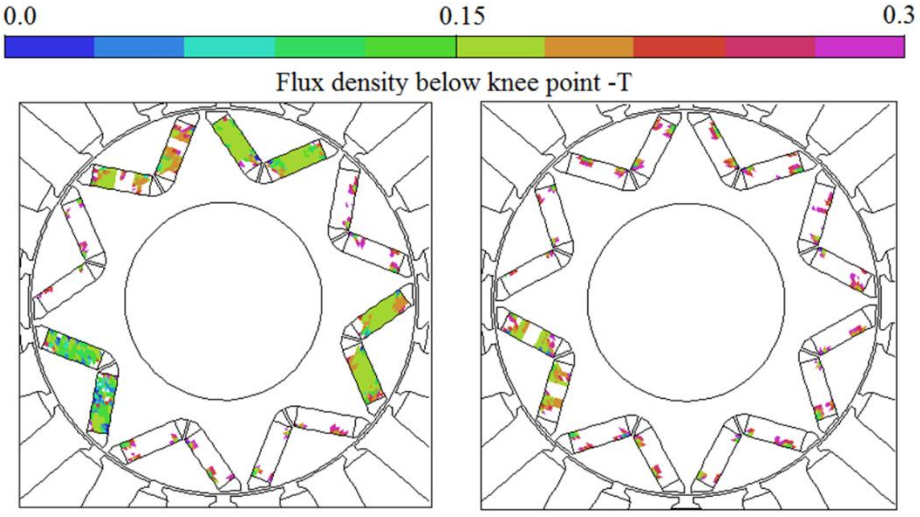

(a) 6-phase SC at peak torque (F2) (b) 3-phase SC at peak torque (F4)

Fig. 8-12. Comparison of demagnetized regions (below 0.3T) after short circuit faults.

From all these results following observations can be made about the continuous demagnetization and the post fault performance:

1) The peak demagnetizing current has a significant impact on the partial demagnetization of the magnets. With an increase in pre-fault operating current, the peak demagnetizing current during fault transient also increases and, hence the magnets become more susceptible for partial demagnetization.
2) In the case of 3- phase faults, the minimum average flux density observed is lower with respect to the 6- phase faults in some of the magnets, but the overall percentage demagnetization is comparatively lower. This makes the post fault performance after 3-phase faults slightly better than 6-phase faults with the same pre fault current.
3) It is also worth noting that the reduction in the post fault torque capability is not proportional to the percentage of demagnetization, it also depends on the minimum flux density experienced among the different magnet elements. For example, partial demagnetized areas under faults F1 and F4 are 36.8% and 23.7% respectively. However, more reduction in torque under F4 is seen.
4) However, even though the percentage of the demagnetized areas under these fault conditions F1 to F4 are quite high, the reduction in remanence seen in many partially demagnetized areas is relatively small as indicated in Table 8-6, hence torque reduction is also relatively small.

8.3.2 Demagnetization Assessment for Voltage Reversal Faults

A set of more severe faults with respect to demagnetization, F7 to F12, attributed to voltage reversal resulting from inverter losing synchronization with respect to the back EMF voltages of the phases, due to sensing error or inverter fault needed to be investigated. Since the machine has two separate

3-phase winding systems, the failure due to one set of 3-phase supply losing synchronization and all the 6–phases losing synchronization are to be simulated separately to assess the partial demagnetization. Hence 2-D transient FEA is carried out enabling demagnetization model at the pre-fault operating conditions listed in Table 8-3 for the faults F7 to F12, employing the circuit shown in Fig. 8-7.

Table 8-8 compares the peak phase current, the maximum *d*-axis current and the corresponding *q*-axis current during faults F7 to F12. It is seen that the phase currents and hence *d*- and *q*- axis currents are much higher compared to short circuit faults F1 to F6 as observed in Table 8-4.

Table 8-8. Comparison of Peak Currents(A): Faults F7 to F12

Fault	Maximum phase current	Maximum *d*-axis current	Corresponding q-axis current
F7	1745	-1323	-691
F8	1612	-1372	-489
F9	1415	-1473	-487
F10	1272	-1380	-361
F11	251	-228	8
F12	245	-231	12

As it has been done with the short circuit faults, the demagnetized 2-D FEA model obtained after the voltage reversal faults F6 to F12 are operated at the respective pre-fault speed to evaluate the percentage reduction in back EMF compared to the healthy machine. The pre-fault currents are applied to the respective models to evaluate the reduction in rated and peak torque after partial demagnetization. Also considering the post-fault operation at 150^0C, machine pre-fault currents are increased manually in the demagnetized models to evaluate the increased currents which are capable of developing the rated and the peak torques.

Table 8-9 shows the reduction in back EMF voltage and reduction in the rated and the peak torque as a result of demagnetization associated with faults F7 to F12. The results from the post demagnetization table indicate that all

faults, F7 to F12, have resulted in far more significant partial demagnetization of the magnets.

Table 8-9. Post Demagnetization Assessment Faults F7 to F12

Fault	% Reduction in Back EMF	% reduction in Torque	
		Rated	Peak
F7	34.53 to 37.18	18.48	21.14
F8	31.04 to 40.49	19.27	22.05
F9	20.87 to 38.23	15.43	17.28
F10	20.34 to 37.32	14.77	17.01
F11	4.01 to 5.12	2.11	3.21
F12	5.67 to 6.29	3.94	4.61

It has been observed from Table 8-7 and Table 8-8 that the fault F8 has resulted in the maximum reduction in the machine performance among all the faults under consideration.

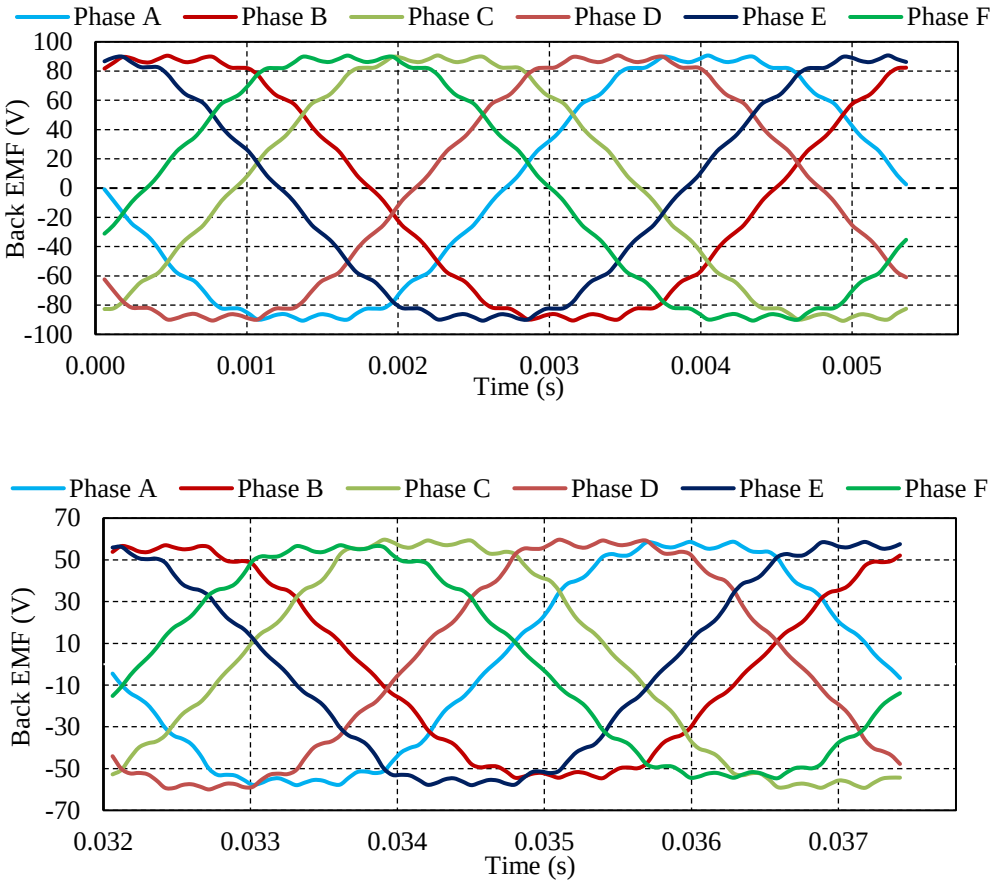

Fig. 8-13. Back EMF before (top plot) and after (bottom plot) F8 at rated speed.

Fig. 8-13 illustrates the comparison of back EMF generated for a cycle before and after F8 at rated speed (2800 rpm). From the above figures it can be seen that F8 has resulted in the maximum reduction in back EMF for phase B, while it has resulted in the minimum reduction for phase D (for the particular electrical cycle captured), clearly indicating the non-uniform demagnetization among the magnets.

Fig. 8-14 illustrates variations in the electromagnetic torque generated before and after F8 at the rated speed.

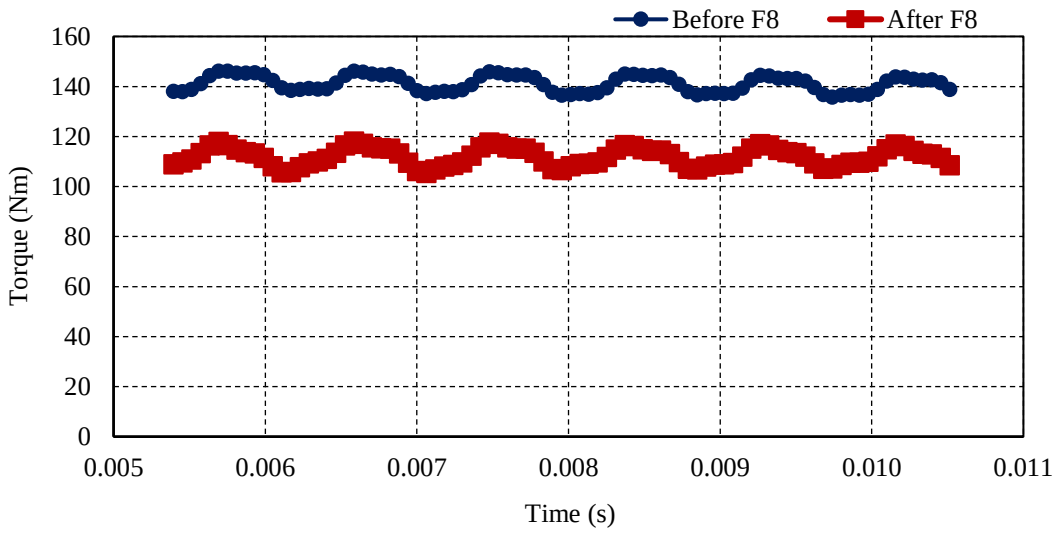

Fig. 8-14. Comparison of peak torque before and after the fault F8.

Fig. 8-15 indicates the increase in the rated current and the peak current in order to produce the rated and the peak torque after the partial demagnetization has occurred.

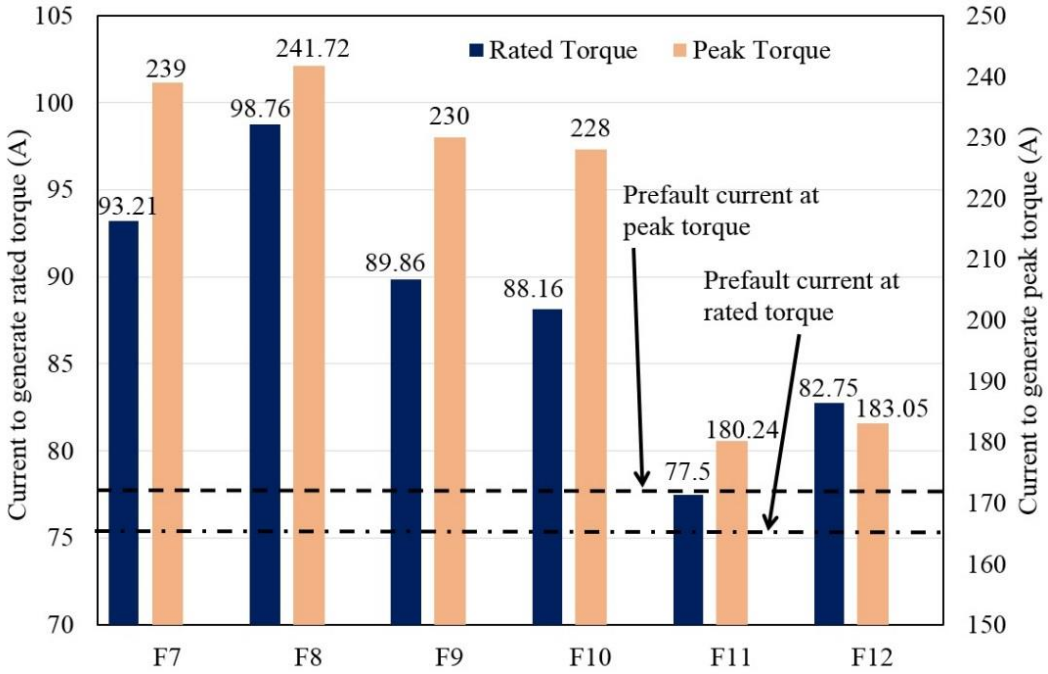

Fig. 8-15. Comparison of post fault current when magnet properties at 150°C for generating rated and peak torque (Faults F1 to F6).

Table 8-10 compares the average value of the minimum flux density in the partially demagnetized regions of all the magnets during voltage reversal faults, F7 to F12. Fault F9 has created the maximum demagnetizing current which pushes the minimum average flux density in the magnet M2P3 to -1.91T. The extent of partial demagnetization is not shown here as a table similar to the case with short circuit faults because only small regions of the magnets from faults F11 and F12 has not under gone some degree of partial demagnetization, while every element of each magnets has gone below 0.3T in Faults F7 to F10.

Table 8-10. Comparison of the Average Minimum Flux Density (T) in the Partially Demagnetized Regions of all Magnets under Various Fault Conditions

	F7	F8	F9	F10	F11	F12
M1P1	-0.52	-0.58	-0.55	-0.33	0.19	0.19
M1P2	-0.88	-0.62	-0.35	-0.42	0.16	0.16
M2P1	-0.53	-1.13	-0.63	-0.57	0.21	0.18
M2P2	-0.62	-0.61	-0.83	-0.61	0.22	0.14
M1P3	-0.91	-0.96	-0.53	-0.80	0.14	0.14
M2P3	-1.01	-0.98	-1.91	-0.76	0.15	0.14
M1P4	-0.49	-0.54	-0.82	-1.77	0.18	0.17
M2P4	-0.63	-0.52	-0.90	-0.79	0.20	0.16
M1P5	-1.17	-1.01	-0.99	-0.69	0.22	0.17
M2P5	-0.91	-1.00	-0.56	-0.79	0.20	0.16
M1P6	-0.67	-0.68	-0.38	-0.50	0.24	0.17
M2P6	-0.85	-0.93	-0.17	-0.09	0.17	0.08
M1P7	-0.73	-0.75	-0.29	-0.67	0.22	0.16
M2P7	-0.97	-0.96	-0.26	-0.51	0.24	0.16
M1P8	-1.31	-1.55	-0.65	-0.43	0.12	0.11
M2P8	-1.10	-1.09	-0.54	-0.41	0.15	0.12
Overall minimum average	-0.83	-0.87	-0.65	-0.63	0.19	0.15

The following observations can be made from the results obtained from the simulation of Faults F7 to F12.

1) First the value of the maximum *d*-axis current during the faults, not the peak phase current prior to the fault, influences the extent of partial demagnetization.
2) It is observed that the 3-phase voltage reversal faults (F9 & F10) could create the maximum demagnetization current compared to the 6-phase voltage reversal faults (F7 & F8) for the same pre-fault currents even with the currents in the healthy 3-phase under faults F9 & F10 are not affected. This is because of the mutual magnetic coupling between the faulty phases and the heathy phases in the 3-phase reversal faults.
3) However, in the case of 3- phase faults (F9 & F10), the overall average minimum flux density observed among all the magnets is higher

with respect to the corresponding 6- phase faults (F7 & F8) with same pre fault current. This makes the post fault performance after 3-phase faults slightly better than 6-phase faults with the same pre fault current

4) Further the post-fault currents to generate the peak torque after faults F7 to F10 are closer to the maximum 6 – phase short circuit current for a healthy machine at 150^{0}C. Thus, if adequate post fault de-rating is not applied further demagnetization is likely to take place when magnet temperature is above 150^{0}C.
5) It should also be noted from Table 8-8 that the fault currents associated with F11 and F12 at high speeds are much lower than those at the base speed. This is because in high speeds the machine exhibits high impedance which helps in reducing the fault current and hence the severity of demagnetization.
6) The extent of partial demagnetization not only depends on the maximum d –axis current, but also on time duration for which the magnets are exposed to it. This is because a longer duration makes more area of the magnet exposed to higher demagnetizing currents. For example, the maximum d-axis current in voltage reversal fault (F12) is marginally lower than that in short circuit fault (F2), but produces a more partially demagnetized area. This is evident from the comparison of locus of the d- and q- axis currents for the faults F2 and F12 as shown in Fig. 8-16.
7) It is also worth noting from Fig. 8-15 that the percentage increase of current in generating the torque at the rated conditions is lower than that at the peak load conditions. This can be accounted by the combined effect of reduction in the magnet torque due to lower remanence as a result of partial demagnetization and the reduction in the reluctance torque due to increased saturation.
8) It is observed that the uneven de-magnetization after the fault can result in an increase in torque ripple. For example, the torque ripple

after the fault F8 has been increased from 5.59 % to 11.8% at peak torque conditions as shown in Fig. 8-14.

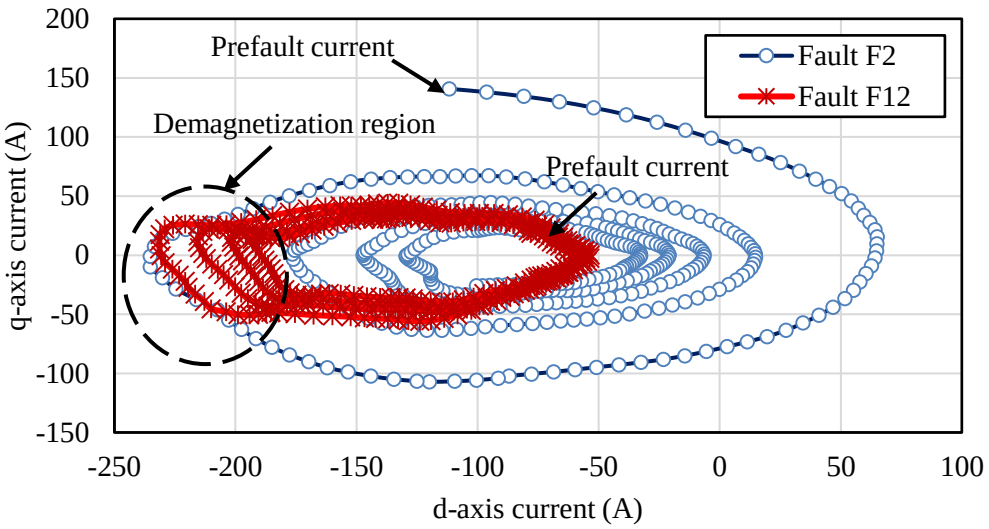

Fig. 8-16. Comparison of locus of d and q axis current for the Faults F2 and F12.

8.4 Experimental Validation

8.4.1 Experimental Testing Leading to Partial Demagnetization

A test was conducted at The University of Sheffield [190] as a part improvising the current control of the inverter at all speed and torque levels within the designed capability of the 18-slot, 8–pole IPM machine prototype. The prototype was developed as part of the FP7 CASTOR project [190]. The schematic of the inverter control system having independent control for both set of three phase system is explained in [191]. The experimental set-up is shown in Fig. 8-17.

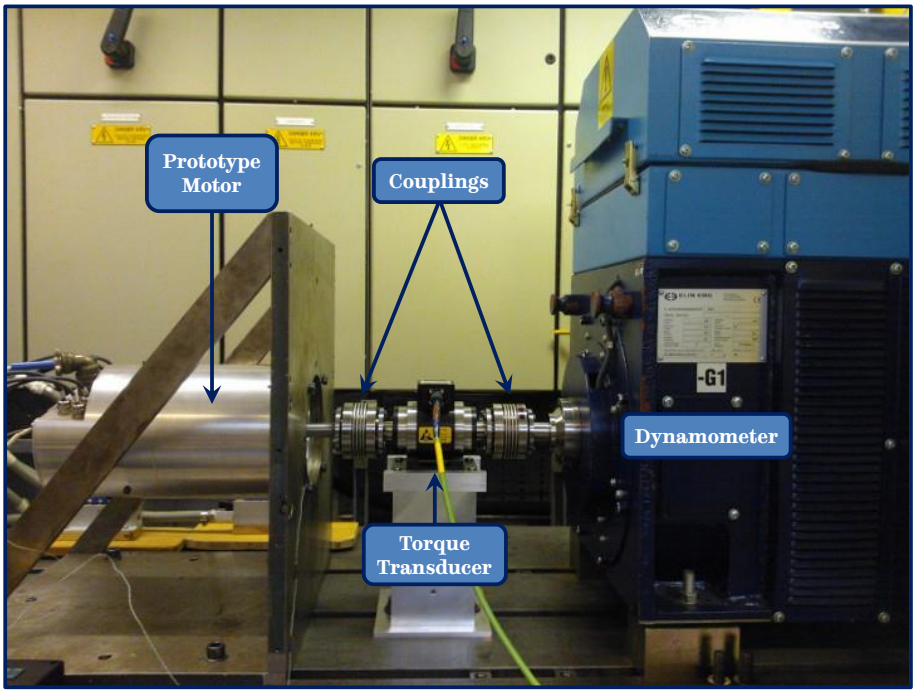

Fig. 8-17. Prototype motor mounted on the test bench with inline torque transducer.

The test started with 30 N·m demand from lower speed. As speed increased, the torque demand was reduced to ensure the motor operation at 22 kW. When dynamometer speed was increased from 10500 rpm to 10750 rpm, the motor was running under control for some time with a torque demand of 20 N·m. This is followed by one set of 3-phase system (A-B-C) losing synchronization with the voltage vector being opposite to the back-EMF, leading to much higher currents. The torque, armature currents, machine acceleration and speed captured against time during the experiment is shown in Fig. 8-18. However, due to limited storage capacity, the data was recorded only for every 20ms, and therefore the peak surge in ABC current magnitude was not captured. Upon observing the abnormal behaviour, the speed of the dynamometer was reduced to zero. The currents in A-B-C windings did not reduce until the speed reached ~3000 rpm. After that, the A-B-C phase currents drop to zero instantly. This confirms that the control of A-B-C system through inverter was lost and A-B-C system of the motor was in generation mode. Also it was observed that DC link voltage was set at 250 V. Hence the motor was operating under deep field weakening when the testing was continued beyond

its maximum operating speed (8600 rpm for 250V) as the rated voltage for the motor is 320 V.

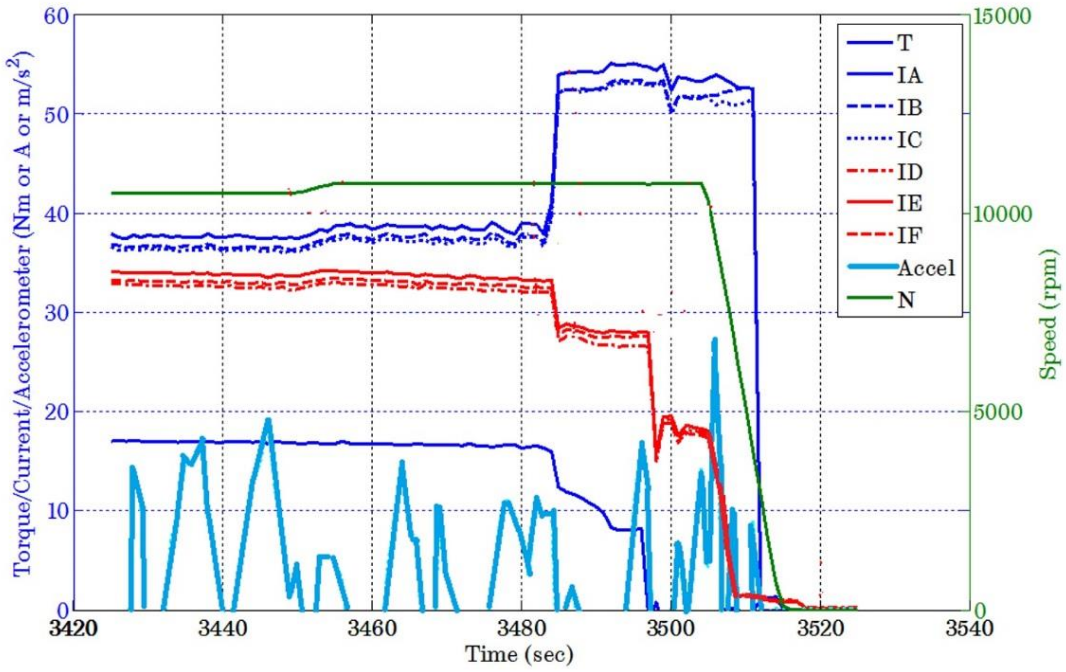

Fig. 8-18. Sequence of events during the incident of partial demagnetization of the prototype motor.

When the test is resumed, it was noted that the back-EMF of the prototype motor is reduced than the previously measured values, confirming partial demagnetization.

8.4.2 Electromagnetic and Thermal Analysis of the Test Condition

It can be concluded that the motor was operating in deep field weakening region with 250 V from medium speed (~5850 rpm) till the timing of the incident leading to possibility of losing control, overheat and risk of partial demagnetization. In deep field weakening operation, higher concentration of flux towards the rotor and higher order harmonics penetrating deeply inside the rotor increase the rotor losses in fractional-slot PM machines. Since field weakening is employed with lower DC link voltage, then higher d-axis current

is required to produce the same torque at a given speed resulting into much higher flux concentration & penetration in the rotor.

Since the rotor temperature was not measured, electromagnetic and thermal analysis with the machine model calibrated by the measurement data at the rated and the peak conditions is used to estimate the rotor temperature. Losses analysis is carried out in FEA to evaluate stator, rotor iron loss and armature copper loss at 10750 rpm with 16 N·m (measured torque at the time of experiment while losing synchronization) while operating at 250 V. The loss analysis is repeated at the same operating conditions at 320 V for the comparison purpose.

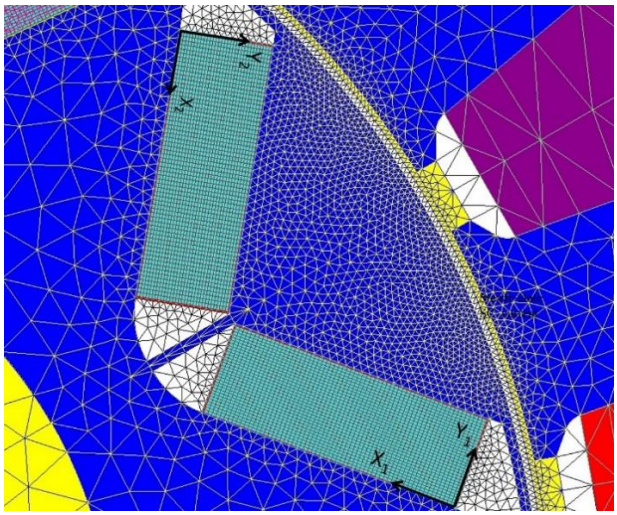

Fig. 8-19. Mesh grids constructed over the magnets and are attached to separate coordinate system.

3D Fourier method is employed to evaluate the magnet loss at the test conditions for both 250 and 320V. To implement 3D loss evaluation in the imaging method, the flux density values are captured to form a matrix as discussed in Chapter 6. Hence the magnetic flux density values from the 2D FEA are extracted using a mesh grid constructed over the magnets. For the machine under consideration, each magnet attached to a separate coordinate system is discretized into sixty-four divisions along the x and thirty-two divisions along y directions as shown in Fig. 8-19.

The 3-D magnet loss evaluation process is implemented in the imaging method at the fundamental phase-currents both at 250 and 320V. The loss variation with axial segmentation is obtained as Fig. 8-20.

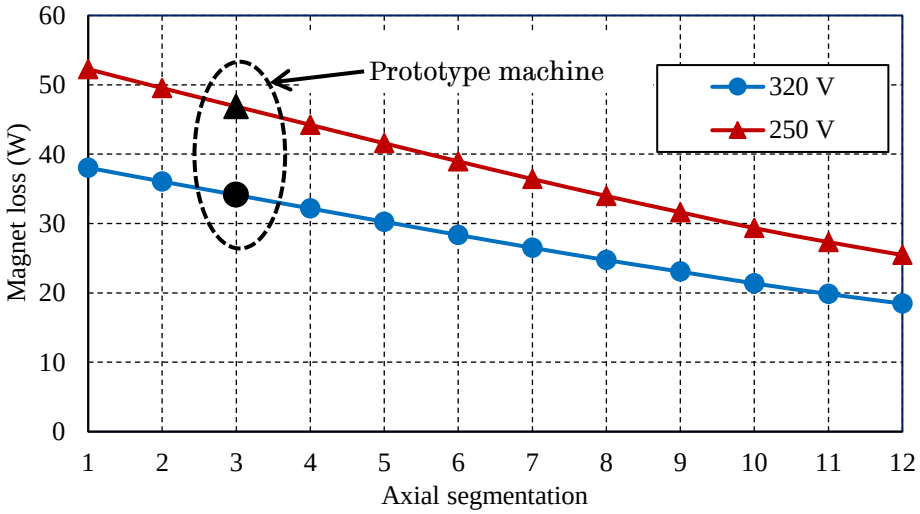

Fig. 8-20. Variation of magnet loss with axial segmentation evaluated from 3D imaging method.

As the prototype machine is built with three axial segments, the corresponding loss values at this segment number (marked in black) is employed in the thermal analysis. Since the measurement data fail to replicate the exact current waveform in the machine during the experiment, the contribution of the higher order current harmonics towards the magnet loss is not quantified. Hence, the actual magnet loss in prototype machine could be a bit more than these predicted values.

The thermal model of the motor is defined in Motor-CAD, and is shown in Fig. 8-21. The thermal analysis is carried out at 20^0C ambient air and water inlet temperature, and 15 litre/minute water flow as per recorded test data, with the loss evaluated from the electromagnetic and the imaging method. The water flow rate is adjusted to 15 litre/minute as per the recorded test data [190, 195] .

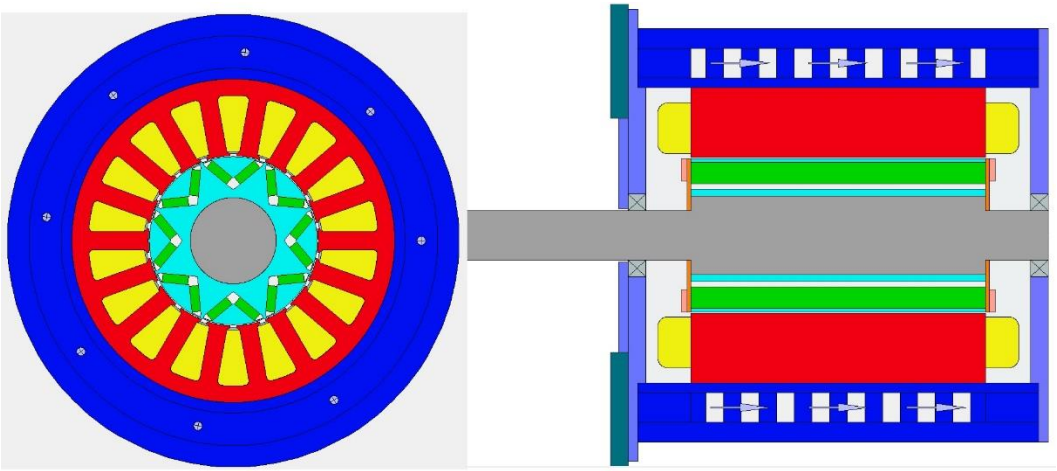

Fig. 8-21. Radial and axial cross-section of the machine model in Motor-CAD.

The results obtained from the loss evaluation and the thermal analysis are shown in Table 8-11. The transient temperature response of various machine components (Magnets, Stator Surface, Rotor surface, Winding) at 250V and 320V while running at 10750 rpm is shown in Fig. 8-22.

Table 8-11. Results of Loss Evaluation and Temperature Estimation

DC link voltage	250 V	320 V
Controller voltage limit (% of DC link voltage)	95%	95%
Phase RMS current	42.1 A	35.7 A
Torque produced	15.8N·m	15.8N·m
Line-line voltage (fundamental)	236.7 V	301.63 V
Copper loss	597 W	430 W
Iron loss – stator	519.79 W	495.7 W
Iron loss – rotor	277 W	233.67 W
Eddy current loss in magnets	46.87W	34.12 W
Total rotor loss to be dissipated	323.87W	265.79W
Rotor back iron temperature	193.7°C	163.4°C
Rotor magnet temperature	192.4°C	160.7°C
Rotor surface temperature	190.6°C	158.1°C
Stator surface temperature	113.4°C	98.2°C
Stator tooth temperature	104.0°C	90.4°C
Average winding temperature	116.5°C	97.9°C

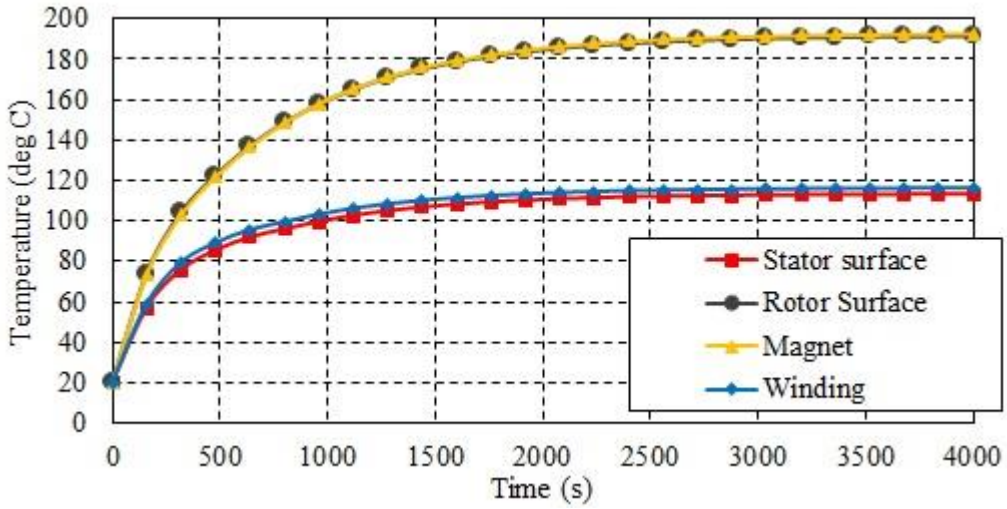

(a) Transient temperature response of motor components at 250V.

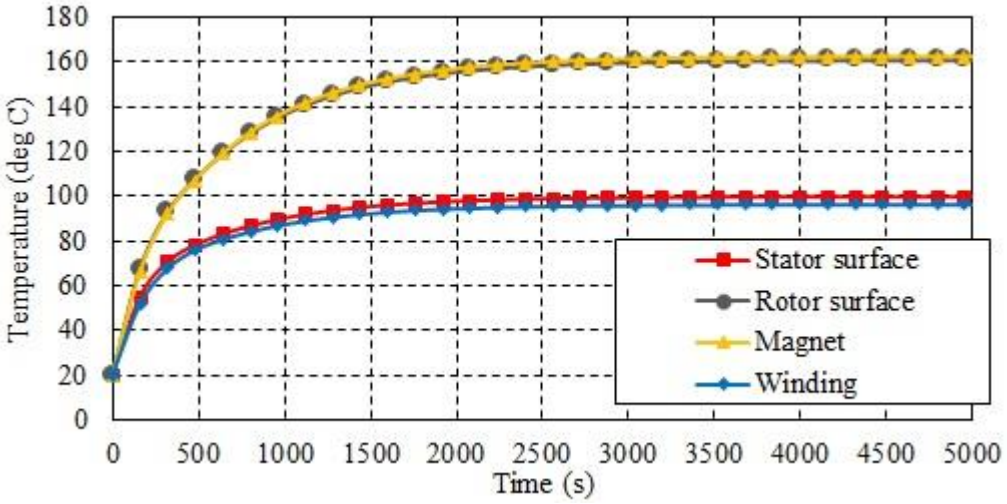

(b) Transient temperature response of motor components at 320V.

Fig. 8-22. Transient temperature response of the motor components at 250V and 320V at 10750 rpm.

The results of continuous running of the motor at 10750 rpm shows that the 3D eddy current loss in the magnets is increased by 12.75W when operated on 250V compared to its operation at 320V. Also the thermal simulation indicates that rotor magnet temperature can go up to 192.4°C which is almost 30°C higher than that would have been if operating at 320V DC link voltage. The transient temperature response shows the magnet temperature reaches the steady- state in ~3000 seconds. As the 3-phase system (A-B-C) has lost its synchronization ~3485 seconds from the start of the experiment, it can be concluded that the magnet temperature should have been close to 190 °C while

the incident leading to partial demagnetization has happened. It is worth remembering at this point that the magnets used in the prototype motor also have demagnetizing characteristics if operated beyond 150^{0}C, as shown in Fig. 8-2.

8.4.3 Controller-drive Simulations to Replicate the Observed Behaviour During the Incident

The controller-drive simulations were carried out in MATLAB replicating the test behaviour at the time of incident [190]. It was observed that the case with A-B-C losing synchronization of the motor over 0.5 sec replicates the test behaviour in the best way. Also the simulated currents in A-B-C, D-E-F and generated torque matches quite well with the recorded test data.

It is found that peak *d*- and *q*- axis currents of the faulted A-B-C system has reached 175A and 50A respectively during the time when the inverter losing synchronization. The details of the inverter control system is explained in [190, 191], Hence it is likely that the increased magnet temperature along with the peak transient demagnetizing current at the instant when phase A-B-C losing control were responsible for the partial demagnetization of the prototype motor.

8.4.4 FE Analysis of Partial Demagnetization and Validation of Continuous Demagnetization Model

It is clear from the above analysis that the magnet temperature was close to 190^{0}C and the peak transient currents in the ABC phases was close to 180A in the experiment. Also it is observed before as shown in Fig. 8-2 partial demagnetization is said to have occurred if the flux density along the direction of magnetization has gone below 0.42T at 190°C.

The same experiment sequence shown in Fig. 8-18 is repeated in FEA with continues demagnetization model enabled, supplied with demagnetization

curve for the magnetic material at 190^{0}C. The circuit shown in Fig. 8-7 which is used for voltage reversal faults is employed here. At a speed of 10750 r/min, phase D-E-F was carrying current close to 48A peak, while 52A peak current was flowing in phase A-B-C. A sudden voltage reversal is applied for 0.1ms allowing the transients to flow in A-B-C system. It is observed that the peak transient current is close to 185A in phase-A as obtained from the drive system simulations discussed previously. The rest of the experiment is repeated as in Fig. 8-18 but at reduced time scale as this part has not much to do with the partial demagnetization.

Fig. 8-23. shows the sequence at which phase currents are applied for the FE demagnetization model for repeating the experimental process. Fig. 8-24 shows the variation of torque observed while the machine is operated with currents as in the experiment. It can be seen that there is transient fluctuation in the torque during the interval when the voltage got reversed which is not registered during the experimental process explained in section 8.4.1.

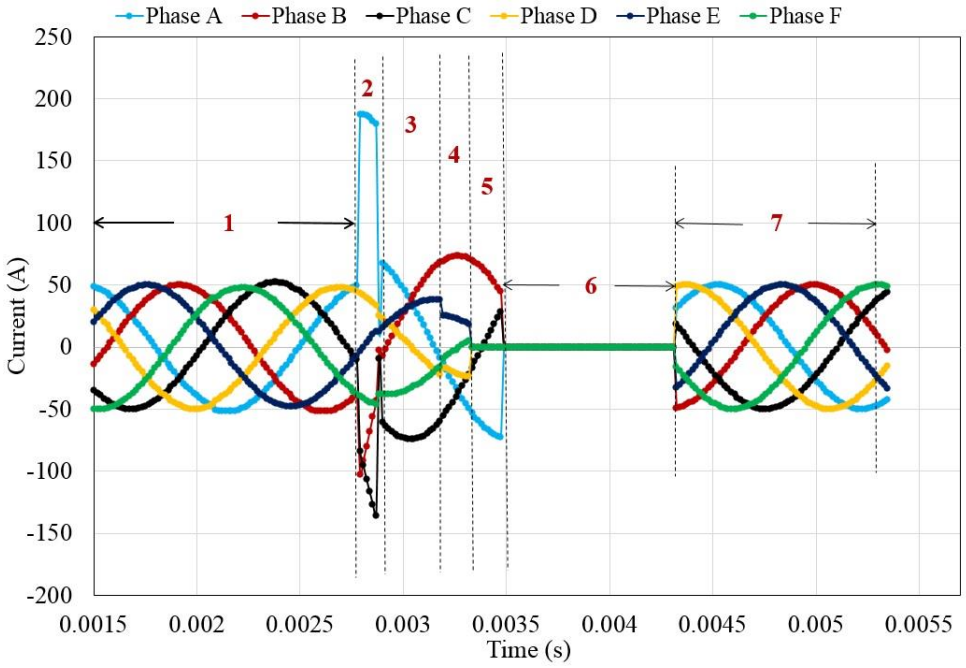

Fig. 8-23. Sequence of phase current's applied /observed in demagnetization model to replicate the experiment.

Region (1): I_{ABC} = 52A, I_{DEF} = 48A, Region (2): Phase ABC on fault, peak current observed on Phase-A= 15A, I_{DEF} = 48A, Region (3): I_{ABC} = 78.4A, I_{DEF} = 38.2A, Region (4): I_{ABC} = 73.2A, I_{DEF} = 25.5A, Region (5): I_{ABC} = 73.2A, I_{DEF} = 2.8A, Region (6):Region created to measure post fault back-EMF, I_{ABC} = 0 A, I_{DEF} = 0A, Region (7): Post fault operation, I_{ABC} = 50 A, I_{DEF} = 50A,

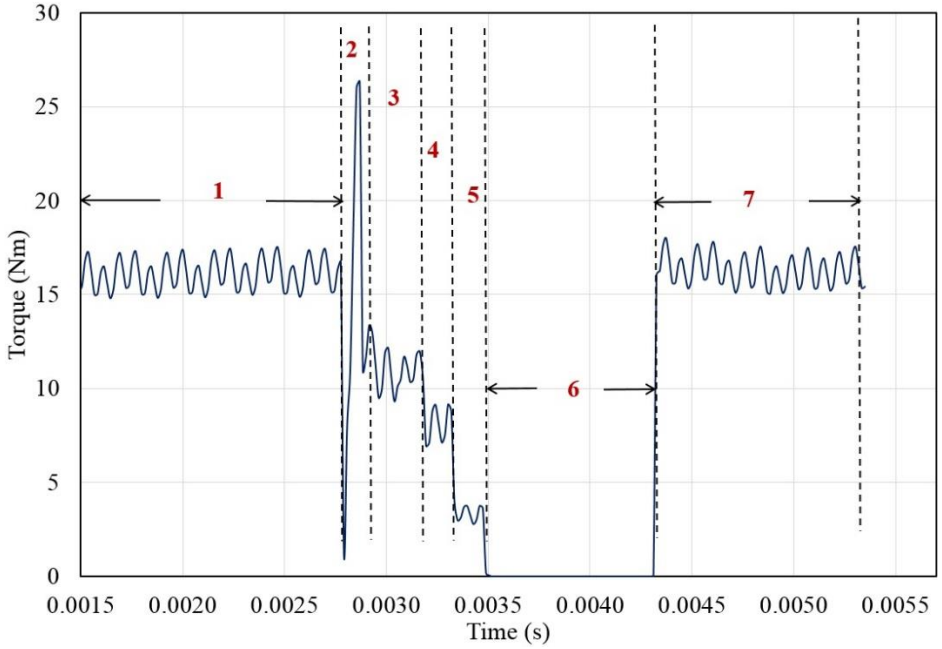

Fig. 8-24. Torque observed in demagnetization model during the sequence of operation in Fig. 8-18.

8.4.5 Post Demagnetization Performance Following the Loss of Synchronization

The prototype IPM machine after the voltage reversal experiment described in section 8.4.1 has been run under no load conditions at 2800 rpm to quantify the post fault back-EMF. It is observed that the back EMF of the motor is reduced by ~26% compared to the measured value during healthy operation, confirming partial demagnetization of the rotor magnets.

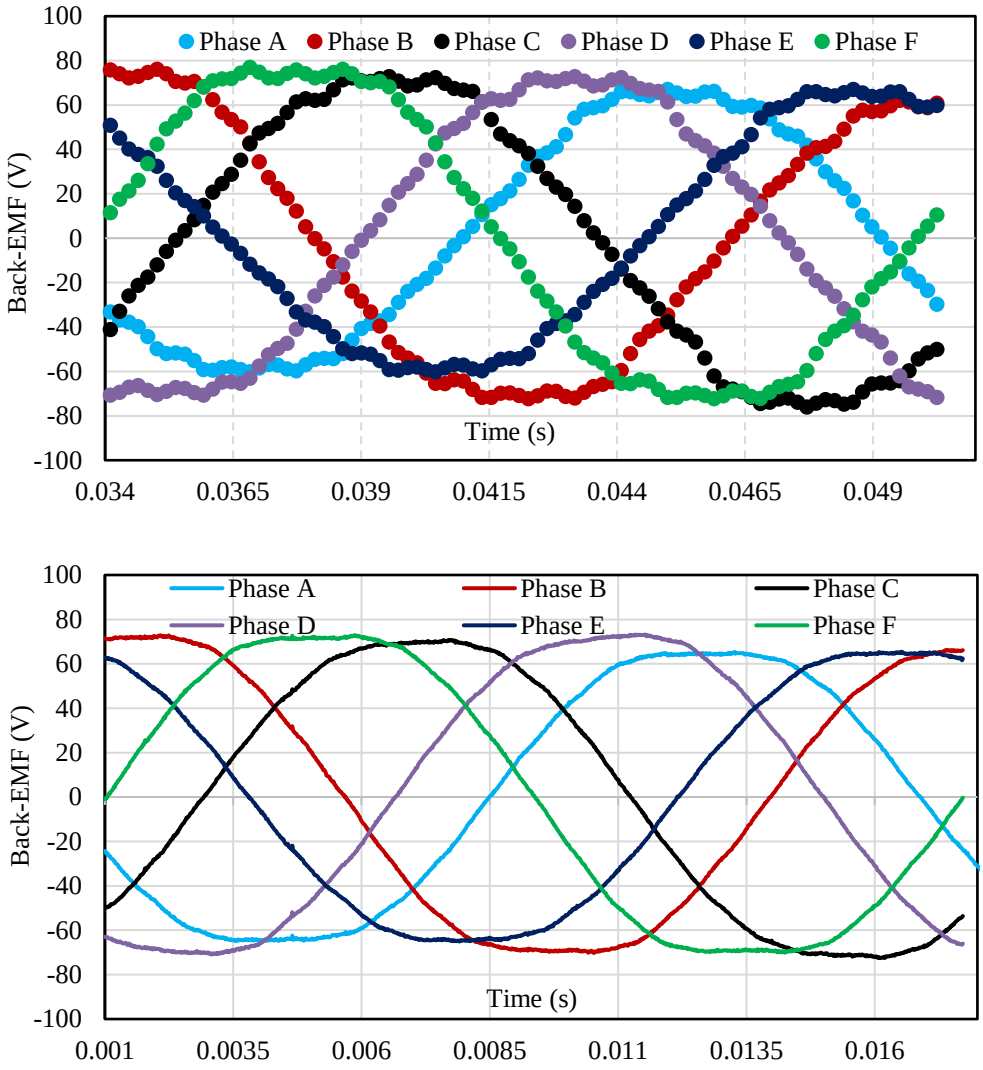

Fig. 8-25. Comparison of post fault back EMF from the experimental set-up (top plot) and the continuous demagnetization model (bottom plot).

The comparison of the actual back EMF measured at 2800 rpm after the demagnetization experiment and the FE simulation predictions from the

continuous demagnetization model is shown in Fig. 8-25. It can be seen from the figure that the magnets are partially demagnetized non uniformly as discussed before. The result indicates that the peak of the measured back EMF has a variation of 19.25 to 28.52% while the simulations showing a variation of 15.1 to 27.0%.

The partially demagnetized machine is run at peak power (11000 rpm) conditions with the set DC link voltage of 320V. The comparison of the average value of the measured torque before and after the partial demagnetization with the post fault 2D FE simulated value after partial demagnetization at the rated DC link voltage is shown in Fig. 8-26.

It is observed at 11000 rpm that the measured torque is reduced to 16.2 Nm from 19 Nm while simulation shows it is reduced to an average value of 16.5 Nm. This validates the FE model for continuous demagnetization presented in this paper.

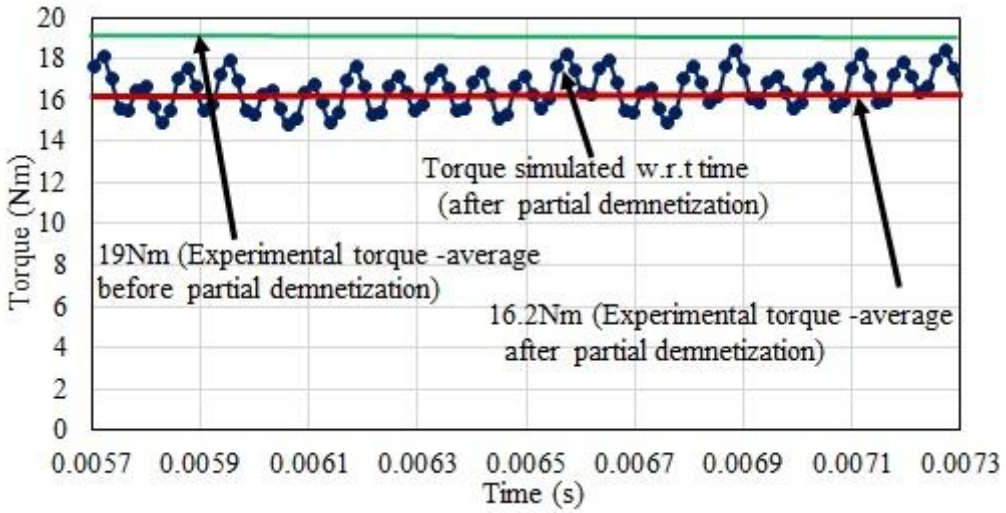

Fig. 8-26. Comparison of the torque from the experiment and continuous demagnetization model (DC link voltage: 320V).

It should be noted that the percentage of torque reduction is lower than that of the back EMF, since the torque produced by the PM field contributes to ~60% of the total torque. The rest is the reluctance torque which is not affected by the partial demagnetization. Hence the machine can be operated

further with a reduced rated toque capacity by about 17% Nm which corresponds to 28% reduction in the magnet torque because of partial demagnetization. The de-rating of the machine is necessary in order to prevent overheating and hence potentially further demagnetization.

8.5 Conclusion

The partial demagnetization of IPM machine with fractional pole-slot configuration has been comprehensively assessed under worst operating conditions using continuous demagnetization method. It has been shown that although partially demagnetized areas are quite large under the worst short-circuit conditions, the reduction of machine torque capability is relatively small. Voltage reversal caused by position sensor failure or controller failure leads to a far severe demagnetization on the machine and the resultant demagnetization current could be an order of magnitude greater than the rated current. The demagnetized model is employed for predicting post fault machine performance and the phase currents required for given torque at any load conditions following a fault condition that has led to partial demagnetization. This helps in making more reliable and robust machine against all potential fault scenarios, during the design phase, and also to quantify de-rating of the machine for subsequent usage to prevent any further partial demagnetization while in operation. The assessment technique has been validated by demagnetization experiments on a prototype machine, and is applicable to any PM machines.

CHAPTER 9
Conclusion

9.1 Conclusion

This thesis proposes computationally efficient techniques for the prediction of 3D eddy current loss in the magnets and the retaining sleeve of PM machines. The proposed computationally efficient methods are totally analytical from field calculations to the resistance limited 3D eddy current formulation for SPM machines. However, they are partly analytical employing the field information's from the 2D time-stepped FE analysis for high frequency eddy current prediction in SPM machines and also for the complete magnet loss prediction in the IPM machines accounting its complex geometry. This thesis also proposes the more accurate continuous demagnetization method for assessing the demagnetization pattern in the permanent magnets working at increased temperatures, when the PM machine encounters fault while operating under worst conditions. The post fault currents are predicted for delivering the designed torque requirements at peak and rated conditions of an IPM traction machine.

The analytical method developed in Chapter 2 and the 3D Fourier method in Chapter 3 accounts for the slotting effect, the field produced by the permanent magnets, flux density variations within the magnet along its radial direction while predicting the 3D magnet eddy current loss. As the magnet loss is evaluated for each circumferential segment separately in the proposed methods, the designer can have a better control in taking necessary steps in mitigating it. From the eddy current source examination in Chapter 2, it is observed that magnet loss field variations generated by the slotting harmonics goes out of phase with the corresponding field variations associated with armature harmonics at deep field weakening conditions of the PM machine. This results in the reduction of total magnet loss under such conditions. Also the 3D loss evaluation proves that the PM machines designed

with lower magnet pole arc angle will have reduced magnet eddy current loss at deep field weakening in contrast to machines with higher pole arc angles which incurs higher magnet loss at the same operating conditions.

The accuracy of the results predicted by the 3D Fourier method justifies the rectangular shape approximation of permanent magnets neglecting any of its curvature effect. Also with increase in number of circumferential segmentations each magnet segment becomes more rectangular and hence the effect of magnet curvature while predicting the 3D magnet loss becomes less significant. The loss prediction employing 3D Fourier method proves the contribution of tangential component towards the magnet loss can be up to 5% of the total magnet eddy current loss. However, its contribution has reduced by an order of 2 at high frequencies and hence can be neglected while predicting the magnet loss under such conditions. Also the detailed analysis of the eddy current density components proves the contribution of the y–component towards the magnet loss is negligible when compared to the other two (x, z) current density components.

The 3D Fourier method proposed in Chapter 3 accounts for the interaction of source harmonics of the same frequency within the magnet. The low frequency magnet loss evaluation employing source harmonics of the same order proves that the circumferential segmentation is more effective in reducing the magnet loss associated which those harmonic components with their wavelength higher than the magnet width. However, the method of axial segmentation provides a better reduction in magnet loss for those harmonic components with their wavelength much lower than the magnet width. It is also observed that the rate of loss reduction with increase in axial number of segments reduces as the harmonic order of the eddy current sources is increased. As the width of the magnet segment reduces faster with increase in circumferential segmentation compared to reduction in its height with increase in axial segmentation in most SPM machines (because of large machine axial length compared to the magnet pole arc length) the method of

circumferential segmentation become more effective in reducing the total magnet loss for most of the cases.

The eddy current sources associated with high frequency armature harmonics is observed to vary largely along the axial plane of the magnet due to eddy current reaction, hence this variation is necessary to be included for predicting magnet loss under such conditions. The actual magnet loss predicted accounting the axial source variation is confined between the loss evaluated employing the source values obtained from 2D FE with and without accounting eddy current reaction. For the magnets with larger axial length ($L_z >> L_x$), with a minor increase in circumferential segmentation the eddy current source variations spreads, becomes more or less uniform along the axial directions. However, a larger increase in the resistance towards the eddy current flow causes the magnet loss to reduce at an increased rate when compared to increase in axial number of segments. The total magnet loss associated with all the frequency components in the armature current can be evaluated as the sum of the loss associated for each frequency components in SPM machines as the core saturation is less significant.

The results obtained from the experimental measurements re-confirms the accuracy of the proposed 3D Fourier method. It is observed that the loss associated with high frequency switching harmonics can be significant and its value could be as much as 50% of the loss associated with fundamental frequency component in the real operating conditions of the SPM machine. It is advisable to perform circumferential segmentation rather than axial segmentation for the reduction of the magnet loss associated with high frequency phase current harmonics.

For the case with IPM machines it is observed that the machine non linearity prevents the prediction of total magnet eddy current loss associated with all the supply frequency components as the superimposition of the loss associated with individual harmonic components. Hence in such cases the

total eddy current loss can be evaluated employing frozen permeability concept while extracting the flux density information from the FE analysis.

The proposed 3D Fourier method is employed for eddy loss prediction in the retaining sleeve altering the source equations duly satisfying its natural boundary conditions. The accuracy results obtained justifies the proposed method, unrolling the sleeve as a thin rectangular sheet neglecting its curvature. As observed with permanent magnets, it is also seen for the retaining sleeve that the rate of loss reduction with increase in axial number of segments reduces as the harmonic order of the eddy current source is increased.

To Summarize, the computationally efficient methods proposed in this thesis for evaluating the 3D eddy current loss within the rotor can account for the following machine and the computational complexities,

1) Slotting effect
2) Field produced by the permanent magnet itself
3) Radial variation of the magnetic field inside the magnet
4) Inclusion of the tangential component of magnetic field (in low frequency magnet loss estimation and assessing its importance at high frequencies)
5) Interaction between the harmonics of the same frequency with the magnet
6) No linearity's of the core materials (using the field information from 2D FE)
7) Eddy current reaction effect
8) Eddy current loss in the retaining sleeve
9) Total magnet loss considering all the armature supply harmonics

The computational efficiency of the 3D Fourier method per case when compared with 3D FEA for low and high frequency rotor eddy current loss

evaluation employing the same computational resources (discussed in the previous chapters) is summarized below in Table 9-1 and Table 9-2.

Table 9-1. Comparison of Computation Time for 3D Fourier Method and 3D FE at Low Frequencies.

	SPM		IPM		Retaining Sleeve	
	3D Fourier method (minutes)	3D FEA	3D Fourier method (minutes)	3D FEA	3D Fourier Method (minutes)	3D FEA
No axial segments	2	1.5 days	5	7 days	8	7 days
10 axial segments	2	8.5 hours	5	1 day	8	1.5 days

Table 9-2.Comparison of Computation Time for 3D Fourier Method and 3D FE at High Frequencies

	SPM		IPM		Retaining Sleeve	
	3D Fourier method (minutes)	3D FEA	3D Fourier method (minutes)	3D FEA	3D Fourier Method (minutes)	3D FEA
No axial segments	15	6 days	18	10 days	20	10 days
12 axial segments	15	1 day	18	1.5 days	20	1.5 days

It is worth noting that the 3D loss prediction method employing 3D Fourier method takes close to 30 to 60 seconds for each of the cases depending on the number of time instants considered, the rest of the time per case is associated with gathering the flux density information from the analytical or 2D FE models. Hence the time associated per case is evaluated as the average of the total time from the starting of evaluation of field information to the loss

prediction up to 12 segments for low frequency cases and up to 20 segments for high frequency cases.

As the rotor eddy current loss can increase its temperature and can force the magnets to operate on a BH curve with reduced knee point flux density value, it is proved that a sudden short circuit at the machine terminals under such conditions can lead to partial irreversible demagnetization. Among the different faults considered the voltage reversal faults are more fatal when compared to short circuit faults as the demagnetizing current observed is several times higher than the machine rated current. It is observed from the experimental results that the severity of the partial demagnetization is lower for torque production in an IPM machine as total torque generated is the resultant of the magnetic and also the reluctance torque. The continuous demagnetization model proposed can be employed for predicting the machine post fault performance and thus aids in de-rating the PM machine for subsequent usage.

9.2 Scope of Future Work

The pitfalls associated with the 3D analytical method developed in Chapter 2 is very well accounted in the 3D Fourier method described in Chapter 3 for SPM machines. However, there exists a possibility of extending the magnet loss evaluation employing the proposed 3D Fourier method to other PM machines such as axial flux, flux switching machines etc.

The main drawback of the 3D Fourier method is that it fails to accommodate the curvature effect of the magnet. Hence the method can result in minor variation in the loss prediction if the pole arc angle and the thickness of the magnet segments are significantly large. However, this may be possible only if a lower number of circumferential segments adopted to reduce the eddy the current loss generated within it. Also the method may also result in reduced accuracy in eddy current loss prediction for the magnets in some special machines designed with irregular shapes.

This is because in 3D Fourier method the physical boundary of the magnets is removed and the eddy current sources are extended as infinitely repeating image sources in all three dimensions. If the employed magnet has a curvature this reoccurring image sources may also fall within the physical boundary of the magnet and hence makes the eddy current source formulation in the form of repeating sinusoids merely impossible. Also in the 3D domain where the axial dimension exists, the image sources derived from 2D boundaries can no longer satisfy conditions on the curved axial surface boundaries. Hence there exist a possibility of improving the eddy current source formulation in the proposed method accommodating irregular magnet shapes for different PM machines.

For the high frequency loss evaluation accounting eddy current reaction effect in SPM machines, the proposed method evaluates the axial source variation based on the current density values evaluated analytically at the mean magnet radius. The rate of diffusion of the eddy current source values may vary a bit along the different magnet radius, which needs to be included (as a correction factor) as the further step for accurate 3D eddy current loss prediction.

Also for the case with IPM machines, the diffusion of the magnetic field is derived the solution to diffusion equation assuming the magnet is surround by a uniform field. However, the core saturation in these machines makes the field more or less non uniform and hence can result errors in loss predictions. Hence a more accurate solution to the eddy current diffusion can improve the accuracy of the magnet loss prediction in IPM machines.

The proposed 3D Fourier method is validated on SPM machines under locked rotor conditions by the author in this thesis. However, a better experimental setup is preferred which can separate/measure the magnet loss at the real operating conditions of the PM machine. A contactless temperature measurement from the rotating magnets and transfer the information to a

stationary unit outside the machine is suggested as it can mitigate the errors associated with voltage drop in the slip rings.

The continuous demagnetization model proposed in assumes a uniform magnet temperature across the magnet cross section and hence all the magnet elements are considered to be operating on the same BH curves intended for this same operating temperature. However, in a practical machine there can be a wide temperature variation along the different magnet regions especially when the eddy current reaction is acting. Hence the partial demagnetization model may result in erroneous results while predicting the demagnetization pattern under different fault conditions. This proposes a scope for improvement of the proposed model which can accommodate separate temperature dependent BH curves for different magnet elements. Also a closed loop electromagnetic- thermal- demagnetization model is preferred for the PM machines for improving the accuracy of the predicted results.

REFERENCES

[1] A. Fratta, A. Vagati, and F. Villata, "On the evolution of AC machines for spindle drive applications," *Industry Applications, IEEE Transactions on,* vol. 28, pp. 1081-1086, 1992.

[2] N. Bianchi, S. Bolognani, and F. Luise, "Potentials and limits of high-speed PM motors," *Industry Applications, IEEE Transactions on,* vol. 40, pp. 1570-1578, 2004.

[3] N. Bernard, F. Martin, and M. E. H. Zaim, "Design Methodology of a Permanent Magnet Synchronous Machine for a Screwdriver Application," *Energy Conversion, IEEE Transactions on* vol. 27, pp. 624-633, 2012.

[4] F. J. H. Kalluf, L. N. Tutelea, I. Boldea, and A. Espindola, "2/4-POLE Split-Phase Capacitor Motor for Small Compressors: A Comprehensive Motor Characterization," *Industry Applications, IEEE Transactions on,* vol. 50, pp. 356-363, 2014.

[5] F. Zhang, G. Du, T. Wang, F. Wang, W. Cao, and J. L. Kirtley, "Electromagnetic Design and Loss Calculations of a 1.12-MW High-Speed Permanent-Magnet Motor for Compressor Applications," *IEEE Transactions on Energy Conversion,* vol. 31, pp. 132-140, 2016.

[6] Z. Q. Zhu and D. Howe, "Electrical Machines and Drives for Electric, Hybrid, and Fuel Cell Vehicles," *Proceedings of the IEEE,* vol. 95, pp. 746-765, 2007.

[7] K. Yoshida, Y. Hita, and K. Kesamaru, "Eddy-current loss analysis in PM of surface-mounted-PM SM for electric vehicles," *Magnetics, IEEE Transactions on,* vol. 36, pp. 1941-1944, 2000.

[8] J. Wang, X. Ping, Z., and D. Howe, "Three-phase modular permanent magnet brushless Machine for torque boosting on a downsized ICE vehicle," *Vehicular Technology, IEEE Transactions on,* vol. 54, pp. 809-816, 2005.

[9] L. Parsa and H. A. Toliyat, "Fault-Tolerant Interior-Permanent-Magnet Machines for Hybrid Electric Vehicle Applications," *Vehicular Technology, IEEE Transactions on,* vol. 56, pp. 1546-1552, 2007.

[10] G. Pellegrino, A. Vagati, P. Guglielmi, and B. Boazzo, "Performance Comparison Between Surface-Mounted and Interior PM Motor Drives for Electric Vehicle Application," *Industrial Electronics, IEEE Transactions on,* vol. 59, pp. 803-811, 2012.

[11] K. Urase, N. Yabu, K. Kiyota, H. Sugimoto, A. Chiba, M. Takemoto, *et al.*, "Energy Efficiency of SR and IPM Generators for Hybrid Electric Vehicle," *Industry Applications, IEEE Transactions on,* vol. 51, pp. 2874-2883, 2015.

[12] X. Jiang, W. Huang, R. Cao, Z. Hao, and W. Jiang, "Electric Drive System of Dual-Winding Fault-Tolerant Permanent-Magnet Motor for Aerospace Applications," *Industrial Electronics, IEEE Transactions on,* vol. 62, pp. 7322-7330, 2015.

[13] A. Sarigiannidis, M. Beniakar, P. Kakosimos, A. Kladas, L. Papini, and C. Gerada, "Fault Tolerant Design of Fractional Slot Winding Permanent Magnet Aerospace Actuator," *IEEE Transactions on Transportation Electrification,* vol. PP, pp. 1-1, 2016.

[14] C. Yicheng, P. Pillay, and A. Khan, "PM wind generator topologies," *Industry Applications, IEEE Transactions on,* vol. 41, pp. 1619-1626, 2005.

[15] J. Yan, H. Lin, Y. Feng, X. Guo, Y. Huang, and Z. Q. Zhu, "Improved sliding mode model reference adaptive system speed observer for fuzzy control of direct-drive permanent magnet synchronous generator wind power generation system," *IET Renewable Power Generation,* vol. 7, pp. 28-35, 2013.

[16] R. Missoum, N. Bernard, M. E. Zaim, and J. Bonnefous, "Optimization of high speed surface mounted permanent magnet synchronous machines," in *Electrical Machines and Power Electronics, 2007. ACEMP '07. International Aegean Conference on*, 2007, pp. 446-451.

[17] Y. L. Karnavas and C. D. Korkas, "Optimization methods evaluation for the design of radial flux surface PMSM," in *Electrical Machines (ICEM), 2014 International Conference on*, 2014, pp. 1348-1355.

[18] G. Jubb and R. McCurrie, "Hysteresis and magnetic viscosity in a Nd-Fe-B permanent magnet," *Magnetics, IEEE Transactions on* vol. 23, pp. 1801-1805, 1987.

[19] J. Pyrh, x00F, nen, S. Ruoho, J. Nerg, M. Paju*, et al.*, "Hysteresis Losses in Sintered NdFeB Permanent Magnets in Rotating Electrical Machines," *Industrial Electronics, IEEE Transactions on,* vol. 62, pp. 857-865, 2015.

[20] I. Petrov, D. Egorov, J. Link, R. Stern, S. Ruoho, and J. Pyrhonen, "Hysteresis losses in different types of permanent magnets used in PMSMs," *IEEE Transactions on Industrial Electronics,* vol. PP, pp. 1-1, 2016.

[21] K. Atallah, J. Wang, and D. Howe, "Torque-ripple minimization in modular permanent-magnet brushless machines," *Industry Applications, IEEE Transactions on,* vol. 39, pp. 1689-1695, 2003.

[22] H. Toda, X. Zhenping, J. Wang, K. Atallah, and D. Howe, "Rotor eddy-current loss in permanent magnet brushless machines," *Magnetics, IEEE Transactions on,* vol. 40, pp. 2104-2106, 2004.

[23] J. Wang, K. Atallah, Z. Q. Zhu, and D. Howe, "Modular 3-Phase Permanent Magnet Brushless Machines for In-Wheel Applications," in *Vehicle Power and Propulsion Conference, 2006. VPPC '06. IEEE*, 2006, pp. 1-6.

[24] R. Wrobel and P. H. Mellor, "Design Considerations of a Direct Drive Brushless Machine With Concentrated Windings," *Energy Conversion, IEEE Transactions on,* vol. 23, pp. 1-8, 2008.

[25] S. Chaithongsuk, N. Takorabet, and S. Kreuawan, "Reduction of Eddy-Current Losses in Fractional-Slot Concentrated-Winding Synchronous PM Motors," *Magnetics, IEEE Transactions on,* vol. 51, pp. 1-4, 2015.

[26] P. Sergeant and A. Van den Bossche, "Segmentation of Magnets to Reduce Losses in Permanent-Magnet Synchronous Machines," *Magnetics, IEEE Transactions on,* vol. 44, pp. 4409-4412, 2008.

[27] K. Yamazaki, M. Shina, Y. Kanou, M. Miwa, and J. Hagiwara, "Effect of Eddy Current Loss Reduction by Segmentation of Magnets in Synchronous Motors: Difference Between Interior and Surface Types," *Magnetics, IEEE Transactions on,* vol. 45, pp. 4756-4759, 2009.

[28] S. Ruoho, J. Kolehmainen, J. Ikaheimo, and A. Arkkio, "Interdependence of Demagnetization, Loading, and Temperature Rise in a Permanent-Magnet Synchronous Motor," *Magnetics, IEEE Transactions on,* vol. 46, pp. 949-953, 2010.

[29] P. Zhou, D. Lin, Y. Xiao, N. Lambert, and M. A. Rahman, "Temperature-Dependent Demagnetization Model of Permanent Magnets for Finite Element Analysis," *Magnetics, IEEE Transactions on,* vol. 48, pp. 1031-1034, 2012.

[30] V. I. Patel and J. Wang, "Demagnetization assessment of 6-phase fractional-slot permanent magnet machines with low space harmonics under various fault conditions," in *Power Electronics, Machines and Drives (PEMD 2014), 7th IET International Conference on*, 2014, pp. 1-6.

[31] Z. Nannan, Z. Q. Zhu, and L. Weiguo, "Rotor Eddy Current Loss Calculation and Thermal Analysis of Permanent Magnet Motor and Generator," *Magnetics, IEEE Transactions on,* vol. 47, pp. 4199-4202, 2011.

[32] X. Hung Vu, D. Lahaye, M. J. Hoeijmakers, H. Polinder, and J. A. Ferreira, "Studying rotor eddy current loss of PM machines using nonlinear FEM including rotor motion," in *Electrical Machines (ICEM), 2010 XIX International Conference on*, 2010, pp. 1-7.

[33] Z. Belli and M. R. Mekideche, "Optimization of magnets segmentation for eddy current losses reduction in permanent magnets electrical machines," in *Ecological Vehicles and Renewable Energies (EVER), 2013 8th International Conference and Exhibition on*, 2013, pp. 1-7.

[34] F. Zhang, G. Du, T. Wang, F. Wang, W. Cao, and J. L. Kirtley, "Electromagnetic Design and Loss Calculations of a 1.12-MW High-Speed Permanent-Magnet Motor for Compressor Applications," *Energy Conversion, IEEE Transactions on,* vol. PP, pp. 1-9, 2015.

[35] R. Kaczmarek, W. Y. Huang, and J. C. Vannier, "Magnetic losses simulation in PM SM drive by FE: Harmonic superposition by method of locked rotor," in *2007 9th International Conference on Electrical Power Quality and Utilisation*, 2007, pp. 1-4.

[36] M. v. d. Geest, H. Polinder, and J. A. Ferreira, "Efficient finite element based rotor loss calculation for permanent magnet synchronous machines," in *Electrical Machines (ICEM), 2014 International Conference on*, 2014, pp. 1133-1138.

[37] G. J. Atkinson, B. C. Mecrow, A. G. Jack, D. J. Atkinson, P. Sangha, and M. Benarous, "The Analysis of Losses in High-Power Fault-Tolerant Machines for Aerospace Applications," *Industry Applications, IEEE Transactions on,* vol. 42, pp. 1162-1170, 2006.

[38] L. Jian, C. Da-Woon, C. Chang-Hum, K. Dae-hyun, and C. Yun-Hyun, "Eddy-Current Calculation of Solid Components in Fractional Slot Axial Flux Permanent Magnet Synchronous Machines," *Magnetics, IEEE Transactions on,* vol. 47, pp. 4254-4257, 2011.

[39] K. Yamazaki and S. Watari, "Loss analysis of permanent-magnet motor considering carrier harmonics of PWM inverter using combination of 2-D and 3-D finite-element method," *Magnetics, IEEE Transactions on,* vol. 41, pp. 1980-1983, 2005.

[40] K. Magyari, M. M. Radulescu, F. Laza, and D. Coutellier, "Eddy-current loss analysis of small interior-permanent-magnet synchronous motors with fractional-slot concentrated windings," in *SPEEDAM 2010*, 2010, pp. 1603-1606.

[41] M. v. d. Geest, J. J. Wolmarans, H. Polinder, J. A. Ferreira, and D. Zeilstra, "Rotor losses in laminated magnets and an anisotropic carbon fiber sleeve," in *Power Electronics, Machines and Drives (PEMD 2012), 6th IET International Conference on*, 2012, pp. 1-6.

[42] Y. Kawase, T. Ota, and H. Fukunaga, "3-D eddy current analysis in permanent magnet of interior permanent magnet motors," *Magnetics, IEEE Transactions on,* vol. 36, pp. 1863-1866, 2000.

[43] R. Benlamine, F. Dubas, S. A. Randi, D. Lhotellier, and C. Espanet, "3-D Numerical Hybrid Method for PM Eddy-Current Losses Calculation: Application to Axial-Flux PMSMs," *Magnetics, IEEE Transactions on,* vol. 51, pp. 1-10, 2015.

[44] G. Choi and T. Jahns, "Reduction of Eddy-Current Losses in Fractional-Slot Concentrated-Winding Synchronous PM Machines," *Magnetics, IEEE Transactions on,* vol. PP, pp. 1-1, 2016.

[45] K. Yamazaki, Y. Kato, T. Ikemi, and S. Ohki, "Reduction of Rotor Losses in Multilayer Interior Permanent-Magnet Synchronous Motors by Introducing Novel Topology of Rotor Flux Barriers," *Industry Applications, IEEE Transactions on,* vol. 50, pp. 3185-3193, 2014.

[46] N. Kesavamurthy and A. K. Basu, "Effects of Traveling Field on Ferromagnetic Plates of Finite Thickness," *Power Apparatus and Systems, IEEE Transactions on,* vol. PAS-86, pp. 1565-1571, 1967.

[47] R. L. Stoll, *The analysis of eddy currents*: Clarendon Press, 1974.

[48] A. Jassal, H. Polinder, and J. A. Ferreira, "Literature survey of eddy-current loss analysis in rotating electrical machines," *IET Electric Power Applications,* vol. 6, pp. 743-752, 2012.

[49] H. Polinder and M. J. Hoeijmakers, "Eddy-current losses in the segmented surface-mounted magnets of a PM machine," *IEE Proceedings - Electric Power Applications,* vol. 146, pp. 261-266, 1999.

[50] Z. Q. Zhu and D. Howe, "Instantaneous magnetic field distribution in brushless permanent magnet DC motors. II. Armature-reaction field," *Magnetics, IEEE Transactions on* vol. 29, pp. 136-142, 1993.

[51] Z. Q. Zhu, D. Howe, E. Bolte, and B. Ackermann, "Instantaneous magnetic field distribution in brushless permanent magnet DC motors. I. Open-circuit field," *Magnetics, IEEE Transactions on* vol. 29, pp. 124-135, 1993.

[52] Z. Q. Zhu, D. Howe, and C. C. Chan, "Improved analytical model for predicting the magnetic field distribution in brushless permanent-magnet machines," *Magnetics, IEEE Transactions on* vol. 38, pp. 229-238, 2002.

[53] K. Atallah, D. Howe, P. H. Mellor, and D. A. Stone, "Rotor loss in permanent-magnet brushless AC machines," *Industry Applications, IEEE Transactions on,* vol. 36, pp. 1612-1618, 2000.

[54] D. Ishak, Z. Q. Zhu, and D. Howe, "Eddy-current loss in the rotor magnets of permanent-magnet brushless machines having a fractional number of slots per pole," *Magnetics, IEEE Transactions on,* vol. 41, pp. 2462-2469, 2005.

[55] J. Alexandrova, H. Jussila, J. Nerg, Pyrho, x, and J. nen, "Comparison between models for eddy-current loss calculations in rotor surface-mounted permanent magnets," in *Electrical Machines (ICEM), 2010 XIX International Conference on*, 2010, pp. 1-6.

[56] S. M. Abu Sharkh, M. R. Harris, and N. T. Irenji, "Calculation of rotor eddy-current loss in high-speed PM alternators," in *Electrical Machines and Drives, 1997 Eighth International Conference on (Conf. Publ. No. 444)*, 1997, pp. 170-174.

[57] N. Schofield, K. Ng, Z. Q. Zhu, and D. Howe, "Parasitic rotor losses in a brushless permanent magnet traction machine," in *Electrical Machines and Drives, 1997 Eighth International Conference on (Conf. Publ. No. 444)*, 1997, pp. 200-204.

[58] A. Jassal, H. Polinder, D. Lahaye, and J. A. Ferreira, "Analytical and FE calculation of eddy-current losses in PM concentrated winding machines for wind turbines," in *2011 IEEE International Electric Machines & Drives Conference (IEMDC)*, 2011, pp. 717-722.

[59] X. Ding and C. Mi, "Modeling of eddy current loss in the magnets of permanent magnet machines for hybrid and electric vehicle traction applications," in *2009 IEEE Vehicle Power and Propulsion Conference*, 2009, pp. 419-424.

[60] J. Wang, K. Atallah, R. Chin, W. M. Arshad, and H. Lendenmann, "Rotor Eddy-Current Loss in Permanent-Magnet Brushless AC Machines," *Magnetics, IEEE Transactions on,* vol. 46, pp. 2701-2707, 2010.

[61] A. Rahideh and T. Korakianitis, "Analytical magnetic field distribution of slotless brushless permanent magnet motors - Part 1. Armature reaction field, inductance and rotor eddy current loss calculations," *Electric Power Applications, IET,* vol. 6, pp. 628-638, 2012.

[62] D. Fang, "Commutation-caused eddy-current losses in permanent-magnet brushless DC motors," *Magnetics, IEEE Transactions on* vol. 33, pp. 4310-4318, 1997.

[63] D. Fang, "Improved analytical modeling of commutation losses including space harmonic effects in permanent magnet brushless DC motors," in *Industry Applications Conference, 1998. Thirty-Third IAS Annual Meeting. The 1998 IEEE*, 1998, pp. 380-386 vol.1.

[64] Z. Q. Zhu, K. Ng, N. Schofield, and D. Howe, "Improved analytical modelling of rotor eddy current loss in brushless machines equipped with surface-mounted permanent magnets," *Electric Power Applications, IEE Proceedings,* vol. 151, pp. 641-650, 2004.

[65] M. Markovic and Y. Perriard, "A simplified determination of the permanent magnet (PM) eddy current losses due to slotting in a PM rotating motor," in *Electrical Machines and Systems, 2008. ICEMS 2008. International Conference on*, 2008, pp. 309-313.

[66] N. Bianchi and E. Fornasiero, "Impact of MMF Space Harmonic on Rotor Losses in Fractional-Slot Permanent-Magnet Machines," *Energy Conversion, IEEE Transactions on* vol. 24, pp. 323-328, 2009.

[67] N. Bianchi and E. Fornasiero, "Index of rotor losses in three-phase fractional-slot permanent magnet machines," *IET Electric Power Applications,* vol. 3, pp. 381-388, 2009.

[68] N. Bianchi, S. Bolognani, and E. Fornasiero, "An Overview of Rotor Losses Determination in Three-Phase Fractional-Slot PM Machines," *Industry Applications, IEEE Transactions on,* vol. 46, pp. 2338-2345, 2010.

[69] Z. Q. Zhu, K. Ng, N. Schofield, and D. Howe, "Analytical prediction of rotor eddy current loss in brushless machines equipped with surface-mounted permanent magnets. I. Magnetostatic field model," in *Electrical Machines and Systems, 2001. ICEMS 2001. Proceedings of the Fifth International Conference on*, 2001, pp. 806-809 vol.2.

[70] Z. Q. Zhu and D. Howe, "Instantaneous magnetic field distribution in brushless permanent magnet DC motors. III. Effect of stator slotting," *Magnetics, IEEE Transactions on* vol. 29, pp. 143-151, 1993.

[71] D. A. Wills and M. J. Kamper, "Analytical prediction of rotor eddy current loss due to stator slotting in PM machines," in *2010 IEEE Energy Conversion Congress and Exposition*, 2010, pp. 992-995.

[72] Z. X. Fang, Z. Q. Zhu, L. J. Wu, and Z. P. Xia, "Simple and accurate analytical estimation of slotting effect on magnet loss in fractional-slot surface-mounted PM machines," in *Electrical Machines (ICEM), 2012 XXth International Conference on*, 2012, pp. 464-470.

[73] C. Bode and W. R. Canders, "Advanced calculation of eddy current losses in PMSM with tooth windings," in *Electrical Machines (ICEM), 2010 XIX International Conference on*, 2010, pp. 1-6.

[74] D. Zarko, D. Ban, and T. A. Lipo, "Analytical calculation of magnetic field distribution in the slotted air gap of a surface permanent-magnet motor using complex relative air-gap permeance," *Magnetics, IEEE Transactions on,* vol. 42, pp. 1828-1837, 2006.

[75] D. Zarko, D. Ban, and T. A. Lipo, "Analytical Solution for Cogging Torque in Surface Permanent-Magnet Motors Using Conformal Mapping," *Magnetics, IEEE Transactions on,* vol. 44, pp. 52-65, 2008.

[76] K. Boughrara, R. Ibtiouen, x, D. arko, O. Touhami, and A. Rezzoug, "Magnetic Field Analysis of External Rotor Permanent-Magnet Synchronous Motors Using Conformal Mapping," *Magnetics, IEEE Transactions on,* vol. 46, pp. 3684-3693, 2010.

[77] A. A. Qazalbash, S. M. Sharkh, N. T. Irenji, R. G. Wills, and M. A. Abusara, "Rotor eddy loss in high-speed permanent magnet synchronous generators," *Electric Power Applications, IET,* vol. 9, pp. 370-376, 2015.

[78] F. Dubas and C. Espanet, "Analytical Solution of the Magnetic Field in Permanent-Magnet Motors Taking Into Account Slotting Effect: No-Load Vector Potential and Flux Density Calculation," *Magnetics, IEEE Transactions on,* vol. 45, pp. 2097-2109, 2009.

[79] T. Lubin, S. Mezani, and A. Rezzoug, "Exact Analytical Method for Magnetic Field Computation in the Air Gap of Cylindrical Electrical Machines Considering Slotting Effects," *Magnetics, IEEE Transactions on,* vol. 46, pp. 1092-1099, 2010.

[80] Z. Q. Zhu, L. J. Wu, and Z. P. Xia, "An Accurate Subdomain Model for Magnetic Field Computation in Slotted Surface-Mounted Permanent-Magnet Machines," *Magnetics, IEEE Transactions on,* vol. 46, pp. 1100-1115, 2010.

[81] A. Bellara, H. Bali, Y. Amara, G. Barakat, and P. Reghem, "Analytical prediction of open-circuit eddy-current loss in series double excitation synchronous machines," in *2010 IEEE Energy Conversion Congress and Exposition*, 2010, pp. 1737-1744.

[82] L. J. Wu, Z. Q. Zhu, D. Staton, M. Popescu, and D. Hawkins, "Analytical Modeling and Analysis of Open-Circuit Magnet Loss in Surface-Mounted Permanent-Magnet Machines," *Magnetics, IEEE Transactions on,* vol. 48, pp. 1234-1247, 2012.

[83] T. Lubin, S. Mezani, and A. Rezzoug, "2-D Exact Analytical Model for Surface-Mounted Permanent-Magnet Motors With Semi-Closed Slots," *Magnetics, IEEE Transactions on,* vol. 47, pp. 479-492, 2011.

[84] L. J. Wu, Z. Q. Zhu, D. Staton, M. Popescu, and D. Hawkins, "Analytical prediction of electromagnetic performance of surface-mounted PM machines based on subdomain model accounting for tooth-tips," *Electric Power Applications, IET,* vol. 5, pp. 597-609, 2011.

[85] L. J. Wu, Z. Q. Zhu, D. Staton, M. Popescu, and D. Hawkins, "An Improved Subdomain Model for Predicting Magnetic Field of Surface-Mounted Permanent Magnet Machines Accounting for Tooth-Tips," *Magnetics, IEEE Transactions on,* vol. 47, pp. 1693-1704, 2011.

[86] O. de la Barriere, S. Hlioui, H. Ben Ahmed, and M. Gabsi, "An analytical model for the computation of no-load eddy current losses in the rotor of a permanent magnet synchronous machine," *Magnetics, IEEE Transactions on,* vol. PP, pp. 1-1, 2013.

[87] W. Y. Huang, A. Bettayeb, R. Kaczmarek, and J. C. Vannier, "Optimization of Magnet Segmentation for Reduction of Eddy-Current Losses in Permanent Magnet Synchronous Machine," *Energy Conversion, IEEE Transactions on* vol. 25, pp. 381-387, 2010.

[88] S. Ruoho, T. Santa-Nokki, J. Kolehmainen, and A. Arkkio, "Modeling Magnet Length In 2-D Finite-Element Analysis of Electric Machines," *Magnetics, IEEE Transactions on,* vol. 45, pp. 3114-3120, 2009.

[89] L. Sang-Yub and J. Hyun-Kyo, "Eddy current loss analysis in the rotor of permanent magnet traction motor with high power density," in *Vehicle Power and Propulsion Conference (VPPC), 2012 IEEE*, 2012, pp. 210-214.

[90] K. Yamazaki and Y. Fukushima, "Effect of Eddy-Current Loss Reduction by Magnet Segmentation in Synchronous Motors With Concentrated Windings," *Industry Applications, IEEE Transactions on,* vol. 47, pp. 779-788, 2011.

[91] M. Mirzaei, A. Binder, and C. Deak, "3D analysis of circumferential and axial segmentation effect on magnet eddy current losses in permanent magnet synchronous machines with concentrated windings," in *Electrical Machines (ICEM), 2010 XIX International Conference on*, 2010, pp. 1-6.

[92] M. Mirzaei, A. Binder, B. Funieru, and M. Susic, "Analytical Calculations of Induced Eddy Currents Losses in the Magnets of Surface Mounted PM Machines With Consideration of Circumferential and Axial Segmentation Effects," *Magnetics, IEEE Transactions on,* vol. 48, pp. 4831-4841, 2012.

[93] B. Aslan, E. Semail, and J. Legranger, "General Analytical Model of Magnet Average Eddy-Current Volume Losses for Comparison of Multiphase PM Machines With Concentrated Winding," *Energy Conversion, IEEE Transactions on,* vol. 29, pp. 72-83, 2014.

[94] J. Pyrhonen, H. Jussila, Y. Alexandrova, P. Rafajdus, and J. Nerg, "Harmonic Loss Calculation in Rotor Surface Permanent Magnets- ;New Analytic Approach," *Magnetics, IEEE Transactions on,* vol. 48, pp. 2358-2366, 2012.

[95] F. Martin, M. E. H. Zaim, A. Tounzi, and N. Bernard, "Improved Analytical Determination of Eddy Current Losses in Surface Mounted Permanent Magnets of Synchronous Machine," *Magnetics, IEEE Transactions on,* vol. 50, pp. 1-9, 2014.

[96] M. Paradkar and J. Bocker, "3D analytical model for estimation of eddy currentlosses in the magnets of IPM machine considering the reaction field of the induced eddy currents," in *Energy Conversion Congress and Exposition (ECCE), 2015 IEEE*, 2015, pp. 2862-2869.

[97] A. Balamurali, C. Lai, A. Mollaeian, V. Loukanov, and N. Kar, "Analytical Investigation of Magnet Eddy Current Losses in Interior Permanent Magnet Motor Using Modified Winding Function Theory Accounting for Pulse Width Modulation Harmonics," *Magnetics, IEEE Transactions on,* vol. PP, pp. 1-1, 2016.

[98] J. D. Ede, K. Atallah, G. W. Jewell, J. Wang, and D. Howe, "Effect of Axial Segmentation of Permanent Magnets on Rotor Loss in Modular Permanent-Magnet Brushless Machines," *Industry Applications, IEEE Transactions on,* vol. 43, pp. 1207-1213, 2007.

[99] J. Wang, F. Papini, R. Chin, W. M. Arshad, and H. Lendenmann, "Computationally efficient approaches for evaluation of rotor eddy current loss in permanent magnet brushless machines," in *Electrical Machines and Systems, 2009. ICEMS 2009. International Conference on*, 2009, pp. 1-6.

[100] X. Wu, R. Wrobel, P. H. Mellor, and C. Zhang, "A Computationally Efficient PM Power Loss Mapping for Brushless AC PM Machines with Surface-Mounted PM Rotor Construction," *Industrial Electronics, IEEE Transactions on,* vol. PP, pp. 1-1, 2015.

[101] Z. Peng, G. Y. Sizov, H. Jiangbiao, D. M. Ionel, and N. A. O. Demerdash, "Calculation of magnet losses in concentrated-winding permanent magnet synchronous machines using a Computationally Efficient - Finite Element method," in *Energy Conversion Congress and Exposition (ECCE), 2012 IEEE*, 2012, pp. 3363-3370.

[102] Z. Peng, G. Y. Sizov, H. Jiangbiao, D. M. Ionel, and N. A. O. Demerdash, "Calculation of Magnet Losses in Concentrated-Winding Permanent-Magnet Synchronous Machines Using a Computationally Efficient Finite-Element Method," *Industry Applications, IEEE Transactions on,* vol. 49, pp. 2524-2532, 2013.

[103] T. Okitsu, D. Matsuhashi, and K. Muramatsu, "Method for Evaluating the Eddy Current Loss of a Permanent Magnet in a PM Motor Driven by an Inverter Power Supply Using Coupled 2-D and 3-D Finite Element Analyses," *Magnetics, IEEE Transactions on,* vol. 45, pp. 4574-4577, 2009.

[104] K. Yamazaki and Y. Kanou, "Rotor Loss Analysis of Interior Permanent Magnet Motors Using Combination of 2-D and 3-D Finite Element Method," *Magnetics, IEEE Transactions on,* vol. 45, pp. 1772-1775, 2009.

[105] M. v. d. Geest, H. Polinder, and J. A. Ferreira, "Computationally efficient 3D FEM rotor eddy-current loss calculation for permanent magnet synchronous machines," in *2015 IEEE International Electric Machines & Drives Conference (IEMDC)*, 2015, pp. 1165-1169.

[106] T. Okitsu, D. Matsuhashi, G. Yanhui, and K. Muramatsu, "Coupled 2-D and 3-D Eddy Current Analyses for Evaluating Eddy Current Loss of a Permanent Magnet in Surface PM Motors," *Magnetics, IEEE Transactions on,* vol. 48, pp. 3100-3103, 2012.

[107] L. J. Wu, Z. Q. Zhu, D. Staton, M. Popescu, and D. Hawkins, "Analytical Model for Predicting Magnet Loss of Surface-Mounted Permanent Magnet Machines Accounting for Slotting Effect and Load," *Magnetics, IEEE Transactions on,* vol. 48, pp. 107-117, 2012.

[108] A. Masmoudi and A. Masmoudi, "3-D Analytical Model With the End Effect Dedicated to the Prediction of PM Eddy-Current Loss in FSPMMs," *Magnetics, IEEE Transactions on,* vol. 51, pp. 1-11, 2015.

[109] S. S. Nair, J. Wang, R. Chin, and L. Chen, "3D analytical slotting-effect model for predicting magnet eddy current loss in surface mounted PM machines," in *2015 IEEE Magnetics Conference (INTERMAG)*, 2015, pp. 1-1.

[110] S. S. Nair, J. Wang, R. Chin, L. Chen, and T. Sun, "Analytical Prediction of 3D Magnet Eddy Current Losses in Surface Mounted PM Machines Accounting Slotting Effect " *Energy Conversion, IEEE Transactions on* in revision.

[111] H. Bolton, "Transverse edge effect in sheet-rotor induction motors," *Electrical Engineers, Proceedings of the Institution of,* vol. 116, pp. 725-731, 1969.

[112] T. W. Preston and A. B. J. Reece, "Corrigendum: Transverse edge effects in linear induction motors," *Electrical Engineers, Proceedings of the Institution of,* vol. 117, p. 1808, 1970.

[113] R. Lin and A. Arkkio, "Calculation and Analysis of Stator End-Winding Leakage Inductance of an Induction Machine," *Magnetics, IEEE Transactions on,* vol. 45, pp. 2009-2014, 2009.

[114] D. Li, W. Li, X. Zhang, J. Fang, H. Qiu, J. Shen, *et al.*, "A New Approach to Evaluate Influence of Transverse Edge Effect of a Single-Sided HTS Linear Induction Motor Used for Linear Metro," *Magnetics, IEEE Transactions on,* vol. 51, pp. 1-4, 2015.

[115] J. Wang, V. I. Patel, and W. Weiya, "Fractional-Slot Permanent Magnet Brushless Machines with Low Space Harmonic Contents," *Magnetics, IEEE Transactions on,* vol. 50, pp. 1-9, 2014.

[116] S. M. Sharkh, M. R. Harris, and N. T. Irenji, "Calculation of rotor eddy-current loss in high-speed PM alternators," in *Electrical Machines and Drives, 1997 Eighth International Conference on (Conf. Publ. No. 444)*, 1997, pp. 170-174.

[117] S. A. Sharkh, N. T. Irenji, and M. Harris, "Effect of power factor on rotor loss in high-speed PM alternators," in *Electrical Machines and Drives, 1999. Ninth International Conference on (Conf. Publ. No. 468)*, 1999, pp. 346-350.

[118] D. Fang and T. W. Nehl, "Analytical modeling of eddy-current losses caused by pulse-width-modulation switching in permanent-magnet brushless direct-current motors," *Magnetics, IEEE Transactions on* vol. 34, pp. 3728-3736, 1998.

[119] Z. Q. Zhu, K. Ng, N. Schofield, and D. Howe, "Analytical prediction of rotor eddy current loss in brushless machines equipped with surface-mounted permanent magnets. II. Accounting for eddy current reaction field," in *Electrical Machines and Systems, 2001. ICEMS 2001. Proceedings of the Fifth International Conference on*, 2001, pp. 810-813 vol.2.

[120] H. Wan-Ying, A. Bettayeb, R. Kaczmarek, and J. C. Vannier, "Optimization of Magnet Segmentation for Reduction of Eddy-Current Losses in Permanent Magnet

Synchronous Machine," *Energy Conversion, IEEE Transactions on,* vol. 25, pp. 381-387, 2010.

[121] L. Chen, J. Wang, and S. S. Nair, "An Analytical Method for Predicting 3-D Eddy Current Loss in Permanent Magnet Machines Based on Generalized Image Theory," *Magnetics, IEEE Transactions on,* vol. 52, pp. 1-11, 2016.

[122] S. S. Nair, L. Chen, J. Wang, R. Chin, I.Manolas, and D.Svechkarenko, "Computationally efficient 3D analytical magnet loss prediction in SPM machines," *Electric Power Applications, IET,* vol. pp, pp. 1-25, 2016 (Early Access).

[123] S. S. Nair, L.Chen, J.Wang, R.Chin, I.Manolas, and D.Svechkarenko, "3D analytical slotting-effect model for magnet loss prediction in SPM machines," in *Power Electronics, Machines and Drives (PEMD 2016), 8th IET International Conference on.*, 2016, pp. 1-6.

[124] C. Liang, J. Wang, "Evaluation of rotor eddy current loss in permanent magnet machines employing fractional-slot windings with low space harmonics," in *Conferences Magnetics (INTERMAG), IEEE Int. Conf. Magnetics* 2014, Dresden, Germany.

[125] P. Lazari, J. Wang, and C. Liang, "A Computationally Efficient Design Technique for Electric-Vehicle Traction Machines," *Industry Applications, IEEE Transactions on,* vol. 50, pp. 3203-3213, 2014.

[126] A. G. Sarigiannidis and A. G. Kladas, "Switching Frequency Impact on Permanent Magnet Motors Drive System for Electric Actuation Applications," *Magnetics, IEEE Transactions on,* vol. 51, pp. 1-4, 2015.

[127] K. Basu, J. Prasad, and G. Narayanan, "Minimization of Torque Ripple in PWM AC Drives," *Industrial Electronics, IEEE Transactions on,* vol. 56, pp. 553-558, 2009.

[128] B. M. Ebrahimi and J. Faiz, "Demagnetization Fault Diagnosis in Surface Mounted Permanent Magnet Synchronous Motors," *Magnetics, IEEE Transactions on,* vol. 49, pp. 1185-1192, 2013.

[129] K. Ki-Chan, L. Seung-Bin, K. Dae-Hyun, and L. Ju, "The Shape Design of Permanent Magnet for Permanent Magnet Synchronous Motor Considering Partial Demagnetization," *Magnetics, IEEE Transactions on,* vol. 42, pp. 3485-3487, 2006.

[130] S. S. Nair, J. Wang, L. Chen, R. Chin, I. Manolas, and D. Svechkarenko, "Prediction of 3-D High-Frequency Eddy Current Loss in Rotor Magnets of SPM Machines," *Magnetics, IEEE Transactions on,* vol. 52, pp. 1-10, 2016.

[131] K. Yamazaki and A. Abe, "Loss Investigation of Interior Permanent-Magnet Motors Considering Carrier Harmonics and Magnet Eddy Currents," *Industry Applications, IEEE Transactions on,* vol. 45, pp. 659-665, 2009.

[132] Y. Aoyama, K. Miyata, and K. Ohashi, "Simulations and experiments on eddy current in Nd-Fe-B magnet," *Magnetics, IEEE Transactions on,* vol. 41, pp. 3790-3792, 2005.

[133] K. Yamazaki, M. Shina, M. Miwa, and J. Hagiwara, "Investigation of Eddy Current Loss in Divided Nd–Fe–B Sintered Magnets for Synchronous Motors Due to Insulation Resistance and Frequency," *Magnetics, IEEE Transactions on,* vol. 44, pp. 4269-4272, 2008.

[134] K. Yamazaki, Y. Kanou, Y. Fukushima, S. Ohki, A. Nezu, T. Ikemi*, et al.*, "Reduction of Magnet Eddy-Current Loss in Interior Permanent-Magnet Motors With Concentrated Windings," *Industry Applications, IEEE Transactions on,* vol. 46, pp. 2434-2441, 2010.

[135] D. Liu, A. Jassal, H. Polinder, and J. A. Ferreira, "Validation of eddy current loss models for permanent magnet machines with fractional-slot concentrated windings," in *Electric Machines & Drives Conference (IEMDC), 2013 IEEE International*, 2013, pp. 678-685.

[136] K. Yamazaki, T. Fukuoka, K. Akatsu, N. Nakao, and A. Ruderman, "Investigation of Locked Rotor Test for Estimation of Magnet PWM Carrier Eddy Current Loss in Synchronous Machines," *Magnetics, IEEE Transactions on,* vol. 48, pp. 3327-3330, 2012.

[137] L. Chen, J. Wang, and S. S. Nair, "An analytical method for predicting 3D eddy current loss in permanent magnet machines based on generalized image theory," *Magnetics, IEEE Transactions on,* vol. 52, pp. 1-11, 2015.

[138] H. Chen, R. Qu, J. Li, and D. Li, "Demagnetization Performance of a 7 MW Interior Permanent Magnet Wind Generator with Fractional-slot Concentrated Windings," *Magnetics, IEEE Transactions on,* vol. PP, pp. 1-1, 2015.

[139] M. Barcaro, A. Faggion, L. Sgarbossa, N. Bianchi, and S. Bolognani, "Performance evaluation of an integrated starter alternator using an interior permanent magnet machine," *Electric Power Applications, IET,* vol. 4, pp. 539-546, 2010.

[140] A. M. El-Refaie, J. P. Alexander, S. Galioto, P. B. Reddy, H. Kum-Kang, P. de Bock*, et al.*, "Advanced High-Power-Density Interior Permanent Magnet Motor for Traction Applications," *Industry Applications, IEEE Transactions on,* vol. 50, pp. 3235-3248, 2014.

[141] X. Chen, J. Wang, and A. Griffo, "A High-Fidelity and Computationally Efficient Electro-thermally Coupled Model for Interior Permanent-Magnet Machines in Electric Vehicle Traction Applications," *Transportation Electrification, IEEE Transactions on,* vol. PP, pp. 1-1, 2015.

[142] T. M. Jahns and R. C. Van Nocker, "High-performance EHA controls using an interior permanent magnet motor," *Aerospace and Electronic Systems, IEEE Transactions on,* vol. 26, pp. 534-542, 1990.

[143] L. Sun-Kwon, K. Gyu-Hong, and H. Jin, "Finite Element Computation of Magnetic Vibration Sources in 100 kW Two Fractional-Slot Interior Permanent Magnet Machines for Ship," *Magnetics, IEEE Transactions on,* vol. 48, pp. 867-870, 2012.

[144] T. M. Jahns, "Flux-Weakening Regime Operation of an Interior Permanent-Magnet Synchronous Motor Drive," *Industry Applications, IEEE Transactions on,* vol. IA-23, pp. 681-689, 1987.

[145] S. R. Macminn and T. M. Jahns, "Control techniques for improved high-speed performance of interior PM synchronous motor drives," *Industry Applications, IEEE Transactions on,* vol. 27, pp. 997-1004, 1991.

[146] J. Cheol, S. Ji-Yun, and H. In-Joong, "Flux-Weakening Control of IPM Motors With Significant Effect of Magnetic Saturation and Stator Resistance," *Industrial Electronics, IEEE Transactions on,* vol. 55, pp. 1330-1340, 2008.

[147] K. Yamazaki and K. Kitayuguchi, "Teeth shape optimization of surface and interior permanent-magnet motors with concentrated windings to reduce magnet eddy current losses," in *Electrical Machines and Systems (ICEMS), 2010 International Conference on*, 2010, pp. 990-995.

[148] J. Li, Y. Xu, and J. Zou, "Analysis and Reduction of Magnet Loss by Deepening Magnets in Interior Permanent Magnet Machines with a Pole/Slot Ratio of 2/3," *Magnetics, IEEE Transactions on,* vol. PP, pp. 1-1, 2015.

[149] H. Seok-Hee, T. M. Jahns, and Z. Q. Zhu, "Analysis of Rotor Core Eddy-Current Losses in Interior Permanent-Magnet Synchronous Machines," *Industry Applications, IEEE Transactions on,* vol. 46, pp. 196-205, 2010.

[150] L. Zhu, S. Z. Jiang, Z. Q. Zhu, and C. C. Chan, "Analytical Modeling of Open-Circuit Air-Gap Field Distributions in Multisegment and Multilayer Interior Permanent-Magnet Machines," *Magnetics, IEEE Transactions on,* vol. 45, pp. 3121-3130, 2009.

[151] A. Bettayeb, X. Jannot, and J. C. Vannier, "Analytical calculation of rotor magnet eddy-current losses for high speed IPMSM," in *Electrical Machines (ICEM), 2010 XIX International Conference on*, 2010, pp. 1-6.

[152] L. Chen, D. Hopkinson, J. Wang, A. Cockburn, M. Sparkes, and W. O Neill, "Reduced Dysprosium permanent magnets and their applications in electric vehicle traction motors," *Magnetics, IEEE Transactions on,* vol. PP, pp. 1-1, 2015.

[153] L. Chen, J. Wang, P. Lombard, P. Lazari, and V. Leconte, "Design optimisation of permanent magnet assisted synchronous reluctance machines for electric vehicle applications," in *Electrical Machines (ICEM), 2012 XXth International Conference on*, 2012, pp. 2647-2653.

[154] C. Liang, J. Wang, P. Lazari, and C. Xiao, "Optimizations of a permanent magnet machine targeting different driving cycles for electric vehicles," in *Electric Machines & Drives Conference (IEMDC), 2013 IEEE International*, 2013, pp. 855-862.

[155] S. S. Nair, J. Wang, L. Chen, R. Chin, I. Manolas, and D. Svechkarenko, "Computationally Efficient 3D Eddy Current Loss Prediction in Magnets of Interior Permanent Magnet Machines," *Magnetics, IEEE Transactions on,* vol. 52, pp. 1-10, 2016.

[156] X. Chen, J. Wang, V. I. Patel, P. Lazari, L. Chen, and P. Lombard, "Reluctance torque evaluation for interior permanent magnet machines using frozen permeability," in *Power Electronics, Machines and Drives (PEMD 2014), 7th IET International Conference on*, 2014, pp. 1-6.

[157] W. Q. Chu and Z. Q. Zhu, "Average Torque Separation in Permanent Magnet Synchronous Machines Using Frozen Permeability," *Magnetics, IEEE Transactions on,* vol. 49, pp. 1202-1210, 2013.

[158] A. Chebak, P. Viarouge, and J. Cros, "Improved Analytical Model for Predicting the Magnetic Field Distribution in High-Speed Slotless Permanent-Magnet Machines," *Magnetics, IEEE Transactions on,* vol. 51, pp. 1-4, 2015.

[159] J. Hyun-Woo, L. Ju, L. Hyung-Woo, and K. Won-Ho, "Study on the Optimal Rotor Retaining Sleeve Structure for the Reduction of Eddy-Current Loss in High-Speed SPMSM," *Magnetics, IEEE Transactions on,* vol. 51, pp. 1-4, 2015.

[160] F. Zhang, G. Du, T. Wang, G. Liu, and W. Cao, "Rotor Retaining Sleeve Design for a 1.12-MW High-Speed PM Machine," *Industry Applications, IEEE Transactions on,* vol. 51, pp. 3675-3685, 2015.

[161] H. Polinder and M. J. Hoeijmakers, "Effect of a shielding cylinder an the rotor losses in a rectifier-loaded PM machine," in *Industry Applications Conference, 2000. Conference Record of the 2000 IEEE*, 2000, pp. 163-170 vol.1.

[162] F. Zhou, S. Jianxin, F. Weizhong, and L. Ruiguang, "Study of Retaining Sleeve and Conductive Shield and Their Influence on Rotor Loss in High-Speed PM BLDC Motors," *Magnetics, IEEE Transactions on,* vol. 42, pp. 3398-3400, 2006.

[163] S. Jian-Xin, H. He, J. Meng-Jia, and Y. Cheng, "Reduction of Rotor Eddy Current Loss in High Speed PM Brushless Machines by Grooving Retaining Sleeve," *Magnetics, IEEE Transactions on,* vol. 49, pp. 3973-3976, 2013.

[164] C. Han-Wook, J. Seok-Myeong, and C. Sang-Kyu, "A Design Approach to Reduce Rotor Losses in High-Speed Permanent Magnet Machine for Turbo-Compressor," *Magnetics, IEEE Transactions on,* vol. 42, pp. 3521-3523, 2006.

[165] L. J. Wu, Z. Q. Zhu, D. Staton, M. Popescu, and D. Hawkins, "Analytical modeling of eddy current loss in retaining sleeve of surface-mounted PM machines accounting for influence of slot opening," in *Industrial Electronics (ISIE), 2012 IEEE International Symposium on*, 2012, pp. 611-616.

[166] M. R. Shah and A. M. El-Refaie, "Eddy-Current Loss Minimization in Conducting Sleeves of Surface PM Machine Rotors With Fractional-Slot Concentrated Armature Windings by Optimal Axial Segmentation and Copper Cladding," *Industry Applications, IEEE Transactions on,* vol. 45, pp. 720-728, 2009.

[167] S. S. Nair, J. Wang, L. Chen, R. Chin, I. Manolas, and D. Svechkarenko, "Computationally efficent 3D rotor eddy current loss prediction in permanent magnet

machines," in *Electrical Machines (ICEM), 2016 XXII International Conference on*, 2016, pp. 1-7.

[168] A. Sarikhani and O. A. Mohammed, "Demagnetization Control for Reliable Flux Weakening Control in PM Synchronous Machine," *Energy Conversion, IEEE Transactions on,* vol. 27, pp. 1046-1055, 2012.

[169] V. I. Patel, J. Wang, W. Wang, and X. Chen, "Six-Phase Fractional-Slot-per-Pole-per-Phase Permanent-Magnet Machines With Low Space Harmonics for Electric Vehicle Application," *Industry Applications, IEEE Transactions on,* vol. 50, pp. 2554-2563, 2014.

[170] A. Vagati, B. Boazzo, P. Guglielmi, and G. Pellegrino, "Design of Ferrite-Assisted Synchronous Reluctance Machines Robust Toward Demagnetization," *Industry Applications, IEEE Transactions on,* vol. 50, pp. 1768-1779, 2014.

[171] A. Tessarolo, M. Mezzarobba, and R. Menis, "Modeling, Analysis, and Testing of a Novel Spoke-Type Interior Permanent Magnet Motor With Improved Flux Weakening Capability," *Magnetics, IEEE Transactions on,* vol. 51, pp. 1-10, 2015.

[172] M. S. Toulabi, J. Salmon, and A. M. Knight, "Concentrated winding IPM synchronous motor design for wide field weakening applications," in *Energy Conversion Congress and Exposition (ECCE), 2015 IEEE*, 2015, pp. 3865-3871.

[173] V. I. Patel, J. Wang, and S. S. Nair, "Demagnetization Assessment of Fractional-Slot and Distributed Wound 6-Phase Permanent Magnet Machines," *Magnetics, IEEE Transactions on,* vol. 51, pp. 1-11, 2015.

[174] H. Jongman, P. Sanguk, H. Doosoo, K. Tae-june, L. Sang Bin, C. Kral*, et al.*, "Detection and Classification of Rotor Demagnetization and Eccentricity Faults for PM Synchronous Motors," *Industry Applications, IEEE Transactions on,* vol. 48, pp. 923-932, 2012.

[175] H. Xiong, J. Zhang, M. W. Degner, C. Rong, F. Liang, and W. Li, "Permanent Magnet Demagnetization Test Fixture Design and Validation," *Industry Applications, IEEE Transactions on,* vol. PP, pp. 1-1, 2016.

[176] P. Sergeant and A. P. M. V. d. Bossche, "Influence of the Amount of Permanent-Magnet Material in Fractional-Slot Permanent-Magnet Synchronous Machines," *Industrial Electronics, IEEE Transactions on,* vol. 61, pp. 4979-4989, 2014.

[177] J. Wang, W. Wang, K. Atallah, and D. Howe, "Demagnetization Assessment for Three-Phase Tubular Brushless Permanent-Magnet Machines," *Magnetics, IEEE Transactions on,* vol. 44, pp. 2195-2203, 2008.

[178] K. Ki-Chan, K. Kwangsoo, K. Hee-jun, and L. Ju, "Demagnetization Analysis of Permanent Magnets According to Rotor Types of Interior Permanent Magnet Synchronous Motor," *Magnetics, IEEE Transactions on,* vol. 45, pp. 2799-2802, 2009.

[179] S. Ruoho, E. Dlala, and A. Arkkio, "Comparison of Demagnetization Models for Finite-Element Analysis of Permanent-Magnet Synchronous Machines," *Magnetics, IEEE Transactions on,* vol. 43, pp. 3964-3968, 2007.

[180] K. Gyu-Hong, H. Jin, N. Hyuk, H. Jung-Pyo, and K. Gyu-Tak, "Analysis of irreversible magnet demagnetization in line-start motors based on the finite-element method," *Magnetics, IEEE Transactions on,* vol. 39, pp. 1488-1491, 2003.

[181] Y. Zhilichev, "Analysis of Permanent Magnet Demagnetization Accounting for Minor B-H Curves," *Magnetics, IEEE Transactions on,* vol. 44, pp. 4285-4288, 2008.

[182] K. Hyung-Kyu, H. Jin, K. Byeong-Woo, and K. Gyu-Hong, "Characteristic analysis of IPM type BLDC motor considering the demagnetization of PM by stator turn fault," in *Energy Conversion Congress and Exposition (ECCE), 2010 IEEE*, 2010, pp. 3063-3070.

[183] L. Yoon-Seok, K. Kyung-Tae, and H. Jin, "Finite-Element Analysis of the Demagnetization of IPM-Type BLDC Motor With Stator Turn Fault," *Magnetics, IEEE Transactions on,* vol. 50, pp. 889-892, 2014.

[184] C. Gilsu and T. M. Jahns, "Interior permanent magnet synchronous machine rotor demagnetization characteristics under fault conditions," in *Energy Conversion Congress and Exposition (ECCE), 2013 IEEE*, 2013, pp. 2500-2507.

[185] J. D. McFarland and T. M. Jahns, "Investigation of the Rotor Demagnetization Characteristics of Interior PM Synchronous Machines During Fault Conditions," *Industry Applications, IEEE Transactions on,* vol. 50, pp. 2768-2775, 2014.

[186] C. Gilsu and T. M. Jahns, "Post-demagnetization characteristics of permanent magnet synchronous machines," in *Energy Conversion Congress and Exposition (ECCE), 2015 IEEE*, 2015, pp. 1781-1788.

[187] U. G. OPERA-2D, Vector Fields Ltd., Oxford, U.K, 2013.

[188] A. M. Technologies, *Neodymium-Iron-Boron Magnet Catalogs. Available:* http://www.arnoldmagnetics.com/Neodymium_Literature.aspx.

[189] S. S. Nair, V. I. Patel, and J. Wang, "Post-Demagnetization Performance Assessment for Interior Permanent Magnet AC Machines," *Magnetics, IEEE Transactions on,* vol. 52, pp. 1-10, 2016.

[190] V. I. Patel, "Novel 6-phase fractional-slot permanent magnet machine for electric vehicle applications," Department of Electronic and Electrcial Engineering, PhD Thesis, The University of Sheffield The University of Sheffield, UK, 2014.

[191] V. Patel, J. Wang, D. Nugraha, R. Vuletic, and J. Tousen, "Enhanced Availability of Drivetrain through Novel Multi-phase Permanent Magnet Machine Drive," *Industrial Electronics, IEEE Transactions on,* vol. PP, pp. 1-1, 2015.

[192] V. I. Patel, J. Wang, W. Wang, and X. Chen, "Analysis and design of 6-phase fractional slot per pole per phase permanent magnet machines with low space harmonics," in *IEEE International Electric Machines & Drives Conference (IEMDC)*, 2013, pp. 386-393.

[193] V. Patel, J. Wang, W. Wang, and X. Chen, "6-phase Fractional Slot per Pole per Phase Permanent Magnet Machines with Low Space Harmonics for Electric Vehicle Application," *Industry Applications, IEEE Transactions on,* vol. PP, pp. 1-1, 2014.

[194] V. I. Patel, J. Wang, W. Wang, and C. Xiao, "Analysis and design of 6-phase fractional slot per pole per phase permanent magnet machines with low space harmonics," in *Electric Machines & Drives Conference (IEMDC), 2013 IEEE International*, 2013, pp. 386-393.

[195] V. I. Patel, J. Wang, W. Wang, and X. Chen, "Thermal design and analysis of 6-phase fractional slot permanent magnet machines considering driving cycles," in *Power Electronics, Machines and Drives (PEMD 2014), 7th IET International Conference on*, 2014, pp. 1-6.

TABLE OF FIGURES

Table of figures

Table of figures

LIST OF TABLES

List of tables

APPENDIX A
Derivation of the Imaging Method for 3-D Eddy Current Field.

Consider infinitely large two conducting regions, as shown in Fig. A-1 (a) Region 1 is assumed to have a conductivity σ_1 and occupies in the space where z > 0, and the rest of the region is denoted by Region 2 with conductivity σ_2. Assume there exists a source of excitation, $S_{(x1,y1,z1)}$ in the Region 1.

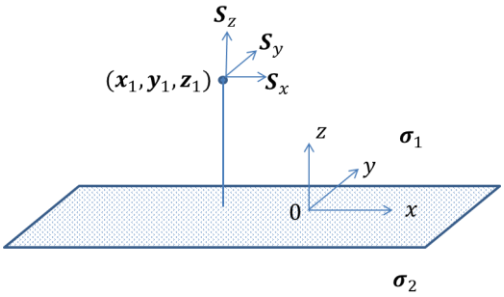

(a)

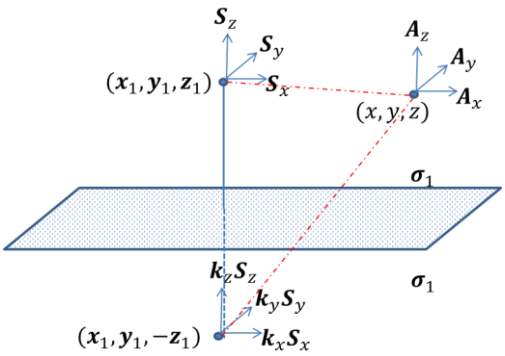

(b)

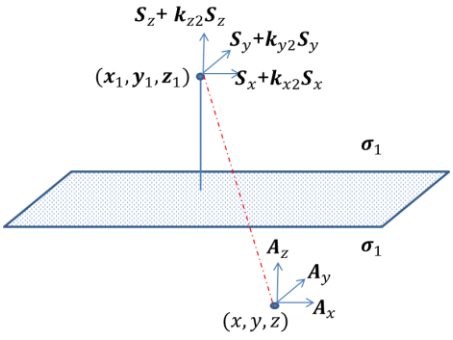

(c)

Fig.A-1. (a) Two semi-infinitely long conductor with sources only in the upper half; (b) Solution to the current density in upper half with the image sources in the lower half; (c) Solution to the current density in the lower half with the image sources in the upper half.

In order to quantify the magnetic field distribution in Region 1, the effect of the boundary conditions may be represented by an image source, $\left(k_x S_{x(x1,y1,-z1)}, k_y S_{y(x1,y1,-z1)}, k_z S_{z(x1,y1,-z1)}\right)$ in the Region 2 . The

conductivity of the Region 2 being set to σ_1, as shown in Fig. A-1 (b). Similarly, for the field distribution assumed in Region 2, its effect of on the boundary conditions may be further represented by another image source, $\left(k_{x2}\, S_{x_{(x1,y1,z1)}},\, k_{y2}\, S_{y_{(x1,y1,z1)}},\, k_{z2}\, S_{z_{(x1,y1,z1)}}\right)$, in Region 1 with the conductivity in Region 2 being set to σ_1, as shown in Fig.A1-1(c).

Now k_x, k_y, k_z and k_{x2}, k_{y2}, k_{z2} are image coefficients to be determined based on the boundary conditions to satisfy for the eddy current density J and the electric field E, are given by.

$$J_{1z} = J_{2z} \tag{A-1}$$

$$E_{1x} = E_{2x} \tag{A-2}$$

$$E_{1y} = E_{2y} \tag{A-3}$$

As the field region in Fig.A1.2 has become homogenous and also extending to infinity, the current vector potential A_i that satisfies $\nabla^2 A_i = -\sigma S$ in Region 1 can be obtained using the volume integration given by,

$$A_{i1x} = \iiint \left(\frac{-\sigma_1 S_x}{4\pi r_1} + \frac{-\sigma_1 k_x S_x}{4\pi r_2}\right) dx_1 dy_1 dz_1 \tag{A-4}$$

$$A_{i1y} = \iiint \left(\frac{-\sigma_1 S_y}{4\pi r_1} + \frac{-\sigma_1 k_y S_y}{4\pi r_2}\right) dx_1 dy_1 dz_1 \tag{A-5}$$

$$A_{i1z} = \iiint \left(\frac{-\sigma_1 S_z}{4\pi r_1} + \frac{-\sigma_1 k_z S_z}{4\pi r_2}\right) dx_1 dy_1 dz_1 \tag{A-6}$$

Similarly, the current vectors in the Region 2 also can be derived as,

$$A_{i2x} = \iiint \left(\frac{-\sigma_1 S_x}{4\pi r_1} + \frac{-\sigma_1 k_{x2} S_x}{4\pi r_2}\right) dx_1 dy_1 dz_1 \tag{A-7}$$

$$A_{i2y} = \iiint \left(\frac{-\sigma_1 S_y}{4\pi r_1} + \frac{-\sigma_1 k_{y2} S_y}{4\pi r_2}\right) dx_1 dy_1 dz_1 \tag{A-8}$$

$$A_{i2z} = \iiint \left(\frac{-\sigma_1 S_z}{4\pi r_1} + \frac{-\sigma_1 k_{z2} S_z}{4\pi r_2}\right) dx_1 dy_1 dz_1 \tag{A-9}$$

where,

$r_1 = \sqrt{(x-x_1)^2 + (y-y_1)^2 + (z-z_1)^2}$ and

$r_2 = \sqrt{(x-x_1)^2 + (y-y_1)^2 + (z+z_1)^2}$

Applying the boundary conditions in terms of current vector potential A-1 to A-3 can be derived as,

$$\left(\frac{\partial A_{i1y}}{\partial x} - \frac{\partial A_{i1x}}{\partial y}\right) = \left(\frac{\partial A_{i2y}}{\partial x} - \frac{\partial A_{i2x}}{\partial y}\right) \tag{A-10}$$

$$\frac{1}{\sigma_1}\left(\frac{\partial A_{i1z}}{\partial y} - \frac{\partial A_{i1y}}{\partial z}\right) = \frac{1}{\sigma_2}\left(\frac{\partial A_{i2z}}{\partial y} - \frac{\partial A_{i2y}}{\partial z}\right) \tag{A-11}$$

$$\frac{1}{\sigma_1}\left(\frac{\partial A_{i1x}}{\partial z} - \frac{\partial A_{i1z}}{\partial x}\right) = \frac{1}{\sigma_2}\left(\frac{\partial A_{i2x}}{\partial z} - \frac{\partial A_{i2z}}{\partial x}\right) \tag{A-12}$$

Substituting for current vector potential components $A_{i1x}, A_{i1y}, A_{i1z}$ and $A_{i2x}, A_{i2y}, A_{i2z}$ from A- 4 to A-9 , the image coefficients can be determined as,

$$k_x = k_{x2} = k_y = k_{y2} = \frac{\sigma_2 - \sigma_1}{\sigma_2 + \sigma_1} \tag{A-13}$$

$$k_z = -k_{z2} = \frac{\sigma_1 - \sigma_2}{\sigma_2 + \sigma_1} \tag{A-14}$$

As for the case with Magnets in Region 2 is non-conductive, $\sigma_2 = 0$, it can be seen that

$$k_x = k_y = -1, k_z = 1 \tag{A-15}$$

Hence , to represent the effect of an infinite boundary at $z = 0$ on the eddy current field, the boundary can be removed employing an image source which is located in the position symmetrical with respect to the boundary plane in non-conducting Region 2.

It can be seen that the image vector components are having the same amplitude. Also the z-component is having the identical sign as that of the original source. However, the x and y-components whose directions are in

parallel with the boundary plane is having the opposite sign as that of the source.

APPENDIX B
Solution to Diffusion Equation Evaluating the Current Density Components

The current density components (J_z,J_θ) are derived in polar coordinate system,

$$J_z = \sum_{n=1,3,5,7} \left(C_{1n}.cosh(\gamma.R_{mean}/R_s.\theta).e^{j\omega_s t} + C_{2n}.sinh(\gamma\, R_{mean}/R_s.\theta).e^{j\omega_s t} - J_{pn}.e^{j(\omega_s t - p.R_{mean}/R_s.\theta)}\right) cos(n\,\pi/L_z.z) \quad \text{(B-1)}$$

$$J_\theta = \sum_{n=1,3,5,7} \left(R_s.\frac{C_{1n}}{\gamma}.sinh(\gamma.R_{mean}/R_s.\theta).e^{j\omega_s t} + R_s.\frac{C_{2n}}{\gamma}.cosh(\gamma.R_{mean}/R_s.\theta).e^{j\omega_s t} - \frac{J_{pn}}{(-j\,p/R_s)}.e^{j(\omega_s t - p.R_{mean}/R_s.\theta)}\right).\left(\frac{n\pi}{L_z}\right) sin(n\,\pi/L_z.z) \quad \text{(B-2)}$$

However, neglecting any magnet curvature, $J_x = J_\theta$.

where $R_{mean} = (R_r + R_m)/2$ and ,

$$J_{pn} = \frac{J_{pn1}}{J_{pn2}} \quad \text{(B-3)}$$

$$J_{pn2} = p^2 + (R_s.n\,\pi/L_z)^2 + j\omega_s\mu_0\frac{1}{\rho}\frac{d}{g}{R_s}^2 \quad \text{(B-4)}$$

$$J_{pn2} = j\omega_s\mu_0\frac{1}{\rho}J_m\frac{d}{g}.4/n\pi.sin(n\,\pi/2).{R_s}^2 \quad \text{(B-5)}$$

$$\gamma = R_s \sqrt{\left(\left(\frac{n\pi}{L_z}\right)^2 + j\omega_s \mu_0 . \frac{1}{\rho} . \frac{d}{g}\right)} \tag{B-6}$$

As in (4-8) for polar coordiantes,

$$J_\theta \left(\theta = \frac{-\beta_m}{2}\right) = J_\theta \left(\theta = \frac{\beta_m}{2}\right) = 0$$

and,

$$\text{and,} C_{1n} = j\omega_s \gamma J_m \frac{1}{\rho}\frac{d}{g} . 4/n\pi . sin(n\pi/2)/p . C_{11n} \tag{B-7}$$

$$C_{11n} = \mu_0 {R_s}^2 . \frac{sin(p\ R_{mean}/R_s . \beta_m/2)}{sinh(\gamma R_{mean}/R_s . \beta_m/2)} . \frac{1}{J_{pn2}} \tag{B-8}$$

$$C_{2n} = -\omega_s \gamma J_m \frac{1}{\rho}\frac{d}{g} . 4/n\pi . sin(n\pi/2)/p . C_{22n} \tag{B-9}$$

$$C_{22n} = \mu_0 {R_s}^2 . \frac{cos(p . R_{mean}/R_s . \beta_m/2)}{cosh(\gamma . R_{mean}/R_s . \beta_m/2)} . \frac{1}{J_{pn2}} \tag{B-20}$$

For the case with retaining sleeve, the current densities J_{sl_z} and J_{sl_x} described in Chapter 7 can also be defined using the equations (A-1) and (A-2) with $R_{mean} = R_m + t_s/2$

and $\beta_m = 2\pi$.

APPENDIX C
Fourier Series Expansion of Flux Density Coefficients in the Retaining Sleeve and the Definition of Simplified Coefficients

As the coefficients A_2, B_2, C_2 and D_2 vary with rotor position, it can be expressed as Fourier series [165] as,

$$A_2 = \sum_l a_{2l} \cos(lp\omega_r t + \psi_{a2l}) \tag{C-1}$$

$$B_2 = \sum_l b_{2l} \cos(lp\omega_r t + \psi_{b2l}) \tag{C-2}$$

$$C_2 = \sum_l c_{2l} \cos(lp\omega_r t + \psi_{c2l}) \tag{C-3}$$

$$D_2 = \sum_l d_{2l} \cos(lp\omega_r t + \psi_{d2l}) \tag{C-4}$$

After simplification, the coefficients $a_{1b}, a_{1f,}\ a_{2b}, a_{2f}$ and their corresponding phase angles $\psi_{1b}, \psi_{1f}, \psi_{2b}, \psi_{1f}$ can be defined as,

$$a_{1b} = \left| a_{2l} e^{j\psi_{a2l}} + c_{2l} e^{j\left(\psi_{c2l} - \frac{\pi}{2}\right)} \right| / 2 \tag{C-5}$$

$$a_{1f} = \left| a_{2l} e^{-j\psi_{a2l}} + c_{2l} e^{-j\left(\psi_{c2l} + \frac{\pi}{2}\right)} \right| / 2 \tag{C-6}$$

$$a_{2b} = \left| b_{2l} e^{j\psi_{b2l}} + d_{2l} e^{j\left(\psi_{d2l} - \frac{\pi}{2}\right)} \right| / 2 \tag{C-7}$$

$$a_{2f} = \left| b_{2l} e^{-j\psi_{b2l}} + d_{2l} e^{-j\left(\psi_{d2l} + \frac{\pi}{2}\right)} \right| / 2 \tag{C-8}$$

$$\psi_{1b} = angle\left(a_{2l} e^{j\psi_{a2l}} + c_{2l} e^{j\left(\psi_{c2l} - \frac{\pi}{2}\right)} \right) \tag{C-9}$$

$$\psi_{1f} = angle\left(a_{2l} e^{-j\psi_{a2l}} + c_{2l} e^{-j\left(\psi_{c2l} + \frac{\pi}{2}\right)} \right) \tag{C-10}$$

$$\psi_{2b} = angle\left(b_{2l}e^{j\psi_{b2l}} + d_{2l}e^{j\left(\psi_{d2l}-\frac{\pi}{2}\right)}\right) \tag{C-11}$$

$$\psi_{2f} = angle\left(b_{2l}e^{-j\psi_{b2l}} + d_{2l}e^{-j\left(\psi_{d2l}+\frac{\pi}{2}\right)}\right) \tag{C-12}$$

APPENDIX D
Flux Density Evaluation in the Magnet and the Retaining Sleeve from the Subdomain Model for SPM Machines

The MATLAB script to evaluate the flux density information for each time instant within the magnet and the retaining sleeve is described in this section. The script is developed based on the more accurate subdomain model proposed in [84].

SCRIPT-1 has to run along with SCRIPT-2 to-5 for evaluation of coefficients A1, C1, A2, B2, C2 and D2. The harmonics associated with the flux density is evaluated in SCRIPT-6 and SCRIPT-7 for the implication of 3D magnet loss prediction in SCRIPT-8 and SCRIPT-9 in Appendix D and E.

```
%%%% SCRIPT-1

%%% Main Script to evaluate the coefficients A1, C1, A2, B2, C2 and D2
from the solutions of simultaneous equation in subdomain model %%%%%%%%

clear; clc;

% INPUTS:

% name                  [unit]      [description]
p       =  4; %           []      Number of pole pairs
Ns      =  18; %          []      Total number of slots
gap     =  0.955e-3; %    [m]     Air Gap Length
hm      =  3.0e-3; %      [m]     Magnet Thickness
ur      =  1.05; %        []      Magnet relative permeability
Brm     =  1.1; %         [T]     Magnet remanent flux density
Rso     =  70.59e-3; %    [m]     Stator Outer Radius
Rs      =  33.45e-3; %    [m]     Stator Inner Radius
Rm      =  (Rs-gap); %    [m]     Rotor Outer Radius
Syh     =  7.99e-3; %     [m]     Stator Yoke Height
tgd     =  2.75e-3; %     [m]     Teeth Tip Height
sospr   =  0.1739; %      [R]     Slot Opening/slot pitch
swspr   =  0.48; %        [R]     Slot width/slot pitch
ap      =  0.9722; %      [R]     Magnet pole arc/pole pitch
Kmag    =  0; %           []      Magnetization: Radial/Parallel(0,1)
N       =  4500;          [rpm]   Speed


% Calculated Parameters
Qp        =  Ns/p; %          []      Number of stator slots/pole
```

```
Rt       =  Rs+tgd; %       [m]    Radius  below Teeth Tip
Rr       =  Rm-hm; %        [m]    Magnet inner radius
Rsb      =  Rso-Syh; %      [m]    Stator back iron radius
theta_p  =  pi/p; %         [rad]  Magnet pole pitch
boa      = (2*pi/Ns)*sospr;%[rad]  Slot opening width in radians
boa      = boa*0.99; %      [rad]  (adjusted for gamma)
bsa      =(2*pi/Ns)*swspr;% [rad]  Slot Width
d        = bsa/2; %         [m]    J (current density) width
theta_th = 2*pi/Ns-boa; %   [rad]  Teeth width at air gap in radians;
w        = 2*pi*N/60; %   [rad/s]  Speed in radians per second;

% Constants and other Variables
u0=4*pi*1e-7; %           Air magnetic permeability
alpha_0=(2*pi/p)/4; %     Rotor Initial Position
alpha_i=(2*pi/Ns)/2; %    Position of the 'i' th slot
nk=200; %                 Number of Magnet space harmonics- Magnet
nn=100; %                 Number of Current Space harmonics-Slot
nm=100; %                 Number of Space harmonics-slot opening
k=((0:nk-1)+1); %    space harmonic ranks (magnet); k=1,3,5..
n=((0:nn-1)+1); %    space harmonic ranks (slot); n=1,2,3..
m=((0:nm-1)+1); %    space harmonic ranks (slot opening); m=1,2,3..
Gamma_D=240; %       Advance angle in degree
Jm=3.09*1e6; %       Peak Current density (IA,B,C peak = 55A )
nomega=720; %        Number of divisions (mechanical in 360)
omegar_t=(linspace(0,359,nomega))*2/p*(pi/180);%

% Harmonic Coefficients for Magnet
A1=zeros(nk,nomega); C1=zeros(nk,nomega);
%% Harmonic Coefficients for the Air gap (Retaining Sleeve)
A2=zeros(nk,nomega); B2=zeros(nk,nomega); %
C2=zeros(nk,nomega); D2=zeros(nk,nomega; %
Mrck1=zeros(nk,nomega);Mrsk1=zeros(nk,nomega); %
Mack1=zeros(nk,nomega);Mask1=zeros(nk,nomega); %
ia=1;%

for io=1:nomega
Ja=Jm*sin(p*omegar_t(io)+(Gamma_D+90)*pi/180);
Jb=Jm*sin(p*omegar_t(io)+(Gamma_D+90)*pi/180-2*pi/3);
Jc=Jm*sin(p*omegar_t(io)+(Gamma_D+90)*pi/180+2*pi/3);
J=[Ja Ja Jb -Jc -Ja -Ja Jc Jc Ja -Jb -Jc -Jc Jb Jb Jc -Ja -Jb -Jb...
   Ja Ja Jb -Jc -Ja -Ja Jc Jc Ja -Jb -Jc -Jc Jb Jb Jc -Ja -Jb -Jb];%

%%%%%%%%%%%%%%%%%Interface between PM and AG%%%%%%%%%%%%%%%%%%%%%%%%%

%%%%%% B1r@Rm == B2r@Rm
G1_1=(Rr/Rm).^k;G1=diag(G1_1);
G2_1=(Rm/Rs).^k;G2=diag(G2_1);
K=diag(k);IK=eye(nk);
K11=IK+G1^2; K22=IK+G1^2; K13=-G2; K25=-G2; K14=-IK; K26=-
IK;%(K11,K22,K13,K25,K14,K26 are k x k Matrices)
[Mrck,Mrsk,Mack,Mask] =...
Magnetization_C1(ap,theta_p,k,nk,Brm,p,Kmag,omegar_t(io),alpha_0) ;
Y_1= ...
-u0*((k.^2-1).^-1).*((Rr*k.*G1_1+Rm).*Mack'-(Rr*G1_1+Rm*k).*Mrsk');
Y_1(1)=0;Y1=Y_1'; % Y1 is kx1 Matrix
Y_2= ...
-u0*((k.^2-1).^-1).*((Rr*k.*G1_1+Rm).*Mask'+(Rr*G1_1+Rm*k).*Mrck');
Y_2(1)=0;Y2=Y_2'; % Y2 is kx1 Matrix
K31=IK-G1^2; K42=IK-G1^2; K33=-ur*G2; K45=-ur*G2; K34=ur*IK;
K46=ur*IK;%(K31,K42,K33,K45,K34,K46 are kxk Matrices)
```

```
Y_3=-u0*((k.^2-1).^-1).*(k.*(Rm-Rr*G1_1).*Mack'-(Rm-Rr*G1_1).*Mrsk');
Y_3(1)=0;Y3=Y_3';% Y3 is kx1 Matrix
Y_4=-u0*((k.^2-1).^-1).*(k.*(Rm-Rr*G1_1).*Mask'+(Rm-Rr*G1_1).*Mrck');
Y_4(1)=0;Y4=Y_4'; % Y4 is kx1 Matrix

%%%%%%%%%%%%%% Interface between Slot Opening and Slot %%%%%%%%%%%%%%%

%%%%%%%%% B3ia at Rt =B4ia at Rt
Fm_1=m*pi/boa; Fm=diag(Fm_1);
En_1=n*pi/bsa; En=diag(En_1);%Fm is mxm Matrix and En = nxn Matrix
G3=(Rt/Rsb)^En; G4=(Rs/Rt)^Fm;%G3 is nxn Matrix and G4 is mxm Matrix
[gamma,zeta,J0,Y9,Y8,Jn] = Current_OC(Rt,Rsb,bsa,boa,nm,nn,Ns,J,d);
K97_1=gamma'*Fm;
K98_1=-gamma'*Fm*G4;IN=eye(nn);K99_1=-En*(G3^2-IN);% K97_1,K98_1,K99_1
are nxm Matrix
T = cell(1,Ns);for j=1:Ns; T{j}1-3 =K97_1; end ; K97 = blkdiag(T{:}1-
3);%K97 is Ns*mxn Matrix with Matrix K97_1 as diagonal
T = cell(1,Ns);for j=1:Ns; T{j} =K98_1; end ; K98 =blkdiag(T{:});%K98
is Ns*mxn Matrix with Matrix K98_1 as diagonal
T = cell(1,Ns);for j=1:Ns; T{j} =K99_1; end ; K99 = blkdiag(T{:});%K99
is Ns*mxn Matrix with Matrix K99_1 as diagonal

%%%%%%%%%%  Az4i@Rt =Az3i@Rt
IM=eye(nm);K87_1=IM;K88_1=G4;%K87_1,K88_1 are mxm Matrix
K89_1=-zeta*(G3^2+IN);% K89_1 is mxn Matrix
T = cell(1,Ns);for j=1:Ns; T{j} =K87_1; end ; K87 = blkdiag(T{:});%K87
is Ns*mxm Matrix with Matrix K87_1 as diagonal
T = cell(1,Ns);for j=1:Ns; T{j} =K88_1; end ; K88 = blkdiag(T{:});%K88
is Ns*mxm Matrix with Matrix K88_1 as diagonal
T = cell(1,Ns);for j=1:Ns; T{j} =K89_1; end ; K89 = blkdiag(T{:});%K89
is Ns*mxn Matrix with Matrix K89_1 as diagonal

%%%%%%%%%%%%%% Interface Between Slot Opening and Air %%%%%%%%%%%%%%%

%%%%%%%%%%  B4ia@Rs = B2a@Rs
[eta,xi,Ftm,G4t,eta0,xi0] = ...
etaxi_MagAR_C1(boa,nm,nk,alpha_i,Ns,Rs,Rt,p);
K53=-K;K65=-K;% K54 and K65 are kxk Matrix
K54=G2*K;K66=G2*K;% K54 and K66 are kxk Matrix
K57=eta'*Ftm*G4t;K58=-eta'*Ftm;K67=xi'*Ftm*G4t;
K68=-xi'*Ftm;% K57,K58,K67,K68 are kx(m*Ns) Matrix
Y5= -(u0/2)*(bsa/boa)*(Rsb^2-Rt^2)*eta0*J0; % size (k,1)
Y6= -(u0/2)*(bsa/boa)*(Rsb^2-Rt^2)*xi0*J0;% size (k,1)
%%%%%%%%%%  Az2@Rs = Az4@Rs
sigma=2*pi/boa*eta;tau=2*pi/boa*xi;
K73=sigma;K74=sigma*G2;
K75=tau;K76=tau*G2;% K73,K74,K75,K76 are (m*Ns)xk Matrices
K77=-G4t;K78 =-eye(nm*Ns);%K78,K77 are (m*Ns)x(m*Ns) Matrices
%%%%%%% Null Matrices
K0k_k=zeros(nk);K0k_mNs=zeros(nk,nm*Ns);K0k_nNs=zeros(nk,nn*Ns);
K0mNs_k=zeros(nm*Ns,nk);K0nNs_k=zeros(nn*Ns,nk);
K0mNs_nNs=zeros(nm*Ns,nn*Ns);
Y0mNs=zeros(nm*Ns,1);Y0nNs=zeros(nn*Ns,1);
```

```
%%%%%%%%%%  Matrix D formation %%%%%%%%%%%%%%%%%%%%%%%%%%%%%%%%%%%%%%%%%%%%%%%%%
D= [K11 K0k_k  K13 K14  K0k_k  K0k_k  K0k_mNs K0k_mNs K0k_nNs;...
    K0k_k K22  K0k_k  K0k_k  K25  K26  K0k_mNs K0k_mNs K0k_nNs;...
    K31  K0k_k  K33  K34  K0k_k  K0k_k  K0k_mNs K0k_mNs K0k_nNs;...
    K0k_k  K42  K0k_k  K0k_k  K45   K46   K0k_mNs K0k_mNs K0k_nNs;...
    K0k_k  K0k_k  K53  K54   K0k_k   K0k_k  K57  K58   K0k_nNs;...
    K0k_k  K0k_k  K0k_k  K0k_k  K65  K66    K67  K68   K0k_nNs;...
    K0mNs_k K0mNs_k K73  K74    K75  K76    K77  K78   K0mNs_nNs;...
    K0mNs_k K0mNs_k K0mNs_k K0mNs_k K0mNs_k K0mNs_k K87 K88 K89;...
    K0nNs_k K0nNs_k K0nNs_k K0nNs_k K0nNs_k K0nNs_k K97 K98 K99];

Y=[Y1;Y2;Y3;Y4;Y5;Y6;Y0mNs;Y8;Y9];
Co=(D\Y)';

%%%%%%%%%% Determination of Coefficients%%%%%%%%%%%%%%%%%%%%%%%%%%%%%%%%
A1(:,ia)=Co(1:nk);C1(:,ia)=Co(nk+1:2*nk);
A2(:,ia)=Co(2*nk+1:3*nk);B2(:,ia)=Co(3*nk+1:4*nk);
C2(:,ia)=Co(4*nk+1:5*nk);D2(:,ia)=Co(5*nk+1:6*nk);
Mrck1(:,ia)= Mrck;Mrsk1(:,ia)=Mrsk;Mack1(:,ia)=Mack;Mask1(:,ia)=Mask;

ia=ia+1;
end;
%%%%%%%%%%%%%%%%%%%%%%%%%%%%%%%%%%%%%%%%%%%%%%%%%%%%%%%%%%%%%%%%%%%%%%%%%%%%


%%%% SCRIPT-2

%%%%%%% Magnetization Function to evaluate Mrck, Mrsk, Mack, Mask in
Script-1%%%

function [Mrck,Mrsk,Mack,Mask] = ...
Magnetization_C1(ap,theta_p,k,nk,Brm,p,Kmag,omegar_t,alpha_0)
%parallel magnetization
if Kmag==1
A1k=mysinc_C1((k+1),ap,theta_p,nk,p,Kmag);
A2k=mysinc_C1((k-1),ap,theta_p,nk,p,Kmag);% magnet width dependent
Mrk=(Brm/u0)*ap*(A1k+A2k); Mak=(Brm/u0)*ap*(A1k-A2k);
Mrck_1=  Mrk.*cos(k*omegar_t+k*alpha_0);
Mrsk_1=Mrk.*sin(k*omegar_t+k*alpha_0);
Mack_1= -Mak.*sin(k*omegar_t+k*alpha_0);
Mask_1=Mak.*cos(k*omegar_t+k*alpha_0);
Mrck=Mrck_1';Mrsk=Mrsk_1';Mack=Mack_1';Mask=Mask_1';
end
%radial magnetization
if Kmag==0
Kma=mysinc_C1(k,ap,theta_p,nk,p,Kmag); % magnet width dependent
Mak=0.*k; Mrk=2*(Brm/u0)*ap*Kma;
Mrck_1= Mrk.*cos(k*omegar_t+k*alpha_0);
Mrsk_1=Mrk.*sin(k*omegar_t+k*alpha_0);
Mack_1= -Mak.*sin(k*omegar_t+k*alpha_0);
Mask_1=Mak.*cos(k*omegar_t+k*alpha_0);
Mrck=Mrck_1';Mrsk=Mrsk_1';Mack=Mack_1';Mask=Mask_1';
end
alpha=linspace(0,2*pi/p,360);npa=length(alpha);
[xalpha,xnp] = meshgrid(alpha,k);z1=xnp.*xalpha;
xMrck=repmat(Mrck_1,[npa 1])';
xMrsk=repmat(Mrsk_1,[npa 1])';
xMack=repmat(Mack_1,[npa 1])';
xMask=repmat(Mask_1,[npa 1])';
```

```
Mr=sum(xMrck.*cos(z1)+xMrsk.*sin(z1),1);
Mt=sum(xMack.*cos(z1)+xMask.*sin(z1),1);
%%%%%%%%%%%%%%%%%%%%%%%%%%%%%%%%%%%%%%%%%%%%%%%%%%%%%%%%%%%%%%%%%%%%%%
```

```
%%%% SCRIPT-3

%%%%%%% mysinc Function to evaluate A1k A2k Kma in Script-3%%%

function y = mysinc_C1(x,ap,theta_p,nk,p,Kmag)
y=zeros(1,nk);x;
if Kmag==0
x1=(2*(0:nk-1)+1)*p;
a1=ismember(x,x1);
for i=((0:nk-1)+1)
    if a1(i)==1
      x(i); x1(i);
      y(i)=sin(x(i)*ap*theta_p/2)./(x(i)*ap*theta_p/2)   ;
    else
      x(i); y(i)=0;
    end
end;
end;
if Kmag==1
   if x(1)==2;
      x2=(2*(0:nk-1)+1)*p+1;
      a1=ismember(x,x2);
      for i=((0:nk-1)+1)
         if a1(i)==1
            x(i); x2(i);
            y(i)=sin(x(i)*ap*theta_p/2)./(x(i)*ap*theta_p/2) ;
         else
            x(i);y(i)=0;
         end
      end;
else if x(1)==0;
          x3=(2*(0:nk-1)+1)*p-1;
          a1=ismember(x,x3);
          for i=((0:nk-1)+1);
             if a1(i)==1
                x(i);x3(i);
                y(i)=sin(x(i)*ap*theta_p/2)./(x(i)*ap*theta_p/2) ;
             else
                x(i);y(i)=0;
             end
          end;
        end
   end
end
%%%%%%%%%%%%%%%%%%%%%%%%%%%%%%%%%%%%%%%%%%%%%%%%%%%%%%%%%%%%%%%%%%%%%%
```

```
%%%% SCRIPT-4

%%%%%%% Current_OC function to evaluate gamma, zeta, J0, Y9, Y8, Jn
in Script-1%%%

function[gamma,zeta,J0,Y9,Y8,Jn] = ...
Current_OC(Rt,Rsb,bsa,boa,nm,nn,Ns,J,d)
a1=(2*pi/Ns)/2;

%%%%%% Jn(i) and J0(i)Calculation
Jn = zeros(Ns,nn);i=1;
for j=1:Ns
   for n1=1:nn
    Jn(j,n1)=2/(n1*pi)*(J(i)+J(i+1)*cos(n1*pi))*sin(n1*pi*d/bsa);
   end;
    i=i+2;
end;
Jn=Jn';
J0_1 = zeros(1,Ns);i=1;
for j=1:Ns
    J0_1(j)=(J(i)+J(i+1))/2; i=i+2;
end;
J0=J0_1';

%%%%%%%%%%%%% Y9 Calculation
for i=1:Ns
Y9_1(:,i)=2*u0*(Rt^2*IN-Rsb^2*G3)/(En^2-4*IN)*Jn(:,i)...
    -u0/2*(bsa/boa)*(Rsb^2-Rt^2)*gamma0'*J0_1(:,i);
end;
for j=1:Ns;T{j} =Y9_1(:,j)';end;
Y9 = horzcat(T{:})';

%%%%%%% Gamma and Zeta Calculation
i=1;j=1; gamma=zeros(nm,nn); % gamma is mxn Matrix
for m1=((0:nm-1)+1);
    for n2=((0:nn-1)+1);
      En_2=n2*pi/bsa;Fm_2=m1*pi/boa;
      gamma(i,j)= -(2/bsa)*En_2/(Fm_2^2-
      En_2^2)*(cos(m1*pi)*sin(En_2*(bsa+boa)/2) ...
      -sin(En_2*(bsa-boa)/2));
      j=j+1;
    end;
    j=1;i=i+1;
end;
zeta= (bsa/boa)*gamma;

%%%%%%%%%% Y6 Calculation
Y8_1=zeros(nm,nn,Ns);Y8_2=zeros(nm,Ns);
for i=1:Ns
Y8_1(:,:,i)=u0*zeta*(Rt^2*En-2*Rsb^2*G3)...
/((En^2-4*IN)*En); %
Y8_2(:,i)=Y8_1(:,:,i)*Jn(:,i);
end;
for j=1:Ns;U{j} =Y8_2(:,j)';end;
Y8 = horzcat(U{:})';
%%%%%%%%%%%%%%%%%%%%%%%%%%%%%%%%%%%%%%%%%%%%%%%%%%%%%%%%%%%%%%%%%%%%%%%%%%%%
```

```
%%%% SCRIPT-5

%%%%%%% etaxi Function to evaluate eta, xi, Ftm, G4t, eta0, xi0
in Script-1%%%

function[eta,xi,Ftm,G4t,eta0,xi0] = ...
etaxi_MagAR_C1(boa,nm,nk,alpha_i,Ns,Rs,Rt,p)

a=alpha_i*180/pi;
%%%%%%%%%%%%%% eta,xi Calculation
i=1;j=1;k=1; eta_1=zeros(nm,nk,Ns);
xi_1=zeros(nm,nk,Ns);% eta and xi are mxk Matrix
for a1=((0:360/Ns:359)+a)*pi/180;
 for m1=((0:nm-1)+1);
    for k1=((0:nk-1)+1);
      Fm=m1*pi/boa;
      eta_1(i,j,k)= -1/pi*(k1/(Fm^2-k1^2))...
      *(cos(m1*pi)*sin(k1*a1+k1*boa/2)-sin(k1*a1-k1*boa/2));
      xi_1(i,j,k) =  1/pi*(k1/(Fm^2-k1^2)) ...
      *(cos(m1*pi)*cos(k1*a1+k1*boa/2)-cos(k1*a1-k1*boa/2));
      j=j+1;
     end;
    j=1;i=i+1;
 end;
k=k+1;i=1;j=1;
end;
T = cell(1,Ns);Z=cell(1,Ns);
for j=1:Ns;
T{j} =eta_1(:,:,j)';
Z{j} =xi_1(:,:,j)';
end
eta = horzcat(T{:})';
xi =  horzcat(Z{:})';

%%%%%%%%% Ftm ,G3t Calculation
m=((0:nm-1)+1);
Fm_1=m*pi/boa;Fm_2=diag(Fm_1);
T1 = cell(1,Ns);for j=1:Ns; T1{j} =Fm_2; end ; Ftm = blkdiag(T1{:});
G4_1= (Rs/Rt)^Fm_2;
T2= cell(1,Ns);for j=1:Ns; T2{j} =G4_1; end ; G4t = blkdiag(T2{:});

%%%%%%%%%%%%%% eta0 ,xi0 Calculation
i=1;j=1;k=1; eta0_1=zeros(nk,Ns);
xi0_1=zeros(nk,Ns);% eta and xi are mxk Matrix
for a1=((0:360/Ns:359)+a)*pi/180;
    for k1=((0:nk-1)+1);
      eta0_1(j,k)= 2/(k1*pi)*sin(k1*boa/2)*cos(k1*a1);
      xi0_1(j,k) = 2/(k1*pi)*sin(k1*boa/2)*sin(k1*a1);
      j=j+1;
     end;
    j=1;
k=k+1;
end;
eta0=eta0_1;
xi0=xi0_1;
end
%%%%%%%%%%%%%%%%%%%%%%%%%%%%%%%%%%%%%%%%%%%%%%%%%%%%%%%%%%%%%%%%%%%%%%%%%%%%%%%
```

```
%%%% SCRIPT-6

%%%%%%% Evaluation of Harmonics in the Magnets for implementation in
Appendix E %%%

Brv1h=zeros(hn,na);Brv2h=zeros(hn,na);
pafh=zeros(hn,na); pabh=zeros(hn,na);

na=50;
for h =((0:hn-1)+1
fft_a1h=fft(A1(h,:))*2/length(A1(h,:));
fft_c1h=fft(C1(h,:))*2/length(C1(h,:));
a1h_1=(fft_a1h(2:end/2)); c1h_1=(fft_c1h(2:end/2));
a1h=abs(a1h_1);c1h=abs(c1h_1);
pa1h=angle(a1h_1);pc1h=angle(c1h_1);

%%%%%%%%%%%%%% to find the forward and backward field %%%%%%%%%%#
hl=na;
a1h=a1h(1:hl);pa1h=pa1h(1:hl);c1h=c1h(1:hl);pc1h=pc1h(1:hl);
%%%% For radial field
afh_r(hn1,:)=abs(-a1h.*exp(-j*pa1h)+c1h.*exp(-j*(pc1h-pi/2)))/2;
abh_r(hn1,:)=abs(-a1h.*exp( j*pa1h)-c1h.*exp( j*(pc1h-pi/2)))/2;
pafh1_r(hn1,:)=angle(-a1h.*exp(-j*pa1h)+c1h.*exp(-j*(pc1h-pi/2)));
pabh1_r(hn1,:)=angle(-a1h.*exp( j*pa1h)-c1h.*exp( j*(pc1h-pi/2)));

for j1=((0:na-1)+1)
     Brv1h(hn1,j1)= (h+j1*p)*w*abh_r(hn1,j1);%*C2k(h);
     Brv2h(hn1,j1)= (h-j1*p)*w*afh_r(hn1,j1);%*C2k(h)
     pafh(hn1,j1)=pafh1_r(hn1,j1);
     pabh(hn1,j1)=pabh1_r(hn1,j1);
end;
hn1=hn1+1;
end;

%%%%%%%%%%%%%%%%%%%%%%%%%%%%%%%%%%%%%%%%%%%%%%%%%%%%%%%%%%%%%%%%%%%%%%%%%%%%%%%
```

```
%%%% SCRIPT-7

%%%%%%% Evaluation of Harmonics in the Magnets and Retaining Sleeve
(Air Gap ur =1) for implementation in Appendix F %%%

hn=100;
na=50;
afh_r=zeros(hn,na);abh_r=zeros(hn,na);
pafh1_r=zeros(hn,na);pabh1_r=zeros(hn,na);
afh_t=zeros(hn,na);abh_t=zeros(hn,na);
pafh1_t=zeros(hn,na);pabh1_t=zeros(hn,na);
hn1=1; hl=na;

for h =((0:hn-1)+1);

%%%%%%%%%%%%% Evolution of harmonic components in the Magnets %%%%%%%%
fft_a1h=fft(A1(h,:))*2/length(A1(h,:));
fft_c1h=fft(C1(h,:))*2/length(C1(h,:));
a1h_1=(fft_a1h(2:end/2)); c1h_1=(fft_c1h(2:end/2));
a1h=abs(a1h_1);c1h=abs(c1h_1);pa1h=angle(a1h_1);pc1h=angle(c1h_1);

a1h=a1h(1:hl);pa1h=pa1h(1:hl);c1h=c1h(1:hl);pc1h=pc1h(1:hl);
%%%% For radial field
afh_r(hn1,:)=abs(-a1h.*exp(-j*pa1h)+c1h.*exp(-j*(pc1h-pi/2)))/2;
abh_r(hn1,:)=abs(-a1h.*exp( j*pa1h)-c1h.*exp( j*(pc1h-pi/2)))/2;
pafh1_r(hn1,:)=angle(-a1h.*exp(-j*pa1h)+c1h.*exp(-j*(pc1h-pi/2)));
pabh1_r(hn1,:)=angle(-a1h.*exp( j*pa1h)-c1h.*exp( j*(pc1h-pi/2)));
%%%%  For tangential field
afh_t(hn1,:)=abs( a1h.*exp(-j*(pa1h-pi/2))+c1h.*exp(-j*pc1h))/2;
abh_t(hn1,:)=abs(-a1h.*exp(j*(pa1h-pi/2))+c1h.*exp( j*pc1h))/2;
pafh1_t(hn1,:)=angle( a1h.*exp(-j*(pa1h-pi/2))+c1h.*exp(-j*pc1h));
pabh1_t(hn1,:)=angle(-a1h.*exp(j*(pa1h-pi/2))+c1h.*exp( j*pc1h));

%%%%%%%%%%%%% Evolution of harmonic components in the Sleeve %%%%%%%%

fft_a2h=fft(A2(h,:))*2/length(A2(h,:));
fft_c2h=fft(C2(h,:))*2/length(C2(h,:));
a2h_1=(fft_a2h(2:end/2));c2h_1=(fft_c2h(2:end/2));
a2h=abs(a2h_1);c2h=abs(c2h_1);pa2h=angle(a2h_1);pc2h=angle(c2h_1);

fft_b2h=fft(B2(h,:))*2/length(B2(h,:));
fft_d2h=fft(D2(h,:))*2/length(D2(h,:));
b2h_1=(fft_b2h(2:end/2)); d2h_1=(fft_d2h(2:end/2));
b2h=abs(b2h_1);d2h=abs(d2h_1);pb2h=angle(b2h_1);pd2h=angle(d2h_1);
a2h=a2h(1:hl);pa2h=pa2h(1:hl);c2h=c2h(1:hl);pc2h=pc2h(1:hl);
b2h=b2h(1:hl);pb2h=pb2h(1:hl);d2h=d2h(1:hl);pd2h=pd2h(1:hl);

%%%% For radial field
a1fh_r(hn1,:)=abs(a2h.*exp(-j*pa2h)+c2h.*exp(-j*(pc2h+pi/2)))/2;
a1bh_r(hn1,:)=abs(a2h.*exp( j*pa2h)+c2h.*exp( j*(pc2h-pi/2)))/2;
pa1fh_r(hn1,:)=angle(a2h.*exp(-j*pa2h)+c2h.*exp(-j*(pc2h+pi/2)));
pa1bh_r(hn1,:)=angle(a2h.*exp( j*pa2h)+c2h.*exp( j*(pc2h-pi/2)));
%%%%  For tangential field
a1fh_t(hn1,:)=a1fh_r(hn1,:);a1bh_t(hn1,:)=a1bh_r(hn1,:);
pa1fh_t(hn1,:)=pa1fh_r(hn1,:);pa1bh_t(hn1,:)=pa1bh_r(hn1,:);
%%%% For radial field
a2fh_r(hn1,:)=abs(b2h.*exp(-j*pb2h)+d2h.*exp(-j*(pd2h+pi/2)))/2;
a2bh_r(hn1,:)=abs(b2h.*exp( j*pb2h)+d2h.*exp( j*(pd2h-pi/2)))/2;
pa2fh_r(hn1,:)=angle(b2h.*exp(-j*pb2h)+d2h.*exp(-j*(pd2h+pi/2)));
pa2bh_r(hn1,:)=angle(b2h.*exp( j*pb2h)+d2h.*exp( j*(pd2h-pi/2)));
```

```
%%%%  For tangential field
a2fh_t(hn1,:)=a2fh_r(hn1,:);
a2bh_t(hn1,:)=a2bh_r(hn1,:);
pa2fh_t(hn1,:)=pa2fh_r(hn1,:);
pa2bh_t(hn1,:)=pa2bh_r(hn1,:);

hn1=hn1+1;
end;
%%%%%%%%%%%%%%%%%%%%%%%%%%%%%%%%%%%%%%%%%%%%%%%%%%%%%%%%%%%%%%%%%%%%%%%%%%%%%%%
```

APPENDIX E
3D Magnet Loss Prediction in SPM Machines Accounting Slotting Effect (based on Chapter-2)

```
%%%% SCRIPT-8

%%%%% This script to be run after the evaluation of harmonics in
Magnets based on SCRIPT-1 and SCRIPT-6 %%%%%%%%%%%%%%%%%%%%%%%%%%%%%%%%

 INPUTS:
% name                  [unit]          [description]
p      =      4;%           []      Number of pole pairs
Ns     =      18;%          []      Total number of slots
Qp     =      Ns/p;%        []      Number of stator slots per pole
lM1    =      118*1e-3;%    [m]     Axial length (magnet length)
hm     =      5e-3;%        [m]     Magnet Thickness
ur     =      1.05;%        []      Magnet relative permeability
Brm    =      1.1;%         [T]     Magnet remanent flux density
Rso    =      75.599e-3;%   [m]     Stator Outer Radius
Rs     =      38.455e-3;%   [m]     Stator Inner Radius
Rm     =      (Rs-gap);%    [m]     Rotor Outer Radius
Ap     =      0.6533;%      []      Magnet pole arc to pole pitch ratio
kM     =      1/(1.8E-6);%[S/m]   Electrical Conductivity of SmCo magnets

% Calculated Parameters
Rr       =    Rm-hm;%       [m]    Magnet inner radius
theta_p  =    pi/p;%        [R]    Magnet pole pitch
rmean    =    (Rr+Rm)/2;%   [m]    mean magnet radius
r        =    rmean;%
bM1      =    theta_p*Ap;%  [m]    wagnet width

% Constants and other Variables
u0=4*pi*1e-7;          % air magnetic permeability
j=sqrt(-1);            %imaginary part
ncf= 1;                %circumferential segmentation
ml=input (' Number of Axial Segmentation) =');
lM=lM1/nax;            % Segmented Axial length of magnet
bM=bM1/ncf;            % Segmented Circumferential length of magnet.
nl=na;                 %  Number of Magnet space harmonics- Magnet (l)
k1=h;                  % space harmonic ranks (By); v=1,2,3..
n1=k1/r;
nld=24;                % Number of flux density harmonics in z direction
ld=(2*(0:nld-1)+1);  % space harmonic ran
thetap=theta_p*Ap;
Mag_As=alpha_0-thetap/2; Mag_Af=alpha_0+thetap/2;
nt=30;
P_Meddy=zeros(1,nt);te=1;
nra=20;
rm1=linspace(Rr,Rm,nra);
rm=rm1(2:nra);nr=length(rm);
%%%%%%%%%%%%%%%%%%%%%%%%%%%%%%%%%%%%%%%%%%%%%%%%%%%%%%%%%%%%%%%%%%%%%%%%
```

```
for aa= ((0:nt-1)*4+1)
Iz1=zeros(nr,hn);Iz2=zeros(nr,hn);Iz3=zeros(nr,hn);Iz4=zeros(nr,hn);
Iz5=zeros(nr,hn);Iz6=zeros(nr,hn);Iz7=zeros(nr,hn);Iz11=zeros(nr,hn);
Iz21=zeros(nr,hn);Iz31=zeros(nr,hn);Iz41=zeros(nr,hn);
Iz51=zeros(nr,hn);Iz61=zeros(nr,hn);Iz71=zeros(nr,hn);
Ix1=zeros(nr,hn);Ix2=zeros(nr,hn);Ix3=zeros(nr,hn);
Ix4=zeros(nr,hn);Ix5=zeros(nr,hn);Ix6=zeros(nr,hn);Ix7=zeros(nr,hn);
Ix11=zeros(nr,hn);Ix21=zeros(nr,hn);Ix31=zeros(nr,hn);
Ix41=zeros(nr,hn);Ix51=zeros(nr,hn);Ix61=zeros(nr,hn);
Ix71=zeros(nr,hn);
hn1=1;rn1=1;
a11=(0+Mag_As+omegar_t(aa));a12=(bM1+Mag_As+omegar_t(aa));
a11c=a11/ncf;a12c=a12/ncf;
for i1=((0:nr-1)+1)
r=rm(i1);
for h=((0:hn-1)+1)
C1h=((r/Rm)^h+G1_1(h)*(r/Rr)^-h); C2h=h/r*C1h;
n1=h/r;
rmu=(rm1(i1)+rm1(i1+1))/2;
for  l=((0:nl-1)+1)
for ld1=((0:nld-1)+1)
K1b=kM*Brv1h(h,l)*4/(pi*ld(ld1))*sin(0.5*pi*ld(ld1))*C2h;
K2f=kM*Brv2h(h,l)*4/(pi*ld(ld1))*sin(0.5*pi*ld(ld1))*C2h;
m=ld(ld1)*pi/lM; n2m2=(n1^2+m^2);sinhmrbm=sinh(m*r*bM);
K1=K1b/(n2m2*sinhmrbm);K2=K2f/(n2m2*sinhmrbm);
A=(K1*m*cos(h*a11c+(h+l*p)*omegar_t(aa)+pabh(h,l))+ ...
K2*m*cos(h*a11c+(h-l*p)*omegar_t(aa)+pafh(h,l)));
B=-K1*m*cos(h*a12c+(h+l*p)*omegar_t(aa)+pabh(h,l))+ ...
K2*m*cos(h*a12c+(h-l*p)*omegar_t(aa)+pafh(h,l)));
C=-h/r*sinhmrbm; D=m*sinh(m*r*bM);
for ap= a12c  ; z= lM/2;
Iz1(rn1,h)=Iz1(rn1,h)+(A^2*ap)/2-(A^2*sinh(2*m*r*(a12c-ap)))/(4*m*r);
Iz2(rn1,h)=Iz2(rn1,h)+(B^2*ap)/2-(B^2*sinh(2*m*r*(a11c-ap)))/(4*m*r);
Iz3(rn1,h)=Iz3(rn1,h)+(C^2*(2*ap*K1^2+4*ap*cos(pabh(h,l)-pafh(h,l)+...
  2*l*omegar_t(aa)*p)*K1*K2+2*ap*K2^2))/4-(C^2*(sin(2*pabh(h,l)+ ...
  2*ap*h+2*h*omegar_t(aa)+ 2*l*omegar_t(aa)*p)*K1^2+2*sin(pabh(h,l)+
  pafh(h,l)+2*ap*h+2*h*omegar_t(aa))*K1*K2+ sin(2*pafh(h,l)+...
  2*ap*h+2*h*omegar_t(aa)-2*l*omegar_t(aa)*p)*K2^2))/(4*h);
Iz5(rn1,h)=Iz5(rn1,h)-...
 (2*A*C*K1*(h*cosh(-m*r*(a12c-ap))*cos(pabh(h,l)+ 4*ap*h+...
  omegar_t(aa)*(h+l*p))- m*r*sinh(-m*r*(a12c- ap))*sin(pabh(h,l)+...
  omegar_t(aa)*(h + l*p))))/(h^2 + m^2*r^2)-...
 (2*A*C*K2*(h*cosh(-m*r*(a12c - ap))*cos(pafh(h,l+...
  omegar_t(aa)*(h-l*p))-m*r*sinh(-m*r*(a12c - ap))*sin(pafh(h,l)+...
  omegar_t(aa)*(h - l*p))))/(h^2 + m^2*r^2);
Iz6(rn1,h)=Iz61(rn1,h)-...
  (2*B*C*K1*(h*cosh(-m*r*(a11c-ap))*cos(pabh(h,l)+ 4*ap*h+...
  omegar_t(aa)*(h+l*p))-m*r*sinh(-m*r*(a11c-ap))*sin(pabh(h,l)+...
  omegar_t(aa)*(h+l*p))))/(h^2+ m^2*r^2)-...
  (2*B*C*K2*h*cosh(-m*r*(a11c-ap))*cos(pafh(h,l)+...
  omegar_t(aa)*(h-l*p))-m*r*sinh(-m*r*(a11c-ap))*sin(pafh(h,l))+...
  omegar_t(aa)*(h - l*p))))/(h^2 + m^2*r^2);
Ix1(rn1,h)=Ix1(rn1,h)-...
  (A^2*ap)/2-(A^2*sinh(2*m*r*(a12c-ap)))/(4*m*r);
Ix2(rn1,h)=Ix2(rn1,h)-...
  (B^2*ap)/2-(B^2*sinh(2*m*r*(a11c-ap)))/(4*m*r);
Ix3(rn1,h)=Ix3(rn1,h)+...
 (D^2*(2*ap*K1^2+4*ap*cos(pabh(h,l)-pafh(h,l)+...
  2*l*omegar_t(aa)*p)*K1*K2 + 2*ap*K2^2))/4+...
 (D^2*(sin(2*pabh(h,l)+2*ap*h+2*h*omegar_t(aa)+...
```

```
  2*l*omegar_t(aa)*p)*K1^2+ 2*sin(pabh(h,l)+ pafh(h,l)+...
  2*ap*h + 2*h*omegar_t(aa))*K1*K2 + sin(2*pafh(h,l)+...
  2*ap*h + 2*h*omegar_t(aa) - 2*l*omegar_t(aa)*p)*K2^2))/(4*h);
Ix4(rn1,h)=Ix4(rn1,h)-...
 (A*B*(ap*m*cosh(m*r*(a11c-ap))*cosh(m*r*(a12c - ap))-...
  ap*m*sinh(m*r*(a11c-ap))*sinh(m*r*(a12c-ap))))/m- ...
 (A*B*cosh(m*r*(a12c-ap))*sinh(m*r*(a11c-ap)))/(m*r);
Ix5(rn1,h)=Ix5(rn1,h) +...
 (A*K2*(h*sinh(-m*r*(a12c-ap))*sin(pafh(h,l)+...
  4*ap*h + omegar_t(aa)*(h-l*p))+...
  m*r*cosh(-m*r*(a12c-ap))*cos(pafh(h,l)+...
  omegar_t(aa)*(h-l*p))))/(h^2 + m^2*r^2) +...
 (2*A*D*K1*(h*sinh(-m*r*(a12c - ap))*sin(pabh(h,l) +...
  omegar_t(aa)*(h+l*p))+ m*r*cosh(-m*r*(a12c-ap))*cos(pabh(h,l)+...
  omegar_t(aa)*(h + l*p))))/(h^2 + m^2*r^2);
Ix6(rn1,h)=Ix6(rn1,h) +...
 (B*K2*(h*sinh(-m*r*(a11c-ap))*sin(pafh(h,l)+4*ap*h+...
  omegar_t(aa)*(h-l*p))= m*r*cosh(-m*r*(a11c- ap))*cos(pafh(h,l)+...
   omegar_t(aa)*(h-l*p))))/(h^2+m^2*r^2)+ ...
  (2*B*D*K1*(h*sinh(-m*r*(a11c-ap))*sin(pabh(h,l)+ ...
  omegar_t(aa)*(h+l*p))+ m*r*cosh(-m*r*(a11c-ap))*cos(pabh(h,l)+ ...
  omegar_t(aa)*(h+l*p))))/(h^2+m^2*r^2);
Iz7(rn1,h)=(2*m*z+sin(2*m*z))/(4*m)*rmu;
Ix7(rn1,h)=(z/2 - sin(2*m*z)/(4*m))*rmu;
end;
for ap= a11c; z= -lM/2;
Iz11(rn1,h)=Iz11(rn1,h) +...
 (A^2*ap)/2-(A^2*sinh(2*m*r*(a12c-ap)))/(4*m*r);
Iz21(rn1,h)=Iz21(rn1,h) +...
 (B^2*ap)/2-(B^2*sinh(2*m*r*(a11c-ap)))/(4*m*r);
Iz31(rn1,h)=Iz31(rn1,h) +...
 (C^2*(2*ap*K1^2+4*ap*cos(pabh(h,l)-pafh(h,l)+...
  2*l*omegar_t(aa)*p)*K1*K2+2*ap*K2^2))/4-(C^2*(sin(2*pabh(h,l)+ ...
  2*ap*h+2*h*omegar_t(aa)+ 2*l*omegar_t(aa)*p)*K1^2+2*sin(pabh(h,l)+
  pafh(h,l)+2*ap*h+2*h*omegar_t(aa))*K1*K2+ sin(2*pafh(h,l)+...
  2*ap*h+2*h*omegar_t(aa)-2*l*omegar_t(aa)*p)*K2^2))/(4*h);
Iz51(rn1,h)=Iz51(rn1,h)-...
 (2*A*C*K1*(h*cosh(-m*r*(a12c-ap))*cos(pabh(h,l)+ 4*ap*h+...
  omegar_t(aa)*(h+l*p))- m*r*sinh(-m*r*(a12c- ap))*sin(pabh(h,l)+...
  omegar_t(aa)*(h + l*p))))/(h^2 + m^2*r^2)-...
 (2*A*C*K2*(h*cosh(-m*r*(a12c - ap))*cos(pafh(h,l+...
  omegar_t(aa)*(h-l*p))-m*r*sinh(-m*r*(a12c - ap))*sin(pafh(h,l)+...
  omegar_t(aa)*(h - l*p))))/(h^2 + m^2*r^2);
Iz61(rn1,h)=Iz61(rn1,h)-...
  (2*B*C*K1*(h*cosh(-m*r*(a11c-ap))*cos(pabh(h,l)+ 4*ap*h+...
  omegar_t(aa)*(h+l*p))-m*r*sinh(-m*r*(a11c-ap))*sin(pabh(h,l)+...
  omegar_t(aa)*(h+l*p))))/(h^2+ m^2*r^2)-...
  (2*B*C*K2*h*cosh(-m*r*(a11c-ap))*cos(pafh(h,l)+...
  omegar_t(aa)*(h-l*p))-m*r*sinh(-m*r*(a11c-ap))*sin(pafh(h,l))+...
  omegar_t(aa)*(h - l*p))))/(h^2 + m^2*r^2);
Ix11(rn1,h)=Ix11(rn1,h)-...
  (A^2*ap)/2-(A^2*sinh(2*m*r*(a12c-ap)))/(4*m*r);
Ix21(rn1,h)=Ix21(rn1,h)-...
  (B^2*ap)/2-(B^2*sinh(2*m*r*(a11c-ap)))/(4*m*r);
Ix31(rn1,h)=Ix31(rn1,h)+...
 (D^2*(2*ap*K1^2+4*ap*cos(pabh(h,l)-pafh(h,l)+...
  2*l*omegar_t(aa)*p)*K1*K2 + 2*ap*K2^2))/4+...
 (D^2*(sin(2*pabh(h,l)+2*ap*h+2*h*omegar_t(aa)+...
  2*l*omegar_t(aa)*p)*K1^2+ 2*sin(pabh(h,l)+ pafh(h,l)+...
  2*ap*h + 2*h*omegar_t(aa))*K1*K2 + sin(2*pafh(h,l)+...
  2*ap*h + 2*h*omegar_t(aa) - 2*l*omegar_t(aa)*p)*K2^2))/(4*h);
```

```
Ix41(rn1,h)=Ix41(rn1,h)-...
 (A*B*(ap*m*cosh(m*r*(a11c-ap))*cosh(m*r*(a12c - ap))-...
  ap*m*sinh(m*r*(a11c-ap))*sinh(m*r*(a12c-ap))))/m- ...
 (A*B*cosh(m*r*(a12c-ap))*sinh(m*r*(a11c-ap)))/(m*r);
Ix51(rn1,h)=Ix51(rn1,h) +...
 (A*K2*(h*sinh(-m*r*(a12c-ap))*sin(pafh(h,l)+...
  4*ap*h + omegar_t(aa)*(h-l*p))+...
  m*r*cosh(-m*r*(a12c-ap))*cos(pafh(h,l)+...
  omegar_t(aa)*(h-l*p))))/(h^2 + m^2*r^2) +...
 (2*A*D*K1*(h*sinh(-m*r*(a12c - ap))*sin(pabh(h,l) +...
  omegar_t(aa)*(h+l*p))+ m*r*cosh(-m*r*(a12c-ap))*cos(pabh(h,l)+...
  omegar_t(aa)*(h + l*p))))/(h^2 + m^2*r^2);
Ix61(rn1,h)=Ix61(rn1,h) +...
 (B*K2*(h*sinh(-m*r*(a11c-ap))*sin(pafh(h,l)+4*ap*h+...
  omegar_t(aa)*(h-l*p))= m*r*cosh(-m*r*(a11c- ap))*cos(pafh(h,l)+...
   omegar_t(aa)*(h-l*p))))/(h^2+m^2*r^2)+ ...
  (2*B*D*K1*(h*sinh(-m*r*(a11c-ap))*sin(pabh(h,l)+ ...
  omegar_t(aa)*(h+l*p))+ m*r*cosh(-m*r*(a11c-ap))*cos(pabh(h,l)+ ...
  omegar_t(aa)*(h+l*p))))/(h^2+m^2*r^2);
Iz71(rn1,h)=(2*m*z+sin(2*m*z))/(4*m)*rmu;
Ix71(rn1,h)=(z/2-sin(2*m*z)/(4*m))*rmu;
end;
end;
end;
hn1=hn1+1;
end;
hn1=1;
rn1=rn1+1;
end;
TL=hm/(2*kM)*nax*ncf;
Pzuap=zeros(nr,hn);Pzuz=zeros(nr,hn);Pzlap=zeros(nr,hn);
Pzlz=zeros(nr,hn);pzt=zeros(nr,hn);Pzt=zeros(1,nr);
Pxuap=zeros(nr,hn);Pxuz=zeros(nr,hn);Pxlap=zeros(nr,hn);
Pxlz=zeros(nr,hn);pxt=zeros(nr,hn);Pxt=zeros(1,nr);
Pzuap=Iz1+Iz2+Iz3+Iz4+Iz5+Iz6; Pzuz=Iz7;
Pzlap=Iz11+Iz21+Iz31+Iz41+Iz51+Iz61;Pzlz=Iz71;
pzt=(Pzuap-Pzlap).*(Pzuz-Pzlz);
Pzt=sum(pzt,2)*TL*2*p;
Pxuap=Ix1+Ix2+Ix3+Ix4+Ix5+Ix6;Pxuz=Ix7;
Pxlap=Ix11+Ix21+Ix31+Ix41+Ix51+Ix61;Pxlz=Ix71;
pxt=(Pxuap-Pxlap).*(Pxuz-Pxlz);
Pxt=sum(pxt,2)*TL*2*p;
P_magnet1=Pzt+Pxt;
P_Meddy(te)=sum((Pzt+Pxt))/(nr);
te=te+1;
end;
%%%%%%%%%%%%%%%%%%%%%%%%%%%%%%%%%%%%%%%%%%%%%%%%%%%%%%%%%%%%%%%%%%%%%%%%

aa= ((0:nt-1)*4+1);thetar=omega(aa);
figure; plot(thetar,P_Meddy);
```

APPENDIX F
3D Magnet Eddy Current Loss Prediction in Based on 3D Fourier Method

```
%%%% SCRIPT-9

%%%%% This script to be run after the evaluation of harmonics in
Magnets based on SCRIPT-1 and SCRIPT-7 %%%%%%%%%%%%%%%%%%%%%%%%%%%%%%%%

INPUTS:

% name                          [unit]         [description]
uo      = 1.0*4*pi*1.0e-07;%    [H/m]       Permeability of free space
res     = 180e-08;%             [ohm-m]     Resistivity of magnets
seg_a   = input (' Number of Axial Segmentation) =');
seg_c   = input (' Number of Circumferential Segmentation) =');
npr     = 4; %                   []         Number of pole-pairs
Rm      = 32.5e-3; %             [m]        Magnet outer radius
Rr      = 29.5e-3; %             [m]        Rotor back-iron radius
Rs      = 33.45e-3;%             [m]        Stator bore radius
slm     = 118.0e-3;%             [m]        Machine axial length
% Calculated Parameters
tao=1/res; %                    [S/m]     Conductivity of magnets
ratio = 175/180; %                []      Magnet pole arc/ pole pitch
Ravg=(Rm+Rr)*0.5;
Lx=ratio*(Rm+Rr)*0.5*pi*0.25/seg_c;
Ly=Rm-Rr;
Lz=slm/seg_a;
seg_a_x=1:12;
ploss_seg_a_x=seg_a_x;
%%%%%%%%%%%%%%%%%%%%%%%%%%%%%%%%%%%%%%%%%%%%%%%%%%%%%%%%%%%%%%%%%%%%%%%%%%%

for seg_a=seg_a_x
Lx=ratio*(Rm+Rr)*0.5*pi*0.25/seg_c;
Ly=Rm-Rr;
Lz=slm/seg_a;

NxFFT=2^4;NyFFT=2^4;NzFFT=2^5;
Nx=2*NxFFT;Ny=2*NyFFT;Nz=2*NzFFT;Nfft=Nx*Ny*Nz;
dxh=Lx/NxFFT*0.5;dyh=Ly/NyFFT*0.5;dzh=Lz/NzFFT*0.5;

x_x=Lx/NxFFT*0.5:Lx/NxFFT:Lx-Lx/NxFFT*0.5;
y_x=Ly/NyFFT*0.5:Ly/NyFFT:Ly-Ly/NyFFT*0.5;
z_x=Lz/NzFFT*0.5:Lz/NzFFT:Lz-Lz/NzFFT*0.5;

x2_x=Lx/NxFFT*0.5:Lx/NxFFT:2*Lx-Lx/NxFFT*0.5;
y2_x=Ly/NyFFT*0.5:Ly/NyFFT:2*Ly-Ly/NyFFT*0.5;
z2_x=Lz/NzFFT*0.5:Lz/NzFFT:2*Lz-Lz/NzFFT*0.5;

% generating inverse diagonal matrix for mirror operation
Iy_m=diag(ones(1,NyFFT));
Ix_m=diag(ones(1,NxFFT));
Iyr_m=ones(NyFFT,NyFFT);
Ixr_m=ones(NxFFT,NxFFT);
```

```
for n=1:NyFFT
    Iyr_m(:,n)=Iy_m(:,NyFFT-n+1);
end
for n=1:NxFFT
    Ixr_m(:,n)=Ix_m(:,NxFFT-n+1);
end
%%%% Generate order number matrix%%%%%
pix=pi/Lx; piy=pi/Ly;piz=pi/Lz;
TL=tao*Lx*Ly*Lz/2;
m_v=repmat((horzcat(0:Nx/2,-(Nx/2-1):-1))',[1 Ny Nz/2]);
n_v=repmat((horzcat(0:Ny/2,-(Ny/2-1):-1)),[Nx 1 Nz/2]);
k_v=ones(1,1,Nz/2);
k_v(1,1,:)=(0:Nz/2-1);
k_v=repmat(k_v,[Nx,Ny,1]);
mnks_v=1./((m_v.^2*pix^2+n_v.^2*piy^2+k_v.^2*piz^2).^2)*TL;
mnks_v(1,1,1)=0;
%%%%%%%%%%%%%%%%%%%%%%%%%%%%%%%%%%%%%%%%

%%%% Generating the time sequence%%%%%
time=omegar_t/w;
duration=2*pi/w/npr/6;
Nt=15;
t_x=duration/Nt:duration/Nt:duration;
t_the_x=t_x*w*180/pi;
%%%%%%%%%%%%%%%%%%%%%%%%%%%%%%%%%%%%%%%%

%% Generating field source matrix%%%%
thetap=theta_p*ap;
Mag_As=alpha_0-thetap/2; Mag_Af=alpha_0+thetap/2;
nr=NyFFT;% number of points in 'r' direction
nts=NxFFT;% number of points in 't' direction

ploss_total_pole_x=ones(Nt,4*seg_c);
r_x=y_x+Rr;

for n_pole=1:4
dthe_pole=2*pi/npr/2;
theta_mx=(n_pole-1)*dthe_pole;

for n_segc=1:seg_c
theta_x=x_x./Rm+theta_mx+(n_segc-1)*ratio*pi/npr/seg_c;
ploss_total_x=t_x;
nt=0;

for t=t_x
    nt=nt+1;
  at=floor(t*w*180/pi*60/Nt)+1;

dBrdt=zeros(nr,nts);dBthdt=zeros(nr,nts);hn1=1;ri=1;ti=1;
 for rm=r_x;
    c1k=((rm/Rm).^k+G1_1.*(rm/Rr).^-k); c2k=-k/rm.*c1k*1;
    c1k_t= k.*((rm/Rm).^k-G1_1.*(rm/Rr).^-k);c2k_t=-1/rm*c1k_t*1;
  for tm=theta_x;
   for i1=((0:nk-1)+1)
   dBrdt(ri,ti)=dBrdt(ri,ti)+ ...
         ((c2k(i1)*A1(i1,at)*sin(k(i1)*tm+k(i1)*omegar_t(at))+...
         c2k(i1)*C1(i1,at)*cos(k(i1)*tm+k(i1)*omegar_t(at)))-...
         (-c2k(i1)*A1(i1,at+1)*sin(k(i1)*tm+k(i1)*omegar_t(at+1))+...
```

```
          c2k(i1)*C1(i1,at+1)*cos(k(i1)*tm+k(i1)*omegar_t(at+1))))...
          /(time(at+1)-time(at));
 dBthdt(ri,ti)=dBthdt(ri,ti)+...
          ((c2k_t(i1)*A1(i1,at)*cos(k(i1)*tm+k(i1)*omegar_t(at))+ ...
          c2k_t(i1)*C1(i1,at)*sin(k(i1)*tm+k(i1)*omegar_t(at)))-...
          c2k_t(i1)*A1(i1,at+1)*cos(k(i1)*tm+k(i1)*omegar_t(at+1))+...
          c2k_t(i1)*C1(i1,at+1)*sin(k(i1)*tm+k(i1)*omegar_t(at+1))))...
          /(time(at+1)-time(at));
   end;
  end;
end;

Sx_m1=dBthdt';Sy_m1=dBrdt';
Sx_m2=horzcat(Sx_m1,-Sx_m1*Iyr_m);
Sx_m3=vertcat(Sx_m2,Ixr_m*Sx_m2);
Sx_v1=repmat(Sx_m3,[1 1 NzFFT]);
Sx_v2=cat(3,Sx_v1,-Sx_v1);
Sy_m2=horzcat(Sy_m1,Sy_m1*Iyr_m);
Sy_m3=vertcat(Sy_m2,-Ixr_m*Sy_m2);
Sy_v1=repmat(Sy_m3,[1 1 NzFFT]);
Sy_v2=cat(3,Sy_v1,-Sy_v1);
%%%%%%%%%%%%%%%%%%%%%%%%%%%%%%%%%%%%%%%%%%%%

%%%%% 3D FFT to generate field harmonics

%%%% For vector source in y-direction
fim_v=fftn(Sy_v2)/Nfft;
b_v=2*abs(fim_v(:,:,1:Nz/2));
b_v(:,:,1)=b_v(:,:,1)*0.5;
bangle_v=angle(fim_v(:,:,1:Nz/2));

% For vector source in x-direction
fim_v=fftn(Sx_v2)/Nfft;
a_v=2*abs(fim_v(:,:,1:Nz/2));
a_v(:,:,1)=a_v(:,:,1)*0.5;
aangle_v=angle(fim_v(:,:,1:Nz/2));

%%%%%%%%%%%%%%%%%%%%%%%%%%%%
%%%% Evaluate loss from each harmonic order

ploss_1=sum(sum(sum(b_v.^2.*k_v.^2*piz^2.*mnks_v)));
ploss_2=sum(sum(sum(a_v.^2.*k_v.^2*piz^2.*mnks_v)));
ploss_3=sum(sum(sum(b_v.^2.*m_v.^2*pix^2.*mnks_v)));
ploss_4=sum(sum(sum(a_v.^2.*n_v.^2*piy^2.*mnks_v)));
ploss_5=sum(sum(sum(-2*a_v.*b_v.*m_v*pix.*n_v*piy.*cos(bangle_v-
aangle_v).*mnks_v)));
ploss_total=ploss_1+ploss_2+ploss_3+ploss_4+ploss_5;

ploss_total_x(nt)=ploss_total;
%%%%%%%%%%%%%%%%%%%%%%%%%%%%
end
ploss_total_pole_x(:,(n_pole-1)*seg_c+n_segc)=ploss_total_x';
end
end
ploss_mac=sum(ploss_total_pole_x,2)*2*seg_a;
ploss_mac_seg_a=mean(ploss_mac);
plot(t_x,ploss_mac,'-ro');
ploss_mac_seg_a
```

```
ploss_seg_a_x(seg_a)=ploss_mac_seg_a;
end
%%%%%%%%%%%%%%%%%%%%%%%%%%%%%%%%%%%%%%%%%%%%%%%%%%%%%%%%%%%%%%%%%%%%%%%%%%%%%%%

plot(seg_a_x,ploss_seg_a_x,'-ro');
```

For the case with retaining sleeve, the dBrdt(ri,ti) and dBthdt(ri,ti) has to be evaluated for the sleeve region as per given in Script-7.

Before implementing the magnet loss prediction employing the results from the 2D FEA for both SPM and IPM, the flux density information need to fetched to generate flux density (B_x , B_y) matrices (4-D) carrying information at every x, y for each pole (based on machine symmetry) and each time instant (in steps for $1/6^{th}$ of an electrical cycle) before implementing in Script-7. The eddy current sources can be evaluated as below,

dBrdt (ri, ti) =Br(x, y, time, pole)-Br(x ,y, time-1, pole))/dt

dBthdt (ri, ti) =Bt(x, y, time, pole)-Bt(x, y, time-1, pole))/dt.

APPENDIX G
Evaluation of Axial Flux Density Variation for Implementing in 3D Fourier Method

The Script-10 to be run for evaluation of magnet flux density variation along the axial direction before implementing it with SCRIPT-9 for high frequency loss Prediction in SPM machines.

```
%%%% SCRIPT-10

%%%%%%%%%%%%%%%%%%%%%%%%%%%%%%%%%%%%%%%%%%%%%%%

INPUTS:

% name                        [unit]        [description]
ra      = 33.5e-3;%           [m]       Stator bore radius
rm      = 32.5e-3;%           [m]       Magnets outer radius
ri      = 29.5e-3; %          [m]       Rotor back-iron radius
uo      = 4*pi*1.0e-7;%      H/m]      Permeability of free space
KM      = 5.5556e+5;%       [S/m]      Conductivity of magnets
F       = 20e3; %             [F]       Frequency of the sinusoidal supply
p       = 4; %                []        Number of pole-pairs
Betam   = 0.9722; %           []        Magnet pole arc/pole pitch
LM     = 118.0e-3;%          [m]        Machine axial length
Jm     = 3250; %             [A/m]      peak current density
speed = 4500;%               [rpm]      Speed
seg_a   = input (' Number of Axial Segmentation) =');

seg_c   = input (' Number of Circumferential Segmentation) =');

% Calculated Parameters
rmean=(rm+ri)/2; %                [m]        mean magnet radius
d=(rm-ri) ;%                      [m]        Magnet height
Ag=(ra-rm);%                      [m]        Air gap  length
thetaM=360/(2*p)*pi/180*Betam;  [deg]      Magnet Angle
LM1=LM/ml;%                       [m]        Segmented axial length
tau=rmean*2*pi/(2*p);%            [m]        Magnet pole pitch
lm=rmean*thetaM;%                 [m]        Magnet width
lm1=thetaM/nl;%                   [m]        Segmented width
j=sqrt(-1);
g=d+Ag;
wb=2*pi*f;
w=2*pi*speed/60*p;
duration=(theta_rf*pi/180)/w;
Nt=180;
t_x=duration/Nt:duration/Nt:duration;
dt=t_x(1);t=dt;

%%%%%%%%%%%%%%%%%%%%%%%%%%%%%%%%%%%%%%%%%%%%%%%%%%%%%%%%%%%%%%%%%%%%%%%%%%%%%%%
```

```
NzFFT=200;
NxFFT=2^6;
nb=(1:2:100);
gamma = ra*sqrt((nb*pi/LM1).^2+(j*wb*uo*KM*d/g));
Jpn1=j*wb*uo*KM*Jm*d/g*4./(nb*pi).*sin(nb*pi/2)*ra^2;
Jpn2= (p)^2+(ra*nb*pi/LM1).^2+j*wb*uo*KM*d/g*ra^2;
Jpn=Jpn1./Jpn2;
C11n=uo*ra^2*sin(p*rmean/ra*lm1/2)./sinh(gamma*rmean/ra*lm1/2)./Jpn2;
C1n=j*wb*gamma*Jm*KM*d/g*4./(nb*pi).*sin(nb*pi/2)/(p).*C11n;
C22n=uo*ra^2*cos(p*rmean/ra*lm1/2)./cosh(gamma*rmean/ra*lm1/2)./Jpn2;
C2n=-wb*gamma*Jm*KM*d/g*4./(nb*pi).*sin(nb*pi/2)/(p).*C22n;

Jz=zeros(NzFFT,NxFFT);dJzbdx=zeros(NzFFT,NxFFT);Jx=zeros(NzFFT,NxFFT);
dJxbdz=zeros(NzFFT,NxFFT);
dBdtb=zeros(NzFFT,NxFFT);
ib=1;jb=1;

z_z=LM1/NzFFT*0.5:LM1/NzFFT:LM1-LM1/NzFFT*0.5;
x_x=lm1/NxFFT*0.5:lm1/NxFFT:lm1-lm1/NxFFT*0.5;

Phi=1*lm1;
for z=z_z-LM1/2
jb=1;
for x=x_x-lm1/2

Jzb=((C1n.*cosh(gamma*rmean/ra*x)*exp(j*(wb*t+Phi)) +...
    C2n.*sinh(gamma*rmean/ra*x)*exp(j*(wb*t+Phi)) -...
    Jpn.*exp(j*(wb*t-p*rmean/ra*x+Phi))).*cos(nb*pi/LM1*z))';

dJzbdx_b=((C1n.*gamma*rmean/ra.*sinh(gamma*rmean/ra*x)...
   *exp(j*(wb*t+Phi))+C2n.*gamma*rmean/ra.*cosh(gamma*rmean/ra*x...
   *exp(j*(wb*t+Phi))+j*p*rmean/ra*Jpn...
   .*exp(j*(wb*t-p*rmean/ra*x+Phi))).*cos(nb*pi/LM1*z))';

Jxb=((ra*C1n./gamma.*sinh(gamma*rmean/ra*x)*exp(j*(wb*t+Phi))+...
    ra*C2n./gamma.*cosh(gamma*rmean/ra*x)*exp(j*(wb*t+Phi))-...
    Jpn/(-j*p/ra).*exp(j*(wb*t-p*rmean/ra*x+Mag_t+Phi)))...
    .*(nb*pi/LM1).*sin(nb*pi/LM1*z))';

dJxbdz_b=((ra*C1n./gamma.*sinh(gamma*rmean/ra*x)...
      *exp(j*(wb*t+Phi))+ra*C2n./gamma.*cosh(gamma*rmean/ra*x)...
      *exp(j*(wb*t+Phi))-Jpn/(-j*p/ra)...
      .*exp(j*(wb*t-p*rmean/ra*x+Mag_t+Phi)))...
      .*((nb*pi/LM1).^2).*cos(nb*pi/LM1*z))';

Jz(ib,jb)= real(sum(Jzb,1));
dJzbdx(ib,jb)= sum(dJzbdx_b,1);
Jx(ib,jb)= sum(Jxb,1);
dJxbdz(ib,jb)= sum(dJxbdz_b,1);
dBdtb(ib,jb)=abs((1/rmean*dJzbdx(ib,jb)-dJxbdz(ib,jb))*1/(KM*d));

jb=jb+1;

end;
ib=ib+1;
end;
%%%%%%%%%%%%%%%%%%%%%%%%%%%%%%%%%%%%%%%%%%%%%%%%%%%%%%%%%%%%%%%%%%%%%%%%%%%%%%%
```